Titre: Title:	Amélioration de la simulation et de l'opération des puits à colonne permanente par des modèles adaptés aux contextes réels et incertains
Auteur: Author:	Louis Jacques
Date:	2025
Type:	Mémoire ou thèse / Dissertation or Thesis
Référence: Citation:	Jacques, L. (2025). Amélioration de la simulation et de l'opération des puits à colonne permanente par des modèles adaptés aux contextes réels et incertains [Thèse de doctorat, Polytechnique Montréal]. PolyPublie. https://publications.polymtl.ca/66991/

URL de PolyPublie: PolyPublie URL:	https://publications.polymtl.ca/66991/
Directeurs de recherche: Advisors:	Philippe Pasquier
Programme: Program:	Génie minéral

POLYTECHNIQUE MONTRÉAL
affiliée à l'Université de Montréal

Amélioration de la simulation et de l'opération des puits à colonne permanente par des modèles adaptés aux contextes réels et incertains

LOUIS JACQUES
Département de génies civil, géologique et des mines

Thèse présentée en vue de l'obtention du diplôme de *Philosophiæ Doctor*
Génie minéral

Juin 2025

POLYTECHNIQUE MONTRÉAL
affiliée à l'Université de Montréal

Cette thèse intitulée :

Amélioration de la simulation et de l'opération des puits à colonne permanente par des modèles adaptés aux contextes réels et incertains

présentée par **Louis JACQUES**
en vue de l'obtention du diplôme de *Philosophiæ Doctor*
a été dûment acceptée par le jury d'examen constitué de :

Ahmad SHAKIBAEINIA, Ph.D., président
Philippe PASQUIER, Ph.D., membre et directeur de recherche
Dany LAUZON, Ph.D.,membre
John MOLSON, Ph.D.,membre externe

DÉDICACE

It is the tension between creativity and skepticism that has produced the stunning and unexpected findings of science. – Carl Sagan

REMERCIEMENTS

En pleine période d'incertitude liée à la pandémie de COVID-19, Philippe Pasquier m'a offert l'opportunité de poursuivre des études doctorales au sein de la Chaire de recherche en géothermie sur l'intégration des puits à colonne permanente. Je tiens donc à le remercier non seulement pour la confiance qu'il m'a accordée, mais aussi pour sa grande disponibilité et sa sagesse.

Ensuite, je souhaite également exprimer ma profonde gratitude aux membres du jury, Ahmad Shakibaeinia, Dany Lauzon et John Molson, pour le temps qu'ils ont consacré à la lecture de cette thèse. Leurs commentaires pertinents et leur regard critique ont grandement contribué à enrichir ce travail.

À mes collègues, Gabriel Dion, Léo Cerclet et Gabrielle Beaudry, je tiens à exprimer mes plus chaleureux remerciements pour le soutien apporté, ainsi que pour vos conseils inestimables. Bien sûr, je remercie aussi mes nombreux autres collègues d'étude pour toutes les discussions constructives et les moments partagés. Enfin, je tiens également à remercier mes collègues de CanmetÉNERGIE, en particulier Alain Nguyen, dont l'expertise et l'engagement ont apporté un appui précieux à plusieurs étapes de ce travail.

Merci à ma conjointe de vie, Sarah-Jane, pour sa patience et ses encouragements tout au long de cette aventure. Un grand merci à ma famille et mes amis pour leur soutien indéfectible et pour ne pas avoir trop souvent posé la question qui tue. Il y a un proverbe qui dit qu'« il faut un village pour élevé un enfant » et cette expérience m'a également appris qu'il faut un village pour accomplir un doctorat.

Finalement, j'offre mes plus sincères remerciements aux partenaires de la Chaire de recherche en géothermie sur l'intégration des PCP dans les bâtiments institutionnels, plus précisément, Hydro-Québec, le Ministère de l'Enseignement supérieur du Québec, Centre de services scolaire des Mille-Îles, Centre de services scolaire de Montréal, Centre de services scolaire des Samares, Versaprofiles, Marmott Énergies, CanmetÉNERGIE et le Conseil de recherches en sciences naturelles et en génie du Canada.

RÉSUMÉ

Les pompes à chaleur géothermiques offrent une solution pour atteindre les objectifs canadiens de carboneutralité dans le secteur du bâtiment. Grâce à leurs performances élevées, ces systèmes assurent également une réduction de l'appel de puissance électrique sur les réseaux. Parmi les différents types d'échangeurs de chaleur souterrains, les puits à colonne permanente se distinguent par leur efficacité thermique supérieure, leur coût de construction moindre et leur capacité à s'adapter à des milieux aux urbains denses. Tout ceci est dû à plusieurs facteurs, à savoir une construction profonde et ouverte au roc, l'échange de chaleur direct avec l'eau souterraine, une flexibilité offerte par la gestion des débits de circulation et par l'opération d'une saignée. À cet effet, l'activation d'une saignée engendre un écoulement convergent forcé d'eau souterraine, ce qui renforce considérablement le transfert thermique par advection et donc également les performances thermiques du système.

Pour soutenir les objectifs de carboneutralité dans le secteur du bâtiment, l'implantation des puits à colonne permanente doit être accélérée et il convient de fournir aux professionnels les outils nécessaires pour concevoir et opérer plus simplement ces échangeurs. Les outils requis doivent notamment inclure des modèles et méthodes de simulation adaptés à la dynamique hydraulique et thermique relative à l'opération des puits à colonne permanente. Les modèles analytiques offrent généralement une grande rapidité de calcul, permettant d'accéder à des analyses de sensibilité et à des études stochastiques. À ce jour, pour les puits à colonne permanente, un seul modèle analytique considère le transfert de chaleur advectif sollicité par l'opération de la saignée, mais ce modèle n'a toutefois pas été validé expérimentalement. Puis, les modèles numériques incluent un niveau de détail supérieur, tel que les phénomènes régionaux, les interactions entre plusieurs puits et le contexte hydrostratigraphique, notamment une l'hétérogénéité sous forme de couches horizontales. Cette sophistication rend ces derniers complexes à concevoir et requiert davantage de puissance de calcul. Une dernière gamme concerne les modèles empiriques expérimentaux construits à l'aide d'algorithmes de déconvolution. Par construction, ces derniers sont moins flexibles que les autres types de modèles, mais deviennent essentiels pour analyser la performance thermique des systèmes et évaluer le comportement des puits à colonne permanente selon différentes stratégies d'opération. Les principales stratégies comprennent la recirculation complète ou l'opération d'une saignée. Cependant, la saignée nécessite généralement un puits d'injection pour retourner l'eau dans l'aquifère d'origine, ce qui engendre des coûts supplémentaires pour sa construction et son entretien. Pour résoudre ce problème, une stratégie existe pour la réinjection des rejets de saignée entre les puits à colonne permanente, mais son efficacité n'a jamais été démontrée

sur un bâtiment en fonctionnement.

Alors, l'objectif général de cette thèse est d'améliorer l'applicabilité, la robustesse et la précision des modèles et des stratégies d'opération des puits à colonne permanente afin de favoriser leur adoption par l'industrie et de diminuer l'empreinte énergétique du secteur du bâtiment. L'étape initiale est d'étendre la portée de l'unique modèle analytique incorporant l'opération de la saignée, afin de le valider expérimentalement pour la première fois et de faciliter son utilisation dans des conditions réalistes d'exploitation. Dans un contexte hydrostratigraphique présentant une hétérogénéité en couches, des modèles numériques ont déjà été validés expérimentalement, mais l'impact de l'incertitude des paramètres d'entrée n'a jamais été exploré. Or, cette incertitude affecte directement la fiabilité des simulations utilisées en phase de conception. Alors, une deuxième étape consiste à quantifier l'incertitude des propriétés thermiques et hydrauliques ceinturant un puits à colonne permanente, afin d'améliorer la robustesse des simulations. En dernier lieu, la stratégie d'opération par réinjection entre puits est étudiée comme alternative aux puits d'injection requis lors de la saignée. Pour ce faire, une étude est réalisée à l'aide de modèles empiriques déduits de mesures expérimentales.

Le modèle analytique original est développé dans un milieu homogène et isotrope et se limite à la variation de température à la paroi du forage. La validation du modèle analytique nécessite alors le développement de nouvelles relations mathématiques permettant une utilisation dans un contexte expérimental *in situ*. De nouvelles approches ont donc été proposés afin de considérer l'hétérogénéité en couches par des propriétés effectives et de calculer le transfert thermique dans le puits à l'aide d'un réseau de résistances thermiques. Ce nouveau cadre théorique a été confronté à trois essais de terrain différents, permettant de démontrer une justesse du modèle par une moyenne des erreurs absolues variant de 0,28 à 0,37 °C, soit du même ordre de grandeur que la justesse des capteurs de température. Les approches proposées constituent une avancée significative dans la modélisation des puits à colonne permanente. La rapidité de calcul, la simplicité et la justesse de ce modèle, désormais démontrées, en font un choix par excellence pour concevoir un système par le biais d'optimisations ou d'analyses paramétriques.

Ensuite, les modèles numériques restent les plus exacts pour simuler un contexte hydrostratigraphique hétérogène, et ce, pour différents ordres de grandeur de conductivités hydrauliques. Ainsi, pour démontrer l'effet de l'incertitude des propriétés hydrauliques et thermiques dans un milieu géologique fortement hétérogène, un essai de réponse thermique a été interprété dans un cadre bayésien en utilisant un réseau neuronal artificiel pour émuler un modèle numérique. Une précision variant de 14 à 18 % a été démontrée concernant les propriétés hydrauliques et thermiques identifiées pour les différentes unités hydrostratigraphiques et

unités géologiques. Les températures résultantes de l'inférence des propriétés ont maintenues une justesse de 0,04 °C. L'inférence des propriétés hydrauliques a donc été réalisée à partir de mesures de la température uniquement, ce qui souligne l'importance de la composante advective dans la dynamique des puits à colonne permanente.

L'opération de la saignée tire avantage de la chaleur transférée par advection, ce qui augmente l'efficacité des puits à colonne permanente. Typiquement, des puits d'injection sont nécessaires pour recevoir les volumes d'eau rejetés, ce qui augmente les coûts de construction des systèmes de puits à colonne permanente. Dans un système à multiple puits à colonne permanente, la réinjection entre puits permet de simplifier la gestion de l'eau souterraine rejetée par l'opération de la saignée, en la redirigeant vers d'autres puits à colonne permanente dans le système. Un essai de 35 jours avec cinq puits à colonne permanente échangeant la chaleur avec un bâtiment en opération a démontré que la réinjection entre puits est caractérisée par une efficacité accrue par rapport à l'opération de base de recirculation complète des puits. Cette efficacité thermique est cependant légèrement inférieure à celle d'une opération purement en saignée, mais conserve les volumes d'eau dans les puits à colonne permanente, permettant de s'affranchir d'un puits d'injection pour la gestion de l'eau de saignée. Cette démonstration a été réalisée à l'aide d'analyses de modèles empiriques expérimentaux obtenus par déconvolution, chacun de ces modèles représentant une stratégie d'opération unique. L'utilisation à rebours de ces modèles empiriques pour reproduire les températures observées a montré une moyenne des erreurs absolues d'environ 0,04 °C, ce qui démontre la justesse de ces modèles.

En conclusion, les modèles analytiques, numériques et empiriques étudiés dans cette thèse présentent tous des justesses appréciables suivant des validations expérimentales. Leurs utilités, limites et avantages distincts en font un ensemble d'outils complémentaires et cohérents pour soutenir la caractérisation, la conception et la simulation de différentes stratégies de contrôle des puits à colonne permanente. Ces travaux contribuent à surmonter des obstacles techniques importants et à accélérer l'adoption des puits à colonne permanente comme une solution clé pour la transition énergétique.

ABSTRACT

Ground source heat pumps offer a solution to meeting Canada's net-zero emissions targets in the building sector. Because of their high performance, these systems also enable a reduction in peak electricity demand on the grid. Among the various types of ground heat exchangers, standing column wells stand out for their superior thermal efficiency, lower construction costs and ability to adapt to dense urban environments. This is due to a number of factors, including deep and open construction in rock, direct heat exchange with groundwater and the flexibility offered by flow management and bleed activation. To this end, the bleed operation creates a forced convergent flow of groundwater, which significantly enhances heat transfer by advection and therefore the thermal performance of the system.

To support net-zero targets in the building sector, the implementation of standing column wells needs to be accelerated and professionals need to be given the tools to design and operate these exchangers more simply. In particular, the tools required must include simulation models and methods adapted to the hydraulic and thermal dynamics involved in their operation. Analytical models generally offer high computational speed, enabling sensitivity analysis and stochastic studies. To date, only one analytical model for standing column wells considers advective heat transfer associated with the bleed operation, yet this model has not been experimentally validated. In comparison, numerical models incorporate a higher level of detail, such as regional phenomena, the interactions between multiple wells and the hydrostratigraphic context, particularly heterogeneity in the form of horizontal layers. This sophistication makes them complex to design and requires more computing capacity. The last category concerns empirical models built using deconvolution algorithms and experimental data. The latter category is less flexible by design than other types of models, but is essential for analyzing the thermal performance of systems and evaluating the behavior of standing column wells under different operating strategies. The main strategies include full recirculation or bleed operation. However, the bleed operation generally requires the use of an injection well to return the water to the original aquifer, which incurs additional well construction and maintenance costs. To solve this problem, a reinjection strategy exists to maintain discharge among standing column wells, but its performance has never been demonstrated with an actual building in operation.

Therefore, the overall objective of this thesis is to improve the applicability, robustness, and accuracy of models and operational strategies for standing column wells in order to promote their adoption for industry and reduce the energy footprint of the building sector. The

first step is to extend the scope of the only analytical model that includes bleed operation to provide previously unattempted experimental validation and facilitate use under realistic operating conditions. In a hydrostratigraphic context with layered heterogeneity, numerical models have already been experimentally validated, but the impact of input parameter uncertainty has never been explored. In fact, the uncertainty directly affects the reliability of the simulations used in the design phase. Therefore, a second step is to quantify the uncertainty of the thermal and hydraulic properties surrounding a standing column well, in order to improve the robustness of the simulations. Lastly, the strategy of inter-well reinjection is studied as an alternative to the injection wells required for the bleed operation. To this end, empirical models derived from experimental measurements are used.

The original analytical model is developed for a homogeneous, isotropic medium and is limited to temperature variation at the borehole wall. Validation of the analytical model requires the development of new mathematical relationships for use in an experimental *in situ* context. Therefore, new approaches have been proposed to account for layer heterogeneity through effective properties and to calculate heat transfer in the well using a network of thermal resistances. This new theoretical framework is then tested with three different field experiments, demonstrating the accuracy of the model with mean absolute errors ranging from 0.28 to 0.37 °C, which is in the same order of magnitude as the accuracy of the temperature sensors. The proposed approaches represent significant breakthroughs in the modelling of standing column wells. The high computational speed, simplicity, and accuracy of this now-validated model make it an unparalleled choice for system design through optimization or parametric analysis.

On the other hand, numerical models remain the most accurate for simulating a heterogeneous hydrostratigraphic context, for different orders of magnitude of hydraulic conductivities. Thus, to demonstrate the effect of uncertainty in hydraulic and thermal properties in a highly heterogeneous geological environment, a thermal response test has been interpreted in a Bayesian framework using an artificial neural network to emulate a numerical model. A precision of 14 to 18% has been demonstrated for the hydraulic and thermal properties identified for the different hydrostratigraphic and geological units. Temperatures resulting from the property inference maintained an accuracy of 0.04 °C. Inference of hydraulic properties has therefore been based on temperature measurements alone, underlining the importance of the advective component in the dynamics of standing column wells.

Bleed operation takes advantage of heat transfer by advection, which enhances the performance of standing column wells. Typically, injection wells are required to receive the volumes of water discharged, which increases the construction cost of standing column well

systems. In a system with multiple standing column wells, inter-well reinjection simplifies the management of groundwater rejected by the bleed operation by diverting it to other standing column wells in the system. A 35-day experiment with five standing column wells exchanging heat with an operating building demonstrated that inter-well reinjection is more efficient than the basic operation of full recirculation. This thermal efficiency is slightly less than a bleed-only operation, but preserves the water volumes in the standing column well system, making it possible to dispense with an injection well for bleed water management. This demonstration has been carried out using analyses of experimental empirical models obtained by deconvolution, each representing a unique operating strategy. Using these empirical models to reproduce observed temperatures showed an mean absolute error of about 0.04 °C, demonstrating the accuracy of these models.

In conclusion, the analytical, numerical and empirical models studied in this thesis all show appreciable accuracy after experimental validation. Their different capabilities, limitations and advantages make them a complementary and coherent set of tools to support the characterization, design, and simulation of various control strategies for standing column wells. The work presented in this thesis contributes to overcome major technical obstacles and accelerate the adoption of standing column wells as a leading solution for the energy transition.

TABLE DES MATIÈRES

LISTE DES TABLEAUX

LISTE DES FIGURES

LISTE DES SIGLES ET ABRÉVIATIONS

Acronymes

ÉCS	Échangeur de chaleur souterrain
ERT	Essai de réponse thermique
GES	Gaz à effet de serre
LIT	Linéaires invariants dans le temps
PàC	Pompe à chaleur
PBF	Puits en boucle fermée
PCP	Puits à colonne permanente
PI	Puits d'injection
SCI	Source cylindrique infinie
SLF	Source linéique finie
SLI	Source linéique infinie
RCT	Résistance et capacité thermique
RNA	Réseau de neurones artificiel

LISTE DES ANNEXES

CHAPITRE 1 INTRODUCTION

Dans le cadre de la lutte contre les changements climatiques, l'Accord de Paris, ratifié par la communauté internationale en 2015, établit l'objectif suivant : limiter l'augmentation de la température mondiale moyenne à moins de 2 °C par rapport aux niveaux préindustriels [1]. Afin d'atteindre cet objectif, le Canada et 16 autres pays ont adopté en 2022 un cadre de travail commun en vue de la carboneutralité, soit un bilan net nul d'émissions de gaz à effet de serre (GES) d'ici 2050 [2]. Dans cette optique, le gouvernement du Canada s'est doté d'une stratégie à multiples volets, prévoyant notamment que toutes les nouvelles constructions fédérales soient carboneutres [3]. Cet objectif ambitieux souligne la nécessité de repenser les systèmes énergétiques, en particulier pour faciliter la transition vers des énergies renouvelables et des solutions plus efficaces.

À l'heure actuelle, le secteur du bâtiment au Canada représente environ 25% de la consommation énergétique totale du pays, dont plus de 50% est attribuable à l'utilisation de combustibles fossiles [4]. Pour le chauffage et la climatisation des bâtiments, la transition énergétique repose principalement sur deux leviers complémentaires : la substitution des énergies fossiles par des énergies renouvelables et la diminution de la demande énergétique grâce à des mesures d'efficacité énergétique [5]. Ces leviers sont interdépendants puisque le remplacement des équipements alimentés par des énergies fossiles par des systèmes reliés au réseau électrique augmentera inévitablement la demande énergétique, exerçant ainsi une pression accrue sur le réseau électrique. Or, malgré l'existence de solutions technologiques éprouvées, un sous-investissement dans les infrastructures électriques pourrait freiner l'atteinte des objectifs de carboneutralité d'ici 2050 [5].

Parmi les différentes options technologiques permettant de réduire la dépendance aux combustibles fossiles dans le secteur du bâtiment, la géothermie s'impose comme une solution prometteuse puisqu'elle contribue également à alléger la pression sur le réseau électrique [6]. Contrairement à certaines idées préconçues, la géothermie utilisée pour le chauffage des bâtiments au Canada mise bien plus sur les basses températures accessibles près de la surface que sur les hautes températures en profondeur. En effet, dans certaines régions clés comme les Basses-terres du Saint-Laurent, le gradient thermique est relativement faible [7], et il faut forer à plus de 2 km de profondeur pour atteindre une température suffisante au chauffage direct d'un espace, soit plus de 60 °C [8]. Cela dit, les coûts élevés du forage pour atteindre ces profondeurs rendent cette option peu réaliste. Ainsi, le chauffage et la climatisation des bâtiments par la géothermie reposent principalement sur des systèmes indirects, faisant appel

à une pompe à chaleur (PàC) couplée à un échangeur de chaleur souterrain (ÉCS). L'ÉCS est constitué d'un réseau de tuyauterie souterrain dans lequel circule un fluide chargé d'échanger de la chaleur avec le sol et la roche à proximité, par extraction ou dissipation, selon les besoins énergétiques du bâtiment. Les systèmes de PàC géothermiques constituent aujourd'hui la principale forme d'application de la géothermie dans le secteur du bâtiment au Canada. Dans les systèmes de PàC géothermique, l'énergie thermique produite est 3 à 5 fois supérieure à l'énergie électrique consommée [9]. Ce rendement élevé assure non seulement d'améliorer l'efficacité énergétique des bâtiments, mais aussi de réduire l'appel de puissance électrique au réseau.

Les gains d'efficacité énergétique découlant de l'utilisation de PàC géothermiques passent par le dimensionnement, par les stratégies de contrôle et par le choix du type d'ÉCS [10, 11]. Parmi les différents types d'ÉCS, les puits en boucle fermée verticale (PBF) demeurent les plus couramment étudiés et installés [12–14]. Comme illustré à la Figure 1.1 (a), l'opération des PBF verticaux s'effectue à l'aide d'un fluide caloporteur qui circule dans un réseau de tuyauterie fermée, installé dans un forage vertical. L'échange de chaleur conductif entre le fluide et le milieu géologique s'effectue indirectement à travers les tuyaux et les matériaux de remplissage. Généralement, le fluide caloporteur est un mélange de propylène glycol et d'eau, ce qui permet d'abaisser le point de congélation et d'opérer à des températures plus basses, tandis que les tuyaux sont en PEHD et les matériaux de remplissage sont composés d'un mélange de sable et de bentonite [10]. Ce type d'ÉCS est souvent préconisé en raison de la facilité de construction, de conception et des faibles coûts d'entretien. Son niveau de maturité se reflète dans l'existence de nombreux systèmes comportant des centaines de puits, à l'instar de celui de l'aéroport de Vancouver, qui compte 850 PBF de 152 m, l'un des plus grands projets de ce type au Canada [15].

Ainsi, il est important d'expliquer que lors du dimensionnement des ÉCS, une des principales variables guidant le nombre de puits requis sont les besoins énergétiques du bâtiment en chauffage et climatisation [16]. Le nombre de puits sera également contraint par la superficie disponible sur le site du projet. Cette limitation de l'espace, particulièrement en milieu urbain dense, peut devenir un obstacle majeur pour les systèmes géothermiques reposant sur les PBF. Ceux-ci nécessitent en effet un vaste espace pour installer de nombreux puits.

Afin de s'affranchir des limitations des PBF, un autre type d'ÉCS s'impose comme une solution : le puits à colonne permanente (PCP). Comme présenté à la Figure 1.1 (b), l'exploitation des PCP utilise l'eau souterraine comme fluide caloporteur dans une boucle semi-ouverte. Ce principe améliore l'efficacité des échanges thermiques, en combinant la conduction directe avec la paroi du forage et l'advection avec l'aquifère environnant. En pratique, la capacité

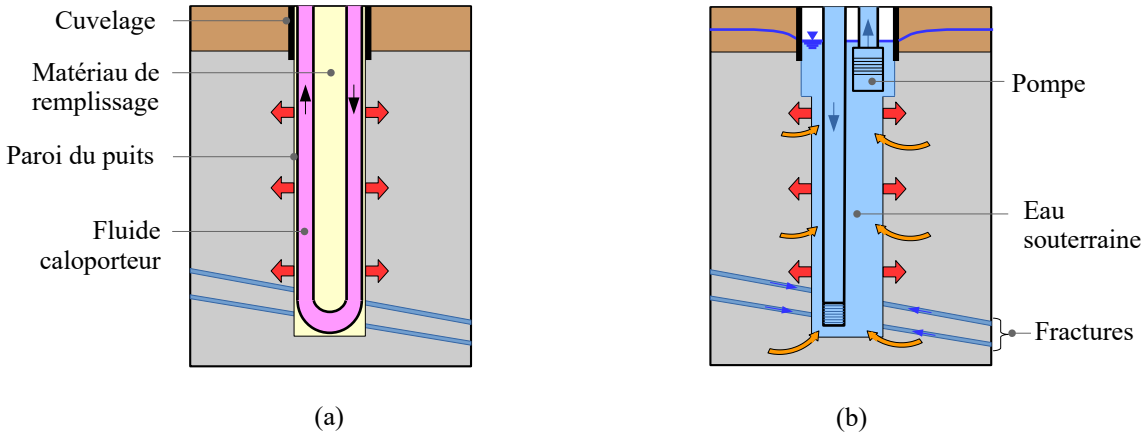

FIGURE 1.1 Représentation schématique d'un ÉCS de type a) puits en boucle fermée verticale et b) puits à colonne permanente, où les flèches rouges indiquent un échange de chaleur par conduction et les flèches orange par advection. ; aucune échelle.

des PCP à échanger des puissances plus élevées se traduit par un nombre réduit de puits, par rapport aux PBF, pour satisfaire les besoins énergétiques d'un bâtiment donné [17]. De plus, les PCP sont généralement forés à des profondeurs plus importantes que les PBF, comme indiqué au Tableau 1.1, ce qui, combiné à leur puissance linéaire plus élevée, permet de diminuer l'empreinte au sol des projets.

TABLEAU 1.1 Comparaison des principales caractéristiques des ÉCS de type PCP et PBF.

ÉCS	**PBF**	**PCP**
Profondeur	50 à 150 m [18–20]	75 à 670 m [21–23]
Puissance linéaire	50 à 80 W/m [14, 24]	105 à 385 W/m [21, 25]
Transferts de chaleur	Conduction	Conduction & Advection
Milieux de transfert	Dépôt meuble et roc	Roc
Fluide caloporteur	Eau et antigel	Eau souterraine

Dans un système de PCP, l'eau est pompée et retournée dans le même puits selon deux modes de réinjection : la recirculation complète ou la réinjection partielle par l'utilisation d'une saignée [26]. Dans l'opération par recirculation complète, l'entièreté du débit d'eau pompé est réinjectée dans le PCP et, à moins de venues d'eau importantes, la chaleur est majoritairement échangée par conduction le long de la paroi de forage [27]. En revanche, dans le mode avec saignée, une fraction du débit d'eau pompé, variant de 0 à 30% en pratique [26, 28], est déviée hors du PCP. Ce rejet partiel crée une dépression au sein du PCP, ce qui sollicite un écoulement convergent d'eau souterraine fraîche. Alors, cet écoulement convergent engendré par l'opération de la saignée améliore significativement les performances thermiques,

en augmentant la contribution de l'advection par rapport à la conduction [22, 26]. De plus, l'action de la saignée contribue à restaurer les conditions thermiques du sous-sol autour du PCP, permettant de s'affranchir partiellement, voire totalement, du besoin de balancer les charges thermiques saisonnières qui contraint les systèmes de PBF. Pour cette raison et pour leurs performances accrues, les coûts d'investissement initiaux des systèmes de PCP sont de 32% à 80% inférieurs à ceux des systèmes de PBF, en plus de délais de construction moindre [17,29]. Ainsi, les PCP s'avèrent être un choix idéal dans le contexte de décarbonation, car ils sont moins coûteux et plus rapides à construire, plus efficaces et adaptés aux milieux urbains denses.

La Cathédrale Saint-Patrick, en plein cœur de Manhattan à New York, est un parfait exemple de l'implantation d'un système géothermique utilisant des PCP dans un environnement densément construit. Ce système utilise un nombre de 10 PCP, forés à 670 m de profondeur dans un espace restreint en périphérie du bâtiment, pour couvrir l'ensemble des besoins de chauffage et de climatisation, qui atteignent respectivement des puissances maximales de 850 kW et 940 kW [23, 30]. De plus, l'utilisation de la géothermie a permis d'éviter l'agrandissement de la salle mécanique, une solution qui aurait été nécessaire avec un système conventionnel de chauffage et climatisation [31]. Un autre exemple notable se trouve au Zoo du Bronx, où cinq PCP de 460 m de profondeur ont été installés pour des puissances maximales en chauffage de 310 kW et en climatisation de 200 kW au bâtiment du Lion [32]. Dans ces deux projets à New York, les PCP assurent une puissance thermique de 135 à 140 W/m, soit bien plus que les puissances thermiques typiques rapportées pour les PBF de l'ordre de 50 à 80 W/m [14, 24]. Ces résultats confirment l'efficacité supérieure des PCP en matière de performances thermiques et leur application en milieu urbain dense.

Selon Orio (1994) [33], l'idée des PCP a émergé à la fin des années 1970 parmi les foreurs et hydrogéologues de l'état du Maine et une première publication sur le sujet date de 1983 par Braud [34]. Orio (1994) [33] rapporte que, sur cinq projets de PCP construits et opérés entre 1980 et 1994, la puissance thermique unitaire des PCP variait de 105 à 385 W/m. Une décennie plus tard, Orio (2005,2006) [21, 35] analyse les performances de 22 systèmes, totalisant 40 PCP, et note une variation de puissance thermique unitaire allant de 176 W/m à 385 W/m. Des études plus récentes dans des climats froids ont confirmé des puissances thermiques variant de 120 à 300 W/m [14, 17, 25, 36]. Dans ces climats, les puissances élevées des PCP représentent alors entre 1.5 à 6 fois plus de puissance que les PBF.

Il est à noter que la recherche appliquée aux PCP a progressé à un rythme plus lent que celle dédiée aux PBF [14], limitant ainsi le développement d'outils adaptés et ralentissant leur déploiement. Afin de s'aligner avec les recommandations de l'Institut Trottier visant à

atteindre la décarbonation du secteur du bâtiment d'ici 2050 au Canada, il devient impératif d'accélérer la recherche et d'outiller les professionnels [5]. C'est dans cette perspective que s'inscrit la présente thèse, réalisée au sein de la Chaire de recherche en géothermie sur l'intégration des PCP dans les bâtiments institutionnels [37]. Elle vise à analyser et valider expérimentalement des solutions permettant de lever certaines barrières techniques, notamment en lien avec la modélisation des PCP, la caractérisation du sous-sol et les stratégies d'opération. La revue de littérature qui suit explore ces enjeux, en suivant le cheminement naturel d'un projet PCP : de la simulation préliminaire, à la mesure des propriétés réelles, jusqu'à l'opération du système et sa validation expérimentale.

CHAPITRE 2 REVUE DE LITTÉRATURE

Les avancées scientifiques concernant les PCP sont confrontées à plusieurs défis, principalement liés à la modélisation des échanges thermiques et hydrauliques dans ou autour des PCP. En effet, les hypothèses, les limites et les incertitudes des modèles jouent un rôle déterminant dans l'exactitude des simulations et, par conséquent, dans le dimensionnement des systèmes. Cette revue de littérature propose donc d'explorer les enjeux de la modélisation et de la simulation des PCP, en passant par la caractérisation du sous-sol, les modes d'opération des systèmes et la validation expérimentale.

2.1 Modéliser et simuler les PCP : naviguer entre justesse, rapidité et complexité

La simulation est un outil essentiel pour reproduire la performance thermique des systèmes, optimiser leur conception et leur fonctionnement, et évaluer les impacts à long terme sur la ressource souterraine. La simulation des PCP repose sur des modèles capables de représenter l'écoulement souterrain ainsi que les transferts de chaleur par conduction et advection autour des puits. Différentes approches de modélisation ont été développées, se distinguant par leur niveau de détail et leur efficacité de calcul. Certaines approches se limitent à un puits dans un milieu poreux homogène, tandis que d'autres intègrent des processus plus fins, comme l'effet de la saignée, l'hétérogénéité de l'aquifère ou les interactions entre plusieurs puits.

2.1.1 Modélisation

La modélisation physique des PCP vise à représenter les principaux mécanismes qui influencent leur performance, soit les propriétés thermiques et hydrauliques des unités hydrostratigraphiques, l'écoulement souterrain et les effets induits par l'opération du puits [27,38–40]. La simulation de l'effet de la saignée est cruciale pour reproduire avec justesse les performances thermiques à long terme, ce qui souligne l'importance de son intégration dans les modèles physiques [26]. Pour représenter les phénomènes susmentionnés, la Figure 2.1 présente l'évolution des principes proposés dans le développement des modèles analytiques pour PCP dans la littérature.

Des modèles analytiques purement conductifs ont été utilisés pour analyser la réponse thermique d'un PCP, comme le modèle classique de la source linéique infinie (SLI) [41, 42]. La Figure 2.1 (a) présente le principe du modèle de la SLI, à savoir la superposition infinie de

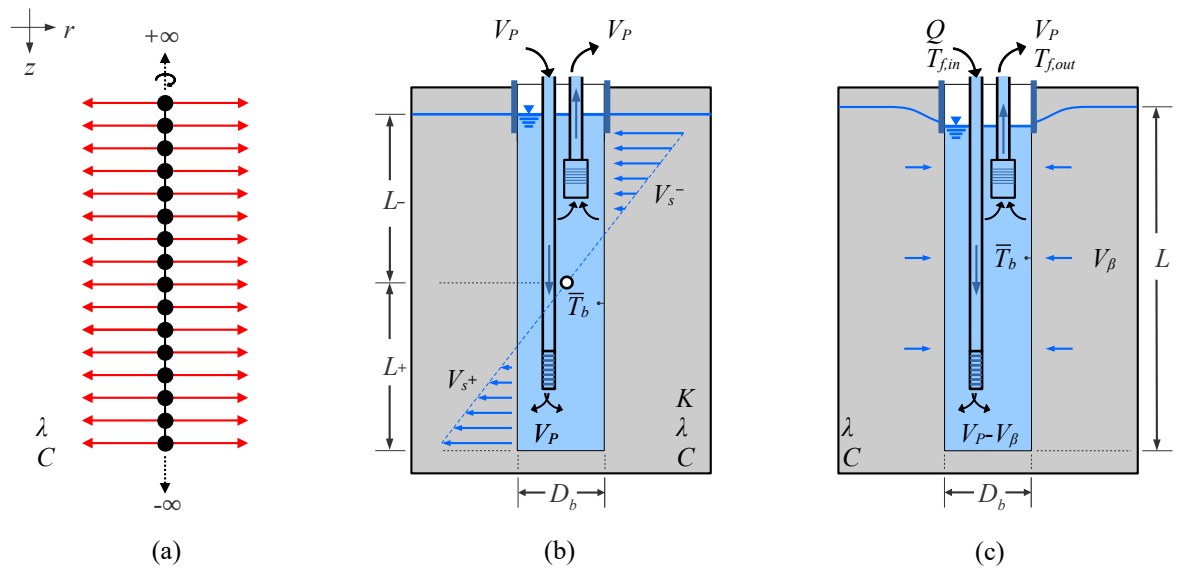

FIGURE 2.1 Représentation des principes utilisés dans les modèles analytiques pour les PCP, soit a) la conduction comme une source linéique infinie, b) l'écoulement autour d'un PCP en recirculation continue et c) l'opération de la saignée.

sources ponctuelles de chaleur sur une ligne verticale, alors que l'équation 2.1 décrit ce modèle en y ajoutant la température non perturbée du milieu géologique (T_0) :

$$\overline{T}_b(t) = T_0 + \frac{q}{4\pi\lambda}\int_u^\infty \frac{e^{-\psi}}{\psi}d\psi \quad \text{, avec} \quad u = \frac{r_b^2}{4t}\frac{C}{\lambda} \tag{2.1}$$

où la variable $\overline{T}_b$ est la température moyenne à la paroi du forage, q est l'impulsion de chaleur linéaire, r_b est le rayon du forage et C et λ sont respectivement la capacité thermique volumique et la conductivité thermique. Le modèle de la SLI ne prend pas en compte le transfert de chaleur par advection, ce qui réduit la justesse de ce modèle pour reproduire la réponse thermique d'un PCP lorsque la conductivité hydraulique (K) devient élevée, typiquement lorsque $K > 5$ x 10^{-5} m/s [39]. Il est par ailleurs important de noter que, dans de telles conditions, l'advection peut fortement influencer les échanges thermiques, même en mode de recirculation complète, c'est-à-dire sans saignée [27].

Le pompage et la réinjection dans un PCP modifient le champ de pression de l'eau souterraine, entraînant un écoulement convergent vers la zone de pompage et un écoulement divergent autour du point de réinjection (Figure 2.1 (b)). Pour calculer l'effet du transfert de chaleur advectif engendré par cet écoulement, Yuill et Mikler (1995) [38] ont introduit le principe du point de balance pour un milieu homogène et isotrope, ainsi qu'un cadre théorique

permettant de calculer l'amplitude d'écoulement convergent et divergent. Pour utiliser cette dernière approche, il faut au préalable observer les niveaux d'eau avant et après l'activation du PCP et estimer la conductivité hydraulique du milieu. Le modèle développé ne considère cependant pas l'écoulement de la saignée et n'offre pas une solution lorsque le contexte hydrostratigraphique est hétérogène.

Dans ce même contexte, sans l'opération d'une saignée et en milieu homogène, un modèle approximatif a été développé dans l'objectif de guider l'espacement des PCP lors du dimensionnement [43]. Ce modèle approximatif calcule un facteur d'interférence thermique dans une série de PCP installés sur une ligne horizontale infinie. Toutefois, cette approche demeure conservatrice, car elle néglige l'écoulement souterrain induit par la saignée, lequel peut considérablement altérer la réponse thermique d'un PCP [25, 44].

Récemment, un modèle analytique considérant l'opération de la saignée sur un seul PCP a été développé par Nguyen et al. (2025) [45]. Ce modèle, nommé β-SLI dans le présent document, est présenté à la Figure 2.1 (c) et son développement est rapporté en Annexe A. Le modèle β-SLI repose sur une expression analytique inspirée par les travaux de Thiéry (2022) [46] concernant des essais de traceurs en hydrogéologie. En présence de la saignée, le modèle β-SLI utilise une fonction agissant comme facteur d'échelle pour ajuster la réponse thermique du modèle de la SLI en fonction de l'amplitude de l'écoulement radial et convergent. Ainsi, Nguyen et al. (2025) [45] ont démontré que ce modèle d'advection et diffusion offre une solution juste, est facile d'utilisation et possède un coût de calcul négligeable, tout en utilisant des propriétés adimensionnelles.

Avant la publication du modèle β-SLI, les modèles numériques étaient les seuls à même de reproduire l'effet de la saignée sur la réponse thermique. Ces modèles ont d'abord été développés avec la même hypothèse d'un milieu homogène et isotrope, comme l'illustre la Figure 2.2 (a) [26, 28, 47–49]. Dans ces modèles, la simulation de l'effet de la saignée est rendue possible grâce au couplage des physiques de transfert de chaleur et d'écoulement de l'eau souterraine. Plusieurs niveaux de complexité ont été proposés pour ces modèles, dont une modélisation tridimensionnelle intégrant la géométrie du puits [48] et l'ajout de plusieurs puits [49], ou visant une rapidité de calcul par une axisymétrie [50] ou une méthode de différences finies [28].

Considérant que des PCP ont été construits jusqu'à des profondeurs de 670 m (voir le Tableau 1.1), il est peu probable que le contexte hydrostratigraphique soit homogène sur une telle épaisseur. Ainsi, plusieurs modèles numériques ont été développés pour intégrer les effets de l'écoulement en milieu fracturé et de l'hétérogénéité en couches par la définition des unités hydrostratigraphiques, comme présentée à la Figure 2.2 (b) pour un modèle axisymétrique

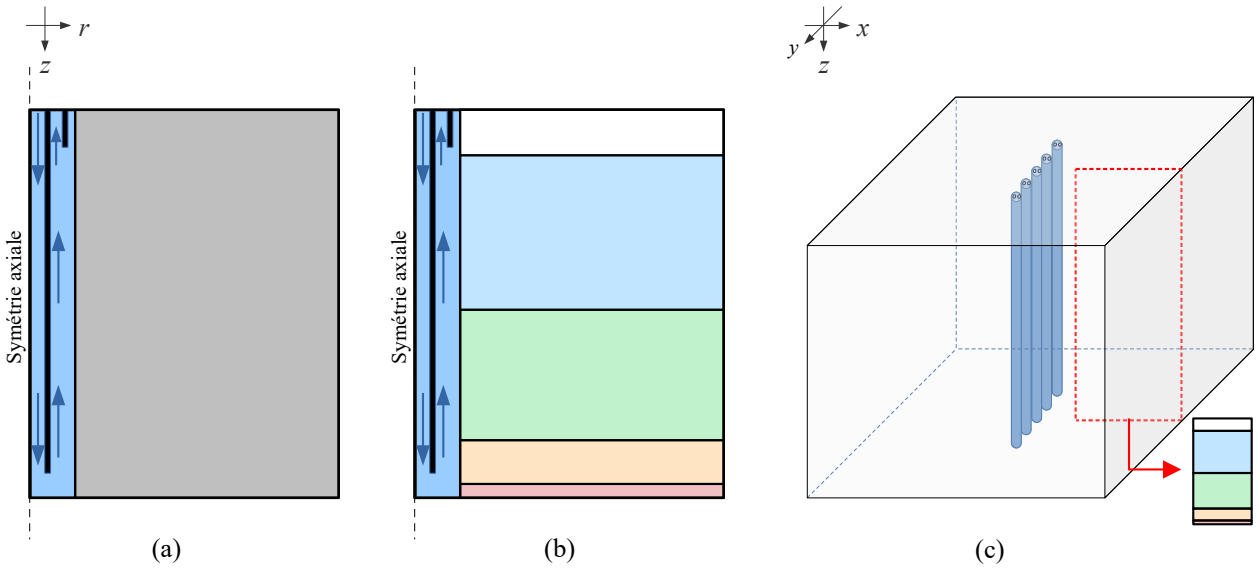

FIGURE 2.2 Représentation des types de modèles numériques pour les PCP, soit a) axisymétrie et homogénéité, b) axisymétrie et hétérogénéité en couches, et c) tridimensionnel, où l'encadré en rouge tireté représente une hétérogénéité en couches ; aucune échelle.

[40, 51] et à la Figure 2.2 (c) pour un modèle tridimensionnel [27, 52]. Dans ces travaux, les unités hydrostratigraphiques sont délimitées de manière grossière à partir d'un modèle conceptuel hydrogéologique issu de l'interprétation des observations réalisées lors du forage. En couplant les physiques de transfert de chaleur et d'écoulement en milieu poreux, les modèles numériques reproduisent avec justesse l'impact de la saignée dans des aquifères rocheux fracturés [40].

Tel que mentionné précédemment, le niveau de complexité des modèles varie en fonction de l'objectif. Pour la rapidité de calcul, les modèles de différences finies [51] et à éléments finis axisymétriques [40, 50] ont été développés. Pour intégrer des composantes régionales et géométriques, des modèles plus complexes ont été développés, notamment des modèles tridimensionnels pour un puits [27], des modèles tridimensionnels avec plusieurs puits [52], et même des modèles prenant en compte plusieurs systèmes de PCP afin d'évaluer la propagation des panaches thermiques à long terme [53]. D'ailleurs, il a été démontré qu'une modélisation plus réaliste, représentant les fractures sous formes de minces couches distinctes, augmente la justesse des résultats comparativement à l'intégration de leurs effets dans des unités hydrostratigraphiques plus grossières, telles que les unités illustrées aux sous-figures 2.2 (b) et (c) [52]. Ces modèles numériques ont également été couplés avec du transport réactif afin d'évaluer des effets géochimiques lors de l'utilisation de la saignée, comme le dégazage de CO_2 [54] ou la précipitation de la calcite [55].

Les modèles numériques permettent ainsi de simuler avec justesse des phénomènes complexes, tels que les transferts de chaleur par diffusion et advection et l'écoulement non uniforme dans des milieux hétérogènes. La plupart des modèles numériques proposés ont été démontrés ou validés expérimentalement [26,27,40,52,55]. Toutefois, la complexité de développement de ces modèles numériques et le temps de calcul sont deux facteurs qui freinent leur utilisation dans les projets pratiques. Pour pallier ces limitations, le modèle analytique β-SLI [45] qui simule un PCP opérant avec une saignée apparaît comme une solution intéressante. Cependant, le modèle β-SLI est conçu pour un contexte hydrostratigraphique homogène et n'a pas encore fait l'objet d'une validation expérimentale.

2.1.2 Simulation

La simulation d'un modèle numérique est réalisée selon les contraintes temporelles établies par l'utilisateur, en matière de durée et d'intervalles de temps. Dans ces modèles, il est possible d'inclure des phénomènes non stationnaires, comme la variation du débit de pompage et de saignée [52,53]. L'utilisation de simulations complètes du signal, intégrant l'hydraulique et la thermique, s'avère souvent lourde et coûteuse en temps de calcul [25]. Pour que les simulations soient accélérées tout en conservant une bonne justesse, les méthodes de simulation par superposition temporelle en utilisant des systèmes linéaires invariants dans le temps (LIT) sont de plus en plus employées. Selon la théorie des systèmes LIT, la variation de température s'exprime comme suit :

$$\Delta T(t) = \int_0^t f(\tau) \cdot g(t-\tau)\, d\tau \tag{2.2}$$

avec,

$$f(t_i) = q(t_i) - q(t_{i-1}) \quad \forall i, 1 \leq i \leq n \tag{2.3}$$

Dans les équations 2.2 et 2.3, la fonction f représente l'incrément des charges thermiques, tandis que g est une fonction de transfert. Une fonction de transfert est une réponse thermique à une impulsion unitaire et constante dans un mode d'opération distinct. Telle que présentée à la Figure 2.3, la fonction de transfert est lisse, positive et strictement croissante. L'intégrale de l'équation 2.2 peut être résolue dans le domaine temporel par une somme récursive, tel que :

$$\Delta T(t_i) = \sum_{j=1}^{i} f(t_j) \cdot g(t_i - t_{j-1}) \quad \forall i, 1 \leq i \leq n \tag{2.4}$$

Pour une simulation discrétisée en n pas de temps, la température au temps i est obtenue par une sommation d'un nombre i de termes considérant tous les instants précédents ($j = 1$

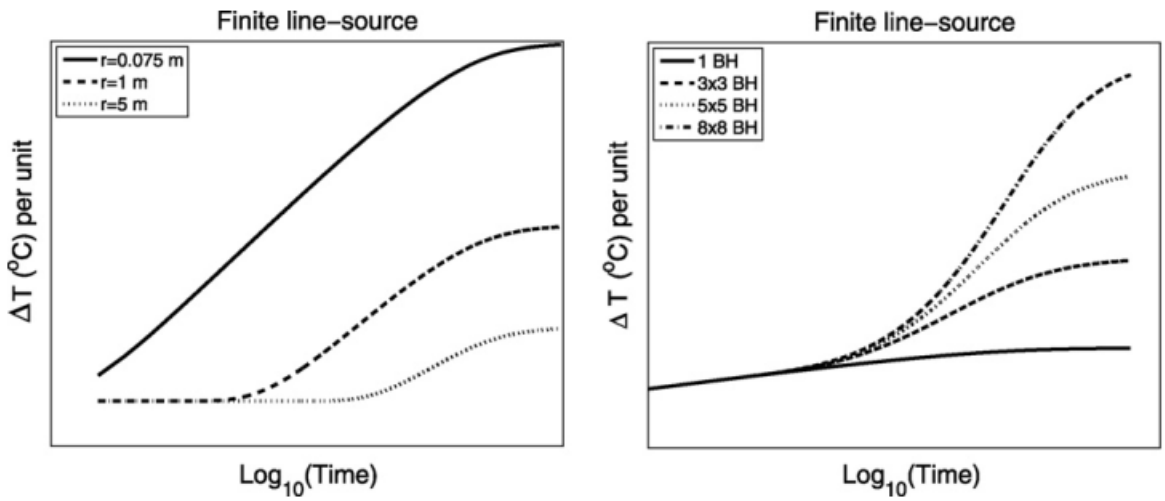

FIGURE 2.3 Exemple de fonctions de transfert pour (gauche) différentes distances du puits et (droite) différents agencements d'ÉCS sur une grille régulière ; l'échelle des deux graphiques n'est pas la même et les deux lignes pleines partagent les mêmes valeurs (tiré de Marcotte et Pasquier, 2008).

à $j = i$), et qui croît jusqu'à atteindre un nombre de n termes au dernier pas de temps. Dans cette formulation, les charges thermiques sont traitées de façon cumulative à chaque pas de temps (Figure 2.4), ce qui fait augmenter le temps de calcul proportionnellement avec la taille du signal. Pour alléger ces calculs, des méthodes d'agrégation des charges thermiques ont été proposées [56,57]. Cependant, cette approche entraîne une perte de justesse. Lamarche (2009) [58] a donc développé une méthode basée sur la transformée inverse de Laplace, qui permet de réduire la complexité de calcul tout en préservant une bonne justesse. Dans la même lignée, Marcotte et Pasquier (2008) [59] ont proposé une méthode utilisant un produit de convolution dans le domaine spectral, ce qui permet d'effectuer la superposition temporelle de tout le signal en une seule opération mathématique. La convolution dans le domaine spectral prend la forme suivante :

$$\Delta T(t) = (f * g)(t) = \mathcal{F}^{-1}\left(\mathcal{F}(f) \cdot \mathcal{F}(g)\right) \tag{2.5}$$

Pour les systèmes de PCP, la théorie des systèmes LIT ne s'applique pas lorsque le débit de saignée est activé ou lorsque le débit de circulation varie, puisque le système perd alors sa stationnarité. Récemment, Beaudry et al. (2021,2023) [60, 61] ont introduit une approche de convolution non stationnaire qui combine plusieurs systèmes linéaires afin de prendre en compte les variations de débits. Cette approche reproduit des simulations de modèles numériques dynamiques avec justesse en une fraction du temps requis par le modèle numé-

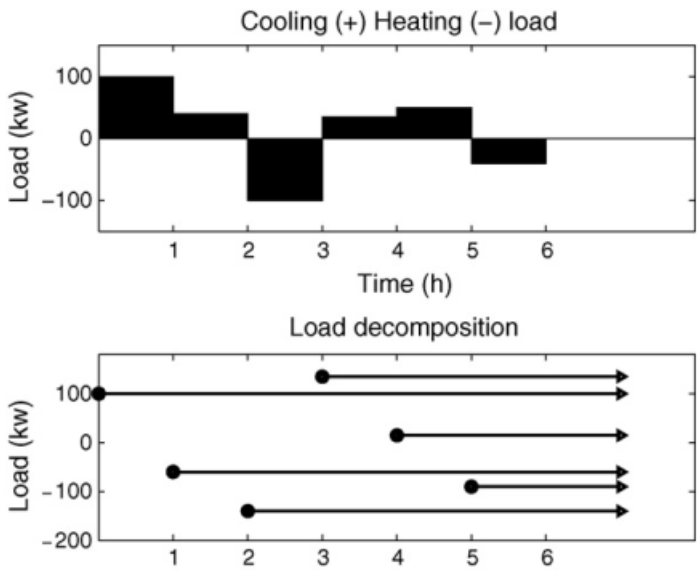

FIGURE 2.4 Représentation du principe de superposition temporelle où (haut) une charge thermique à un temps donné est vue comme (bas) une charge incrémentale (tiré de Marcotte et Pasquier, 2008).

rique [60, 61]. La dernière formulation de la convolution non stationnaire [61] s'écrit comme suit :

$$\Delta T(t) = \int_0^t f(\tau, t) \cdot g(t - \tau)\, d\tau \tag{2.6}$$

et peut être résolue dans le domaine spectral selon l'équation suivante :

$$\Delta T(t) = (\mathbf{F_j} * \mathbf{G_j})(t) = \sum_{j=1}^{m} \mathcal{F}^{-1}\left(\mathcal{F}(\mathbf{F_j}) \cdot \mathcal{F}(\mathbf{G_j})\right) \tag{2.7}$$

où $\mathbf{G}_\mathrm{j}$ et $\mathbf{F}_\mathrm{j}$ sont respectivement les vecteurs représentant les fonctions de transfert de chacun des modes d'opération et la charge incrémentale activée lors de ce mode d'opération.

Il est important de noter que le principe de convolution peut être inversé, soit une déconvolution, afin d'estimer une fonction de transfert à partir de signaux expérimentaux (voir la Figure 2.5). La déconvolution a été utilisée pour estimer des fonctions de transfert d'un signal à court terme [62], pour estimer plusieurs fonctions de transfert dans un contexte de non-stationnarité [63], et pour estimer des fonctions de transfert spatialement réparties dans un ÉCS [64]. L'avantage principal est que les fonctions de transfert expérimentales sont obtenues sans faire appel à un modèle mathématique [62]. Par la suite, ces fonctions obtenues par déconvolution peuvent être utilisées pour simuler le fonctionnement du PCP, sans qu'il

soit nécessaire d'évaluer une seule propriété du milieu hydrostratigraphique au préalable. En soi, une fonction de transfert obtenue par déconvolution est un modèle empirique décrivant le comportement linéaire particulier du système et répondant à impulsion unique et constante. Les fonctions obtenues expérimentalement offrent, par conséquent, la possibilité de comparer sur une même échelle les comportements transitoires de différents modes d'opération.

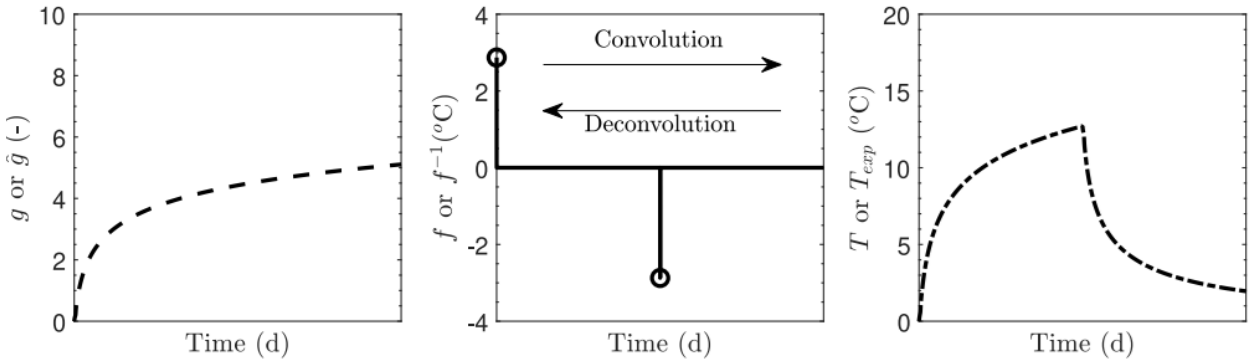

FIGURE 2.5 Représentation de la convolution, soit ici $T_{exp} = f * g$, et de la déconvolution, ici $\hat{g} = 1/f * T$ (tiré de Dion et al., 2022).

2.2 Caractériser le sous-sol : une étape clé encore marquée par l'incertitude

La difficulté à caractériser de façon précise et juste les propriétés du sous-sol continue de constituer un frein à l'adoption des PàC géothermiques [65]. Les incertitudes de caractérisation sont d'autant plus critiques pour les PCP, en raison de leur forte interaction avec les aquifères sollicités, par conduction le long des parois de forage et par advection induite par l'écoulement souterrain [27]. Pour encadrer et guider cette étape, la norme ANSI/CSA/IGSHPA C448 Series-16 (2021) [66] recommande la réalisation d'un forage exploratoire et de sa mise à l'essai, préalablement à tout projet géothermique commercial.

Le forage exploratoire constitue une étape cruciale, car il permet de déterminer les conditions de forage pour l'ensemble du site et de confirmer les informations géologiques et hydrogéologiques qui ont été déduites au préalable de l'étude des cartes et rapports disponibles. Cette phase exploratoire renseigne notamment sur la nature des roches traversées en forage, le débit des venues d'eau souterraine et les risques potentiels pour le projet, tels que la présence de gaz ou les risques d'éboulement. Lors du forage, les déblais générés par l'action de battage et de rotation du trépan sont prélevés et analysés en laboratoire. D'autre part, le débit des venues d'eau est généralement estimé de manière approximative au point de rejet des déblais. Ces méthodes de suivi visuel engendrent toutefois une incertitude importante quant aux contacts

géologiques, à la nature exacte des unités stratigraphiques, ainsi qu'aux profondeurs et aux débits réels des venues d'eau.

Une meilleure justesse dans l'identification des propriétés hydrauliques et thermiques permet de réduire les biais dans la simulation des températures d'opération des PCP [49, 67, 68]. C'est dans cette optique que les essais *in situ* viennent compléter la caractérisation du sous-sol. Les essais peuvent être passifs, comme la réalisation d'un profil de température dans un forage, ou actifs, lorsqu'il s'agit de mesurer et d'analyser la réponse du milieu à proximité de l'ÉCS à une stimulation, afin de déterminer les propriétés hydrauliques ou thermiques du sous-sol. Parmi les essais actifs recommandés par la norme C448 Series-16 (2021) [66], l'essai de réponse thermique (ERT), qui consiste à suivre la variation de la température face à une perturbation thermique, est devenu incontournable dans le dimensionnement des ÉCS. Plus spécifiquement pour les PCP, il est également recommandé de procéder à un essai de pompage, où la variation du niveau d'eau souterraine permet de déterminer la conductivité hydraulique de l'aquifère, et donc les débits exploitables. Il est important de mentionner que l'essai de pompage, dont la revue de littérature accumule près d'un siècle d'avancées [69], ne sera pas traité dans ce document. La section suivante propose plutôt une revue des méthodes d'exécution et d'interprétation des ERT, qui contribuent à réduire les incertitudes associées aux propriétés du sous-sol.

2.2.1 Essai de réponse thermique (ERT)

L'objectif de cet essai *in situ* est de déterminer les propriétés thermiques du milieu géologique et de l'ÉCS, qui sont nécessaires pour simuler et dimensionner le système géothermique à l'aide d'un modèle physique. La réalisation d'un tel essai requiert la mobilisation d'une unité d'essai dédiée aux ERT. Celle-ci est connectée à la tuyauterie de l'ÉCS, comme le montrent les figures 2.6 (a) et 2.6 (b) pour un PCP et un PBF, respectivement.

Le principe de fonctionnement de l'ERT consiste à appliquer une perturbation thermique au puits à l'aide d'éléments chauffants immergés dans le fluide circulant dans l'ÉCS par pompage. Dans ce contexte, les différences majeures entre les systèmes PCP et PBF concernent le type de pompage, qui est une pompe submersible et une pompe de circulation respectivement, et l'amplitude de la puissance thermique qui est injectée dans le fluide. Pour un PBF, cette puissance par mètre de forage est généralement comprise entre 50 et 80 W/m [24, 66], ce qui correspond à la puissance en pointe attendue pour ce type d'ÉCS. Dans ce même ordre d'idée, pour un PCP, la puissance de chauffage lors de l'ERT devrait atteindre 120 à 300 W/m, conformément aux capacités observées pour des systèmes installés en climat froid [14, 17, 25, 36]. Ainsi, cette chaleur injectée dans le fluide se diffuse dans le milieu géologique

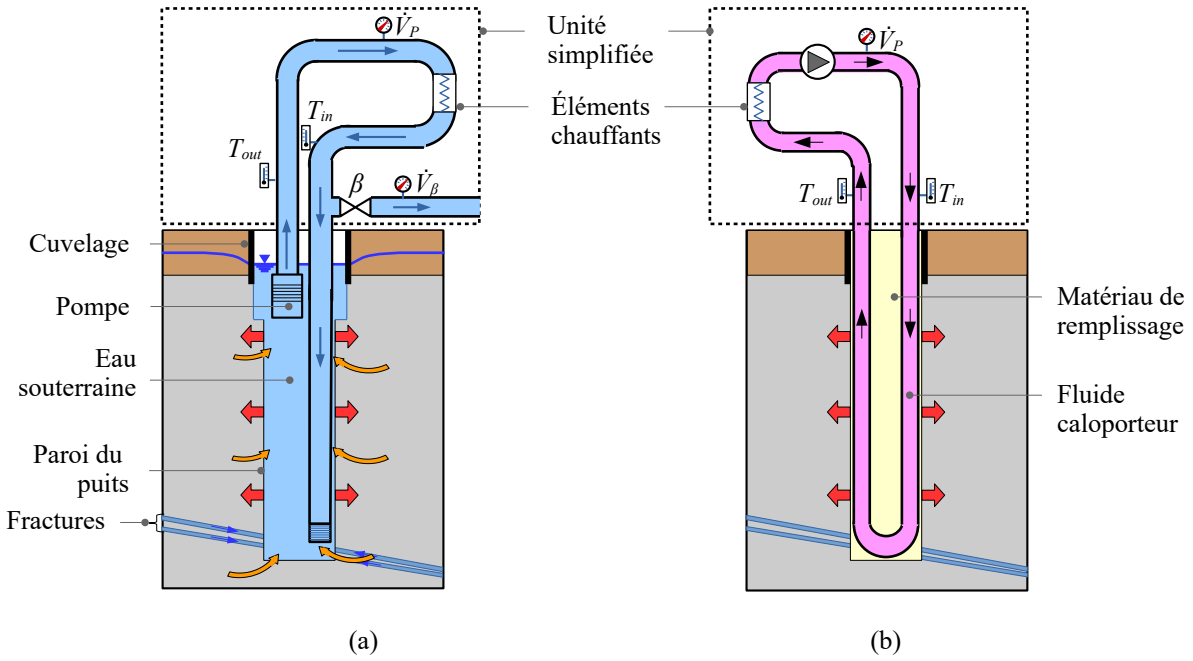

FIGURE 2.6 Représentation du principe de l'ERT sur un ÉCS de type a) PCP et b) PBF ; aucune échelle.

et la réponse thermique est analysée à l'aide des données acquises, à savoir la température à la sortie de l'ÉCS (T_{out}) et à son entrée (T_{in}), le débit de circulation ($\dot{V}$), et la puissance de chauffage (Q).

Les ERT ont été largement étudiés [70, 71] depuis leur invention en 1983 [72]. Plusieurs modèles physiques, qu'ils soient analytiques ou numériques, ont été utilisés pour reproduire le comportement d'un ÉCS. Parmi les modèles analytiques, les plus connus sont ceux de la SLI [41, 42], la source cylindrique infinie (SCI) [42, 73] et de la source linéique finie (SLF) [74, 75]. Des modèles de différences finies ont aussi été utilisés, soit par le principe de résistances et capacités thermiques (RCT) [28, 76]. Finalement, plusieurs auteurs ont utilisé des modèles numériques d'élément finis pour interpréter des ERT en intégrant divers phénomènes, tels que l'écoulement de l'eau souterraine [77, 78], l'hétérogénéité en couches [64, 79], le gradient thermique [78] et les variations climatiques [80].

Cependant, ces modèles numériques complexes sont longs à développer et à simuler. Pour y remédier, des émulateurs ont été développés pour simuler plus rapidement la réponse thermique de l'ÉCS. Dans le domaine de la géothermie, les réseaux de neurones artificiels (RNA) ont été exploités pour leurs capacités à intégrer les phénomènes non linéaires (e.g. le couplage d'une PàC-ÉCS [81]), ce qui peut être ardu à prendre en compte pour d'autres types d'émulateurs, comme les modèles d'ordres réduits [82, 83]. Les RNA sont entraînés sur de

larges bases de données, pour ensuite voir un modèle physique complexe émulé en une fraction de seconde [84, 85]. Ainsi, les RNA deviennent essentiels pour des calculs stochastiques ou d'optimisation qui nécessitent des dizaines de milliers, voire des millions d'appels [86, 87]. À ce jour, aucun émulateur de la réponse thermique d'un PCP n'a été développé dans la littérature.

Diverses méthodes d'interprétation d'ERT ont été développées pour estimer les propriétés inconnues des modèles physiques. La méthode la plus simple et efficace est la méthode de la pente graphique, soit une approximation de premier ordre de la SLI permettant d'isoler les paramètres thermiques dans une relation directe avec la pente d'une droite logarithmique [88]. Pour accéder à cette approximation, l'ERT doit être opéré à un débit et une puissance de chauffage constants. Les autres méthodes d'interprétation développées sont des méthodes d'inversions, qui consistent à introduire les propriétés recherchées dans un modèle et à minimiser l'erreur entre les résultats produits par ce modèle et les observations [78, 89–91]. L'approche classique consiste à minimiser les résidus entre la température moyenne du fluide ($\overline{T}_f(t)$) observée et simulée, en effectuant la simulation de la manière suivante :

$$\overline{T}_f(t) = T_0 + R_b \cdot q(t) + \Delta\overline{T}_b(t) \tag{2.8}$$

c'est-à-dire en combinant la température non perturbée du milieu géologique (T_0) avec un modèle assemblant les résistances thermiques dans le puits (R_b) et un modèle physique reproduisant la variation de la température à la paroi de forage ($\Delta\overline{T}_b(t)$) [92, 93]. En fonction du modèle physique et de la méthode d'inversion, les propriétés visées par l'inversion peuvent varier. Par exemple, une inversion avec le modèle de la SLI viserait à déterminer au minimum la résistance thermique de l'ÉCS (R_b) et la conductivité thermique équivalente du milieu géologique (λ_{eq}) [70]. Il est aussi possible d'estimer d'autres propriétés, telles que la capacité thermique volumique du sous-sol (C_s) [86] ou l'écoulement de Darcy [94–97]. L'utilisation d'algorithmes de déconvolution pour extraire des fonctions de transfert permet d'obtenir un modèle empirique sur lequel il devient plus facile d'appliquer une inversion lorsqu'un essai est interrompu ou présente une forte variabilité dans l'injection de chaleur [98]. Pour accéder à l'incertitude des propriétés, il est également possible d'effectuer une inversion sur un modèle physique dans un cadre stochastique, soit par une expérience de Monte-Carlo [99], soit par inférence bayésienne des propriétés [86, 100, 101]. Au moment de commencer cette thèse, l'inférence bayésienne de propriétés des matériaux géologiques ceinturant un PCP n'avait pas encore été effectuée.

Dans la littérature, l'identification de propriétés thermiques autour d'un PCP en utilisant

les ERT a peu été étudiée, mais son utilisation a permis plusieurs avancées importantes [27,39,40,102–104]. Par exemple, comme mentionné au chapitre 2.1.1, lorsque la conductivité hydraulique est grande (> 5 x 10^{-5} m/s), l'interprétation avec des modèles analytiques qui ne considèrent pas l'advection (SLI, SCI ou SLF) n'est pas recommandée [27, 39]. Dans tous les cas, lorsque la saignée est activée, l'utilisation de ces modèles purement conductifs a pour effet d'augmenter les valeurs des propriétés thermiques par rapport à celles obtenues avec une recirculation complète du PCP [39, 102]. Il convient alors d'utiliser des modèles numériques pour reproduire la saignée, car ceux-ci prennent en compte la composante advective du transfert de chaleur. Pour assurer la justesse des simulations numériques, il est essentiel de combiner les résultats d'interprétation d'un ERT avec ceux d'un essai de pompage, mais aussi avec la réalisation d'un modèle conceptuel des différentes couches hydrostratigraphiques, tout en prenant en compte le profil vertical de la température dans le forage [40, 103]. En effet, à ce jour, l'utilisation d'un modèle numérique prenant en compte l'hétérogénéité en couches constitue le seul moyen de reproduire avec justesse la température observée lors d'un ERT autour d'un PCP [27]. Cette observation est d'autant plus vraie en présence d'une conductivité hydraulique élevée, comme dans le cas d'un écoulement de fracture, et ce, même lorsque le PCP fonctionne en recirculation complète [27].

En résumé, l'ERT permet de caractériser les propriétés thermiques du milieu géologique et de l'ÉCS. De plus, selon le modèle utilisé, il est aussi possible d'établir des constats sur l'écoulement souterrain. En présence d'une forte conductivité hydraulique, il est préférable d'utiliser des méthodes d'inversion faisant appel à des modèles numériques plutôt qu'à des modèles analytiques conductifs [27, 39]. De cette façon, le transfert par advection et l'hétérogénéité en couches sont pris en compte [27]. Des RNA peuvent être entraînés à reproduire avec exactitude un modèle numérique, ce qui permet d'effectuer des études stochastiques et d'accélérer le calcul.

2.2.2 Quantification de l'incertitude

L'interprétation d'un ERT dans un cadre déterministe ne permet pas nécessairement de déterminer les propriétés thermiques avec justesse, en raison des incertitudes associées aux méthodes d'interprétation, au choix du modèle mathématique et à l'incertitude des instruments de mesure [71, 99, 105]. Dans des études paramétriques séparées sur les PCP, Deng et al. (2005) [67] et Ng et al. (2011) [49, 68] indiquent qu'une mauvaise identification des propriétés du milieu géologique, notamment la conductivité thermique et hydraulique, peut avoir un impact significatif sur les températures simulées. Par conséquent, il est important de déterminer les propriétés avec justesse et précision.

En sciences de la terre, les sources d'incertitudes liées à la caractérisation du milieu géologique sont souvent définies dans un cadre stochastique sous forme de distributions conjointes. En amorce, la détermination de ces distributions dites *a priori* est basée sur la documentation géologique du site. La définition d'une distribution comporte des incertitudes structurales, qui sont liées au choix du modèle statistique et de sa paramétrisation [106]. Puis, ces distributions sont affinées par les investigations et les essais. Par exemple, l'interprétation d'un ERT en considérant l'incertitude permet de mettre à jour les distributions *a priori* avec une incertitude structurale réduite. Dans la littérature, cette interprétation est complétée par une étude de Monte-Carlo [99] ou par l'inférence bayésienne de certaines propriétés géologiques [86, 100, 107].

Pour inférer des propriétés, le théorème de Bayes [108] a été appliqué dans plusieurs domaines, tels que l'hydrogéologie [109–113], la géophysique [114, 115], la mécanique du bâtiment [116, 117] et la géothermie [86, 100, 101, 118, 119]. Ce théorème prend la forme suivante :

$$P(\theta|x) \propto P(x|\theta) \cdot P(\theta) \tag{2.9}$$

où $P(\theta)$ est la distribution *a priori* d'un ou de plusieurs paramètres conjoints, $P(x|\theta)$ est la vraisemblance que des observations existent en considérant l'espace des variables et $P(\theta|x)$ est la distribution *a posteriori*, soit la probabilité conjointe que des variables existent en considérant les observations. Dans l'inférence bayésienne de propriétés à partir de données issues d'un ERT, les distributions *a priori*, établies par l'utilisateur, sont mises à jour en calculant la vraisemblance des résidus entre les températures observées et les températures simulées. Les distributions conjointes formant la distribution *a posteriori*, soit le résultat de l'inférence, permettent ainsi d'apprécier l'incertitude des paramètres ciblés.

La définition des distributions *a priori* dans l'espace des variables est une étape importante, puisqu'une définition erronée de ces distributions *a priori* peut mener à des résultats biaisés [120]. Si les hypothèses ne peuvent pas être améliorées par des investigations, une analyse de sensibilité peut être réalisée en modifiant l'espace des variables [121]. Dans la définition de la distribution *a priori*, certains auteurs préconisent l'utilisation de distributions non informatives, telles qu'une distribution uniforme [86, 101], tandis que d'autres auteurs optent pour des distributions informatives, comme des distributions gaussiennes ou triangulaires [87, 100, 107, 122]. Alors que les distributions non informatives assurent de ne pas influencer le résultat, les distributions informatives permettent de converger plus rapidement, mais requièrent toutefois un jugement d'expert.

Sur des PBF, Choi et al. (2018) [100] ont réalisé une première démonstration d'interprétation

d'un ERT dans un cadre bayésien. Les auteurs ont ainsi obtenu les distributions conjointes des variables λ_{eq} et R_b en utilisant le modèle de la SLI comme modèle direct et en se basant sur des données synthétiques obtenues à l'aide d'un modèle numérique. En posant l'hypothèse que les erreurs de modèle et de mesures sont indépendantes, les auteurs ont déterminé que l'incertitude sur les résultats diminue après une durée d'un ERT d'environ 50 h. Leur méthode converge moins bien lorsque l'advection domine. Pasquier et Marcotte (2020) [86] proposent une méthode d'inférence bayésienne de propriétés qui considère la corrélation entre les résidus observés. Ils indiquent que l'hypothèse d'indépendance avancée par Choi et al. (2018) [100, 101] peut mener à des résultats biaisés. Grâce à cette méthode, ils parviennent à déterminer les distributions conjointes des propriétés du sous-sol (λ_s et C_s), du coulis (λ_g et C_g) et le demi-espacement entre les tuyaux (D). D'ailleurs, ils parviennent à définir la variable C_s avec une précision bien supérieure aux valeurs rapportées dans la littérature (16,3 %).

Ainsi, l'interprétation d'un ERT dans un cadre bayésien permet d'estimer les propriétés d'un modèle et, en outre, leurs précisions sous forme de distribution. De plus, cette méthode permet d'inférer des distributions conjointes de propriétés qui étaient auparavant difficiles à estimer (C_s). À ce jour, aucun ERT sur PCP n'a été interprété dans un cadre bayésien. En utilisant des modèles numériques, ce type de méthodologie offre la possibilité d'évaluer l'incertitude des propriétés hydrauliques et thermiques de différentes unités hydrostratigraphiques.

2.3 L'opération des PCP : assurer un contrôle efficace et gérer l'eau de rejet

Tel que décrit au chapitre 1, un PCP peut être opéré de deux manières. L'opération de base d'un PCP consiste en une recirculation complète, où l'ensemble du débit pompé est réinjecté dans le même PCP. La deuxième façon d'opérer est par l'utilisation de la saignée, où un ratio β de la réinjection est rejeté hors du système. Orio (2005) [21] rapporte qu'une forte saignée permet de réduire les longueurs de forage jusqu'à 65 %. En fait, la grande capacité associée aux PCP est due à l'opération d'une saignée efficace, qui passe par un contrôle adéquat.

Pour guider le contrôle de l'opération de la saignée, Nguyen et al. (2015,2020) [14, 28] proposent une méthode par trois paliers de saignée, avec des ratios de 10%, 20% et 30%. Pour une démonstration de 26 jours sur un système de PCP installé dans un socle rocheux peu perméable (5,7 x 10^{-7} m/s), Nguyen et al. (2020) [14] indiquent que le système a requis l'opération de la saignée pour seulement 30% du temps, que le troisième palier n'a jamais été utilisé et que, dans 80% des cas d'activation de la saignée, seul le premier palier a été sollicité. Ces constats s'alignent d'ailleurs avec ceux de Rees et al. (2004) [123] qui indiquent, entre autres, que des taux de saignée de seulement 10% à 15% augmentent significativement les performances d'un PCP. En fait, il est recommandé de contrôler à la baisse le débit de

pompage et le débit de saignée, afin de réduire les coûts d'opération et de limiter le volume d'eau rejeté hors du système [25, 124]. Lorsque les besoins de chauffage et de climatisation sont importants, il est alors recommandé d'augmenter les débits de pompage et de saignée, afin de réduire l'amplitude de l'échange de chaleur retournée vers les PCP [25, 124].

Selon la réglementation québécoise en vigueur, l'eau rejetée par le processus de saignée est dirigée vers un puits d'injection (PI), un plan d'eau ou un réseau d'égouts [22, 53], comme respectivement représenté aux points (i), (ii) et (iii) de la Figure 2.7 (a). Au Québec, les eaux générées par l'opération de la saignée doivent être réinjectées dans le même aquifère. La solution préconisée est alors d'utiliser des PI, ce qui engendre des coûts supplémentaires liés au forage et à l'entretien de ces puits. Par ailleurs, les PI peuvent être sujets à des problèmes de colmatage physique et chimique [104,125–127] ainsi qu'à des interférences thermiques entre les PCP [53,128,129], ce qui limite leur efficacité. Au moment de réaliser cette revue littéraire, seuls Ben Aoun et al. (2024) [130] proposent une solution de rechange à l'utilisation d'un PI. La solution proposée est d'utiliser un réservoir enfoui pour infiltrer l'eau de rejet dans la zone non saturée du sol, comme illustré à la Figure 2.7 (a) au point (iv). Cette méthode implique toutefois d'ajouter des composantes qui devront aussi être entretenues.

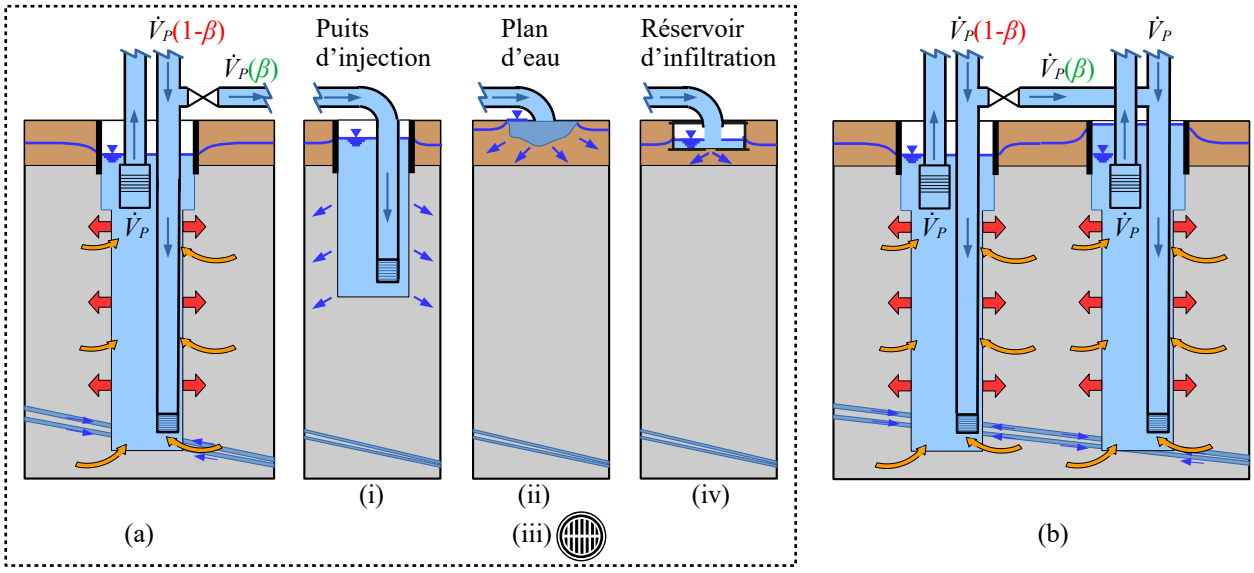

FIGURE 2.7 Représentation de la gestion des eaux engendrées par l'opération de la saignée, soit par a) un rejet vers i) un puits d'injection, ii) un plan d'eau, iii) un réseau d'égoûts ou iv) un réservoir d'infiltration, autrement par b) la réinjection entre plusieurs PCP ; aucune échelle.

Dans un système à au moins deux PCP, un nouveau mode d'opération des PCP a été développé par Kim et al. (2020) [131]. Ce mode consiste à réinjecter l'eau rejetée par l'opération de la saignée vers d'autres PCP dans le système, comme présenté à la Figure 2.7 (b). Cette

méthode de réinjection entre puits conserve l'avantage principal de la saignée, à savoir une augmentation de l'efficacité du PCP par rapport à la recirculation complète. En limitant le rejet d'eau hors du système de PCP, la réinjection entre puits apparaît comme une solution potentielle pour éviter l'utilisation coûteuse de puits d'injection.

La réinjection entre puits a été démontrée expérimentalement à l'aide de deux PCP et de plusieurs ERT [131, 132]. Néanmoins, une validation expérimentale avec un bâtiment réel en fonctionnement est nécessaire pour confirmer l'efficacité de la réinjection entre puits à plus long terme. De plus, une analyse approfondie de la réponse transitoire de la réinjection entre puits est encore manquante. Une telle analyse permettrait de mieux appréhender la dynamique thermique de ce type d'opération et ainsi de réduire les barrières à son utilisation.

2.4 Validation expérimentale : une condition essentielle à l'acceptation des modèles

Afin de faciliter l'adoption de modèles, il est primordial de mener une validation expérimentale. La validation expérimentale doit s'appuyer sur un protocole rigoureux et reproductible, dans lequel les intrants du modèle doivent être déterminés indépendamment des données issues de l'expérience de validation. Dans la littérature, seuls quelques systèmes de PCP ont été suivis pour démontrer l'efficacité accrue de ces types d'ÉCS [21, 33, 35, 36, 133, 134]. Il est important de préciser que ces suivis ne jouent pas nécessairement un rôle de validation expérimentale, mais plutôt de preuve de concept.

Par la suite, plusieurs auteurs ont conduit des démonstrations expérimentales. Deng et al. (2004,2005) [47, 67] démontrent la justesse d'un modèle axisymétrique [47] et d'un modèle unidimensionnel [67]. Il est important de noter qu'aucun essai *in situ* n'a été réalisé et que les propriétés géologiques ont alors été déduites par la calibration des modèles sur les données de démonstration, ce qui ne répond pas aux critères de validation expérimentale précédemment établis. Le modèle axisymétrique a été calibré en utilisant des données provenant de deux systèmes de PCP [67]. Le premier système, installé à l'Université de Pennsylvanie, ne contient qu'un seul PCP d'une profondeur de 320 m. Les données récoltées à l'aide de ce système commencent au démarrage du système et ne contiennent aucune opération de saignée. Deng et al. (2004) [47] attribuent ces données au mémoire de maîtrise de Mikler (1993) [135]. Le deuxième système est installé à la bibliothèque publique de Haverhill et contient quatre PCP de 457 m de profondeur. Ce système a fonctionné avec une stratégie de contrôle d'une saignée de 10%. Les données, qui représentent le fonctionnement du système en 1996, ont été fournies à Deng en 2003 par la firme de consultation CDH Energy Corporation [47]. L'enregistrement des données pour l'essai de Haverhill (1996) a commencé une année après

le démarrage du système et plusieurs périodes de données sont manquantes ou corrompues, ce qui a contraint les auteurs à émettre plusieurs hypothèses supplémentaires [47]. Dans les deux cas, les données provenant des deux systèmes totalisent environ trois à quatre mois de fonctionnement et étaient enregistrées toutes les heures. Deng et al. (2005) [67] ont calibré les paramètres du modèle sur les données provenant des deux sites et ont obtenu une erreur absolue maximale de 1,5 °C (données de Mikler, 1993) et 0,9 °C (données de Haverhill, 1996). Les données de ces deux systèmes ont été récupérées par Ng et al. (2011) [68] et par Jeon et al. (2016) [39], entre autres, pour calibrer leur modèle dans le cadre de leurs études respectives.

Dans des études réalisées en Corée du Sud, deux sites expérimentaux comprenant chacun deux PCP, avec des profondeurs de 300 m dans un cas [132, 136] et des profondeurs de 350 et 400 m dans l'autre cas [137], ont été utilisés pour démontrer l'efficacité de diverses méthodes d'opération des PCP, en réalisant plusieurs ERT sur des périodes d'environ une journée. Ces derniers auteurs ont interprété les ERT avec l'approximation du premier degré du modèle de la SLI, afin de faire une analyse comparative des conductivités thermiques obtenues. Cependant, aucun modèle n'a été validé dans le cadre de ces études.

Beaudry et al. (2018) [103] ont réalisé une validation expérimentale d'un modèle numérique avec un laboratoire mobile de géothermie conçu à l'École Polytechnique de Montréal (voir la Figure 2.8) et installé dans la ville de Varennes, Québec, afin de tester un PCP et un PI. La première étape de la validation consistait à interpréter des essais *in situ*, soit un ERT et un essai de pompage, en utilisant des méthodes indépendantes du modèle numérique. À l'aide des résultats d'interprétation des essais, les auteurs ont calibré un modèle numérique et obtenu une moyenne des erreurs absolues (MAE) de l'ordre de 0,15 °C. Beaudry et al. (2019) [40] ont ensuite validé expérimentalement ce modèle à l'aide de données d'opération dynamique, correspondant à des variations du débit de pompage et de saignée, sur une période de 26 jours. Durant cette opération, une extraction de chaleur a eu lieu à des taux variant d'environ 120 à 160 W/m. La validation du modèle a été conclue avec une MAE de 0,32 °C, ce qui est une erreur faible compte tenu de l'incertitude de 0,2 °C des sondes de température installées dans ce laboratoire. Ainsi, ce type de validation permet ensuite d'exploiter le modèle pour en tirer des conclusions additionnelles. En effet, les auteurs ont démontré qu'un PCP conserve son efficacité lorsque le pompage est en surface, c'est-à-dire à l'intérieur de la chambre de pompage, par rapport à la configuration traditionnelle à l'intérieur d'une conduite d'amenée pour pomper l'eau en profondeur [22]. Ainsi, la nouvelle configuration de pompage en surface facilite l'entretien et l'installation. Finalement, Beaudry et al. (2019) ont démontré que négliger la modélisation du réseau de fractures entraîne une surévaluation de la température, un biais qui pourrait s'accroître lorsque le débit saigné augmente.

Figure 2.8 Laboratoire mobile de géothermie de l'École Polytechnique de Montréal situé installé dans la ville de Varennes, Québec, de gauche à droite et de haut vers le bas : une vue du conteneur maritime, de l'unité de chauffage pour les essais de réponse thermique, des pompes à chaleur et de l'unité de traitement de l'eau (tiré de Beaudry et al., 2019).

Une deuxième validation expérimentale a été conduite à l'école de la Clé-des-Champs située dans la ville de Mirabel, au Québec. Ce système de chauffage et de climatisation est équipé de cinq PCP et d'un PI (voir la Figure 2.9). Robert et al. (2022) [27] ont d'abord réalisé une série d'essais *in situ*, puis ils ont calibré un modèle numérique. Ensuite, Champagne-Péladeau et al. (2025) [52] ont utilisé des données supplémentaires collectées lors de l'opération à long terme du système pour valider une nouvelle méthode de modélisation du contexte hydrostratigraphique autour des PCP. D'ailleurs, Beaudry et al. (2024) [17] ont présenté les performances du système sur une année ainsi que les apprentissages découlant de sa construction et de sa mise en service.

En résumé, la validation expérimentale joue un rôle essentiel dans l'acceptabilité des méthodes de modélisation des PCP. Les études présentées dans ce chapitre démontrent que les démonstrations ou validations expérimentales peuvent être influencées par plusieurs facteurs, dont :

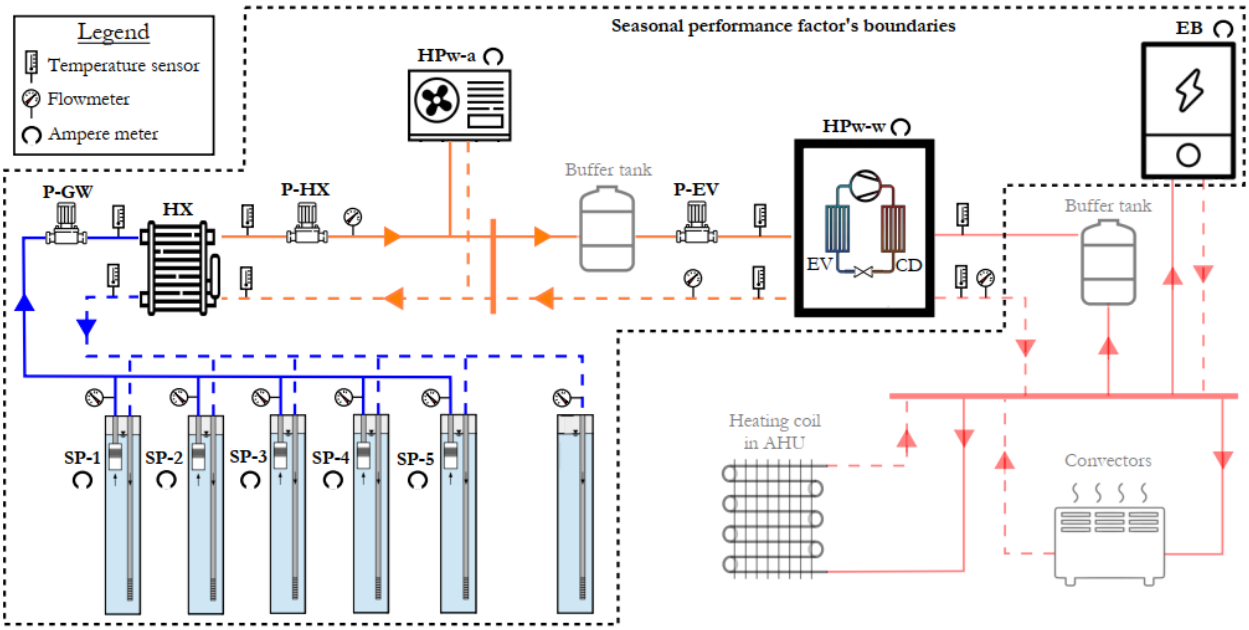

FIGURE 2.9 Représentation du système géothermique contenant cinq PCP et un PI, ainsi que toutes les autres composantes de chauffage et de climatisation installées à l'école de la Clé-des-Champs à Mirabel (Québec), où les variables SP indiquent des pompes submersibles, P des pompes circulatrices, HX un échangeur à plaque, HP des pompes à chaleur, EB une chaudière électrique, EV un évaporateur, CD un condenseur et AHU une unité de traitement d'air (tiré de Beaudry et al., 2024).

- la justesse des propriétés géologiques appliquées au modèle utilisé (peu importe le type de modèle choisi) ;
- la fiabilité du système d'acquisition de données (c'est-à-dire la capacité à emmagasiner et conserver l'ensemble des données) ;
- l'enregistrement des données dès le démarrage du système, afin d'obtenir un état non perturbé.

2.5 Synthèse des lacunes des connaissances

En partie grâce à leur sollicitation du transfert de chaleur advectif, il est indéniable que les PCP offrent un gain d'efficacité en comparaison avec les PBF, soit la technologie actuellement préconisée. Cependant, plusieurs obstacles freinent encore une adoption plus large des PCP. La recherche en matière de modélisation, simulation, investigation et opération demeure fragmentaire, et les innovations proposées sont rarement accompagnées de validations expérimentales. Afin d'accélérer l'acceptation et le transfert d'expertise liés aux PCP, la revue de littérature a mis en évidence la nécessité de développer une modélisation robuste, fiable et

validée du rôle de l'advection dans la dynamique thermique et hydraulique des PCP.

En raison de leur nature profonde, les PCP traversent généralement plusieurs unités hydrostratigraphiques, ce qui nécessite l'utilisation de modèles numériques capables d'intégrer l'hétérogénéité en couches afin de simuler leur comportement avec justesse. Par contre, ces modèles sont complexes à développer et leur coût de calcul est significatif. Pour pallier ces limitations, un modèle analytique a récemment été développé pour simuler la réponse thermique d'un PCP dans un milieu homogène et isotrope. Ce modèle analytique, couplé avec une méthode de simulation par superposition temporelle, permet un calcul quasi instantané de la température moyenne à la paroi du forage, lorsque celui-ci est soumis à un profil de charges thermiques dynamique. Toutefois, au moment de commencer cette thèse, ce modèle n'avait pas encore fait l'objet d'une validation expérimentale. Dans ce contexte, le modèle analytique ne peut actuellement pas considérer une hétérogénéité en couches et son résultat, soit la température moyenne à la paroi du forage, ne correspond pas à une mesure usuelle dans les montages expérimentaux.

L'interprétation d'un ERT réalisé sur un PCP permet de calibrer un modèle en tenant compte du contexte hydrostratigraphique, en particulier en présence d'hétérogénéité. Dans ce cas, les modèles numériques sont, selon l'état de l'art, les plus adaptés pour simuler les transferts de chaleur par advection et conduction autour d'un PCP. Malgré tout, le temps de calcul des modèles numériques rend l'interprétation par inversion fastidieuse en pratique. Pour s'affranchir de ces longs temps de calcul et effectuer des inversions stochastiques, une solution consiste à recourir à des émulateurs, tels que les RNA. Aucun émulateur de modèle de simulation de PCP n'existait dans la littérature, au moment de commencer cette thèse. Pour les PBF, l'application de l'inférence bayésienne de propriétés à partir de données d'ERT a permis de réduire considérablement l'incertitude du paramètre C_s, par rapport à ce qui avait été rapporté dans la littérature à ce moment. De plus, l'inférence dans un cadre bayésien peut être utilisée pour calibrer un modèle et interpréter des ERT dans un contexte d'incertitude, en accédant aux distributions conjointes des propriétés. Cela dit, l'inférence bayésienne de propriétés n'a jamais été testée sur des ERT réalisés sur des PCP, et encore moins sur un PCP dans un contexte hétérogène.

Un défi de la simulation des PCP consiste à reproduire avec justesse et précision la réponse thermique du système dans ses différents modes d'opération. En effet, pour assurer une efficacité, le contrôle des débits de saignée et de pompages est essentiel. De plus, l'opération de la saignée génère des eaux de rejet qui, selon la réglementation provinciale, doivent être réinjectées dans le même aquifère. Cette réinjection est normalement réalisée à l'aide d'un puits d'injection, ce qui entraîne des coûts additionnels. Dans un système à plusieurs PCP,

l'utilisation de la réinjection entre puits offre une solution permettant de s'affranchir, partiellement ou totalement, des puits d'injection. Cependant, cette méthode n'a pas été testée sur un bâtiment réel en fonctionnement. En fait, une analyse de la réinjection entre puits en régime transitoire n'a pas été réalisée dans la littérature. Une façon d'y parvenir passe par l'utilisation de modèles empiriques, soit par l'estimation de fonctions de transfert expérimentales à l'aide d'un algorithme de déconvolution. Une telle démonstration de la portée des modèles empiriques pour les PCP n'a encore jamais été réalisée à partir de données issues d'un bâtiment réel en fonctionnement.

CHAPITRE 3 OBJECTIFS ET DÉMARCHE DE LA RECHERCHE

Le chapitre 1 a mis en valeur les avantages des PCP et leur rôle dans la décarbonation du secteur du bâtiment. Au chapitre 2, la revue de littérature a présenté l'état de la science entourant les PCP, notamment en matière de modélisation, de simulation, d'investigation et d'opération, et a mis en lumière les avancées et les défis restants à relever. La revue a également souligné l'importance de valider expérimentalement toutes les approches proposées, afin d'accroître leur acceptabilité auprès des professionnels susceptibles d'en recommander l'utilisation et d'en faire la conception. En effet, une compréhension approfondie du rôle de l'advection dans les dynamiques thermiques et hydrauliques des PCP permet de diminuer les risques techniques et l'incertitude liés à cette technologie.

La modélisation des PCP occupe ainsi une place centrale dans cette thèse. La littérature place les modèles numériques hétérogènes au sommet des modèles les plus appropriés pour simuler le comportement thermique des PCP. Malgré tout, le nouveau modèle analytique, nommé β-ILS, qui a été développé pour simuler facilement et rapidement la réponse thermique d'un PCP dans un milieu homogène et isotrope, offre une solution à la difficulté de développement des modèles numériques. Peu importe le modèle, la convolution non stationnaire se présente comme une méthode de simulation dynamique efficace, qui consiste à combiner des systèmes linéaires à temps invariable et à utiliser des fonctions de transfert de chaleur. L'utilisation de cette méthode couplée au modèle analytique β-ILS n'a pas été validée expérimentalement ni vérifiée dans un contexte hydrostratigraphique hétérogène. D'autre part, les ERT réalisés sur les PCP n'ont pas été interprétés dans un cadre stochastique, ce qui permettrait de prendre en compte à la fois l'incertitude et les spécificités d'un contexte hydrostratigraphique hétérogène. L'utilisation de l'inférence bayésienne de propriétés pour les PBF a révélé la robustesse de cette méthode et sa capacité à estimer des propriétés autrement difficiles dans un cadre déterministe. Une fois les propriétés d'un modèle estimées avec justesse et précision, celles-ci deviennent des intrants indispensables pour valider expérimentalement des modèles physiques ou pour comparer des résultats obtenus à l'aide d'un modèle empirique, tel que des fonctions de transfert obtenues par déconvolution.

3.1 Objectif général

L'objectif général de cette thèse est d'accroître la portée, d'améliorer l'exactitude des récentes techniques développées pour modéliser et opérer les PCP dans des contextes expérimentaux, c'est-à-dire le modèle analytique homogène et isotrope considérant l'advection, la modéli-

sation numérique par hétérogénéité en couches et les modèles empiriques de fonctions de transfert estimés à l'aide d'algorithmes de déconvolution. Par ailleurs, les constats obtenus permettront d'informer sur les avantages et les lacunes des différents modèles, et de faciliter leur adoption.

3.2 Objectifs spécifiques

En ce sens, les objectifs spécifiques décrits ici guideront la réalisation de ce projet de recherche.

1. **Valider expérimentalement le modèle analytique de simulation des PCP opérant avec saignée**
   Le modèle analytique β-ILS a récemment été développé pour simuler la réponse thermique d'un PCP opérant avec une saignée dans un milieu homogène et isotrope. Le résultat du modèle β-ILS est un vecteur représentant la variation de la température moyenne à la paroi de forage dans le temps, soit une quantité difficile à mesurer. Dans un contexte expérimental *in situ*, le contexte hydrostratigraphique est normalement un milieu hétérogène, avec des profondeurs typiques atteignant plusieurs centaines de mètres pour un PCP. De plus, la dépressurisation autour de la pompe submersible induit un écoulement convergent qui n'est pas pris en compte par le modèle analytique actuel. Ainsi, le premier objectif consiste à :
   Valider expérimentalement le modèle analytique pour un PCP opérant avec saignée et développer un cadre théorique pour tenir compte du contexte expérimental hétérogène.
   Cette validation vise à quantifier la justesse du modèle dans un contexte expérimental, soit en ajoutant des relations qui tiennent compte d'un contexte hydrostratigraphique avec une hétérogénéité en couches, de l'estimation de l'écoulement convergent engendré par la succion de la pompe et de l'estimation d'une lecture ponctuelle de la température du fluide, soit une variable facilement mesurable. Ces ajouts facilitent l'utilisation du modèle analytique β-ILS, ce qui devrait accélérer le transfert des connaissances.
2. **Inférer les distributions conjointes des propriétés thermiques et hydrauliques dans un contexte d'hétérogénéité en couches**
   Il a été démontré que l'inférence bayésienne de propriétés permet d'accéder à leurs distributions conjointes et d'obtenir des propriétés difficilement accessibles dans une inversion déterministe, telle que la capacité thermique volumique. Lorsqu'un contexte hydrostratigraphique présente une hétérogénéité en couches, l'application de cette méthode d'inversion aux modèles numériques, reconnus pour leur justesse dans ce contexte, ouvre la porte à l'estimation des propriétés thermiques et hydrauliques de multiples couches, ainsi que leurs incertitudes. Le deuxième objectif est donc le sui-

vant :
Inférer les distributions conjointes des propriétés thermiques et hydrauliques des différentes unités hydrostratigraphiques d'un milieu contenant une hétérogénéité en couches en utilisant les données d'un essai de réponse thermique d'un PCP en recirculation complète. La méthodologie proposée pour inférer des propriétés dans un cadre bayésien permet d'estimer les propriétés thermiques et hydrauliques, ainsi que leurs précisions, nécessaires à la simulation d'un PCP dans un contexte d'hétérogénéité en couches composé de trois unités géologiques et cinq unités hydrostratigraphiques distinctes. Une connaissance juste et précise des propriétés permet ensuite une simulation plus exacte et fidèle, ce qui diminue les risques lors de la conception des systèmes.

3. **Démontrer l'efficacité de la méthode de réinjection entre puits par comparaison de modèles empiriques expérimentaux**

   Un essai de 35 jours a été réalisé à l'école de la Clé-des-Champs, située à Mirabel, au Québec, afin d'évaluer l'efficacité de différentes méthodes de réinjection sur un système composé de cinq PCP, notamment la réinjection entre puits, deux paliers de saignées et la recirculation complète. La déconvolution sur des données expérimentales permet d'extraire des fonctions de transfert, soit des modèles empiriques, pour les différentes méthodes d'opération testées, et ainsi de pouvoir comparer leurs efficacités respectives en régime transitoire et permanent. Le troisième objectif se présente comme suit :
   Démontrer l'efficacité de la réinjection entre PCP en comparant différentes méthodes d'opération par l'estimation de leurs fonctions de transfert expérimentales à l'aide d'un algorithme de déconvolution, et vérifier la robustesse des modèles empiriques en les comparant à un modèle numérique calibré sur une opération d'un PCP en recirculation continue. Cet objectif consiste à démontrer l'efficacité de la réinjection entre puits dans un bâtiment réel en fonctionnement. De plus, cet objectif permet de mettre en valeur les avantages de l'utilisation de modèles empiriques obtenus par un algorithme de déconvolution.

Les objectifs spécifiques susmentionnés sont réalisés au travers de trois articles scientifiques indépendants, respectivement soumis aux revues *Applied thermal engineering*, *Journal of Hydrology* et *Geothermics*. Au moment du dépôt de cette thèse, un article est toujours en révision (chapitre 4), tandis que les deux autres ont déjà été publiés (chapitres 5 et 6). Ces deux derniers articles de journaux ont également été présentés lors de conférences internationales, donnant lieu à deux articles de conférences revus par des pairs, disponibles aux annexes B et C. Enfin, une discussion entourant l'objectif général de cette thèse est présentée au chapitre 7, suivie d'une conclusion qui présente les contributions et les prochaines étapes.

CHAPITRE 4 ARTICLE 1 – IMPROVEMENT AND EXPERIMENTAL VALIDATION OF AN ANALYTICAL MODEL FOR STANDING COLUMN WELLS OPERATED WITH BLEED

Louis Jacques[a,b,*], Philippe Pasquier[a], Alain Nguyen[b], Gabrielle Beaudry[a]
Applied Thermal Engineering, submitted on May 2, 2025
[a]Department of Civil, Geological and Mining Engineering, Polytechnique Montréal, P.O. Box 6079 Station Centre-Ville, Montreal H3C 3A7, Canada.
[b]CanmetENERGY, Naturel Resources Canada, 1615 Lionel-Boulet, P.O. Box 4800, Varennes, J3X 1S6, Quebec, Canada * Corresponding author : louis.jacques@polymtl.ca
Keywords : Standing column well, Analytical model, Radial groundwater flow, Experimental validation, Numerical verification, Non-stationary convolution, Ground heat exchanger

4.1 Abstract

Standing column wells with bleed enhance thermal performance through groundwater advection. Although numerical models allow for detailed simulations, they are computationally demanding. This study extends a recently developed analytical model, originally based on the assumption of homogeneity, by integrating three key advancements : (1) a method to compute outlet fluid temperatures from borehole wall temperatures ; (2) the inclusion of layered heterogeneity through effective Péclet numbers and effective advection times ; and (3) the consideration of radial horizontal flow induced by simultaneous pumping and reinjection. These developments extend the model's applicability to realistic geological settings and dynamic operational conditions. The novel methodology is verified against numerical simulations and validated using three independent experiments conducted under varying pumping and bleed flow rates. The experimental validation demonstrates mean absolute errors of 0.28–0.37 °C, even under highly dynamic operation, confirming the model's robustness and accuracy close to the accuracy of the temperature sensors. Importantly, the outlet temperature transformation introduces negligible error, and model performance remains stable across a wide range of flow conditions. These improvements address previous model limitations and significantly enhance the model's applicability for rapid simulation and practical design of standing column wells. By reducing reliance on complex numerical simulations, this work contributes to the development of accessible and efficient tools that support the broader adoption of standing column wells in geothermal heat pump systems.

4.2 Introduction

The latest international policies have identified ground-source heat pumps (GSHP) as a key solution to the dual challenges of decarbonization and energy security [6]. Nonetheless, the high initial investment costs, coupled with the difficulties encountered in identifying site-specific ground properties through extensive *in situ* testing, continue to pose significant obstacles to the widespread adoption of this technology [65]. The utilization of efficient ground heat exchangers (GHE) can help reduce initial costs [10, 11].

The standing column well (SCW) is acknowledged as an effective type of GHE, capable of reducing initial costs by 32% to 80% compared to conventional closed-loop systems [17, 29]. The efficiency of SCWs is primarily attributed to the "bleed" operation, which improves heat transfer by enhancing advection [22,26]. This process is initiated by the discharge of a portion of the groundwater pumped from the SCW, creating a pressure drop in the well and inducing a convergent radial groundwater flow towards it. The effective management of pumping and bleed flow rates has been shown to result in a substantial reduction in operational costs [25], indicating that the dynamic simulation of SCWs is crucial.

Currently, the dynamic simulation of SCWs relies on the principle of temporal superposition, which accounts for the cumulative effects of past and present loads. In more specific terms, the present approach employs non-stationary convolution algorithms to capture varying pumping and bleed flow [25, 60, 61]. Convolution is defined as a mathematical operation that applies the principle of superposition by integrating (or summing in a discrete case) the effects of a system's response to past inputs. In the context of a GHE, convolution utilizes a discrete transfer function that characterizes the GHE's response to a unit impulse, thereby enabling the prediction of the cumulative effect of varying inputs over time. Non-stationary convolution involves the implementation of multiple transfer functions, where each transfer function corresponds to a distinct combination of pumping and bleed flow. Thus, complex numerical models are used to generate these transfer functions, as these models effectively address the challenges of accurately predicting temperature responses during bleed operation and flow rate changes. While numerical models require substantial development and computational resources, advances in the field have enhanced their accuracy and expanded their ability to simulate complex hydraulic and thermal processes in SCWs and in their vicinity [27, 52, 53].

To underscore the importance of bleed and to meet design requirements, a number of sophisticated numerical models have been developed over the years. For instance, Spitler et al. (2002) [26] and Abu-Nada et al. (2008) [48] developed two-dimensional numerical models that reproduced the impact of bleed. To account for groundwater flow, Nguyen et al.

(2015) [51] developed a finite difference axisymmetric model focused on fractured aquifers, extending the aforementioned models. Axisymmetric finite element models have also been widely employed to demonstrate various effects, including the effect of pump intake location in the presence of fractures [40] and the influence of bleed on CO_2 degassing and calcite precipitation [54, 55]. Such models were also used recently to identify hydraulic properties of heterogeneous hydrostratigraphic systems [138]. In addition, three-dimensional models are essential for examining regional groundwater flow and its implications on the propagation of thermal plumes, as evidenced by the findings of Robert et al. (2022) [27] and Champagne-Péladeau et al. (2025) [52]. Three-dimensional models are also important for capturing both thermal and hydraulic processes in multi-SCW systems or scenarios with neighbouring GHEs, where groundwater interaction plays a critical role [25, 53, 68, 139]. Advances in modelling have revealed the complexity involved, especially when groundwater flow significantly affects system performance.

Despite their demonstrated high efficiency and the recent advances in modelling, the widespread implementation of SCWs is still restrained by the lack of readily accessible, efficient, and convenient design tools. This is mostly related to the difficulty of simulating the coupled processes of heat transfer and groundwater flow, an issue that also extends to the more conventional types of GHEs [11]. This issue has been addressed for closed-loop GHEs through the development of analytical models, including the moving infinite, or finite, line source models [140, 141]. Research in this field continues to evolve, with Erol and François (2018) [142] expanding the moving finite line source model to include multilayered hydrostratigraphic systems, while Pasquier and Lamarche (2022) [143] proposed two analytical expressions to solve the integral of the moving infinite line source model. Nevertheless, the aforementioned analytical models only consider the influence of unidirectional regional groundwater flow. They are unable to account for radial convergent flow, and are therefore unsuitable for assessing the effect of bleed on the thermal response of a SCW.

To address this challenge, a novel analytical model was recently developed to simulate the temperature response of one SCW under bleed conditions [45]. This model accounts for heat advection-diffusion and radial convergent flow around a SCW located in an isotropic and homogeneous aquifer. For the sake of simplicity, the following paper will refer to it as the β-ILS model. This model is based on an approximate closed-form expression by Thiéry (2022) [46] for the evolution of tracer concentration in aquifers. Drawing an analogy between heat transfer and solute transport, the β-ILS model employs a radial convergent flow expression as a scaling function to adjust the thermal response of the infinite line source (ILS) model, a well-established analytical approach for conductive heat transfer [73]. Accordingly, the β-ILS model uses the ILS model to simulate the thermal response of one SCW in the absence

of bleed and applies a scaling expression when bleed is activated. Nguyen et al. (202 [45] demonstrated that this innovative approach, which is both efficient and convenient through its use of dimensionless properties, offers an accurate solution while significantly reducing the computational burden associated with numerical models.

Although the β-ILS analytical model has been successfully verified against numerical simulations, a formal experimental validation remains to be undertaken. The β-ILS model also does not capture the complexities of layered heterogeneity, nor does it integrate the potentially significant effect of radial groundwater flow resulting from pumping and reinjecting at different depths in the same well. The main goal of this study is to develop and experimentally validate a new theoretical framework that facilitates the rapid and accurate simulation of a single SCW in realistic geological settings characterized by layered stratigraphy and in operating conditions that favor dynamic flow rates. This is achieved by extending the application of the β-ILS analytical model to derive the outlet fluid temperature from the borehole wall temperature, as fluid temperature is the primary measurement in SCWs and is essential for design. Furthermore, an expression for evaluating an effective Peclet number, as well as an approach for estimating a pressure balance point, are integrated. These new contributions enable the integration of layered heterogeneity and radial hydraulic flows influenced by the pumping, reinjection and bleed flows in SCWs. The features mentioned above have not yet been implemented in any analytical models specific to SCWs.

Subsequently, a non-stationary convolution approach is employed to expeditiously evaluate the borehole outlet response to varying pumping and bleed flow rates, thereby representing the actual operation of a dynamically operated SCW system. To evaluate the robustness of the model and the proposed methodology, an experimental validation is carried out using the temperature measurements from three experiments, each conducted at the same location and each with various bleed flow rates. Prior to the presentation of the experimental test cases, a brief numerical verification of the methodology is provided.

4.3 Theoretical background

This section presents the theoretical background that is fundamental for the validation of the β-ILS model and the proposed contributions, in the context of variable pumping and bleed flow rates. First, the β-ILS analytical model is introduced, with an emphasis on its core concepts and its development specific to SCW operation. Subsequently, the convolution-based approach is detailed in order to demonstrate its applicability for dynamic SCW operation.

4.3.1 Analytical model : β-ILS

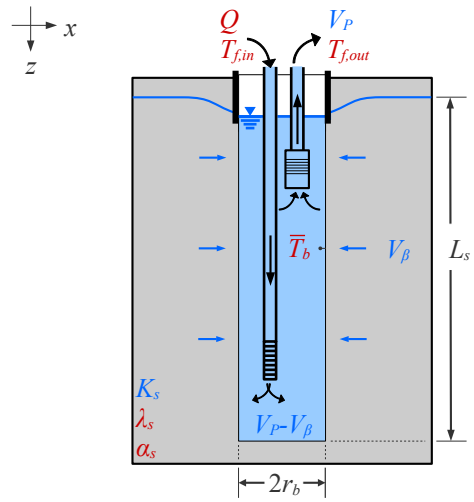

FIGURE 4.1 Schematic representation of a standing column well operating with bleed in a homogeneous and isotropic aquifer and main variables (thermal in red, hydraulic in blue and geometric in black) of the analytical model.

The first analytical model for simulating a SCW operating with bleed was presented by Nguyen et al. (2025) [45]. It was inspired by the work of Thiéry (2022) [46], which was developed to estimate the concentration of a tracer around a well due to radial advection and dispersion in an aquifer. As shown in Figure 4.1, this process is analogous to the bleed operation in a homogeneous and isotropic aquifer, which induces a radially convergent flow field where heat transport occurs through a combination of thermal diffusion and advection. This can be expressed through :

$$g_b(t) = (f_D * h_A)(t) \tag{4.1}$$

where g_b is the SCW's thermal response at the borehole wall, $*$ represents a convolution product between the functions f_D and h_A that integrate diffusive and advective heat transfer, respectively. This elegant and simple formulation encapsulates the cumulative time-dependent interaction of diffusion and advection. Function h_A is a monotonically decreasing and dimensionless function, which contains the advection induced by the radially converging flow field triggered by bleed. For its part, the function f_D quantifies the incremental contribution of diffusion with the well-known ILS model [73] and is given by :

$$f_D(t_i) = g_D(t_i) - g_D(t_{i-1}) \quad \forall i, 1 \leq i \leq n \tag{4.2}$$

with

$$g_D(t) = \frac{Q}{4\pi\lambda_s L_s}\int_u^\infty \frac{e^{-\psi}}{\psi}d\psi \quad \text{and} \quad u = \frac{r_b^2}{4\alpha_s t} \tag{4.3}$$

where g_D is the diffusion function, Q is a constant heat load over time, L_s is defined as the thickness of the subsurface layer solicited by the SCW, which is considered to be saturated, r_b is the borehole radius, λ_s is the thermal conductivity and α_s the thermal diffusivity. In Eq. 4.3, the heat rate $q = Q/L_s$ is normalized to a constant value of 1 W/m, allowing construction of a transfer function in a linear time-invariant system [59]. Note that the diffusion function g_D at time zero is equal to zero.

In Eq. 4.1, the function h_A is expressed as follows :

$$h_A = \epsilon_1(1-\epsilon_2\beta)\left(1+\text{erf}\left(\frac{\sqrt{\text{Pe}}}{\epsilon_3}\left(\frac{1-t_A^{\epsilon_4}}{t_A^{\epsilon_4}}\right)\right)\right) \tag{4.4}$$

with

$$\text{Pe} = \frac{V_\beta/(2\pi L_s)}{\alpha_s} \tag{4.5}$$

$$t_A = \frac{V_\beta t}{\pi L_s r_b^2} \tag{4.6}$$

$$\epsilon_i = a_i \text{Pe}^{b_i} + c_i \tag{4.7}$$

It is worth noting that Eq. 4.4 is dependent on three dimensionless parameters : the bleed ratio β, the thermal Péclet number Pe and the advection time t_A. The bleed ratio β is obtained by dividing the bleed flow rate V_β by the pumping flow rate V_P, both of which are constant over time, to satisfy the conditions of a linear time-invariant system. The Péclet number Pe is a quantitative measure that assesses the ratio between the heat advection transport rate and the heat diffusion rate. Four coefficients ϵ_i are also used in Eq. 4.4. Each coefficient ϵ_i is based on a series of three constants (a_i, b_i and c_i) that were estimated by Nguyen et al. (2025) [45] through calibration with simulations over 50-year periods performed using a two-dimensional axisymmetric numerical model. These values are reported in Table 4.1.

In order to resolve the convolution in Eq. 4.1 at discrete and equal time steps, a formulation in the spectral domain is used [59] and is expressed by :

$$g_b(t) = (f_D * h_A)(t) = \mathcal{F}^{-1}\left(\mathcal{F}(f_D)\cdot\mathcal{F}(h_A)\right) \tag{4.8}$$

where the symbols $\mathcal{F}$ and $\mathcal{F}^{-1}$ represent the fast Fourier transform (FFT) and the inverse

TABLEAU 4.1 Coefficients a_i, b_i and c_i used in Eq. 4.7 to evaluate ϵ_i.

i	a_i	b_i	c_i
1	-0.4478	0.7110	1.0011
2	0.1288	-0.7595	0.7339
3	0.6458	0.7838	0.2383
4	0.1483	0.5114	-0.0100

transform, respectively. In order for Eq. 4.8 to yield consistent results, it is necessary to pad with $n-1$ zeros at the end of each vector f_D and h_A, and retain solely the initial n time steps of the resultant vector g_b [59, 144].

It should be noted that when bleed is not activated ($\beta = 0$) and radial flow is absent (V_β=0), the function g_b is equivalent to function g_D. In all instances, the model output provides the borehole wall temperature, for a constant impulse of 1 W/m at the borehole wall, according to three dimensionless parameters : Pe, t_A and β.

4.3.2 Convolution-based simulation

The thermal response g_b estimated with the analytical model corresponds to a transfer function for a given combination of constant pumping and bleed flow rates. This transfer function can then be employed to evaluate the temperature variation at the borehole wall $\Delta\overline{T}_b$ in response to any time-varying heat rate through a convolution product, as follows :

$$\Delta\overline{T}_b(t) = (f_q * g_b)(t) = \mathcal{F}^{-1}\left(\mathcal{F}(f_q) \cdot \mathcal{F}(g_b)\right) \tag{4.9}$$

with

$$f_q(t_i) = q(t_i) - q(t_{i-1}) \quad \forall i, 1 \leq i \leq n \tag{4.10}$$

where function q is an input function of linear ground load, equivalent to Q/L_s. The convolution product in Eq. 4.9 is also solved in the spectral domain with zero padding of functions f_q and g_b.

While Eq. 4.9 is adequate for constant operating conditions, it does not provide a solution for varying bleed or pumping flow rates. Thus, the non-stationary convolution algorithm of Beaudry et al. (2023) [61] is employed. The latter is expressed by :

$$\Delta\overline{T}_b(t) = (\mathbf{F_{q,j}} * \mathbf{G_{b,j}})(t) = \sum_{j=1}^{m} \mathcal{F}^{-1}\left(\mathcal{F}(\mathbf{F_{q,j}}) \cdot \mathcal{F}(\mathbf{G_{b,j}})\right) \tag{4.11}$$

Here, the sum of the convolution products considers each different combination of bleed and pumping flow rates, hereafter referred to a state. The variable m corresponds to the number of states that are activated within a specified time frame. The matrix $\mathbf{F_{q,j}}$ assigns the values contained in f_q in accordance with the state activation, as follows :

$$\mathbf{F_{q,j}} = \begin{bmatrix} q(t_1) & \cdots & q(t_1) \\ q(t_2) & \cdots & q(t_2) \\ \vdots & \ddots & \vdots \\ q(t_{n-1}) & \cdots & q(t_{n-1}) \\ q(t_n) & \cdots & q(t_n) \end{bmatrix} \odot \begin{bmatrix} s_1(t_1) & \cdots & s_m(t_1) \\ s_1(t_2) & \cdots & s_m(t_2) \\ \vdots & \ddots & \vdots \\ s_1(t_{n-1}) & \cdots & s_m(t_{n-1}) \\ s_1(t_n) & \cdots & s_m(t_n) \end{bmatrix} - \begin{bmatrix} 0 & \cdots & 0 \\ q(t_1) & \cdots & q(t_1) \\ q(t_2) & \cdots & q(t_2) \\ \vdots & \ddots & \vdots \\ q(t_{n-1}) & \cdots & q(t_{n-1}) \end{bmatrix} \odot \begin{bmatrix} 0 & \cdots & 0 \\ s_1(t_1) & \cdots & s_m(t_1) \\ s_1(t_2) & \cdots & s_m(t_2) \\ \vdots & \ddots & \vdots \\ s_1(t_{n-1}) & \cdots & s_m(t_{n-1}) \end{bmatrix} \tag{4.12}$$

where the matrices of heat rate vectors q_j contain each m column, $\odot$ is the Hadamard product, which is an element-wise product, and the matrices of vectors s_j represent the states of activation with binary values indicating whether a given state is active (1) or inactive (0). At each discrete time step t_i, a single state may be activated. The matrix $\mathbf{G_{b,j}}$ comprises all transfer functions $g_{b,j}$ for each observed state j :

$$\mathbf{G_{b,j}} = \begin{bmatrix} g_{b,1}(t_1) & g_{b,2}(t_1) & \cdots & g_{b,m}(t_1) \\ g_{b,1}(t_2) & g_{b,2}(t_2) & \cdots & g_{b,m}(t_2) \\ \vdots & \vdots & \ddots & \vdots \\ g_{b,1}(t_{n-1}) & g_{b,2}(t_{n-1}) & \cdots & g_{b,m}(t_{n-1}) \\ g_{b,1}(t_n) & g_{b,2}(t_n) & \cdots & g_{b,m}(t_n) \end{bmatrix} \tag{4.13}$$

In summary, to simulate the dynamic operation of one SCW, the β-ILS analytical model is first employed to generate a series of transfer functions having distinct combinations of constant pumping and bleed flow rates, each combination representing the temperature variation at the borehole wall $\Delta\overline{T}_b$ for a given state of the system. To simulate the temperature response to a dynamic heat rate, the input function matrix $\mathbf{F_{q,j}}$ and transfer function matrix $\mathbf{G_{b,j}}$ are then convolved within the non-stationary framework of Eq. 4.11.

The β-ILS model neither accounts for a geothermal heat flux, nor does it incorporates the effect of non-uniform initial temperatures along the borehole wall. Such effects can be incorporated using the superposition principle, which involves numerically generating another impulse response function called g_0 [145, 146]. Given that obtaining g_0 requires the development of a numerical model, a common and easier practice is simply to account for a constant initial temperature $T(t_0)$. Since this study aims to experimentally validate the β-ILS model, a constant initial temperature is applied to prevent compounding errors from model superposition.

4.4 Methodology

The methodology section proposes three original contributions that extend the capabilities of the β-ILS analytical model. They involve 1) evaluating the outlet fluid temperature from the analytical model's output, 2) considering the layered heterogeneity of the subsurface, and 3) incorporating the effects of radial convergent flow of groundwater induced by the simultaneous pumping and reinjection of fluid within the same column.

4.4.1 Fluid temperature evaluation

Since the temperature variation at the borehole wall $\Delta\overline{T}_b$ is difficult to measure directly in the field, the outlet fluid temperature $T_{f,out}$ is a much more suitable variable for experimental validation. To establish a relation between the β-ILS's output ($\Delta\overline{T}_b$) and $T_{f,out}$, one must first recognize that a SCW is analogous to a coaxial GHE with its annulus part opened to the rock, given that there is no convergent flow. Thus, the following relationship applies [147] :

$$\overline{T}_{s,b}(t) = \left(\frac{T_{f,in}(t) + T_{f,out}(t)}{2}\right) - q(t)\widetilde{R}_{s,b}(t) \tag{4.14}$$

In Eq. 4.14, the temperature $\overline{T}_{s,b}$ represents the average temperature of the subsurface at the borehole wall, which assumes a linear variation between the temperature at the inlet ($T_{f,in}$) and outlet ($T_{f,out}$), and heat losses dependent on the effective borehole resistance $\widetilde{R}_{s,b}$. The resistance $\widetilde{R}_{s,b}$ includes a series of thermal resistances, as depicted in Figure 4.2 and assumes a uniform flux along the borehole wall [93, 148]. The expression for $\widetilde{R}_{s,b}$ takes the following form :

$$\widetilde{R}_{s,b} = R'_1\left(1 + \frac{R_V^2}{3R'_1R'_{12}}\right) \tag{4.15}$$

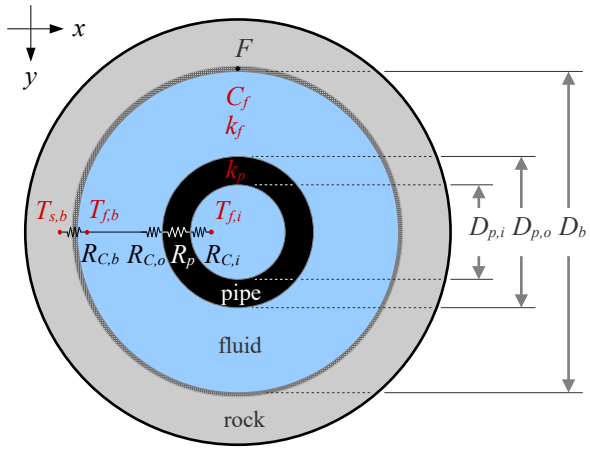

FIGURE 4.2 Thermal resistances in the cross-section of a standing column well.

with

$$R_1' = R_{C,b} \tag{4.16}$$

$$R_{12}' = R_{C,i} + R_p + R_{C,o} \tag{4.17}$$

and

$$R_V = \frac{L_s}{C_f V_P} \tag{4.18}$$

where R_p is the pipe thermal resistance, $R_{C,i}$, $R_{C,o}$ and $R_{C,b}$ are the film convective resistances inside and outside of the pipe and at the borehole wall [28, 93, 149], and where C_f is the volumetric heat capacity of the fluid. As detailed by Claesson and Javed (2019) [150], the quantity R_V has the same units as a thermal resistance. It is imperative to acknowledge that, in contrast to a coaxial GHE, a SCW does not comprise an outer pipe or grout to seal the outer ring from the rock. Consequently, the resistance R_1' does not incorporate any conduction resistances that are usually expected for a coaxial GHE [93]. For the sake of completeness, the equations for the individual resistances are given in Appendix 4.10.

In Eq. 4.14, the outlet fluid temperature $T_{f,out}$ is associated with the mean borehole wall temperature $\overline{T}_{s,b}$. However, this association does not extend to the analytical model's output $\Delta\overline{T}_b$, given that the output is situated on the fluid side of the borehole wall. To establish this link, the following relations are used :

$$\overline{T}_{s,b}(t) = \overline{T}_{f,b}(t) - q(t)R_{C,b}(t) \tag{4.19}$$

where

$$\overline{T}_{f,b}(t) = T(t_0) + \Delta\overline{T}_b(t) \tag{4.20}$$

Of particular significance is the fact that Eq. 4.19 outlines the relation between $\overline{T}_{f,b}$ and $\overline{T}_{s,b}$, respectively the temperature at the borehole wall of the fluid and the subsurface rock, indicating a straightforward relation through the heat rate that crosses the convective resistance at the borehole wall $R_{C,b}$. Additionally, Eq. 4.20 incorporates a constant initial temperature $T(t_0)$ and indicates that the β-ILS model's output is linked to the fluid temperature at the borehole wall. Accordingly, combining Eqs. 4.14, 4.19 and 4.20 , the following relation emerges :

$$\Delta\overline{T}_b(t) = \left(\frac{T_{f,in}(t) + T_{f,out}(t)}{2}\right) - q(t)\widetilde{R}_{f,b}(t) - T(t_0) \tag{4.21}$$

where $\widetilde{R}_{f,b}$ represents the effective borehole resistance on the fluid side and is expressed as a simple subtraction : $\widetilde{R}_{s,b} - R_{C,b}$.

In fact, the temperature $\overline{T}_f$, as defined by the term between the brackets in Eq. 4.21, is expressed by a weighted average of groundwater volumes $\nu_{f,in}$ and $\nu_{f,out}$:

$$\begin{aligned}\overline{T}_f &= \frac{\nu_{f,in}T_{f,in} + \nu_{f,out}T_{f,out}}{\nu_{f,in} + \nu_{f,out}} \\ &= \left(\frac{T_{f,in} + T_{f,out}}{2}\right)\end{aligned} \tag{4.22}$$

where the equality of the volumes $\nu_{f,in}$ and $\nu_{f,out}$ leads to the expression of $\overline{T}_f$ in Eq. 4.21, which is based on the assumption that there is no convergent flow toward the well. In the context of convergent flow induced by bleed, the groundwater volume $\nu_{f,in}$ reinjected in the SCW at temperature $T_{f,in}$ is equal to a volume of $\nu_{f,out}(1-\beta)$. Then, the temperature $\overline{T}_f$ takes the following form :

$$\begin{aligned}\overline{T}_f &= \frac{\nu_{f,out}(1-\beta)T_{f,in} + \nu_{f,out}T_{f,out}}{\nu_{f,out}(1-\beta) + \nu_{f,out}} \\ &= \frac{(1-\beta)T_{f,in} + T_{f,out}}{2-\beta}\end{aligned} \tag{4.23}$$

Thus, in the presence of convergent flow induced by bleed, it is proposed that Eq. 4.21 be modified as follows :

$$\Delta\overline{T}_b(t) = \left(\frac{(1-\beta)T_{f,in}(t) + T_{f,out}(t)}{2-\beta}\right) - (1-\beta)q(t)\widetilde{R}_{f,b}(t) - T(t_0) \tag{4.24}$$

In Eq. 4.24, it should be noted that a no-bleed scenario ($\beta = 0$) corresponds to the limiting case and to Eq. 4.14. For a full ratio ($\beta = 1$), the mean fluid temperature $\overline{T}_f$ matches the outlet fluid temperature $T_{f,out}$, as would be the case in an open-loop type of GHE. The second modification incurred by the bleed ratio β is the amount of heat transferred through the resistance $\widetilde{R}_{f,b}$, as the reinjection flow rate is reduced by a factor of (1-β).

An additional relation details the amount of heat transferred to the GSHP system between temperatures $T_{f,out}$ and $T_{f,in}$ and is expressed by :

$$Q(t) = C_f V_P(t) \left(T_{f,in}(t) - T_{f,out}(t)\right) \tag{4.25}$$

with $Q(t) = q(t)L_s$.

Eq. 4.25 enables the temperature $T_{f,out}$ to be expressed as a function of the analytical model's output $\Delta\overline{T}_b$. Indeed, combining Eqs. 4.18, 4.24 and 4.25 leads to :

$$T_{f,out}(t) = T(t_0) + \Delta\overline{T}_b(t) - (1-\beta)q(t)\left(\frac{R_V(t)}{2-\beta} - \widetilde{R}_{f,b}(t)\right) \tag{4.26}$$

Eq. 4.26 can be rewritten to find the transfer function associated with the outlet fluid temperature. Note that the heat rate in the evaluation of the transfer function should be $q = 1$ W/m and that the subsurface initial temperature should not be included, such as :

$$g_{out}(t) = g_b(t) - (1-\beta)q\left(\frac{R_V}{2-\beta} - \widetilde{R}_{f,b}\right) \tag{4.27}$$

As previously explained, g_b is a transfer function at the borehole wall obtained with the β-ILS model. Several transfer functions $g_{out,j}$ can be used in a non-stationary convolution to represent the different response to dynamic operating flow rates and heat rates (see Eq. 4.11). The evolution of the outlet fluid temperature, which is the desired output to perform experimental validation, is expressed through :

$$T_{f,out}(t) = (\mathbf{f_{q,j}} * \mathbf{g_{out,j}})(t) + T(t_0) \tag{4.28}$$

It can be demonstrated that, by construction, the function g_b is typically close to zero for times smaller than the residence time of the fluid inside the borehole. Therefore, a correction must be applied to the vector g_{out} to eliminate any negative values that may arise due to the downward shift from Eq. 4.27, a direct consequence of the linear approximation assumption made in Eq. 4.14. The required correction is an interpolation between time zero and the

residence time. This correction combined with Eqs. 4.27 and 4.28 form the methodology to simulate the outlet fluid temperatures $T_{f,out}$, the final output of the theoretical framework. Lastly, note that the linearity assumptions of this framework considers requires the fluid properties to be considered constant rather than temperature-dependent.

4.4.2 Assumption of layered heterogeneity

The β-ILS analytical model is based on the assumption of homogeneous and isotropic conditions, which is common to most analytical models developed for radial diffusion [42, 73, 74]. The work of Robert et al. (2022) [27], however, indicated that layered heterogeneity, as illustrated in Figure 4.3, can have an important impact on heat transfer in SCWs.

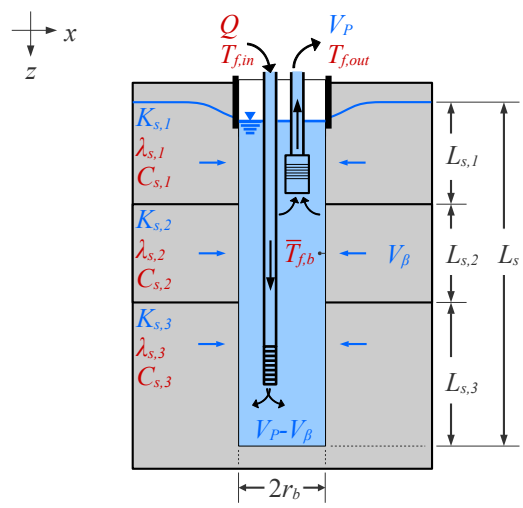

FIGURE 4.3 Representation of a standing column well operating with bleed in an arbitrary layered hydrostratigraphic context.

To account for the effect of layered heterogeneity on advective and diffusive heat transfer, it is proposed to evaluate an effective Péclet number $\widetilde{\mathrm{Pe}}$ and an effective advection time $\widetilde{t}_A$ by modifying Eqs 4.5 and 4.6 as follows :

$$\widetilde{\mathrm{Pe}} = \frac{V_\beta/(2\pi\widetilde{L}_s)}{\widetilde{\alpha}_s} \tag{4.29}$$

$$\widetilde{t}_A = \frac{V_\beta t}{\pi\widetilde{L}_s r_b^2} \tag{4.30}$$

where $\widetilde{L}_s$ is the effective height of the hydrostratigraphic layers and $\widetilde{\alpha}_s$ is the effective thermal diffusivity. The objective of the effective properties is to preserve the structure and analyti-

cal tractability of the β-ILS model by transforming spatially heterogeneous properties into equivalent homogeneous representations. To find the value of $\widetilde{L}_s$, the concept of transformed section [151] is applied through a coordinate transformation from a homogeneous to heterogeneous medium, as follows :

$$\widetilde{L}_s = L_s \frac{\widetilde{K}_s}{K_{s,r}} \quad \text{and} \quad \widetilde{K}_s = \sqrt{K_{s,r} K_{s,z}} \tag{4.31}$$

where $\widetilde{K}_s$ is the effective hydraulic conductivity of the hydrostratigraphic layers expressed as a function of the average hydraulic conductivities in the radial $K_{s,r}$ and vertical $K_{s,z}$ directions. The radial conductivity is an arithmetic average ($K_{s,r} = (\sum_{j=1}^{k} K_{s,j} L_{s,j})/L_s$), while the vertical conductivity is obtained by a harmonic mean ($K_{s,z} = L_s/(\sum_{j=1}^{k} L_{s,j}/K_{s,j})$).

The effective thermal diffusivity $\widetilde{\alpha}_s$ is defined as the ratio of the effective thermal conductivity $\widetilde{\lambda}_s$ to the volumetric heat capacity $\widetilde{C}_s$. Since conductive heat transfer occurs primarily parallel to the layers, the effective thermal conductivity $\widetilde{\lambda}_s$ is evaluated using an arithmetic average ($\widetilde{\lambda}_s = (\sum_{j=1}^{k} \lambda_{s,j} L_{s,j})/L_s$). Since the heat capacity C_s is a scalar property, the effective heat capacity $\widetilde{C}_s$ is calculated as an arithmetic average, ($\widetilde{C}_s = (\sum_{j=1}^{k} C_{s,j} L_{s,j})/L_s$).

In summary, to account for layered heterogeneity, effective hydraulic and thermal properties are estimated and used to evaluate the effective dimensionless parameters $\widetilde{\mathrm{Pe}}$ and $\widetilde{t}_A$. The latter parameters replace their counterparts in the β-ILS model presented in Section 4.3.1, thus modifying the form of the model's output.

4.4.3 Induced convergent flow from SCW operation

In a SCW, flow patterns emerge at both the reinjection and pumping points in response to induced pressure gradients [27, 38, 123]. This phenomenon implies the occurrence of radial convergent flow even without bleed. Figure 4.4 illustrates the patterns of radial groundwater flow in a SCW under the different assumptions of a) homogeneity or b) layered heterogeneity (showing arbitrary layers and groundwater flows). The overpressure at the reinjection point induces a radial outflow, while the depressurization at the pumping point draws water from the hydrostratigraphic layers to the well. Moreover, a balance point exists where radial flow is zero [38, 123]. For a homogeneous hydrostratigraphic layer, the balance point is located at depth $L_s/2$ (see Figure 4.4a). Alternatively, the location of the balance point varies for heterogeneous hydrostratigraphic layers [27].

To account for the induced radial convergent flow from the pump suction V_{s^-}, Eqs. 4.29 and

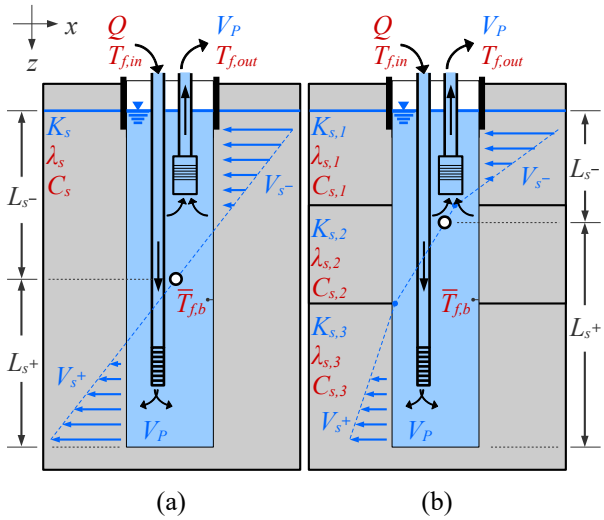

FIGURE 4.4 Representation of radial groundwater flow in a standing column well operating without bleed under the assumption of (a) homogeneity and isotropy and (b) layered heterogeneity with abritrary hydraulic conductivities increasing from units 1 to 3.

4.30 are modified as follows :

$$\widetilde{\mathrm{Pe}} = \frac{(V_{s^-}/\widetilde{L}_{s^-} + V_\beta/\widetilde{L}_s)/(2\pi)}{\widetilde{\alpha}_s} \tag{4.32}$$

$$\widetilde{t}_A = \frac{(V_{s^-}/\widetilde{L}_{s^-} + V_\beta/\widetilde{L}_s)t}{\pi r_b^2} \tag{4.33}$$

where V_{s^-} is the rate of convergent flow induced by pumping and $\widetilde{L}_{s^-}$ is the effective thickness affected by the depressurization.

To find $\widetilde{L}_{s^-}$, one must locate the balance point, according to the hydraulic properties of the hydrostratigraphic layers. Yuill and Mikler (1995) [38] indicate that the rate of convergent flow and divergent flow are equal. As hydraulic transmissivity is a parameter that defines the rate of radial groundwater flow ($T = K_r L_s$), both sections L_{s^-} and L_{s^+} should thus have the same transmissivity. In this work, the values of L_{s^-} and L_{s^+} are identified through the assumption that their transmissivities are equal ($T = K_{s^-,r} L_{s^-} = K_{s^+,r} L_{s^+}$). Once the length of the suction section L_{s^-} is found, the effective length $\widetilde{L}_{s^-}$ is calculated using the same method described for Eq. 4.31 with the conductivities $K_{s,j}$ contained within the length L_{s^-}.

An expression to quantify the rate of convergent flow toward the well (V_{s^-}) is given by Thiem

(1906) [152] :

$$V_{s^-} = \frac{2\pi K_{s^-,r} \Delta H_{s^-} L_{s^-}}{\log(r_\infty / r_b)} \tag{4.34}$$

where $K_{s^-,r}$ is the average radial hydraulic conductivity in the suction section and ΔH_{s^-} is the water head variation due to suction. The radius r_∞ is the radius of influence and is described as the distance where the drawdown of the water table is deemed negligible. The radius of influence and the drawdown can be deduced from measurements in nearby wells, if available, or from analytical equations [153]. The drawdown due to suction ΔH_{s^-} is derived from a relationship linking the observed water head variation in the annulus ΔH_a to the friction loss in the well. It is expressed by :

$$\Delta H_{s^-} = \Delta H_a - F \cdot \frac{L_s}{2r_a} \cdot \frac{\left(V_P / (\pi r_{p,o}^2 - \pi r_b^2)\right)^2}{2g} \tag{4.35}$$

here F is the Darcy friction factor, g is the gravitational acceleration and r_a is the hydraulic radius in the annular space $(r_b - r_{p,o})$. The water head variation ΔH_a is the result of experimental steady-state measurements preceding and following the submersible pump activation, with values generally ranging from millimetres to decimetres depending on the pump characteristics, SCW configuration and site-specific conditions.

To summarize, Section 4.4 presented a novel methodology for evaluating the outlet fluid temperature of SCWs based on the borehole wall temperature, thereby facilitating a fair comparison with measurements made during the operation of a SCW with bleed. Furthermore, it offers a modification of the β-ILS model's equations to account for both layered heterogeneity and radial convergent flow due to depressurization.

4.5 Numerical verification

4.5.1 Model and case configurations

This section provides a numerical verification of the model presented in the previous sections 4.4.1 and 4.4.2, by demonstrating that the analytical implementations accurately reproduce the expected numerical results. Verification data sets are generated using a two-dimensional axisymmetric model inspired by Nguyen et al. (2025) [45]. The modelled hydrostratigraphic context contains three distinct horizontal layers. The boundary conditions are illustrated in Figure 4.5, while Table 4.2 summarizes the values used for the various properties and geometry. Note that the subsurface properties in Table 4.2 represent the average or effective properties, and that the specific properties of each layer vary with the numerical cases

presented according to contrast ratios, which are explained further on in this section.

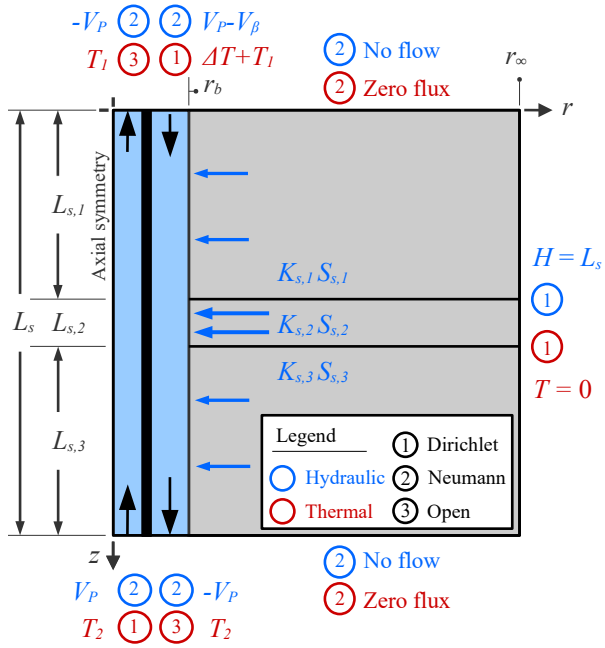

FIGURE 4.5 Illustration of the two-dimensional axisymmetric and coupled numerical model used for verification showing the hydraulic (blue) and thermal (red) boundary conditions, the three layers $L_{s,j}$ (grey area), the groundwater (blue area) and the pipe (bold vertical black line).

TABLEAU 4.2 Geometry and properties used in the numerical model for the verification of the β-ILS model and the methodology proposed in Section 4.4. Subsurface properties are layers' averages.

Parameters	Fluid	Pipe (interior)	Subsurface Layers : 1/2/3
L [m]	-	200	99.5/1/99.5
r [m]	r_b : 0.102	0.0302 (0.0247)	1000
K [m/s]	300	1.0e-9	1.0e-6
S_s [1/m]	4.0e-6	1.3e-7	5.0e-5
λ [W/(mK)]	0.60	0.10	2.50
C [MJ/(m^{3}K)]	4.20	1.56	2.50

In the numerical model depicted in Figure 4.5, layer 2 represents a fractured zone of 1 meter thick. To investigate the effect of layered heterogeneity due to this zone, the hydraulic conductivity $K_{s,j}$ and specific storage $S_{s,j}$ of the subsurface layers (j=1, 2, 3) are adjusted so that the values of $K_{s,2}$ and $S_{s,2}$ are higher, while the average properties are maintained as

listed in Table 4.2. The numerical model employs a concentric pipe configuration to replicate a SCW, with the annular space exposed to the ground. Groundwater is pumped from the central region and reinjected into the annulus at flow rates V_P and $V_P - V_\beta$, respectively. Note that the inverse configuration can also be employed to adapt to different field constraints, as suggested in Figure 4.4. The model is used to generate transfer functions by incorporating a temperature change ($\Delta T = qL_s/(V_P C_f)$) to the observed outlet temperature T_1. Dirichlet boundary conditions are applied at the far-field to reproduce undisturbed conditions. Null heat and hydraulic flow are applied at the upper and lower boundaries of the model. Hydraulic flow and heat transfer in the all domains are obtained by solving, with the finite element method, Darcy's law and the heat continuity equation, which are :

$$\rho_f S_s \frac{\partial P}{\partial t} = -\nabla \cdot (\rho_f v) \quad \text{and} \quad v = \frac{-K_m}{\rho_f g} \nabla P \tag{4.36}$$

$$C_m \frac{\partial T}{\partial t} + C_f v \cdot \nabla T = \nabla \cdot (\lambda_m \nabla T) \tag{4.37}$$

In Eqs. 4.37 and 4.36, g is the gravitational acceleration, v is the groundwater flow velocity, P is the pressure, S_s is the specific storage of the subsurface layer, the subscript m indicates the proprety varies according to the domain and ρ_f is the density of the fluid, which is set to a constant value of 1000 kg/m^3. Eqs. 4.37 and 4.36 also apply to the groundwater in the column (blue domains) and the reinjection pipe (black domain), whereas a very high hydraulic conductivity is given to groundwater and a very low to the pipe, as reported in Table 4.2. This utilization of Darcy's law is a strategy that has been demonstrated and validated through numerous studies [26–28, 40, 50–53]. Note that all properties presented in Table 4.2 are independent of temperature as the assumption of linearity is a prerequisite to create transfer functions, thus allowing quasi-instant temperatures computation through a convolution product. The assumption of temperature-independent properties is standard in most GSHP simulation tools and is justified by the relatively small variation of properties over typical operating temperatures (e.g., 5–30°C).

Three numerical test cases with varying degrees of layered heterogeneity are analyzed and expressed by the contrast ratio ϕ [40, 51] :

$$\phi = \frac{K_{s,\text{fractures}}}{K_{s,\text{matrix}}} \quad \text{and} \quad \phi = \frac{S_{s,\text{fractures}}}{S_{s,\text{matrix}}} \tag{4.38}$$

The mean properties are obtained with :

$$K_{s,r} = \frac{\sum_{j=1}^{k}(K_{s,j}L_{s,j})}{L_s} \quad \text{and} \quad \widetilde{S}_s = \frac{\sum_{j=1}^{k}(S_{s,j}L_{s,j})}{L_s} \tag{4.39}$$

As introduced and presented in Table 4.2 and Figure 4.5, the model contains three horizontal layers. Layer 2 is chosen to reproduce a pervious fractured zone embedded between less permeable layers (1 and 3), referred to as the matrix in Eq. 4.38. Hence, index $j = 2$ in Eq. 4.39 is equivalent to the fractured zone in Eq. 4.38, whereas indices $j = 1{,}3$ correspond to the matrix. For each numerical test case, the same average horizontal hydraulic conductivity $K_{s,r}$ and effective specific storage $\widetilde{S}_s$ are used (as reported in Table 4.2). The system of equations formed by Eqs. 4.38 and 4.39 is used to identify the properties of each layer ($K_{s,j}$ and $S_{s,j}$), depending on the contrast ratio ϕ, which is 1, 10 and 100 for the numerical test cases 1 to 3, respectively. Thus, numerical test case 1 represents a homogeneous aquifer (ϕ=1), with the same properties applied to all three layers. In contrast, numerical test cases 2 and 3 exhibit layered heterogeneity with an increasingly higher contrast ratio (ϕ=10 and 100). Each numerical case simulates the heat transport dynamics induced by four bleed ratios (β =0%, 10%, 20%, 30%), allowing the accuracy of the new methodology to be verified under varying operational conditions. The pumping flow rate applied for the numerical cases is 150 L/min. The Péclet numbers obtained for each numerical test case are presented in Table 4.3, where Eq 4.5 from the original β-ILS model is used for the homogeneous case (test case 1) and Eq 4.29, the proposed effective counterpart, is used to evaluate the heterogeneous cases (test cases 2 and 3).

Tableau 4.3 Calculated Péclet numbers for each numerical test case.

Test case	ϕ	$\beta = 0\%$	$\beta = 10\%$	$\beta = 20\%$	$\beta = 30\%$
1	1	0.000	0.200	0.401	0.601
2	10	0.000	0.204	0.409	0.613
3	100	0.000	0.244	0.489	0.733

4.5.2 Numerical verification results

Figure 4.6 illustrates the numerical transfer functions at the outlet g_{out} compared to the analytical transfer functions obtained using Eq. 4.27. As the numerical test cases 2 (ϕ=10) and 3 (ϕ=100) consider layered heterogeneity, they allow verification of the proposed formulations of effective $\widetilde{\text{Pe}}$ and $\widetilde{t}_A$ (Eqs. 4.29 and 4.30). To verify the accuracy of the proposed methodology, the root mean square relative error (RMSRE) is utilized.

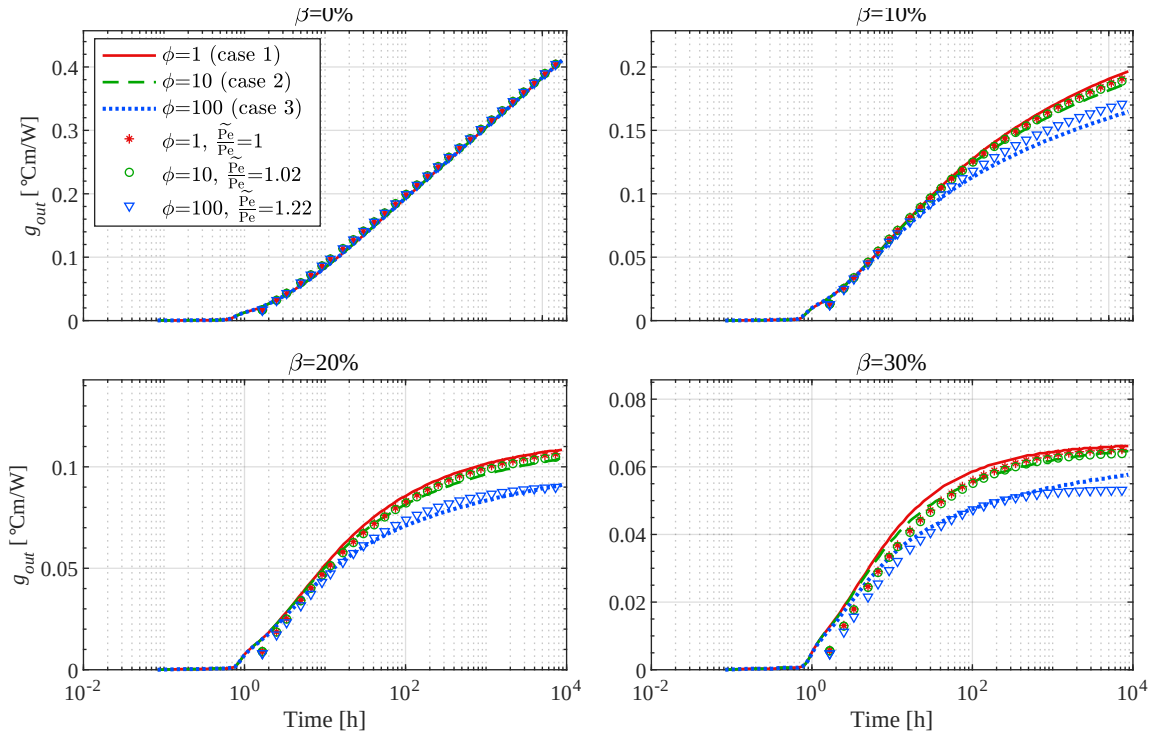

FIGURE 4.6 Transfer functions simulated with the proposed methodology (markers) in comparison with the functions simulated with the numerical model for a heat excitation of 1 W/m over a one-year period and under four bleed ratios.

A statistical analysis of the one-year transfer functions presented in Figure 4.6 offers RMSREs varying from 1.3e-2 to 6.5e-2 with an average of 2.9e-2. These errors are slightly above the range observed by Nguyen et al. (2025) [45] after calibrating their model with a value of 9.8e-3. One must bear in mind that the original β-ILS analytical model exhibited increased error levels for higher Pe values, a phenomenon that is also observed in the present study, as evidenced by the results and the corresponding Pe values shown in Table 4.3. The average RMSRE for numerical test case 1 (ϕ=1) at all bleed levels is 2.3e-2, indicating that in the absence of modification of the Péclet number, the error remains within the same range. Consequently, it can be deduced that the novel contributions to the proposed methodology and the β-ILS analytical model yield good accuracy compared to the numerical simulations.

Without bleed, the analytical transfer functions exhibit a RMSRE of 1.3e-2. As explained in Section 4.3.1, the β-ILS analytical model without bleed corresponds to the ILS model of Ingersoll et al. (1954) [73]. As the bleed ratio and Péclet number increases, the analytical transfer functions exhibit slight discrepancies from their numerical counterparts in the first time steps. This was also observed by Nguyen et al. (2025) [45]. For the highest contrast ratio (ϕ=100) and highest bleed ratio (β=30%) analyzed (blue line and markers at bottom

of Figure 4.6), the long-term response of the analytical transfer function also appears to reach a steady state earlier than its numerical counterpart. Even in these worst case scenarios, the RMSRE remains below 6.5e-2.

To assess the contribution of the transformation applied by Eq. 4.27 to RMSRE, Figure 4.7 compares the numerical functions g_b and the numerical functions g_{out} presented in Fig. 4.6, to the computed functions $\hat{g}_{out}$ obtained by applying Eq. 4.27 to the numerical functions g_b. The RMSRE obtained between $\hat{g}_{out}$ and g_{out}, as illustrated in Figure 4.7, reached 3.0e-6. Compared to the RMSRE observed for the functions in Figure 4.6, it is evident that the errors associated for the transformation are insignificant. Therefore, the proposed transformation for evaluating the outlet temperature based on the borehole wall temperature provides very accurate results. Nevertheless, it is interesting to note that the most important errors observed are associated with the highest contrast and bleed ratios.

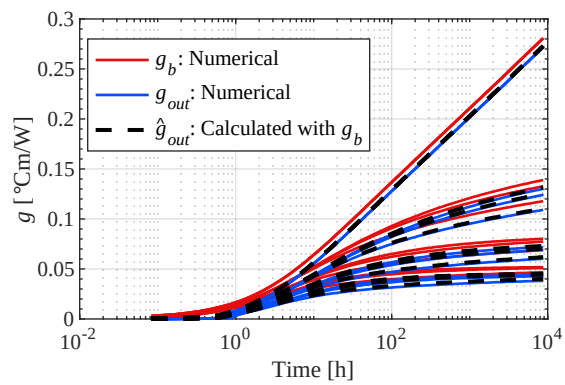

FIGURE 4.7 Comparison of transfer functions calculated at the outlet ($\hat{g}_{out}$) using the numerical g_b and Eq. 4.27, with the one simulated by the numerical model g_{out}.

A concluding numerical verification is conducted to demonstrate the extent to which the linearity assumption underlying the transformation in Eq. 4.24 is valid as a function of the pumping flow rates. Using the properties of numerical test case 1 ($\phi = 1$), Figure 4.8 illustrates the average fluid temperature profiles of the fluid following one day of simulation and for five different pumping flow rates. For each flow rate and in each section of the SCW, a Reynolds number is evaluated assuming a constant viscosity of 0.0013 Pa·s.

The temperature profiles shown in Figure 4.8 demonstrate linear variations for pumping flow rates ranging from 75 to 150 L/min, while curvatures become clear for the lower flow rates (25 and 50 L/min). Thus, the robustness of the linearity assumption used in Eq. 4.14 is diminished when the Reynolds number is lower than 3100 in the upward section. In fact, as illustrated in Figure 4.8, the thermal interference between the reinjection pipe and the

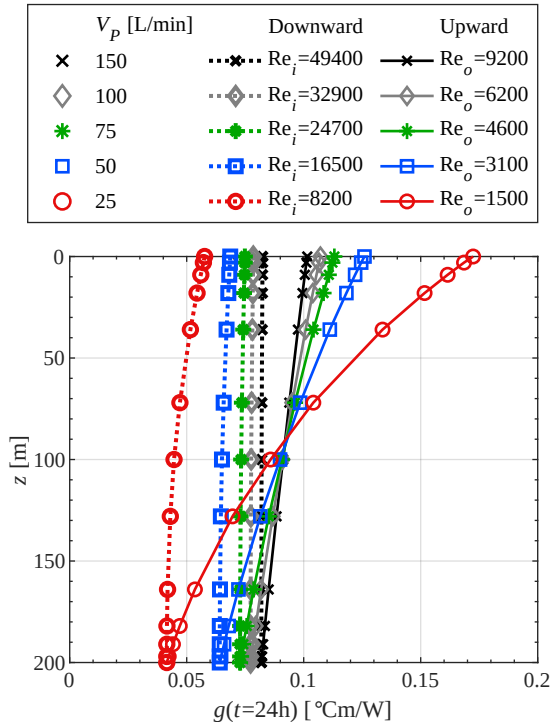

FIGURE 4.8 Vertical fluid temperature profiles at t=24 h obtained for numerical test case 1 ($\phi = 1$) at the inlet (dotted lines) and outlet (solid lines) sections of the SCW and for five pumping flow rates and Reynolds numbers inside the reinjection pipe (Re_i) and in the annular space (Re_o).

annulus increases with small Reynolds numbers. As a result, the relationships between $T_{f,out}$ and $\overline{T}_b$, as presented in Section 4.4, may exhibit a reduced accuracy with laminar flow rates.

4.6 Experimental validation

4.6.1 Experimental site and data

To address the lack of experimental validation of the β-ILS analytical model, three experimental tests conducted at a single site in Varennes, Canada, are used. The site features a SCW and an injection well that are spaced 10 meters apart. The SCW, which reaches a depth of 215 meters, is connected to a mobile geothermal unit equipped with heat pumps for both heating and cooling. Table 4.4 summarizes the site properties and geometry determined by Beaudry et al. (2019) [40], who calibrated a numerical model using experimental data from a 6-day pumping test, a 24-day thermal response test, and a 25-day dynamic winter operation.

The hydrostratigraphic vertical profile at the experimental site consists of approximately 3

Tableau 4.4 Geometry and properties of the studied site, as determined by Beaudry et al, (2019).

Parameters	Fluid	Pipe (interior)	Subsurface Layers : 1/2/3
L [m]	-	-	1/5/207
r [m]	r_b : 0.083	0.0302 (0.0243)	30
K [m/s]	-	-	1.0e-7/1.7e-5/1.7e-7
λ [W/(mK)]	0.59	0.42	1.6/2.74/2.74
C [MJ/(m^{3}K)]	4.18	2.17	2.32/2.00/2.00

meters of overburden (layer 1) followed by a 5-meter-thick zone of fractured rock (layer 2) and then 207 meters of unfractured rock (layer 3). During the various tests, the water level was measured at a depth of approximately 2 meters. The radius of influence (r_∞) is assumed to be 30 meters, as estimated by Beaudry et al. (2019) [40]. Additionally, the data showed that operating the submersible pump at a pumping flow rate of 100 L/min resulted in a drawdown of 5 cm in the annulus (ΔH_a). Finally, the borehole wall roughness (ε_b) is assumed to be 5 mm, which is consistent with the values reported in the literature [154]. The properties listed in Table 4.4, together with the details provided above, are used as direct inputs to the analytical model for simulating and comparing temperatures with those observed in the three experimental tests.

The three experimental validations use data sets from previous studies [40,63], all conducted with the same mobile laboratory installed at the experimental site in Varennes. The first two data sets are associated with thermal response tests conducted by Dion et al. (2023) [63] and lasted approximately six days. Each thermal response test consisted of three two-day sequences of near-constant bleed, with heat injection on day one followed by a recovery period on day two. During these two experimental tests, the pumping flow rate was maintained at approximately 101 and 105 L/min, respectively, while bleed flow rates of 0, 4, 6 and 8 L/min were applied in different orders. The third data set uses the first six days of the 25-day heating experiment conducted by Beaudry et al. (2019) [40], during which pumping and bleed flow rates fluctuated dynamically. The three data sets provide a wide range of pumping and bleed flow rates, thus allowing a comprehensive experimental validation of the novel methodology presented in the previous section. It should be mentioned that the data sets from both Dion et al. (2023) [63] and Beaudry et al. (2019) [40] have been used to validate their modelling strategies, respectively a two-dimensional numerical model and a multi-deconvolution algorithm.

The experimental validation process first involves a stepwise data classification, which consists of examining the experimental data sets to identify the quasi-constant pumping and bleed flow rates to be considered in the calculation of the transfer functions. For test cases 1 and 2, three distinct states involving different pumping and bleed flow rates are considered, which is consistent with the methodology presented by Dion et al. (2023) [63]. For test case 3, 237 states are used, representing an average duration of approximately 36 minutes per state. To reproduce the complete dynamic signal $T_{f,out}$ (Eq. 4.28) for each experimental case, the non-stationary convolution algorithm presented in Section 2.2 is used, whereby the transfer function of each unique state is combined with the excitation function corresponding to its moment of activation.

4.6.2 Experimental validation results

Figures 4.9, 4.10 and 4.11 present the experimental ($T_{f,out}$) and analytical outlet temperatures ($\hat{T}_{f,out}$), along with the corresponding heat loads, pumping flow rates and bleed flow rates during the tests. The residuals ($x = T_{f,out} - \hat{T}_{f,out}$) between the experimental and analytical temperatures are also shown for each experimental validation. The color variations in the temperature curves are indicative of changes in the SCW state of operation.

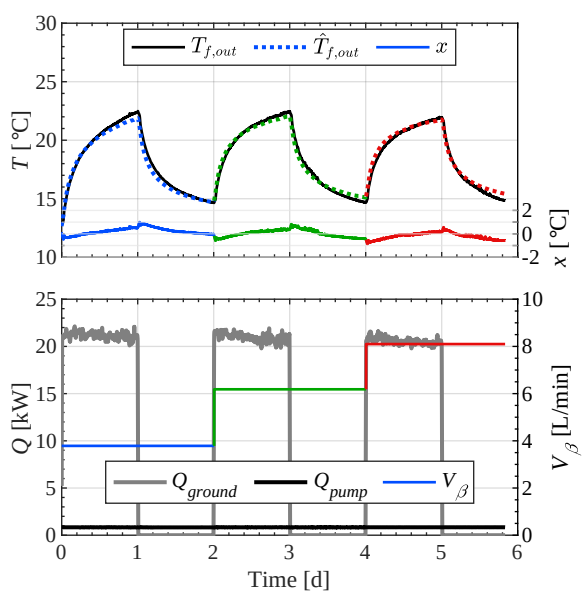

FIGURE 4.9 Experimental test case 1 – Thermal response test on a standing column well with three operating states (indicated by color variations). Top : Experimental ($T_{f,out}$) and analytical ($\hat{T}_{f,out}$) temperatures with residuals (x) on a secondary y-axis. Bottom : Ground heat loads (Q_{ground}) and pump heat output (Q_{pump}), along with bleed flow rates (V_β).

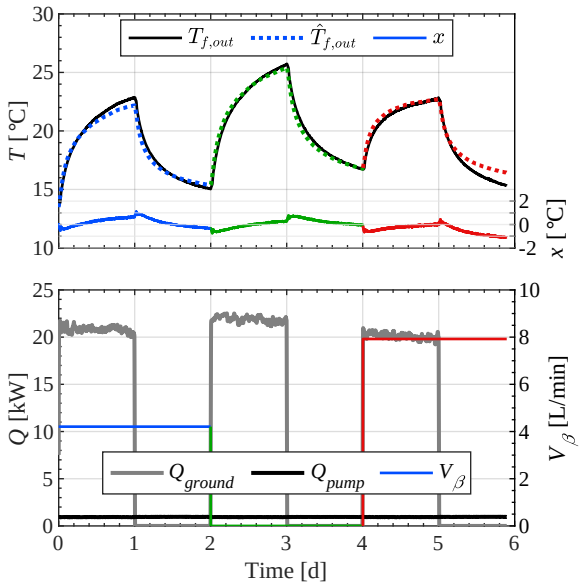

FIGURE 4.10 Experimental test case 2 – Thermal response test on a standing column well with three operating states (indicated by color variations). Top : Experimental ($T_{f,out}$) and analytical ($\hat{T}_{f,out}$) temperatures with residuals (x) on a secondary y-axis. Bottom : Ground heat loads (Q_{ground}) and pump heat output (Q_{pump}), along with bleed flow rates (V_β).

The mean absolute errors (MAE) between experimental and analytical outlet temperatures are 0.28 °C, 0.35 °C and 0.37 °C for test cases 1, 2 and 3, respectively. These errors are in the same range as the accuracy of the temperature sensors, which is ±0.2 °C. For comparison, Beaudry et al. (2019) [40] reported a MAE of 0.32 °C for the calibration of a finite element numerical model on the whole 25-day data set (test case 3), while Dion et al. (2023) [63] reported root mean squared errors of 0.05 and 0.07 °C for reconstructed temperature signals from optimized transfer functions (test case 1 and 2). Therefore, the MAEs obtained in this study demonstrate that the β-ILS analytical model, within the proposed methodology, produces accurate results. A comprehensive evaluation of the residuals suggests that the methodology accurately replicates the outlet temperatures of a SCW operating under highly dynamic ground loads and pumping and bleed flow rates, as illustrated in Figure 4.11. Note that part of these errors can also be attributed to the non-stationary convolution itself. Nevertheless, it should be noted that the results are obtained using the subsurface thermal and hydraulic parameters reported by Beaudry et al. (2019) [40], which were obtained following a first-order approximation and a numerical analysis.

A slight discrepancy is observed in the shape of the analytical thermal responses of test cases 1 and 2 (see Figures 4.9 and 4.10). Indeed, the temperatures simulated with the proposed

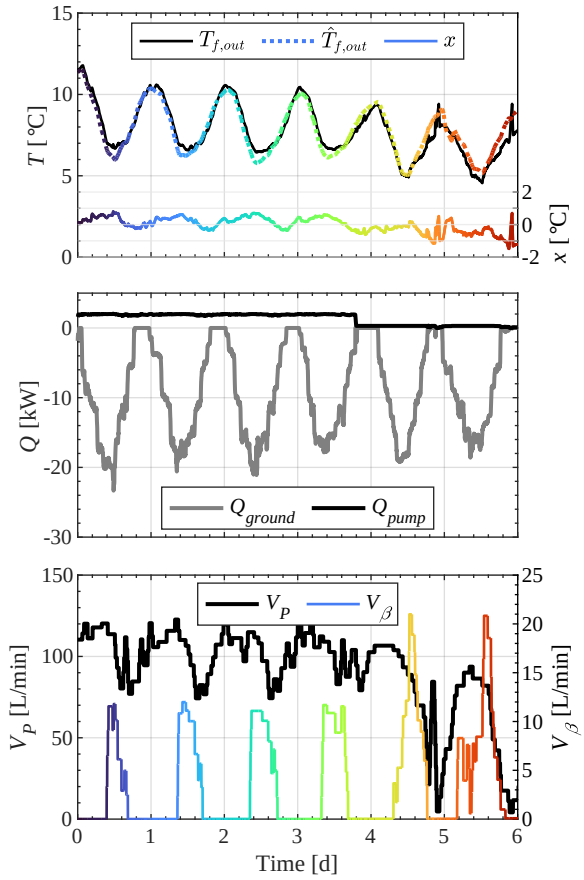

FIGURE 4.11 Experimental test case 3 – Dynamic operation of a standing column well in heating mode. Top : Experimental ($T_{f,out}$) and analytical ($\hat{T}_{f,out}$) temperatures with residuals (x) on a secondary y-axis. Middle : Ground heat loads (Q_{ground}) and pump heat output (Q_{pump}). Bottom : Circulation (V_P) and bleed (V_β) flow rates. Each slight color variation indicates state change, which occurs on average every 36 minutes.

methodology show a more immediate response after a major heating power change. This pattern is constant across all experimental cases. The observation of this behavior in all cases suggests that the shape discrepancy is not directly related to the bleed flow rates. However, the shape discrepancy could indicate that the methodology is less accurate in the short-term transient response, or it could indicate that the parameters could be optimized to provide a better fit.

To further analyze the accuracy of the β-ILS analytical model and the proposed methodology, Figure 4.12 presents the MAE of each state as a function of both the pumping V_P and bleed flow rates V_β, for all three cases. Note that the MAEs of the three test cases follow the color code previously used in their respective Figures 4.9, 4.10 and 4.11. As illustrated in Figure

4.12a, the MAE decreases as the pumping flow rate increases. This entails that high MAE values (approximately 1°C or higher) are associated with lower flow rates, which propagate to higher flow rates following them, as evidenced by the three orange circles observed between 70 L/min and 85 L/min occurring on day 5. One potential explanation for this phenomenon is that it is a direct consequence of the assumption of linearity in Eq. 4.24, which is less valid in a laminar regime, as demonstrated in Figure 4.8. Indeed, the MAE increases for Reynolds numbers below approximately 3500. It is also important to note that the calibration of the weights used in the β-ILS analytical model by Nguyen et al. (2025) [45] excluded laminar flow rates.

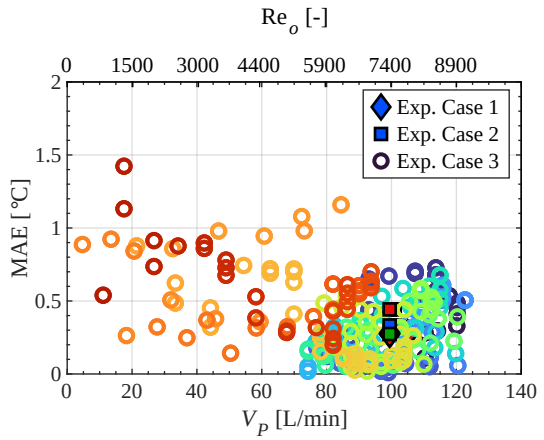

(a)

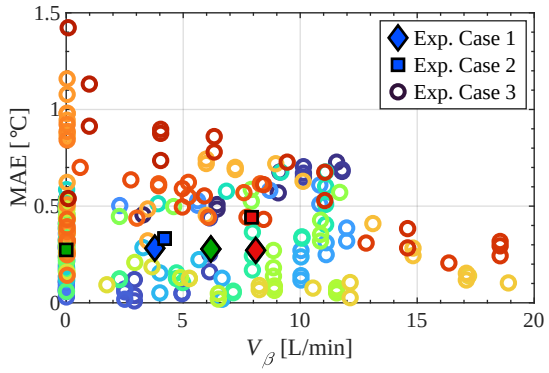

(b)

FIGURE 4.12 Mean absolute error (MAE) calculated for experimental case 1, 2 and 3, in relation with (a) pumping flow rates, Reynolds numbers, and (b) bleed flow rates. Color variations are associated with each state activated, as depicted in Figures 4.9, 4.10 and 4.11.

A last notable observation is regarding the distribution of the MAE values in Figure 4.12b,

with the exclusion of the final two days of test case 3 (oranges to red circles in Figure 4.11), due to the errors associated with low rates, as previously explained. For all others, the MAE values show only a slight increase with the bleed flow rates, corresponding to the increase in errors observed by Nguyen et al. (2025) [45] for higher Pe numbers. In general, it can be concluded that the β-ILS analytical model, along with the theoretical developments herein proposed, maintains a good level of accuracy with a varying level of bleed ratios.

4.7 Conclusions

This study presents new theoretical developments for a recent analytical model that simulates a standing column well operating with bleed. The novelties proposed include : 1) the computation of the outlet fluid temperature instead of only the borehole wall temperature, 2) the integration of layered heterogeneity, and 3) the incorporation of the effects of radial convergent flow of groundwater induced by simultaneous pumping and reinjection. These contributions improve the model's applicability to more realistic standing column well configurations.

To illustrate the robustness of the developed methodology, an experimental validation is performed using three experimental data sets. The validation shows a mean absolute error of the methodology, which extends the analytical model, ranging from 0.28 to 0.37 °C. These errors are consistent with the ranges of temperature sensor accuracy and the error reported for validation with an advanced numerical model, indicating the reliability and accuracy of the analytical model and the proposed methodology in capturing the response of standing column wells in highly dynamic conditions involving various bleed and pumping flow rates. Furthermore, a comparison of the errors with respect to flow rates indicates that the model predictions remain stable across a wide range of operational conditions, further supporting its robustness. As small discrepancies are identified in the short-term transient responses and at low pumping flow rates, additional adjustments will be necessary to more accurately capture thermal interference effects under near-laminar flow conditions. Finally, numerical verifications indicated that the transformation used to infer the outlet temperature from the temperature of the borehole wall introduces negligible error, confirming the robustness of the approach developed in this work.

The proposed contributions to the analytical model of Nguyen et al. (2025) [45] constitute a substantial advancement for the simulation of standing column wells, as they provide an efficient and accurate approach to predict their thermal response under realistic and complex conditions. Subsequent endeavours should concentrate on broadening the model to a wider range of radial distances, thereby facilitating more comprehensive analyses for multi-well sys-

tems. The proposed refinements and expanded validation of the model enhance its potential to become a valuable tool for the design and operation of standing column wells.

4.8 Acknowledgments

The authors acknowledge the support from partners of the Geothermal Research Chair on the Integration of SCWs in Institutional Buildings, namely Hydro-Québec, the Ministry of higher education of Québec, Mille-Îles School Service Centre, Montreal School Service Centre, Samares School Service Centre, Versaprofiles, Marmott Energies, CanmetEnergy and NSERC. Additionally, we thank the anonymous reviewers and colleagues that provided constructive comments, especially Gabriel Dion, who provided much of the experimental data used in this study. This work was financed by the Natural Sciences and Engineering Research Council of Canada through grant number ALLRP 544477-19.

4.9 Nomenclature

Acronyms

β-ILS	radial convergent flow ILS
FFT	fast Fourier transform
GHE	ground heat exchanger
GSHP	ground-source heat pump
ILS	infinite line source
MAE	mean absolute error
SCW	standing column well
RMSRE	root mean square relative error

Greek letters

α	thermal diffusivity [m^2/s]
Δ	difference [-]
β	bleed ratio [-]
ϵ	correction coefficient [-]
ε	roughness [-]
ϕ	contrast ratio [-]
λ	thermal conductivity [W/(m°C)]
ρ	density [kg/m^3]

ν volume [m^3]

Symbols

C volumetric heat capacity [J/(m^3°C)]
D diameter [-]
F Darcy friction factor [-]
$\mathbf{F}$ input matrix [W/m]
f input function [W/m]
$\mathcal{F}$ symbol for fast Fourier transform [-]
$\mathbf{G}$ transfer function matrix [°Cm/W]
g unitary transfer function [°Cm/W]
$\hat{g}$ transfer function simulated analytically [°Cm/W]
h scaling function [-]
H water head loss [m]
K hydraulic conductivity [m/s]
L thickness [m]
m number of states activated [-]
N contribution factor [-]
n number of time steps [-]
Nu Nusselt number [-]
P pressure [Pa]
Pe Péclet number [-]
Pr Prandtl number [-]
Q heat load [W]
q unit heat rate [W/m]
R thermal resistance [m°C/W]
Re Reynolds number [-]
r radius [m]
s state of activation [-]
S_s specific storage [1/m]
T observed temperature [°C]
$\hat{T}$ temperature simulated analytically [°C]
$\overline{T}$ average temperature [°C]
t time [s]
v velocity [m/s]

V	flow rate [m^3/s]
x	temperature residuals [°C]

Subscripts

A	advection
a	annulus
b	borehole
C	convection
D	diffusion
s	subsurface layer
s^+	pressurized subsurface layer due to reinjection
s^-	depressurized subsurface layer due to suction
i	inside
f	fluid
in	inlet
out	outlet
o	outside
p	pipe
r	radial/horizontal
P	pumping
z	vertical

4.10 Appendix : Thermal resistances

As presented in Figure 4.2, the thermal resistances between the analytical model output and the fluid outlet temperature are given as follows :

$$R_p = \frac{ln(r_{p,o}/r_{p,i})}{2\pi\lambda_p} \tag{4.40}$$

$$R_{C,i} = \frac{1}{\mathrm{Nu}_i\lambda_f\pi} \tag{4.41}$$

$$R_{C,o} = \frac{1}{\mathrm{Nu}_o\lambda_f\pi}\frac{r_a}{r_{p,o}} \tag{4.42}$$

$$R_{C,b} = \frac{1}{\mathrm{Nu}_b\lambda_f\pi}\frac{r_a}{r_b} \tag{4.43}$$

where convective resistances R_C are calculated according to Bauer et al. (2011) [149], r_a is the hydraulic radius in the annular space $(r_b - r_{p,o})$ and the Nusselt numbers under a turbulent regime are given by :

$$\mathrm{Nu} = 0.023\mathrm{Re}^{0.8}\mathrm{Pr}^{N} \tag{4.44}$$

with Re being the Reynolds number and Pr the Prandlt number and N a factor which value is 0.4 for heating applications and 0.3 for cooling [155].

For transitional regime or a rock-exposed borehole wall with Re≥2300, the Nusselt number Nu can be expressed as follows [156] :

$$\mathrm{Nu} = \frac{F(\mathrm{Re} - 1000)\mathrm{Pr}}{8\left(1 + 12.7\sqrt{\frac{F}{8}}\right)\left(\mathrm{Pr}^{\frac{2}{3}} - 1\right)} \tag{4.45}$$

where F is the pipe friction factor calculated and is obtained given the Colebrook-White equation as follows :

$$\frac{1}{\sqrt{F}} = -2\log\left(\frac{\varepsilon/(D)}{3.7} + \frac{2.51}{\mathrm{Re}\sqrt{F}}\right) \tag{4.46}$$

where D is the diameter in the space and the variable ε is the surface roughness. In the annular space, ε_a must account for both the pipe and borehole friction :

$$\varepsilon_a = \frac{\varepsilon_b r_b + \varepsilon_o r_{p,o}}{r_b + r_{p,o}} \tag{4.47}$$

CHAPITRE 5 ARTICLE 2 – OBTAINING THE HYDRAULIC AND THERMAL PROPERTIES OF THE MAIN HYDROSTRATIGRAPHIC UNITS SURROUNDING A STANDING COLUMN WELL USING A THERMAL RESPONSE TEST

Louis Jacques*, Philippe Pasquier
Journal of Hydrology, Volume 623 :129823, June 19, 2023
Department of Civil, Geological and Mining Engineering, Polytechnique Montréal, P.O. Box 6079 Station Centre-Ville, Montreal H3C 3A7, Canada.
* Corresponding author : louis.jacques@polymtl.ca
Keywords : Hydraulic properties identification, Thermal properties identification, Thermal response test, Standing column well, Bayesian Inference, Ground heat exchanger

5.1 Abstract

In general, classical interpretations of pumping tests assume homogeneous hydraulic properties and cannot characterize aquifer heterogeneity in the form of a profile. In this work, a thermal response test, which is routinely performed prior to the design of ground source heat pump systems, is conducted on an open-walled borehole to identify the hydraulic conductivity profile and thermal properties of the main geological units. Parameter identification and uncertainty quantification are performed in a Bayesian framework and rely on a neural network and a spectral method to speed up the solution of the direct problem. The analysis of a data set from field testing showed that the use of temperature measurements alone provided a hydraulic conductivity profile, with an average value close to that provided by a conventional pumping test. For the specific conditions observed in the field, it was also possible to precisely identify the thermal properties, as was the case for the main geologic unit, but not for the thin geologic units whose distributions were similar to the priors used for inference. This indicates that in some geologic settings, a thermal response test could fail to provide the thermal properties of some units. The approach, however, paves the way for new characterization techniques.

5.2 Introduction

Identifying the hydraulic properties of aquifers is essential in many fields, such as groundwater management, contaminant hydrogeology, geotechnics and geothermal energy. To estimate

such properties, pumping tests are usually carried out by extracting groundwater from a pumping well and observing the groundwater level response in the nearby aquifer [157]. Traditional interpretation of pumping tests gives, however, only a mean and homogeneous value for the hydraulic properties around the pumping well. Therefore, many research has focused on interpreting classical pumping tests with complex heterogeneous numerical models to obtain the vertical variations of the hydraulic properties [158]. Likewise, several in situ tests have been developed in the last decades to characterize aquifer heterogeneity, such as packer permeability tests [159, 160], oscillatory pumping tests [161, 162], in-well groundwater velocity measurement tests [163, 164], multi-level groundwater sampling [165] and single-well pressure injection-withdrawal tests [166].

In the field of ground source heat pumps, which can provide heating and cooling to buildings, a thermal response test (TRT) [72, 88] is usually carried out before the design of any large closed-loop ground heat exchanger (GHE) [167]. A TRT is, in essence, similar to a pumping test, but instead of drawing water from a well and monitoring the hydraulic head, heat is dissipated in a GHE at a constant rate while the temperature response is monitored. Such a test is usually achieved with a TRT unit containing a water heater, a pump and several temperature probes connected to a data acquisition system (see Fig. 5.1). The analysis of a TRT dataset is generally carried out with a first-order approximation of the infinite line source model [72], a technique similar to the Cooper–Jacob method and provides the thermal conductivity of geological materials, a key parameter for sizing GHEs [92].

The most frequent GHE type is the closed-loop well [168] as shown in Fig. 5.1a). In this GHE, a pair of pipes is inserted in a borehole. Then, the remaining volume is filled with a thermally enhanced grout, the role of which is to increase conductive heat transfer between the pipes and the surrounding bedrock, and to prevent groundwater contamination [169]. Although groundwater flow can increase its thermal performances, the main heat transfer mechanism of a closed-loop well is conduction [170].

After years of research on TRTs, many efforts were deployed to increase the number of estimated parameters and their accuracy [86, 100, 171, 172], to obtain a detailed vertical profile of thermal conductivity [173–176] and to better estimate the Darcy flux (or flow velocity) [94–97]. It is worth noting that identifying hydraulic flow with a thermal test is not exclusive to TRTs. For instance, Simon et al. (2021) [177] made use of active distributed temperature sensing to identify groundwater flow and thermal conductivity of surficial deposits. With the same objective, Klepikova et al. (2011, 2014) [178, 179] used heat tracer tests to assess the hydraulic properties surrounding groundwater wells. The authors noted that heat tracer test interpretation could efficiently identify hydraulic properties only in permeable zones, where

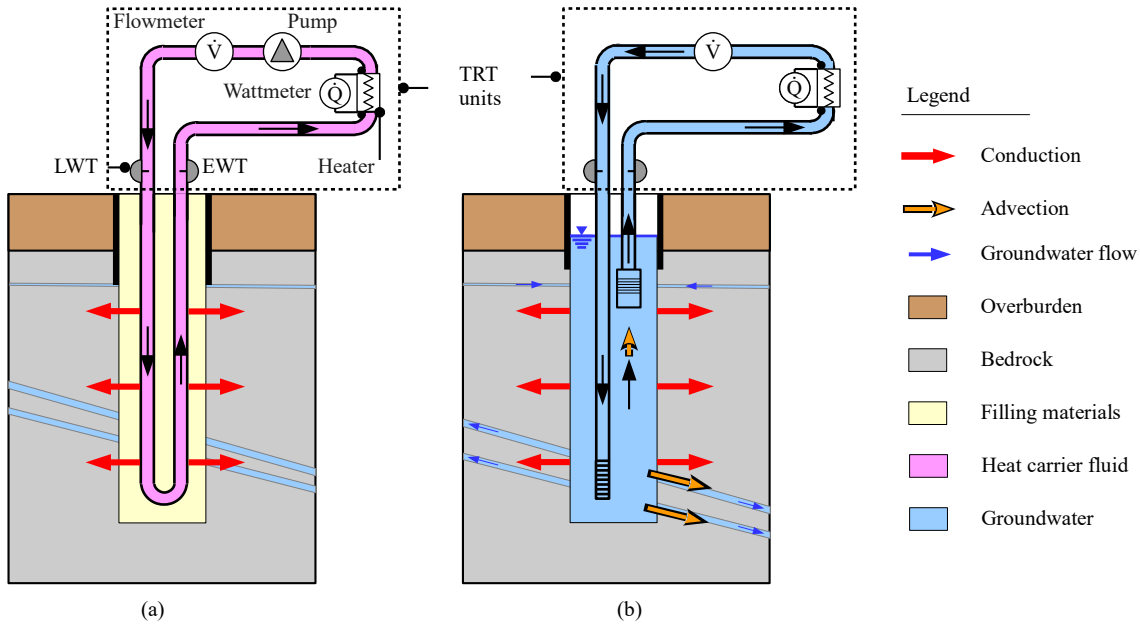

FIGURE 5.1 Two configurations of a GHE connected to a thermal TRT unit. (a) Closed-loop GHE that uses a heat carrier fluid and relies on conduction and (b) standing column well that uses groundwater and exchanges heat through conduction along the borehole wall and through advection as groundwater circulates in the fractures and pores.

advection is dominant.

Standing column wells (SCW) are another type of GHE with great potential in dense urban areas [22, 53], as their configurations have allowed total length reductions of up to 78% compared to closed-loop wells [29]. In SCWs, a submersible pump collects groundwater and directs it to the surface, where heat is exchanged with heat pumps, before being returned to the bottom of the well (or vice versa). As shown in Fig. 5.1b), water exchanges heat by conduction as it recirculates along the borehole wall. However, the SCW being filled with water and connected to the fractures crossing the well, advection is the dominant heat transfer mechanism when a net flowrate is discharged outside the SCW, which is common during peak thermal periods [22, 25]. This operation, known as *bleed*, deviates a fraction (5% to 30 %) of the pumped water out of the well and creates a drawdown that stimulates advective flow towards the SCW. Accurate use of the bleed allows significant energy savings [25] and construction costs reduction [29].

Although bleed is recognized as the main attribute of SCWs and main driver of advective heat transfer, recent works by Robert et al. (2022) [27] showed that even under full recirculation mode (that is no groundwater is discharged outside the SCW) a significant advective heat transfer can occur between the SCW and the water bearing formation. Indeed, even if the

SCW is under full recirculation mode, the groundwater is locally depressurized near the pump intake while overpressures can develop near the injection zones [38]. This pressure pattern induces mostly a vertical flow between the injection zone and pump intake, but also a significant horizontal flow in the permeable layers that modifies the temperature response observed during a TRT [27]. In fact, Jeon et al. (2016) [39] noted that the thermal response of a SCW is modified when hydraulic conductivity is greater than 5×10^{-5} m/s. Since the thermal response of an SCW is a function of both the thermal and hydraulic properties around a SCW, obtaining these properties by means of TRTs must be investigated. This paper aims to illustrate how a TRT performed on a SCW allows measurement of the hydraulic and thermal properties of the main hydrostratigraphic units crossed by an open-walled borehole. In this work, the identification of the parameters is undertaken in a Bayesian framework as it also allows uncertainty quantification and helps in evaluating the robustness of the parameters obtained. The use of Bayesian inference is now more common in geosciences [106,180,181] and has been used, among other methods, to analyze pumping tests and assess aquifer hydraulic properties [162,182,183]. In the field of low temperature geothermal energy, Bayesian inference was used successfully to analyze TRTs and deduce, among other parameters, the thermal conductivity and the volumetric heat capacity of the ground [86, 100, 101].

In this work, the hydrostratigraphic context of an experimental site and the gathered TRT data are first presented. Then, identification of the parameters being formulated as an inverse problem solved by Bayesian inference, the priors used and the approach chosen to evaluate the likelihood are shown in Section 3. To greatly speedup the inference, an artificial neural network (ANN) trained to reproduce the thermal response of an experimental SCW is presented in Section 4. Finally, a numerical validation is performed (Section 5.6) before testing the approach against real TRT data in Section 5.7. In this paper, the presented methodology showcases how hydraulic and thermal properties can be obtained only with the temperature signal measured during a TRT. Therefore, the purpose is to outline a new use for TRTs (other than solely identifying the thermal conductivity of geological materials), using a direct model (ANN) built specifically for this experimental site.

5.3 Description of the experimental test site

The experimental test site analyzed in this work is located in the city of Mirabel in eastern Canada. The test well (SCW-1) used is part of a demonstration project for the integration of SCWs in institutional buildings. Prior to the design phase of the demonstration infrastructure, two boreholes were drilled at the site (SCW-1 and OW-1) to identify the hydrogeological context and estimate the hydraulic regional gradient. The borehole SCW-1 was transformed

into a production SCW and several in situ tests were carried out on it, the most challenging tests being a TRT and a pumping test.

5.3.1 Geological and hydrostratigraphic units

The left side of Fig. 5.2 presents SCW-1 and the geological units (GU) identified with rock cuttings recovered during the drilling operations. From top to bottom, the GUs observed at SCW-1 are a loose deposit composed mainly of till between 0 and 10.05 m depth, followed by sandy dolomite to a depth of 99.06 m. A quartz arenite was observed until the end of the drilling at a depth of 133.20 m. A similar lithology was observed at the OW-1 located 27.4 m downstream of SCW-1 [27].

As shown on the right side of Fig. 5.2, the cumulative groundwater flows were monitored during drilling of the two boreholes. A significant increase of the groundwater fluxes was observed below a depth of 70 m and was interpreted as three different levels of fracturing. The combination of the geological observations and of the observed flow rates has lead to a conceptual model composed of five hydrostratigraphic units (HU) as shown in Fig. 5.2. It is important to note that the hydrostratigraphic units of the conceptual model are not only based on the geological observations, but rather depend on their apparent hydraulic properties.

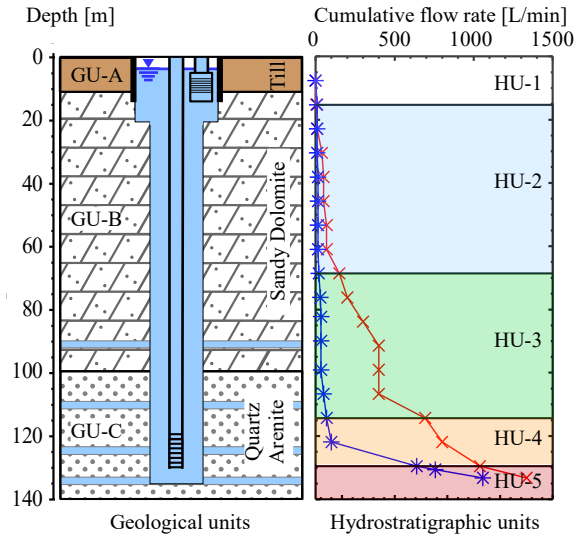

FIGURE 5.2 Conceptual model of the experimental site. Left : Geological units observed at SCW-1. Right : Hydrostratigraphics units HU-1 to HU-5 and cumulative flow rates observed during drilling at boreholes SCW-1 (red marker) and OW-1 (blue marker).

5.3.2 Thermal response test

As reported by Robert et al. (2022) [27], an experimental TRT was conducted on SCW-1 over a period of 101 h (see Fig. 5.3). Before the TRT, the water table was at a depth of 2.5 m and the submersible pump was installed 8.4 m below the ground surface. This TRT is composed of a continuous circulation phase of 18 h during which the heating power was nil (i.e., allowing to reach a steady-state for the groundwater flow in the GHE and the aquifer), followed by a heating phase of 83 h at a mean heating power $\dot{Q}$ of 22 kW, or 165 W/m. The flow rate $\dot{V}$ was interrupted during 103 min before the heating phase, otherwise the mean flow rate was 127.2 L/min, which corresponds to a turbulent regime in the annulus and thus a high convective heat transfer along the borehole wall. The temperature variation ΔT shown in Fig. 5.3 is the difference between the leaving water temperature (LWT) and the entering water temperature (EWT) at the TRT unit. Note that all these experimental data (recorded every 30 s) were smoothed with a low-pass filter (5 min window) to reduce noise. Before performing the TRT, a thermal profile was performed on the two wells and showed an undisturbed temperature of 8.16 °C, observed almost uniformly along the well and, thus, with no apparent geothermal gradient. This temperature was used to simulate EWT and LWT during the TRT.

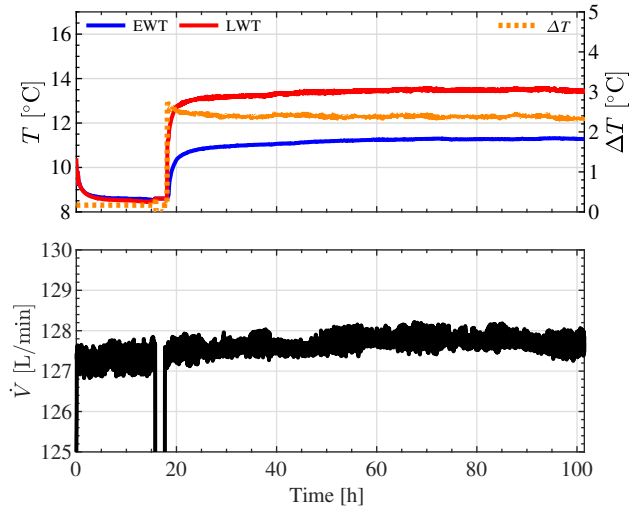

FIGURE 5.3 Smoothed measurements observed during the experimental TRT analyzed in this work, with the heating phase beginning 18 h after the end of the continuous circulation phase. Top : entering (blue) and leaving (red) water temperatures along with the temperature variations (ΔT : orange) imposed at the top of the SCW. Bottom : measured flow rate ($\dot{V}$: black).

It is worth noting that EWT stabilized at 11.07 °C after only 24 h of heating, a small temperature increase of only 2.47 °C for a high heating power of 165 W/m. This is indicative

of the high thermal efficiency developed by SCW-1. Also, Robert et al. (2022) [27] carried out an interpretation with the usual first-order approximation of the infinite line source model and obtained an apparent thermal conductivity of 70 W/(mK). This value, too high for geological units and not retained by the authors, was deemed indicative of advection during the TRT performed under full recirculation mode. In order to consider advection, the authors interpreted the TRT using a 3D finite element model coupling heat transfer and groundwater flow, and concluded that advection plays a major role during the TRT.

5.3.3 Pumping test

A pumping test was conducted on SCW-1 and lasted 72 h at a mean pumping rate of 130.2 L/min. Interpretation of this test with the Cooper–Jacob method has lead to a mean hydraulic conductivity of 6.5×10^{-5} m/s, while it led to a value of 7.9×10^{-5} m/s with the Agarwal method [184]. Finally, the interpretation of the pumping test gave a specific storage of 2.6×10^{-6} m^{-1}, which is typical of a confined aquifer.

In addition, a point reading at SCW-1 and OW-1, located 27.4 m downstream, indicated a hydraulic gradient of 0.0069 m/m. Since Robert et al. (2022) [27] concluded that the hydraulic gradient has a small impact on the thermal response of SCW-1, at least during the TRT duration, the regional groundwater flow has been neglected in the present study.

5.4 Parameters identification by Bayesian inference

The identification of the parameters is performed within a Bayesian framework, which allows to quantify the uncertainty of the parameters by updating their prior distributions based on the observations. In its simple form, Bayes' theorem is given by :

$$P(\theta|x) \propto P(x|\theta) \cdot P(\theta) \tag{5.1}$$

which links the posterior distribution $P(\theta|x)$, the likelihood function $P(x|\theta)$ that is the probability of observing data given hypothetical parameter values, and the prior knowledge $P(\theta)$ that incorporates some estimates about the parameters before making any observation. In Eq. (5.1), θ is a vector containing the unknown parameters, namely the hydraulic conductivity K of the five hydrostratigraphic units, and the thermal conductivity λ and volumetric heat capacity C of the three geological units. Then, x is a vector of residuals obtained through :

$$x(t) = T(t) - \tilde{T}(t) \tag{5.2}$$

where $T(t)$ is the observed temperature at time t and where $\tilde{T}(t)$ is the simulated temperature. In this study, the residuals are computed using $T(t) = LWT(t)$. Finally, the evaluation of the posterior distribution leads to an updated estimate of each parameter.

5.4.1 Evaluation of prior and likelihood

The prior distribution of a parameter is defined by a probability density function (PDF) that represents the spread of uncertainty according to the available information. However, non-informative priors are usually favored as they do not taint the inference results. In their original work, Choi et al. (2018b) [101] and Pasquier and Marcotte (2020) [86] opted for uniform distributions for all priors. In subsequent work, Choi et al. (2018a) [100] used triangle distributions or Gaussian distributions [122] as all previous works inferred Gaussian-like distributions for the thermal parameters. Hence, this study uses Gaussian distributions to describe the priors used to analyze the experimental TRT described previously. For sake of completeness, the multi-Gaussian prior used in this work is described by :

$$P(\theta) = \prod_{i=1}^{n} \frac{1}{\sqrt{2\pi\sigma_i^2}} e^{\frac{-(x-\mu_i)^2}{2\sigma_i^2}} \tag{5.3}$$

where μ_i and σ_i^2 are respectively the mean and variance of parameter i. Note, however, that the validation performed on the synthetic test cases in Section 5.6 uses bounded uniform priors given by :

$$P(\theta) = \begin{cases} \prod_{i=1}^{n} \frac{1}{U_i - L_i} & \text{if} \quad \theta_i \in [L_i, U_i] \\ 0 & \text{otherwise} \end{cases} \tag{5.4}$$

Under the assumption of a multi-Gaussian distribution of the residuals x, the likelihood $P(x|\theta)$ is given by :

$$P(x|\theta) = (2\pi)^{-N/2} |\Sigma|^{-1/2} e^{-\frac{1}{2} x' \Sigma^{-1} x} \tag{5.5}$$

where Σ is the $N \times N$ covariance matrix of the data, where N is the length of the residual vector. It is interesting to note that typically the temperature signal recorded during a TRT contains thousands of entries. Thus, computation and inversion of matrix Σ is time consuming.

In this perspective, Pasquier and Marcotte (2020) [86] proposed an efficient closed-form equation for Eq. (5.5) that, in addition, accounts for the autocorrelation of residuals that is usually not considered when computing the likelihood. Using the ratio of the sampling period to the correlation range $s = \Delta t/a$, the determinant of the precision matrix in Eq. (5.5) can

be expressed algebraically as :

$$|\mathbf{\Sigma}^{-1}| = \frac{e^{2(n-1)\,s}}{\sigma^{2n}(e^{2s}-1)^{(n-1)}} \tag{5.6}$$

Similarly, following the work of Pasquier and Marcotte (2020) [86], the computation of $\mathbf{x'\Sigma^{-1}x}$ in Eq. (5.5) is simplified to :

$$\mathbf{x'\Sigma^{-1}x} = \frac{1}{\sigma^2\ (e^{2s}-1)}\left(e^{2s}(x_1^2+x_n^2)+(e^{2s}+1)\sum_{i=2}^{n-1}x_i^2 - 2e^s\sum_{i=1}^{n-1}x_i x_{i+1}\right) \tag{5.7}$$

This expression involves only $O(n)$ multiplications and is valid if the residuals follow an exponential covariance model of the form :

$$C(h) = \sigma^2 e^{\frac{-h}{a}} \tag{5.8}$$

where a is the correlation range and h is the variogram sill obtained by fitting the experimental variogram of the residuals. The variogram value at the sill corresponds to the variance. The correlation range corresponds to a third of the range at which 95% of the variance is found. It should be noted that using Eqs. (5.6) and (5.7) can save a few days of computation.

5.4.2 Posterior sampling with Markov Chain Monte Carlo and convergence

The Markov Chain Monte Carlo (MCMC) algorithm used to sample $P(\theta|x)$ is the ensemble slice sampler of [185]. The algorithm is a parallel slice sampler [186] that runs simultaneously over m chains or walkers. A feature of this sampler is the fact that the current ensemble of walkers are used to choose the direction of the next moves and adjust the length scale, which limited the initial slice sample algorithms for high-dimensional problems. Because a significant efficiency gain is possible when working with parallel chains, the ensemble slice sampler was chosen in this work with 50 chains in parallel.

Convergence of the MCMC algorithm is calculated using the potential scale reduction factor $\hat{R}$ of Gelman et al. (2014) [187]. Convergence depends on the problem itself and several values for $\hat{R}$ can be chosen. For example, [166] set this criterion to a $\hat{R}$ value below 1.2. After several tests, the criterion for this study was set to an $\hat{R}$ value of 1.05. In Appendix A, Eqs. (5.11) to (5.14) describe the equations to evaluate the potential scale reduction factor. Note that a burn-in period is applied by discarding the draws made before the criterion is reached. The posterior distribution is then computed with at least the same amount of draws. Ultimately, the posterior distribution gives the marginal and joint distributions of all inferred parameters.

5.5 Temperature simulation with a surrogate model

The use of MCMC algorithms requires several million simulations of a TRT. To infer the distributions of the parameters θ in a realistic timeframe, the simulation of the temperatures LWT (i.e. $\tilde{T}(t)$ in Eq. (5.2)) is done with the simulation method developed by Pasquier et al. (2018) [84]. In this approach, an ANN, acting as a surrogate for a numerical model inspired by [27], is used to generate the transfer function (g function) corresponding to LWT. A convolution in the spectral domain is then performed with this function and an excitation function to efficiently consider the variation of the heating power. The following sections summarize the efficient simulation strategy used in this work.

5.5.1 Numerical modeling of the SCW

As the ANN requires a large training dataset, this section describes the axisymmetric coupled finite element model used to generate a set of synthetic numerical examples. The modeling strategy used to simulate the coupled thermal response of SCW-1 is similar to the one used by [188], [40] and [27] for SCWs. As illustrated in Fig. 5.4, a first set of boundary conditions are used to force a vertical flow within the central pipe and SCW. These boundary conditions also induce a horizontal flow, mostly in the permeable layers. A second set of boundary conditions is used to impose a thermal unit impulse of 1 °C at the SCW inlet. This is achieved by first evaluating the outlet temperature EWT, and using the relation $LWT = EWT + 1$ to prescribe the inlet temperature. The remaining boundary conditions are chosen to integrate a uniform initial temperature of 0 °C and an initial hydraulic head of 130.7 m (i.e. water depth of 2.5 m).

Making use of the conceptual model illustrated in Fig. 5.4, three separate sets of thermal properties are used for the three geological units GU-A to GU-C. Similarly, five sets of hydraulic properties are used for hydrostratigraphic units HU-1 to HU-5. As shown in Table 5.1, the resulting model integrates a fixed geometry and several fixed thermal and hydraulic properties summarized by the vector of hyperparameters $\phi = [H, \dot{V}, T_g, \rho, n,\ S_s, b, r, \lambda_p, \lambda_f, C_p, C_f]$. Note that the porosity of each unit is assumed to be constant due to its generally low value in rock, which limits its influence on the thermal response. Also, hydraulic dispersivity, a key property in chemical tracer studies, is disregarded as it has a lesser effect on heat transfer. The unknown parameters inferred in this work are summarized by vector $\theta = [K_1...K_5, \lambda_A...\lambda_C, C_A...C_C]$. To generate a training database covering a wide range of parameters θ, a total of 26,820 random sequences coming from Halton sets [189] were drawn from the uniform distributions $\mathcal{U}(L, U)$ presented in Table 5.1. Then, for each vector θ, the numerical mo-

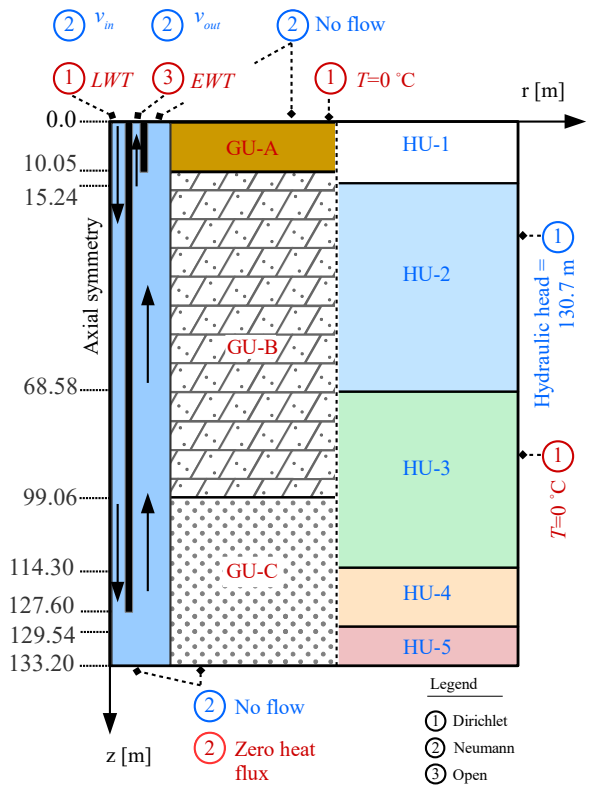

FIGURE 5.4 Geological units (GU), hydrostratigraphic units (HU) and boundary conditions of the coupled finite element model used to generate a training database for the artificial neural network. The blue circles correspond to the hydraulic boundary conditions while the red circles are for the thermal boundary conditions. The radius of the axisymmetric model is 75 m.

del was solved in the [190] environment, resulting in a transfer function g with a temporal discretization following a geometric progression.

Since the model is 2D axisymmetric, the re-injection pipe is represented at the center of the SCW, while the pumping pipe surrounds it. Among the simplifications, no pumping equipment is physically modeled and the screened section of the re-injection pipe (measuring 10 m) is neglected and replaced by a pipe (measuring 5 m) open at the bottom. Additionally, in the upper part of the SCW, the larger diameter of the pumping chamber and the casing are omitted. These assumptions have been used successfully in previous studies [27, 188].

Once constructed, this numerical model does not allow for additional geological or hydrostratigraphic units to be considered. Thus, the choices made during conceptualization have a significant impact on the overall methodology. Omitting key units can lead to a less realistic model, while adding more units and unknown parameters tends to expand the uncertainty

space and lead to greater computational costs [191].

5.5.2 Artificial neural network

Following the work of [86], the ANN architecture is a feedforward multilayer perceptron with hyperbolic tangent activation functions and a linear transfer function on the last layer. The ANN is made of 10 hidden layers with 50 neurons per layer. Note that the last layer contains 95 outputs that correspond to the 95 simulated outputs. To ease network training, the original transfer functions g are transformed with a linearizing function and shifted by a constant value of 4.5 to avoid negative values inside the algorithm.

ANN inputs include parameters (θ) and hyperparameters (ϕ) as reported in Table 5.1. Additional parameters are used to enrich the input vector and facilitate network training. These parameters are described by vector ψ=[$\bar{\lambda}_j$,$\alpha_j = \lambda_j/C_j$, $\bar{K}_i$, $\tau_i = K_i b_i$] and represent the mean thermal conductivity of the geological units (arithmetic average), the thermal diffusivity of each geological unit, the mean hydraulic conductivity (arithmetic average) and the transmissivity of each hydrostratigraphic unit. It is worth noting that before training, the inputs and outputs were normalized between -1 and 1 to reduce the risk of neuron saturation. After the training, the ANN was validated using an additional database containing 2,682 simulations (10% the size of the training database). The mean absolute error (MAE) obtained was 0.001 °C, while the maximum error was 0.01 °C, showing that the ANN is a robust and reliable surrogate of the numerical model. The resulting ANN is able to emulate the numerical model and provide a transfer function g in a few milliseconds.

Tableau 5.1 Fixed hyperparameters ϕ and parameters θ drawn from a uniform distribution $\mathcal{U}(L, U)$ used with the finite element model to generate a training database made of 26,820 transfer functions.

	Parameters	Fluid	Pipe	HU-1	HU-2	HU-3	HU-4	HU-5	GU-A	GU-B	GU-C
	Thickness - b [m]	-	0.00549	15.24	53.34	45.72	15.24	3.66	10.05	89.01	34.14
	Radius - r [m]	0.076	0.0302	75	75	75	75	75	75	75	75
ϕ	Specific storage - S_s [m^{-1}]	-	4e-10	2e-8	2e-8	2e-8	2e-8	2e-8	-	-	-
	Porosity - n [%]	-	0.001	-	-	-	-	-	20	2.2	5.9
	Flow rate - $\dot{V}$ [L/min]	127.2	-	-	-	-	-	-	-	-	-
	Length - H [m]	133.2	127.6	-	-	-	-	-	-	-	-
	Hydraulic conduct. - K $\log_{10}$[m/s]	1.0	-9.0	$\mathcal{U}$(-10, 1)	$\mathcal{U}$(-8, 1)	$\mathcal{U}$(-7,1)	$\mathcal{U}$(-7, 1)	$\mathcal{U}$(-7, 1)	-	-	-
θ	Thermal conduct. - λ [W/(mK)]	0.56	0.40	-	-	-	-	-	$\mathcal{U}$(0.5, 6)	$\mathcal{U}$(1, 8)	$\mathcal{U}$(1, 8)
	Vol. heat capacity - C [MJ/(m^{3}K)]	4.186	2.174	-	-	-	-	-	$\mathcal{U}$(1, 4)	$\mathcal{U}$(1, 4)	$\mathcal{U}$(1, 4)

5.5.3 Simulation by convolution product

To simulate the temperatures at each time step of the experimental TRT, the transfer function g provided by the ANN is interpolated every 30 s and convolved in the spectral domain

as proposed by Marcotte and Pasquier (2008) [59]. Using an initial ground temperature $T_g = 8.16$ °C, the simulated temperature is given by :

$$\tilde{T}(t) = (f * g)(t) + T_g \tag{5.9}$$

where $\tilde{T}(t)$ is the temperature at the inlet of the SCW (LWT) and f is the incremental heat load function given by :

$$f(t) = \Delta T(t_i) - \Delta T(t_{i-1}) \tag{5.10}$$

In Eq. (5.10), $\Delta T(t)$ is proportional to the heating power, temperature difference between EWT and LWT, and to the additional heat dissipated by the submersible pump. This simulation strategy leads to accurate results, in a few milliseconds.

5.6 Validation with two synthetic test cases

Before testing the proposed approach with a real dataset in Section 5.7, two synthetic test cases are used as a proof of concept to illustrate how a TRT can help assess the hydraulic and thermal properties around a SCW.

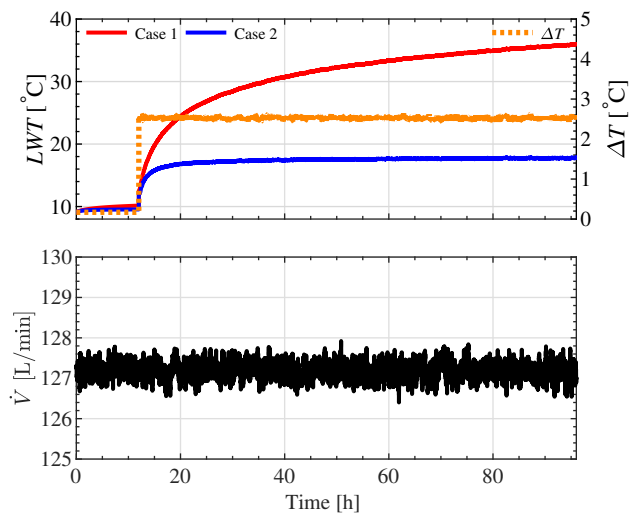

FIGURE 5.5 Synthetic data used for Case 1 and 2. Top : Temperature evolution for low hydraulic conductivity (Case 1 : red) and for high hydraulic conductivity (Case 2 : blue), and temperature variation (ΔT : orange) prescribed at the top of the SCW. Bottom : Circulation flow rate ($\dot{V}$: black).

5.6.1 Description of the synthetic reference datasets

The two validation test cases were designed to illustrate the impact on property identification of low (Case 1) and high (Case 2) hydraulic conductivity for the thinner hydrostratigraphic units HU-4 and HU-5. To ease the discussion, the conceptual model shown in Fig. 5.2 was simplified by combining geological units GU-A and GU-B together. Similarly, units HU-2 and HU-3, as well as HU-4 and HU-5, were combined together. However, the unit HU-1 was retained as a separate unit with a known hydraulic conductivity as it is hydraulically sealed from the well by the steel casing. The reference properties used for Case 1 and 2 are summarized in Table 5.2. Note that the thermal properties are the same in both cases as the goal is to illustrate the impact of the hydrostratigraphic context.

To recreate a realistic TRT, correlated signals are added to the synthetic signals $\dot{V}$ and ΔT by means of 1D geostatistical simulations performed with exponential covariance models [192]. For each test case, LWT is obtained by convolving the transfer function g with the same excitation function f constructed around a heating power of 22 kW, which corresponds to the ΔT signal shown in Fig. 5.5. Note that ΔT has an average of 2.48 °C. One can see clearly in Fig. 5.5 how the high hydraulic conductivity of Case 2 modifies the thermal response of the SCW. Finally, the expression of the likelihood uses a variance of $\sigma^2 = 1 \times 10^{-4}$ °C^2 and a correlation range $a = 6$ h. As illustrated in Table 5.2, the prior of the unknown properties are uniform distributions, which makes the inference more sensitive to the likelihood.

Tableau 5.2 Parameters inferred, reference values and priors used with synthetic Case 1 (low hydraulic conductivity) and Case 2 (high hydraulic conductivity). The priors are uniform distributions ($\mathcal{U}(L, U)$) with lower bound L and upper bound U. When two values are indicated for a bound, the first corresponds to Case 1 and the second to Case 2.

Parameters inferred (θ)	Reference values		Prior distributions
	Case 1	Case 2	$\mathcal{U}$(L, U)
Hydraulic conduct. of HU-1 – K_1 $\log_{10}$[m/s]	-8	-8	-
Hydraulic conduct. of HU-2,3 – $K_{2,3}$ $\log_{10}$[m/s]	-5.3	-5.3	$\mathcal{U}$(-6.3, -4.3)
Hydraulic conduct. of HU-4,5 – $K_{4,5}$ $\log_{10}$[m/s]	-6	-3	$\mathcal{U}$(-7/-4, -5/-2)
Thermal conduct. of GU-A,B – $\lambda_{A,B}$ [W/(mK)]	2	2	$\mathcal{U}$(0.5, 3.5)
Thermal conduct. of GU-C – λ_C [W/(mK)]	3.5	3.5	$\mathcal{U}$(2, 5)
Vol. heat capacity of GU-A,B – $C_{A,B}$ [MJ/(m^{3}K)]	2.16	2.16	$\mathcal{U}$(1.5, 3.5)
Vol. heat capacity of GU-C – C_C [MJ/(m^{3}K)]	2.30	2.30	$\mathcal{U}$(1.5, 3.5)

For each synthetic test case, posterior distributions were sampled with the MCMC algorithm mentioned earlier. To illustrate the statistics of the inferred parameters, box plots are used in Fig. 5.6 with the median (red line), interquartile range (blue box) and percentiles 2.5% and 97.5% (whiskers). The black dot corresponds to the reference property. In addtion, Fig. 5.7

presents the marginal distributions for $K_{2,3}/K_{4,5}$, $\lambda_{A,B}/\lambda_C$ and $C_{A,B}/C_C$ for Case 1 and 2.

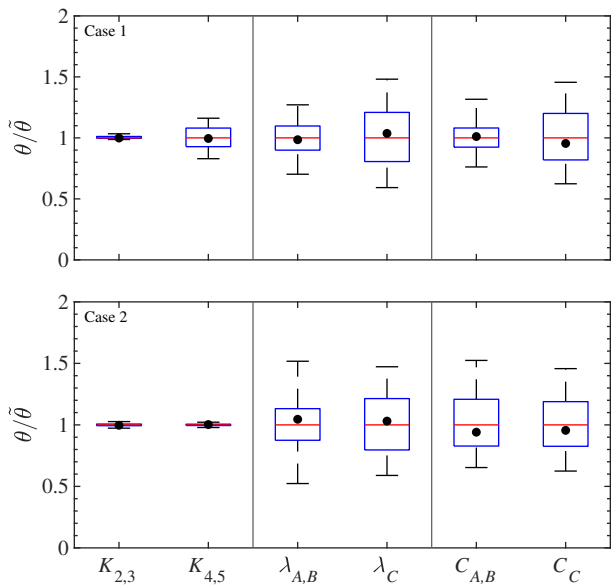

FIGURE 5.6 Impact of hydraulic conductivity of HU-4 and HU-5 ($K_{4,5}$) on properties K ($\log_{10}$[m/s]), λ ([W/(mK)]) and C ([MJ/(m^{3}K)]). Top : Case 1 and Bottom : Case 2. Parameters θ are normalized by their medians $\tilde{\theta}$. The boxes cover the interquartile range while the whiskers correspond to percentiles 2.5% and 97.5%. The median is the red horizontal line and the reference property is the black dot.

5.6.2 Identification of the hydraulic properties

First, from Fig. 5.6 and Fig. 5.7, it is clear that the distributions of $K_{2,3}$ and $K_{4,5}$ encompass their reference properties and are significantly different than the uniform priors used for the inference (except for $K_{4,5}$ in Case 1). In the presence of low (Case 1) and high (Case 2) hydraulic conductivity, $K_{2,3}$ and $K_{4,5}$ were accurately evaluated. Thus, the objective of recovering the hydraulic properties with a thermal test is possible, at least with autocorrelated synthetic data.

Further analysis of Fig. 5.6 shows that as the value of $K_{4,5}$ increases from Case 1 to Case 2, the scattering of the distribution decreases, indicating a better identification of the hydraulic properties for this unit. A comparison between the distributions of $K_{4,5}$ in Case 1 and Case 2 (Fig. 5.7) clearly confirms this assertion. Thus, preliminary results indicate that the presence of a high hydraulic conductivity for the bottom layer of a SCW (i.e. HU-4,5) improves the accurate identification of the hydraulic conductivity.

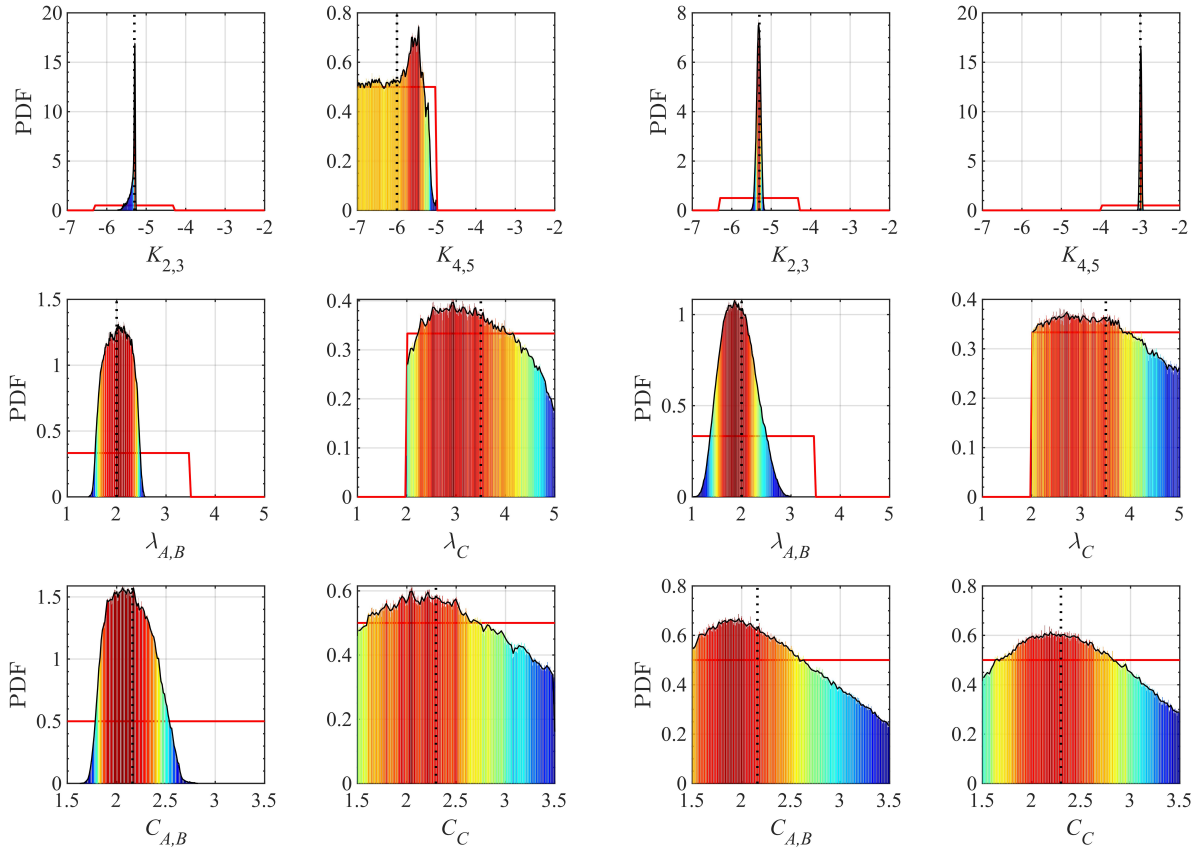

(a) Case 1 (b) Case 2

FIGURE 5.7 Marginal probability density functions (PDF) of hydraulic conductivities (K $\log_{10}$[m/s]), thermal conductivities (λ [W/(mK)]) and volumetric heat capacities (C [MJ/(m^{3}K)]) for (a) Case 1 (low hydraulic conductivity) and (b) Case 2 (high hydraulic conductivity), with reference properties (dotted line) used to generate the synthetic data and the prior distributions used for the inference (red line).

5.6.3 Identification of the thermal properties

Looking at Case 1 in Fig. 5.7, the distribution λ is quite narrow for geological units A and B, indicating that the identification of the thermal conductivity is still possible even if the dominant heat transfer process within the SCW is advection. The distributions inferred for $\lambda_{A,B}$ are also different than the uniform prior used for the inference and the interquartile range is small for test Case 1. This result seems to indicate that conduction plays a greater role since groundwater flows more slowly in HU-4,5 for Case 1. Hence, the identification of thermal properties becomes easier.

The median thermal conductivity in geological unit C (λ_C) is very close to the reference

value. Identification of λ_C is, however, less certain as the distribution has a large dispersion (see Fig. 5.6) and is clearly affected by the prior used (see Fig. 5.7a). Geological unit C being three times thinner than units A and B, GU-C contributes less to conductive heat transfer. Based on these limited results, it appears that the thickness of a geological layer and its vertical location in the stratigraphic column plays a direct role in the estimation of its thermal conductivity.

Measuring heat capacity in situ using a TRT is notoriously difficult [86]. One can see in Fig. 5.7 that the median of the inferred volumetric heat capacities is however very close to the reference value for the two test cases. However, with the exception of C_{AB} in Case 1, the uncertainty associated with this property is large and clearly affected by the prior, as the marginal distributions still carry the uniform model that was initially defined.

In this section, two synthetic test cases were used to illustrate strengths and weaknesses of TRTs to assess material properties around a SCW. These first results indicate that accurate identification of the thermal properties is possible and favored by thicker units located between the pump intake and the reinjection pipe, but becomes nearly impossible below the reinjection pipe and when the global hydraulic conductivity is high, as it is the case at the Mirabel experimental site analyzed in this work.

5.7 Experimental case study

In this section, the experimental TRT dataset presented in Section 5.3.2 is used to infer the thermal and hydraulic properties at the Mirabel demonstration site. The results obtained are then compared against the values retained by Robert et al. (2022) [27] in their optimal solution. It is worth noting that their interpretation indicated a thick rock layer with no major flow in HU-2 and HU-3 followed, at 114.3 m, by high flows in HU-4 and 5. In line with the validation results presented in the previous section, this hydrostratigraphic context is suitable to infer the hydraulic properties, as a small bias was observed in this context (see Case 2).

Table 5.3 presents the inferred unknown parameters and, for each of them, the corresponding value retained by Robert et al. (2022) [27] and the prior used for the Bayesian inference. Take note that the hydraulic conductivity of HU-1 is considered as a known property with a hydraulic conductivity of 5×10^{-8} m/s since this unit is sealed from the well by a steel casing, in reality. Consequently, groundwater in this unit does not directly interact with the SCW during the TRT and the properties of this unit are not inferred in this work.

For the likelihood evaluation, the maximum *a posteriori* method was first used to find a set

Tableau 5.3 Parameters inferred (θ), reference values retained by Robert et al. (2022) [27] and priors used with the experimental dataset described in Section 5.3.2. The priors used are normal distributions ($\mathcal{N}(\mu, \sigma^2)$) with mean μ and variance σ^2.

Parameters inferred (θ)	Reference values	Prior distributions $\mathcal{N}(\mu,\ \sigma^2)$
Hydraulic conduct. of HU-2 – K_2 $\log_{10}$[m/s]	-4.44	$\mathcal{N}$(-5.24, 0.16)
Hydraulic conduct. of HU-3 – K_3 $\log_{10}$[m/s]	-4.13	$\mathcal{N}$(-3.33, 0.16)
Hydraulic conduct. of HU-4 – K_4 $\log_{10}$[m/s]	-3.83	$\mathcal{N}$(-3.03, 0.16)
Hydraulic conduct. of HU-5 – K_5 $\log_{10}$[m/s]	-3.52	$\mathcal{N}$(-4.32, 0.16)
Thermal conduct. of GU-A – λ_A [W/(mK)]	2.7	$\mathcal{N}$(2.1, 0.09)
Thermal conduct. of GU-B – λ_B [W/(mK)]	3.4	$\mathcal{N}$(2.8, 0.09)
Thermal conduct. of GU-C – λ_C [W/(mK)]	5.9	$\mathcal{N}$(5.3, 0.09)
Vol. heat capacity of GU-A – C_A [MJ/(m^{3}K)]	2.30	$\mathcal{N}$(2.10, 0.04)
Vol. heat capacity of GU-B – C_B [MJ/(m^{3}K)]	2.31	$\mathcal{N}$(2.11, 0.04)
Vol. heat capacity of GU-C – C_C [MJ/(m^{3}K)]	2.18	$\mathcal{N}$(1.98, 0.04)

of parameters minimizing the misfit of residuals x. Only the residuals after 4.66 h of heating are considered, since it was found that the flow rate interruption in the circulation phase led to data inconsistencies at the beginning of the heating phase. An exponential covariance model (Eq. (5.8)) was then fitted to the experimental variogram of the residuals as shown in Fig. 5.8. The fitted parameters have a variance $\sigma^2 = 1.4 \times 10^{-3}$ °C^2 (at 95% of the sill) and a correlation range $a = 15$ h. As previously stated, the noisy TRT data was smoothed with a moving average and, therefore, the simulated temperatures were corrected with the same low-pass filter.

5.7.1 MCMC convergence and inference

The MCMC algorithm was used to generate 100,000 θ samples for each of the 50 chains. Fig. 5.9 presents the evolution of the potential scale reduction factor $\hat{R}$. As shown in this figure, convergence was reached after 22,774 samples. Thus, the last 77,226 samples of each chain were kept for analysis. Note that a total of 34.83 million ANN calls were recorded for a computation time of 107 h and an acceptance rate of 14.4%. After convergence, the 50 chains were checked and no abnormal phenomena were observed. To verify the sensitivity of the simulated thermal response to the parameters, several configurations of prior distributions were tested and each resulting marginal distribution was carefully inspected.

As shown in Fig. 5.8, the residuals obtained with the inferred parameters θ are small. Their MAE ranges from 0.03 to 0.10 °C, an error less than the accuracy of 0.25 °C of the temperature sensors used to measure LWT and EWT.

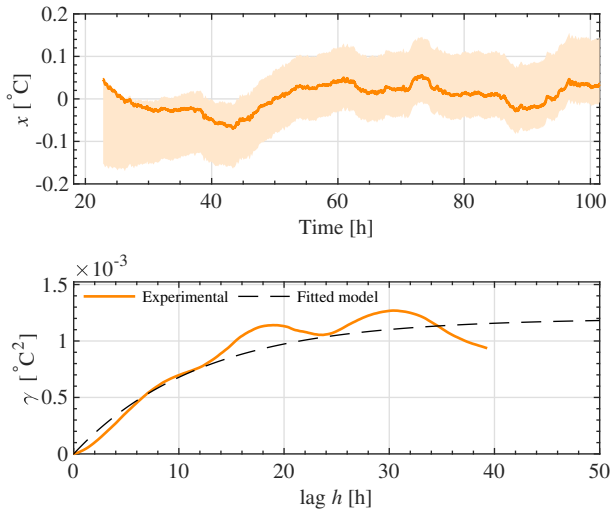

FIGURE 5.8 Variogram model used to compute the likelihood. Top : Residuals vector x obtained with the maximum *a posteriori* method and residuals envelope obtained with the 77,226 set of parameters θ. Bottom : Experimental (orange line) and fitted variogram (black line).

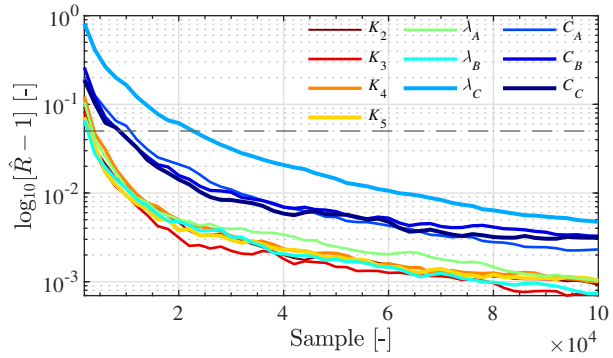

FIGURE 5.9 Potential scale reduction factor ($\hat{R}$) for the 100,000 samples drawn in parallel over the 50 chains and convergence criterion of $\hat{R}$=1.05 (dashed line) for each parameters.

5.7.2 Identification of hydraulic conductivity

The inferred parameters are presented in Fig. 5.10. The latter contains the marginal distributions along the diagonal, the joint distributions on the lower triangle, the priors and the values retained by [27] in their study. Foremost, in Fig. 5.10, the shift between the marginal and prior distributions of the hydraulic properties K_2, K_3 and K_4 shows that the simulated thermal response is mostly sensitive to them and, thus, is a first indicator of the success of a TRT to identify these three parameters. Indeed, the marginal distributions of K_2 to K_4 are all different from their priors, with relative uncertainty ($2\sigma/\mu$) ranging from 7% to 18%, and

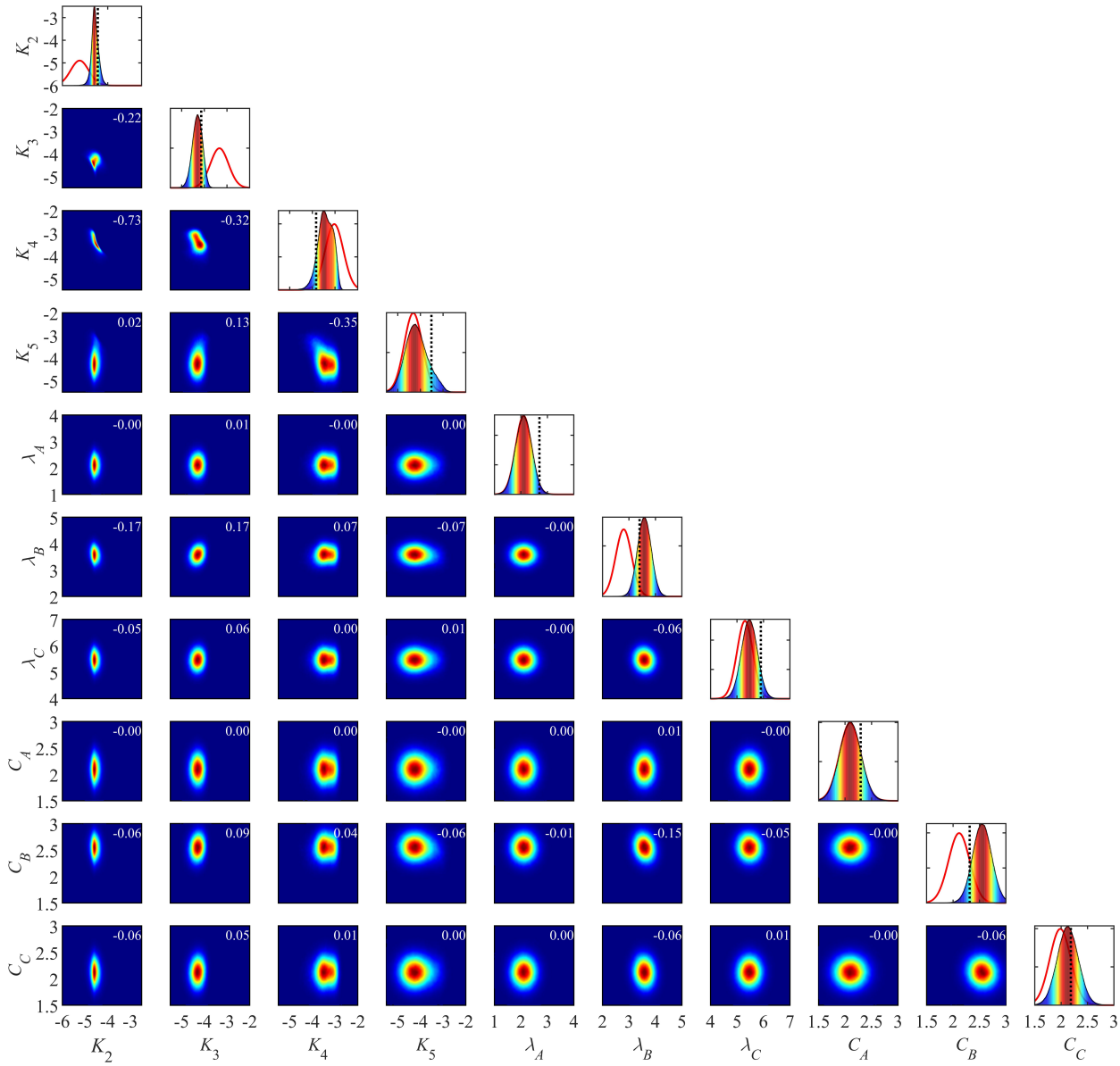

FIGURE 5.10 Inference results for the experimental case study. On the diagonal, the marginal distributions are presented with their prior distributions in red and the dotted black lines are the reference values. The lower triangle shows the pairwise joint distributions and the correlation between pairs is reported at each top right corners. The hydraulic conductivity of the hydrostratigraphic units is in $\log_{10}$[m/s], the thermal conductivity λ is in [W/(mK)] and the volumetric heat capacity C is in [MJ/(m^{3}K)].

their medians not far from the values retained by [27]. However, the hydraulic conductivity distribution of K_5, which corresponds to a relatively thin unit located under the reinjection pipe, is not significantly different from its prior and indicates that the temperature response is less sensitive to this parameter. The joint distributions in Fig. 5.10 all have a unique and

well-defined statistical mode. Surprisingly, the parameters are not (or poorly) correlated with each other, which is rarely the case with the parameters obtained with a TRT [172], with the exception of a strong negative correlation of 0.73 between K_4 and K_2. The interquartile range of K_2 and K_3 is small (see Fig. 5.11) and also supports the claim that a TRT can help to identify the hydraulic conductivity of some hydrostratigraphic units, at least for HU-2 and HU-3.

Fig. 5.12 presents the mean properties $\bar{K}$ along borehole SCW-1 obtained by weighting each marginal distribution by the relative thickness of its associated unit. The average hydraulic conductivity follows a log-normal distribution that encompasses the value provided by the Cooper-Jacob method (6.5×10^{-5} m/s). It should be noted that the subsequent analysis of the pumping test with the Agarwal method [184] was deemed more adequate for this site and led to a hydraulic conductivity closer to the median. Indeed, as shown in Fig. 5.12, the mean hydraulic conductivity provided by the Agarwal method almost perfectly coincides with the mode of the distribution. This is a reassuring result because identification of hydraulic conductivity with a thermal response test was not only able to provide a K value for each hydrostratigraphic unit, but was also able to provide a mean value close to the one obtained with a classical pumping test.

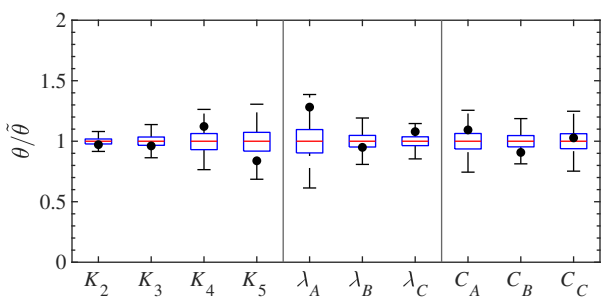

FIGURE 5.11 Precision of the inferred parameters for the experimental case study. K ($\log_{10}$[m/s]), λ ([W/(mK)]) and C ([MJ/(m^{3}K)]) are normalized by their medians $\tilde{\theta}$. The boxes cover the interquartile range while the whiskers correspond to percentiles 2.5% and 97.5%. The median is the red horizontal line and the reference property is the black dot.

5.7.3 Identification of thermal properties

By inspecting parameters λ and C in Fig. 5.10, we can see that the marginal distributions of λ_B and C_B are different from their priors. As shown in Fig. 5.11), the median of the inferred distribution for λ_B (3.58 W/(mK)) is typical of the sandy dolomites of GU-1. Similarly, the inferred distribution of C_B is also significantly different than its prior with a median of 2.55 MJ/(m^3K) and encompasses the reference value (see Fig. 5.11). The reference value is,

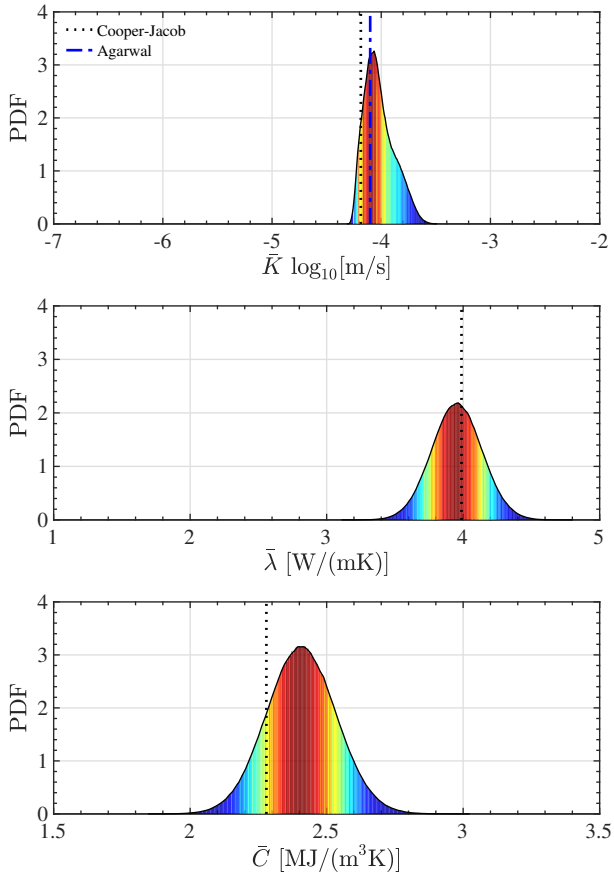

FIGURE 5.12 Distribution of the weighted averages for each inferred parameter.

however, slightly outside the interquartile range. Recall that this value comes from laboratory measurements reported in the literature for this regional geological unit and the inference results are here deemed more accurate. Interestingly, the relative uncertainty ($2\sigma/\mu$) of λ_B and C_B is $\pm 14\%$ for both parameters. This value is similar to the uncertainty reported by Choi et al. (2018a) [100] for the thermal conductivity ($\pm 21\%$) and those reported by Pasquier and Marcotte (2020) [86] ($\pm 2.6\%$ and $\pm 16.3\%$ for the thermal conductivity and volumetric heat capacity, respectively).

The marginal distributions of λ_A and C_A were all similar to their priors, regardless of the mean and variance of the prior used. This indicates that the inference results are tinted only by the expert judgment incorporated in the priors and are not influenced by the data. Thus, the inference results should be use with care for GU-A. A possible explanation for this data insensitivity is the fact that GU-A is a thin unit located at the SCW summit and above the pump suction. Therefore, this layer contributes little to the overall conductive heat flux and does not impact the temperature of the fluid.

As demonstrated in Section 5.6, the precise identification of the thermal properties of the lowest geological layer is nearly impossible when its hydraulic conductivity is high. For this experimental TRT, a relatively high hydraulic conductivity was observed for K_4. This appears to promote advection and mask conductive heat transfer, preventing accurate identification of λ_C and C_C.

Fig. 5.12 shows the mean thermal properties along SCW-1 obtained by weighting λ and C by the thickness of the units. These distributions are relatively close to the marginals of λ_B and C_B, which is the thickest layer. Note that several configurations of priors were tested to verify their effect on the mean properties. It was found that modifying the hydraulic conductivity priors has an insignificant impact on the mean thermal properties. In contrast, changing the shape, magnitude or location of the thermal property priors impacts their marginals. Therefore, the average thermal properties are influenced by their priors and, thus, these averages should be used with caution.

5.8 Discussion and conclusions

The goal of this work was to quantify the hydraulic and thermal properties around a SCW using solely a temperature signal obtained by a thermal response test. Using Bayesian inference and efficient computational methods, the methodology used in this study made it possible to identify the hydraulic conductivities of the hydrostratigraphic units located between the pump intake and the reinjection pipe, with relative uncertainties below 18%. Furthermore, the thermal properties of the geological unit, also located between the pump intake and the reinjection pipe, was obtained with an uncertainty of 14%. For the volumetric heat capacity, which is notoriously difficult to estimate, the relative uncertainty of the unit at the same location was 14%, which is remarkably small compared to values reported in the literature.

A synthetic validation was performed and demonstrated that hydraulic property identification is possible for the hydrostratigraphic context found at the experimental site analyzed in this work, while thermal property identification depends on specific conditions. In fact, it was shown that accurate identification of hydraulic conductivity was possible. In the case of a low hydraulic conductivity unit at the base of a standing column well, the thermal properties are obtained with a relatively small uncertainty. In contrast, the presence of a high hydraulic conductivity unit (1×10^{-3} m/s) at the base of a well penalizes the estimation of volumetric heat capacity, whereas it favors the evaluation of hydraulic properties.

Applying the methodology to a real experimental dataset, the hydraulic conductivities of

the main hydrostratigraphic units were successfully inferred, as their marginal distribution differed greatly from their priors and showed limited dispersion. In addition, the medians of these marginals are close to the expected values. Comparison of the inference results with those interpreted from a pumping test demonstrated that the interpretation of the TRT data leads to similar mean hydraulic conductivity.

It was also possible to successfully identify the thermal properties of the geological unit located between the pump intake and the reinjection point at the bottom of the well. It seemed that below the reinjection pipe, advective heat transfer concealed the identification of thermal properties. For the other two geological units, the inference results are strongly influenced by the prior of the thermal properties, which are based on an expert judgment. Therefore, the inference process must test several priors.

Although this work used a neural network model specific to the experimental site studied, the methodology proposed in this work is general as long as an accurate direct model is available. A flexible and general model, that considers a variable number of hydrostratigraphic and geological units, with variable depths and thicknesses, is not yet available but under development. Once available, the weights and biases of the trained network will be available for integration in a computing code and even in widely used spreadsheets. With such a general direct model, the methodology developed in this work may be tested at other sites and geological environments or used to validate more complex in-house implementations.

Using the experimental data gathered at a demonstration site in eastern Canada, the detailed methodology to identify hydraulic and thermal properties using only temperature measurements is verified. It is hoped that the use of such a technique will make it easier to estimate the hydraulic conductivity profile and reduce the need for additional in situ tests that are usually required to properly characterize the heterogeneity of water bearing formations.

5.9 Acknowledgments

The authors acknowledge the support from partners of the Geothermal Research Chair on the Integration of SCWs in Institutional Buildings, namely Hydro-Québec, the Ministry of higher education of Québec, Mille-Îles School Service Centre, Montreal School Service Centre, Samares School Service Centre, Versaprofiles, Marmott Energies, CanmetEnergy and NSERC. Additionally, we thank the anonymous reviewers and colleagues that provided constructive comments. This work was financed by the Natural Sciences and Engineering Research Council of Canada through grant number ALLRP 544477-19.

5.10 Nomenclature

Acronyms

ANN	articifial neural network
GHE	ground heat exchanger
GU	geological unit
HDPE	high-density polyethylene
HU	hydrostratigraphic unit
MAE	mean absolute error
MCMC	Markov Chain Monte Carlo
OW	observation well
PDF	probability density function
SCW	standing column well
TRT	thermal response test

Greek letters

α	thermal diffusivity [m^2/s]
Δ	difference [-]
γ	variogram [units^2]
λ	thermal conductivity [W/(mK)]
$\mathcal{N}$	Gaussian distribution [-]
$\mathcal{U}$	uniform distribution [-]
μ	average
ϕ	hyperparameters
ψ	enriched parameters
Σ	temperature covariance matrix [K^2]
Σ^{-1}	temperature precision matrix [K^{-2}]
σ	standard deviation
τ	hydraulic transmissivity [m^2/s]
θ	inferred parameters

Symbols

a	correlation range [s]
b	thickness [m]
C	volumetric heat capacity [$J/(m^3K)$]

EWT	entering water temperature [°C]
f	excitation function [°C]
g	transfer function for a unitary excitation [°C]
h	distance/time between two points [units]
H	borehole length [m]
K	hydraulic conductivity $\log_{10}$[m/s]
L	lower bound [-]
LWT	leaving water temperature [°C]
n	porosity [-]
N	length of the residual vector [-]
m	number of chains [-]
P	probability density function [-]
$\dot{Q}$	heating power [W]
r	radius [m]
t	time [s]
T	observed temperature [°C]
$\tilde{T}$	simulated temperature [°C]
U	upper bound [-]
v	velocity [m/s]
$\dot{V}$	circulation flow rate [m^3/s]
x	temperature residuals [°C]

Subscripts

f	fluid
g	ground initial condition
h	distance/time between two points [units]
i	index of the hydrostratigraphic units
in	inlet
j	index of the geological units
m	number of ANN outputs [-]
out	outlet
p	pipe

5.11 Appendix : MCMC Convergence

Eqs. (5.11) to (5.14) summarizes the method to evaluate the potential scale reduction factor ($\hat{R}$) of Gelman et al. (2014) [187]. In this method, each chain is broken in half to create a new set of chains all being half the original length. $\hat{R}$ is given by :

$$\hat{R} = \sqrt{\frac{\tilde{V}(\theta|x)}{W}} \tag{5.11}$$

where $\tilde{V}(\theta|x)$ is an estimation of the marginal posterior variance described by :

$$\tilde{V}(\theta|x) = \frac{k-1}{k}W + \frac{1}{k}B \tag{5.12}$$

where k is the length of the chains. The "within" sequence variance W is obtained by :

$$W = \frac{1}{m}\sum_{j=1}^{m}\sigma_j^2 \tag{5.13}$$

where σ_j^2 is the variance for each chain m :

$$\sigma_j^2 = \frac{1}{k-1}\sum_{i=1}^{m}(\theta_{ij} - \mu_{ij})^2 \tag{5.14}$$

and where B is the so-called between-sequence variance :

$$B = \frac{k}{m-1}\sum_{j=1}^{m}(\mu_{ij} - \mu_j)^2 \tag{5.15}$$

In the previous equations, μ_{ij} and μ_j are computed through :

$$\mu_{ij} = \frac{1}{k}\sum_{i=1}^{k}\theta_{i,j} \quad \text{and} \quad \mu_j = \frac{1}{m}\sum_{j=1}^{m}\mu_{ij} \tag{5.16}$$

where θ represents each chain values.

CHAPITRE 6 ARTICLE 3 – EXPERIMENTAL ASSESSMENT OF INTER-WELL REINJECTION IN STANDING COLUMN WELLS BY ANALYSIS OF TRANSFER FUNCTIONS OBTAINED FROM NON-STATIONARY DECONVOLUTION

Louis Jacques*, Philippe Pasquier, Gabriel Dion, Gabrielle Beaudry
Geothermics, Volume 125 :103184, November 6, 2024
Department of Civil, Geological and Mining Engineering, Polytechnique Montréal, P.O. Box 6079 Station Centre-Ville, Montreal H3C 3A7, Canada.
* Corresponding author : louis.jacques@polymtl.ca
Keywords : Standing column well, Inter-well reinjection, Ground source heat pump, Experimental transfer function, Non-stationary deconvolution

6.1 Abstract

Standing column wells are semi-open-loop ground heat exchangers that can achieve highly efficient thermal exchange rates through the strategic control of the pumping and bleed flow rates. The management of groundwater discharges associated with bleed use remains a challenge. A solution is inter-well reinjection, which proposes to imbalance the return flow rates between the standing column wells. This approach has been shown to be more efficient than fully balanced recirculation, although a direct comparison with a conventional bleed operation has not yet been conducted. To provide a robust evaluation of inter-well reinjection performance, a 35-day-long experiment is conducted on five standing column wells connected to a real building. The experimental transfer functions representing the operating modes tested (full recirculation, bleed, and inter-well reinjection) are evaluated using a non-stationary deconvolution algorithm and their adequacy with the conceptual site model is verified by comparison with numerical transfer functions obtained in a Monte-Carlo experiment. The results indicate that inter-well reinjection leads to a 10% higher thermal efficiency in the scenarios tested compared to full recirculation, albeit with a slightly reduced performance compared to typical bleed use. This confirms the potential of inter-well reinjection for boosting the efficiency of thermal exchange in SCWs while facilitating groundwater management and avoiding the installation of costly injection facilities. The methodology used to evaluate the experimental transfer functions is also found to be robust, as it allowed the reproduction of the measured temperatures with a root mean square error of 0.04 °C. Lastly, comparison of the experimental transfer functions with the Monte-Carlo experiment suggests that the

accuracy of the conceptual model could be improved.

6.2 Introduction

With greenhouse gas emissions from building operations reaching an unprecedented level of approximately 10 $GtCO_2$, the United Nations Environment Programme (2022) [193] has recently underscored the critical importance of decarbonization initiatives. Ground source heat pump (GSHP) systems, when combined with carbon-free energy sources, represent a pivotal technology for addressing this issue [194]. GSHP systems leverage the substantial heat capacity of the ground to facilitate thermal injection or extraction through a ground heat exchanger (GHE). In the context of sustainable development, research efforts are now focused on enhancing system efficiency while maintaining GHE temperatures throughout the system's operational lifetime [11].

A standing column well (SCW) is an interesting type of GHE due to its capacity to achieve high efficiency with minimal performance degradation over extended periods of operation [14, 25, 29, 53]. In SCWs, heat is exchanged by both advective and conductive heat transfer processes through the recirculation of groundwater in an uncased borehole. The process known as "bleed", which involves discharging a fraction of the pumped groundwater at ratios ranging normally between 5% and 25%, can also be employed to enhance advective heat transfer and overall performance of SCWs [26]. In this respect, it has been shown that the flexibility of SCWs is strongly contingent upon the control of pumping and bleed flow rates [25].

Groundwater discharged by a bleed process can be managed by directing it to a sewer or surface water body, provided it complies with local legislation [22]. An alternative solution is to return the discharged water to the original aquifer. Typically, reinjection into the aquifer is accomplished through the use of injection wells (IWs), which require drilling and incur additional costs. IWs can also be subject to a variety of issues, including physical and chemical clogging [125–127] and thermal interference with the SCWs due to the development of thermal plumes [53, 128, 129]. To avoid the inconvenience associated with IWs, Ben Aoun et al. (2024) [130] have proposed the use of an underground infiltration tank located within the unsaturated zone as a means of facilitating the return of bleed water to the subsurface. Nevertheless, the aforementioned solutions for groundwater discharge management entail the incorporation of additional components and introduce new complexities into the GSHP system.

As an alternative to bleed and these typical water management strategies, Kim et al. (2020)

[131] have introduced the concept of the "cross-mixing balancing well". This novel method proposes to operate the SCWs with inter-well reinjection, which involves unbalancing the return flow rates between the standing column wells to stimulate advective heat transfer in the same manner as bleed. This solution does not necessitate alterations to the SCWs themselves, is easily implemented, and avoids the inconveniences associated with injection facilities. In light of this recent development, there are now three distinct modes of operation available for SCWs : (a) full recirculation, (b) bleed activation and (c) inter-well reinjection. These modes are illustrated in Figure 6.1.

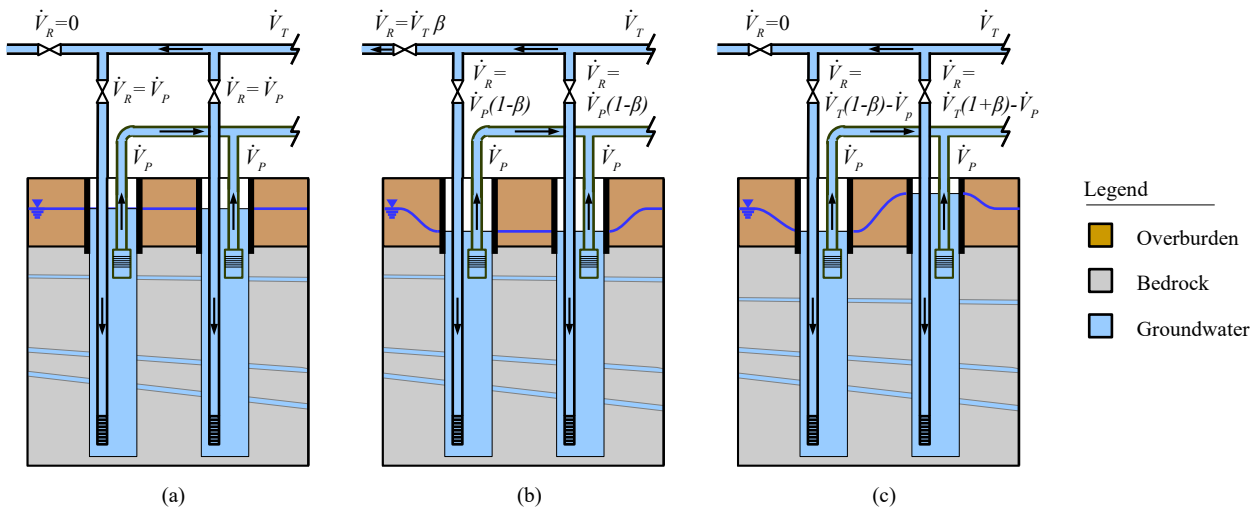

FIGURE 6.1 The three reinjection modes for standing column wells, depicting reinjection flow rates ($\dot{V}_R$), pumping flow rates ($\dot{V}_P$), total flow rate ($\dot{V}_T$), total discharge ratio (β), and groundwater levels (blue-colored lines in the overburden zone). The modes are : (a) full recirculation of all SCWs ($\beta = 0\%$), (b) bleed of groundwater by discharging ($\beta > 0\%$) from the SCWs to an external facility and, (c) inter-well reinjection of groundwater by discharging ($\beta > 0\%$) from one SCW (left) to the over-injected SCW (right).

To assess the efficacy of inter-well reinjection, Kim et al. (2020) [131] have conducted a series of six-hour tests with two SCWs each reaching a depth of 300 m. The SCWs have undergone approximately 18 hours (over the course of three days) of heating and 35 hours (over the course of five days) of cooling, using two distinct flow control strategies : full recirculation and inter-well reinjection with a discharge ratio of 20%. Kim et al. (2020) [131] have concluded that the coefficient of performance (COP) of the heat pump during inter-well reinjection is 23% higher in cooling mode and 12% higher in heating mode than during full recirculation. Using the same experimental site and additional tests, Lim and Lee (2021) [132] have conducted a comparative analysis employing the conductive-only infinite line source heat transfer model to estimate the effective thermal conductivity of the ground for both

reinjection modes. The inter-well reinjection strategy is found to have an effective thermal conductivity approximately three times higher than that estimated for full recirculation.

Previous assessments of inter-well reinjection performance have been based on the analysis of indirect metrics such as heat pump COP and effective ground thermal conductivity, and have been conducted over relatively short time frames of only a few hours. While the results obtained from these metrics are of great significance and value, it should be noted that the COP values are dependent upon the test-specific conditions, namely the temperature variations incurred by the specific quantities of heat introduced or extracted. Furthermore, the thermal conductivity values obtained are not suitable for considering the early transient behavior of the reinjection strategies, as the utilized interpretation method (i.e., the first approximation of the infinite line-source model) is only applicable to stationary conditions. Recently, a suitable alternative has emerged in the use of experimental transfer functions obtained with deconvolution algorithms. This method has shown to provide a more direct measure of heat exchange efficiency, both robust to variable thermal loads [62], to non-stationary conditions resulting from the use of variable pumping and bleeding flow rates, and applicable to long-term tests [195].

The purpose of this study is to experimentally demonstrate the performance of inter-well reinjection under real operating conditions through the analysis of experimental transfer functions, which are also compared with numerical solutions for verification purposes. To compare the effectiveness of inter-well reinjection with that of other typical operating modes of SCWs, namely full recirculation and bleed, a 35-day full-scale experimental test is conducted on an operational SCW system. To the authors' knowledge, this is the longest uninterrupted test conducted with inter-well reinjection. Then, the fluid temperatures measured during the test are fed into a non-stationary deconvolution algorithm to obtain experimental transfer functions representing the thermal response associated with each of these operating modes. The robustness of the method is evaluated by comparing the measured temperatures at the SCWs outlets during the test and the simulated temperatures obtained by feeding the experimental transfer functions and heat load function to a forward non-stationary convolution algorithm. Lastly, a pre-calibrated numerical model is employed to generate numerical transfer functions corresponding to each operating mode in a Monte Carlo experiment, which enabled an in-depth verification of the adequacy between the previous conceptual site model and the experimental data.

6.3 Description of the experimental site and inter-well reinjection tests

The experimental site is part of a larger research project aimed at investigating the integration of SCWs into institutional buildings. Fieldwork at the site began in 2020 with an investigation phase designed to provide data necessary for the design of a SCW system. The system has been commissioned at the end of 2022 and has started operating using standard control strategies, which include full recirculation and occasional bleed to increase the efficiency of thermal exchange during peak demand periods. The inter-well reinjection test discussed in the present study was then conducted during the summer of 2023 with the objective of evaluating the potential of this operating mode as an alternative to bleed. Prior to presenting the details of the inter-well reinjection test, an overview of the SCW system is provided, along with a description of the conceptual model (geological and hydrostratigraphic context) derived from a comprehensive field investigation.

6.3.1 Standing column well system

The SCW system is composed of five SCWs and one IW, which act as a source/sink to heat and cool an elementary school located in Mirabel, Canada. Figure 6.2 provides a detailed illustration of the SCW system configuration and its main components. The depth of the SCWs is approximately 135 m with a nominal diameter of 159 mm. The reinjection pipes, which have an outer diameter of 60 mm, are installed to depths of about 125 m and are perforated on a 5 m section to facilitate reinjection. SCW-1 has been constructed during the investigation phase, which is reflected in the slightly different geometry depicted in Figure 6.2.

As illustrated in Figure 6.2 (b), the SCWs are separated by a minimum distance of 6 m in a quasi-straight line, and connected to a plate heat exchanger via a hydraulic network. At each SCW, the pumping flow rate is individually controlled by a variable-frequency drive, while the return flow is managed by energy valves (for more details, readers are referred to Beaudry et al. (2024) [17]). A data acquisition system is employed to record the outputs of a number of sensors at five-minutes intervals, as detailed in Table 6.1. It is important to note that the SCWs have been designed to allow for the full recirculation mode and bleed activation modes, with groundwater being discharged to the IW in the latter case. Nevertheless, the ability to regulate the outlet and inlet flow rates at each SCW enables easy implementation of inter-well reinjection for the current test and future applications.

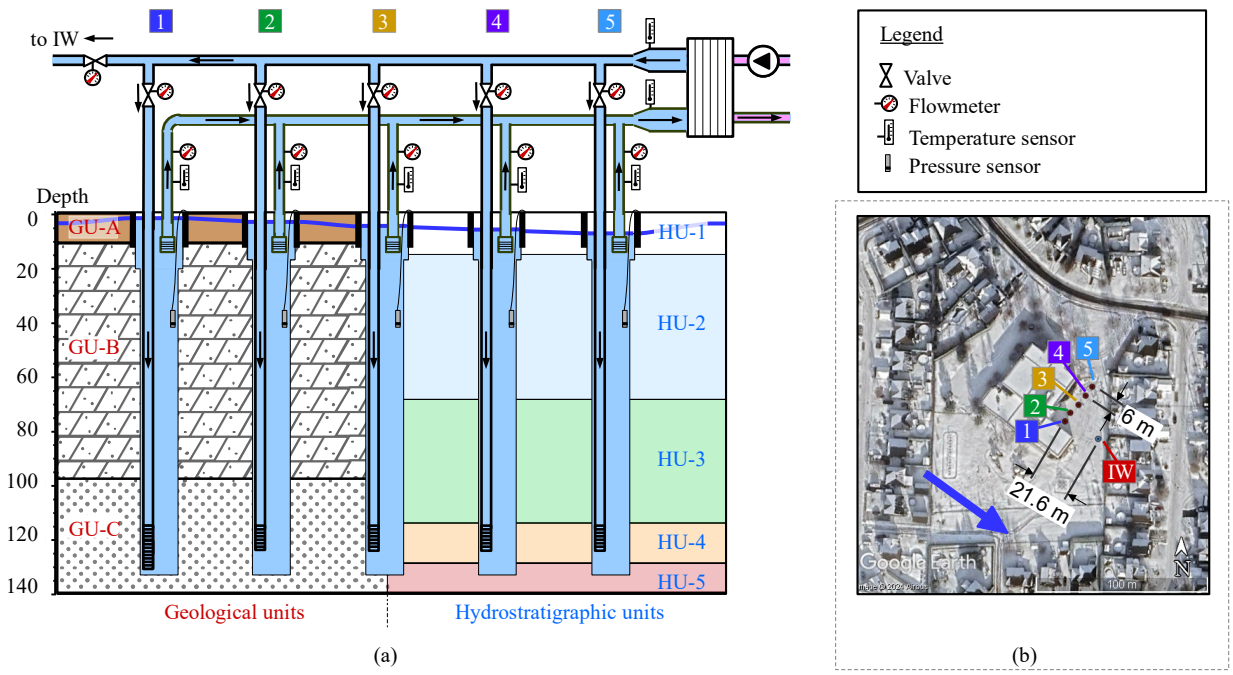

FIGURE 6.2 Standing column well system and conceptual model of the experimental site. (a) : Configuration (i.e., five SCWs, pumps, pipe network and monitoring equipment), geological units (GU), hydrostratigraphic units (HU), and typical groundwater levels for inter-well reinjection (blue line in the overburden) ; (b) : A satellite view of the site and the approximate direction of the regional hydraulic gradient (blue arrow). Note that pressure sensors are installed inside protective tubes (not shown).

TABLEAU 6.1 Monitoring devices and their accuracy.

Component	Accuracy
Flowmeter (pump)	0.4%
Flowmeter (reinjection)	2%
Temperature sensor	0.2 °C
Pressure sensor	2 cmH_2O

6.3.2 Hydrogeological conceptual model

The thermal response of the three reinjection modes is contingent upon the geological and hydrostratigraphic contexts. The geological units (GU) and hydrostratigraphic units (HU) presented in Figure 6.2 (a) are based on previous investigations conducted on SCW-1 by Robert et al. (2022) [27] and Jacques and Pasquier (2023) [138]. The first 10 m of the stratigraphic profile contains a layer of loose deposits, composed of till (GU-A). The rock formations, designated as GU-B and GU-C, are sub-horizontal in nature and consist of a 90 m thick

layer of sandy dolomite (Theresa Formation) followed by 35 m of quartz arenite (Cairnside Formation). Hydrostratigraphic units are derived from the observed yields of groundwater during the drilling of SCW-1, as reported in Robert et al. (2022) [27]. It is noteworthy that the drilling of SCW-2 to SCW-5 has revealed similar layer thicknesses and well yields to those observed in SCW-1. It is therefore postulated that the unit thicknesses, thermal properties of GUs, and hydraulic properties of HUs are constants, and that measurements acquired at SCW-1 can be extrapolated to the other SCWs.

To ascertain the characteristics of each HU and GU, a series of in situ tests has been conducted on SCW-1 (i.e., thermal response test (TRT), temperature profiles, pumping tests, and groundwater level monitoring) by Robert et al. (2022) [27]. A Bayesian inference approach to TRT interpretation has yielded joint distributions of thermal and hydraulic parameters [138], which are presented in Figure 6.3. Hydraulic conductivity distributions indicate that units HU-4 and HU-5 exhibit greater conductivity than other units. This finding is in accordance with the existing literature on this topic, the Cairnside Formation has been demonstrated to produce a considerable quantity of groundwater [196]. Furthermore, the thermal conductivity of the Cairnside Formation (GU-C) is within the higher range observed in sedimentary basin rocks, largely due to a substantial quartz content [7]. The temperature profile along SCW-1 has demonstrated the absence of a perceptible gradient, with an undisturbed mean temperature of 8.16 °C [27]. The mean hydraulic conductivity value from Figure 6.3 is greater than 5×10^{-5} m/s, indicating that thermal transfer in the SCW is sensitive to groundwater flow [39]. In fact, the base of the SCWs has been drilled in a highly productive aquifer, as evidenced by the well yield of 1325 L/min observed in SCW-1 and the low drawdown of 0.8 m observed during the 72-hour-long pumping test conducted on SCW-1 with a pumping flow rate of 130 L/min [27]. Consequently, the aforementioned geological and hydrostratigraphic contexts provide an ideal setting for testing and evaluating the performance of SCW reinjection strategies.

6.3.3 Inter-well reinjection tests

The present study examined four distinct operating modes over a 35-day period in July and August 2023. The four modes, which use different balances of the reinjection flow rates in the SCWs, are 1) inter-well reinjection with a discharge ratio of 15%, 2) full recirculation, 3) full bleed with a discharge ratio of 7.5%, and 4) full bleed with a discharge ratio of 15%. These operating modes are detailed in Table 6.2, with the reinjection flow rates ($\dot{V}_R$) for inter-well reinjection given by :

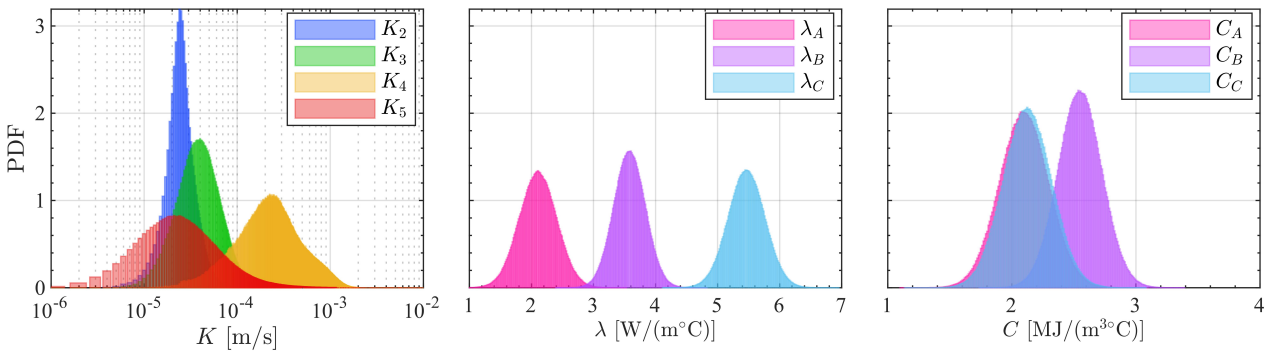

FIGURE 6.3 Joint marginal probability density function (PDF) of hydraulic and thermal properties obtained from a Bayesian inference conducted by Jacques and Pasquier (2023). From left to right : hydraulic conductivity (K [m/s]), thermal conductivity (λ [W/(m°C)]) and volumetric heat capacity (C [J/(m^3°C)]).

$$\dot{V}_{R(-)} = \left(\dot{V}_T(1-\beta) - N_{(+)}\dot{V}_P\right)/N_{(-)} \tag{6.1}$$

$$\dot{V}_{R(+)} = \left(\dot{V}_T(1+\beta) - N_{(-)}\dot{V}_P\right)/N_{(+)} \tag{6.2}$$

where the subscripts $(-)$ and $(+)$ indicate discharging and over-injecting SCWs, respectively. Equations 6.1 and 6.2 are generalization of the equations presented in Figure 6.1 (c), for values of $N_{(-)}$ and $N_{(+)}$ greater than 1.

TABLEAU 6.2 Reinjection flow rates at the SCWs and IW for the four reinjection modes tested. The total pumping flow rate is 500 L/min (100 L/min per SCW) in all scenarios.

Reinjection mode	Reinjection flow rate [L/min]						
	SCW-1	SCW-2	SCW-3	SCW-4	SCW-5	Total SCWs	IW
1 : Inter-well reinjection ($IR_{1,2}$=15%)	137.5	137.5	75	75	75	500	0
2 : Full recirculation ($\beta = 0\%$)	100	100	100	100	100	500	0
3 : First bleed stage (β=7.5%)	92.5	92.5	92.5	92.5	92.5	462.5	37.5
4 : Second bleed stage (β=15%)	85	85	85	85	85	425	75

For all modes, the pumping flow rate is maintained at approximately 100 L/min for each well, resulting in a total flow rate of 500 L/min at the heat plate exchanger. The inter-well reinjection mode entails unbalancing the return flow rates between the SCWs, by discharging a total of 75 L/min from SCW-3, SCW-4 and SCW-5, and returning it to SCW-1 and SCW-2 ($IR_{1,2} = 15\%$ of the total flow rate). The full recirculation mode rather uses balanced return flow rates of 100 L/min for each SCW ($\beta = 0\%$). Lastly, both bleed modes involve discharging an equally distributed flow rate from the SCWs, namely a total of 37.5 L/min ($\beta = 7.5\%$) and 75 L/min ($\beta = 15\%$). In the latter two bleed modes, the discharged flow is redirected to

the injection well, without inducing any overflow.

Figure 6.4 presents the flow rates, temperatures, and ground heat loads measured during the experimental test. The vertical dashed lines in black correspond to changes in the reinjection mode, which have been initiated in the morning, prior to the activation of the building's cooling system and the subsequent release of heat to the ground. The respective reinjection modes are indicated at the top of Figure 6.4. A correction of -0.16 °C is applied to the temperature signal T_{in} presented in Figure 6.4 to account for an offset in the temperature sensor.

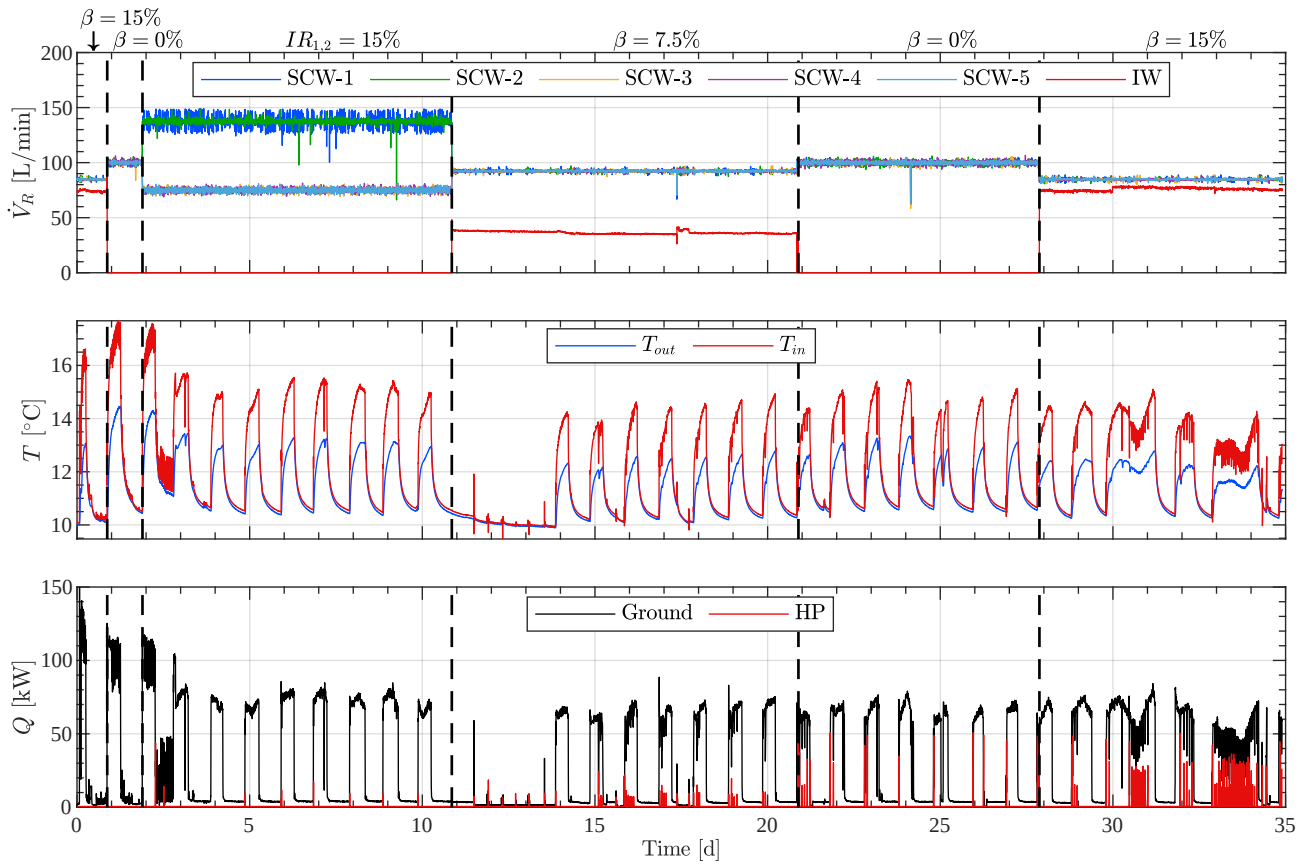

FIGURE 6.4 Experimental data for the inter-well reinjection tests carried out between July 17 and August 21, 2023 ; Top : reinjection flow rates ; Middle : groundwater temperature at the inlet (T_{in}) and outlet (T_{out}) of the SCWs ; Bottom : ground loads and heat pump electrical input. Vertical dashed lines indicate changes in reinjection modes.

6.4 Evaluation of experimental transfer functions

This section outlines the methodology employed to evaluate the transfer functions representing the thermal response associated with each of the four reinjection modes tested. As previously stated, transfer functions provide a direct measure of heat transfer efficiency as they can represent the response of a system (e.g., the outlet fluid temperature of a SCW) to a unitary and constant perturbation (e.g., a heat impulse) in any given linear and stationary conditions (e.g., constant set of properties and flow rates) [59,60,197]. In the present case, the transfer functions are evaluated by feeding the experimental data directly to a non-stationary deconvolution algorithm. The results are then compared with the measured temperatures to verify the algorithm's robustness and with a Monte Carlo numerical experiment to analyze the accuracy of the conceptual model.

6.4.1 Non-stationary deconvolution algorithm

The deconvolution algorithms proposed by Beier (2020) [98] and Dion et al. (2022b) [62] are model-free techniques that can isolate a transfer function corresponding to a specific operating condition. Recent studies have capitalized on deconvolution algorithms to extract transfer functions from experimental data of in situ tests typically conducted prior to the design stage of GSHP systems [62,63,98,198]. To the authors' knowledge, only one study has applied a deconvolution algorithm to data from an operating building. Indeed, Heim et al. (2024) [198] have employed a deconvolution algorithm to estimate the transfer functions of individual closed-loop boreholes connected to a real institutional building, thereby enabling the comparison of their thermal efficiency in stationary conditions (i.e., considering constant flow rates). In situations involving non-stationary conditions (i.e., variable pumping, return, or bleed flow rates), a non-stationary deconvolution algorithm can also be used to estimate the individual transfer functions representing each past system state, as demonstrated and validated by Dion et al. (2023) [63].

The non-stationary deconvolution algorithm used in this paper, which is based on the work of Dion et al. (2023) [63], represents the first instance of the application of this technique to data obtained from multiple SCWs operated under non-stationary conditions in a working GSHP system. First, the forward algorithm relies on a convolution product that expresses the fluid temperature at the SCWs outlets ($T_{out}(t)$) as :

$$T_{out}(t) = \Delta T_{f,out}(t) + T_0 = (f * g)(t, s) + T_0 \tag{6.3}$$

where T_0 is the initial temperature and $\Delta T_{f,out}(t)$ is the thermal response obtained by the

convolution product between multiple transfer functions $g(t,s)$ and a perturbation matrix $f(t,s)$, both their sizes being equal to the time vector t by the state vector s. This non-stationary formulation of the convolution product allows integrating time-varying operating conditions (i.e., flow and bleed rates) and can be solved efficiently in the frequency domain [60, 61] :

$$\begin{aligned}\Delta T_{f,out}(t) &= \sum_{s=1}^{S}(f_s * g_s)(t) \\ &= \sum_{s=1}^{S}\mathcal{F}^{-1}\left(\mathcal{F}\left(f_s(t)\right)\cdot\mathcal{F}\left(g_s(t)\right)\right)\end{aligned} \tag{6.4}$$

Hence, the temperature increment $\Delta T(t)$, at any time t, is obtained through the sum of the convolution products between the incremental load functions $f_s(t)$ and the transfer functions $g_s(t)$, for each state s. It is important to note that, in this work, the transfer functions are obtained in response to a uniform and constant heat load of 1 kW, in accordance with Beaudry et al. (2023) [61]. Consequently, the excitation function $f(t,s)$ is given by :

$$f(t_i,s) = Q(t_i,s) - Q(t_{i-1},s) \tag{6.5}$$

with

$$Q(t,s) = \begin{cases}\dot{V}(t)C_f(T_{in}(t) - T_{out}(t)), & \text{if } s \text{ is activated} \\ 0, & \text{if } s \text{ is not activated}\end{cases} \tag{6.6}$$

Following the nomenclature proposed by Beaudry et al. (2023) [61], heat loads $Q(t,s)$ [kW] are arranged in a matrix, with rows corresponding to time t and columns to state s. The thermal loads are calculated based on the total flow rate $\dot{V}(t)$ [m^3/s], the volumetric heat capacity of the fluid C_f [J/(m^3°C)] and the average temperature difference between the inlet $T_{in}(t)$ [°C] and outlet $T_{out}(t)$ [°C] of the SCWs. Then, the only remaining unknown in Eq. 6.3 are the transfer functions.

Following the deconvolution algorithm presented by Dion et al. (2023) [63], an optimization framework is employed to estimate the transfer function matrix $\hat{g}_s$. The optimization problem is :

$$\hat{g}_s = arg\ min_{\hat{g}_s} E(t_1, ..., t_m)|c_1, c_2 \tag{6.7}$$

where the experimental transfer functions $\hat{g}_s$ are obtained by minimizing the multi-objective function $E(t)$ described as follows :

$$E(t) = E_{\hat{T}} + E_{\hat{g}'} + E_{\hat{g}''} + E_{c_{1,t}} \tag{6.8}$$

with

$$E_{\hat{T}} = W_1 \cdot \|\omega(t)\left(\Delta\hat{T}_{f,out}(t) - \Delta T_{f,out}(t)\right)\|_2 \tag{6.9}$$

$$E_{\hat{g}'} = W_2 \cdot \|\hat{g}'_s(t)\|_2 \tag{6.10}$$

$$E_{\hat{g}''} = W_3 \cdot \|\hat{g}''_s(t)\|_2 \tag{6.11}$$

$$E_{c_{1,t}} = \sum_{j=1}^{p}\sum_{i=1}^{n_i-j} \|min\left(0, \hat{g}_s(t_{i+j}) - \hat{g}_s(t_i)\right)\|_2 \tag{6.12}$$

The first term $E_{\hat{T}}$ of Eq. 6.8 entails the comparison of the simulated temperatures $\Delta\hat{T}_{f,out}$ at each iteration with the observed temperatures $\Delta T_{f,out}$=$T_{out}(t) - T_0$. The second and third terms, designated as $E_{\hat{g}'}$ and $E_{\hat{g}''}$, incorporate the first and second derivatives of the transfer functions, respectively. The last term serves to impose a soft constraint that facilitates the strictly positive progression of the derivative functions $\hat{g}'_s(t_i)$, thus inducing strictly growing functions $\hat{g}_s(t_i)$. In order to guarantee the accurate reconstruction of the initial time steps and achieve a balance in the optimization process, a weighting factor $\omega(t)$ is employed. This factor applies a higher weight (3 instead of 1) to the first 10 time steps. Those 10 time steps, representing a total of 50 minutes, have been selected to encompass a minimum of two times the fluid residence time, which is theoretically evaluated at 22 minutes. It is noteworthy that this assumption yielded satisfactory outcomes in all the cases examined in this study. Finally, the proportionality factor $W_{1\to3}$ regulates the effect of the additional constraints and is obtained by calculating the terms in Eqs. 6.9, 6.10 and 6.11 with a preliminary solution and applying the following equations :

$$P_1 = \frac{E_{\hat{T}}}{E}, \quad P_2 = \frac{E_{\hat{g}'}}{E}, \quad P_3 = \frac{E_{\hat{g}''}}{E} \tag{6.13}$$

$$W_i = \frac{P_{i,\text{fit}}}{P_i} \quad \forall \quad i = (1, 2, 3) \tag{6.14}$$

where, in this study, $P_{i,\text{fit}}$ for $E_{1\to3}$ is set to 50%, 25% and 25%, respectively.

The use of the linear inequality constraints c_1 and c_2 in Eq. 6.7 imposes a realistic form to the transfer functions. It should be noted that the initial solution is obtained through the use of an exponential integral function, which eases convergence. For a more detailed presentation of the methodology, the interested reader is encouraged to consult Dion et al. (2023) [63]. The transfer functions are ultimately obtained by solving the optimization problem using a newly developed algorithm within a hyper-heuristic framework, named Thompson Sampling Optimization (TSO) and proposed by Nguyen (2024) [199]. In TSO, a number of "search agents" are employed to individually solve the multi-objective function and navigate to the

solution by selecting between five heuristic methods with Thompson Sampling. The TSO algorithm, as proposed by Nguyen (2024) [199], reaches convergence after a prescribed number of iterations, effectively stabilizing the objective function. In addressing the specific problem at hand, the population was defined as 100 agents, and the number of iterations was set to 1,750. These assumptions were derived through a process of trial and error and were selected based on their demonstrated efficiency and robustness in solving the multi-objective function. Ultimately, the upper and lower boundaries of the optimization problem are defined by scaling the initial solution at 20% and 1000%, respectively. To prevent the solution from adhering to the boundaries, a random noise with a value equal to 10% of the initial solution is also incorporated into the boundaries.

Once the optimization is completed, the accuracy of the experimental transfer functions is evaluated by feeding the optimized experimental transfer functions and load functions to the convolution algorithm presented in Eq. 6.4, in order to reproduce the observed temperatures. The degree of correspondence between the observed and convolved temperatures is then evaluated through the examination the residuals, both visually and in terms of root mean square error (RMSE). The effectiveness of the deconvolution method is indicated by the absence of significant remaining residuals in the reinjection modes tested, along with a relatively low RMSE for each mode.

6.4.2 Numerical simulation and Monte Carlo experiment

The authors have identified finite element numerical models as an adequate means to accurately simulate the complex coupled phenomena of heat transfer and groundwater flow that occur in and around multi-SCW systems [25, 53, 68]. The model is described in both Figure 6.5 and Table 6.3. It builds upon the two-dimensional axisymmetric model presented by Jacques and Pasquier (2023) [138] and employs the boundary conditions illustrated in Figure 5, which enables the parameter distributions presented in Figure 6.3 to be used. It is pertinent to reiterate that these distributions have been obtained from interpreting field surveys conducted exclusively on SCW-1. In order to streamline the modeling process and to enable direct use of to these distributions, the geometry of SCW-1 is replicated to all other SCWs. Accordingly, the model is calibrated exclusively on SCW-1 and its accompanying thermal response test in full recirculation, which excludes hydraulic stimulation.

Using the boundary conditions depicted in Figure 6.5, the numerical model is used to generate transfer functions that simulate the groundwater temperature at the outlets of the SCWs, denoted by T_{out}, in a manner similar to the methodology described in Beaudry et al. (2022) [25]. This temperature T_{out} varies in time in response to a constant heat impulsion imposed

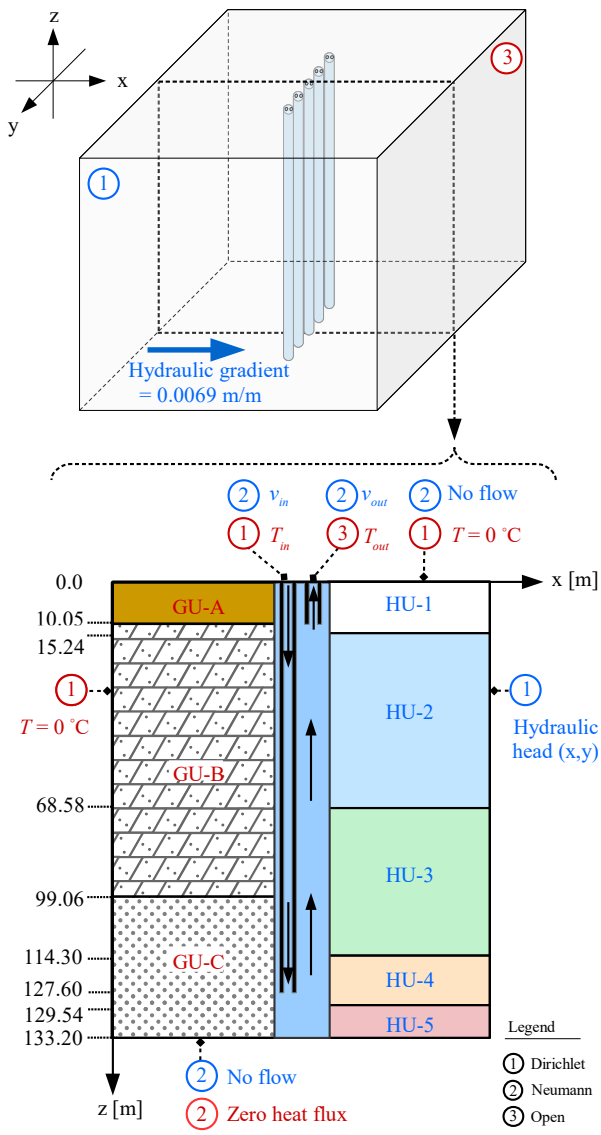

FIGURE 6.5 The coupled finite element model, which includes the hydraulic boundaries (blue circles) and thermal boundary conditions (red circles) ; Top : A three-dimensional representation of the model with the hydraulic gradient ; Bottom : An x-z view centered on SCW-3, which illustrates the geological units (GU), hydrostratigraphic units (HU) and boundary conditions.

at the wells' inlet, such as $T_{in} = \overline{T}_{out} + 1$ kW$/(\dot{V} \cdot C_f)$. A uniform temperature is assumed at the surface and in the far field, with the exception of the downstream boundary, which is left open to advective outflows. To reproduce the flow in each SCW, constant outlet and inlet velocity boundary conditions are applied to the surface of the riser and reinjection pipes, respectively. A regional hydraulic gradient of 0.0069 m/m is applied to the hydraulic boundaries, as determined by Robert et al. (2022) [27] at the experimental site. Lastly, it

Tableau 6.3 Parameters used in the numerical model to simulate the transfer functions representative of each reinjection mode. For each HU and GU, the hydraulic and thermal properties are sampled (x) from their respective distributions shown in Figure 6.3.

Parameters	Fluid	Pipe	HU-1	HU-2	HU-3	HU-4	HU-5	GU-A	GU-B	GU-C
Thickness - b [m]	-	0.00549	15.24	53.34	45.72	15.24	3.66	10.05	89.01	34.14
Radius - r [m]	0.076	0.0302	-	-	-	-	-	-	-	-
Specific storage - S_s [m^{-1}]	-	4e-10	2e-8	2e-8	2e-8	2e-8	2e-8	-	-	-
Porosity - n [%]	-	0.001	-	-	-	-	-	20	2.2	5.9
Length - H [m]	133.2	127.6	-	-	-	-	-	-	-	-
Hydraulic conduct. - K $\log_{10}$[m/s]	1.0	-9.0	-7.3	$x \in K_2$	$x \in K_3$	$x \in K_4$	$x \in K_5$	-	-	-
Thermal conduct. - λ [W/(mK)]	0.56	0.40	-	-	-	-	-	$x \in \lambda_{\mathrm{A}}$	$x \in \lambda_{\mathrm{B}}$	$x \in \lambda_{\mathrm{C}}$
Vol. heat capacity - C [MJ/(m^{3}K)]	4.186	2.174	-	-	-	-	-	$x \in C_{\mathrm{A}}$	$x \in C_{\mathrm{B}}$	$x \in C_{\mathrm{C}}$

should be noted that the surface of the model is a square with sides measuring 200 m.

The model is employed to simulate numerical transfer functions associated with each reinjection mode following a Monte Carlo experiment wherein multiple sets of hydraulic and thermal properties are drawn from the joint distributions using a Halton quasi-random sequence [189]. The purpose of these numerical transfer functions is to verify the adequation between the experimental transfer functions and the previous theoretical understanding of hydraulic and thermal processes.

6.5 Results

This section presents the main findings of the experimental study on a operated SWC system, starting with a comparison of the thermal exchange efficiency between the distinct reinjection modes for SCWs (i.e., inter-well reinjection, full recirculation, and bleed). This comparison is expressed using the experimental transfer functions derived from the 35-day test data using the non-stationary deconvolution algorithm of Dion et al. (2023) [63]. Then, the robustness of the deconvolution algorithm and of the results is demonstrated by comparing the reconstructed temperature signal, obtained by convolving the optimized experimental transfer functions, with the temperatures measured during the test. Lastly, the numerical transfer functions obtained through a Monte Carlo experiment are compared to the experimental transfer functions to gain insight about the conceptual model of the site.

6.5.1 Inter-well reinjection performance

First, the experimental transfer functions are presented in Figure 6.6. A first observation reveals that compared to the full recirculation mode ($\beta = 0\%$), the inter-well reinjection transfer function ($IR_{1,2} = 15\%$) begins to show a diminished thermal response when faced to a 1 kW heat impulsion approximately two hours after activation. The results also show

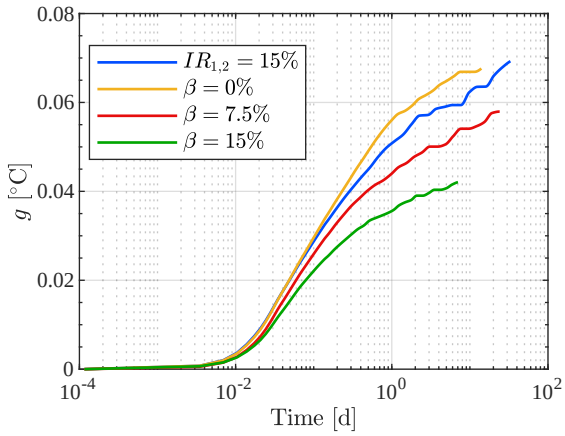

FIGURE 6.6 Experimental transfer functions for each reinjection mode obtained by non-stationary deconvolution : inter-well reinjection ($IR_{1,2} = 15\%$), full recirculation ($\beta = 0\%$) and the two bleed levels ($\beta = 7.5\%$ and $\beta = 15\%$)

that the two bleed levels employed in the experimental test ($\beta = 7.5\%$ and $\beta = 15\%$) reduced the magnitude of the thermal responses compared to both full recirculation and inter-well reinjection immediately after activation. Thus, these results indicate that while not as thermally efficient as full-bleed operation, inter-well reinjection improves well resilience to temperature fluctuations compared to full recirculation. It is therefore concluded that inter-well reinjection is a suitable and easily implemented solution that can increase the efficiency of heat transfer in SCWs while avoiding the need to construct an injection well. This outcome is expected since inter-well reinjection improves advective heat transfer, but is also more sensitive to the thermal interference associated with returning the total flow of heated groundwater (in this case) into SCWs than is the bleed operation, which rather discharges part of it downstream through an injection well. In this respect, it should be added that the specific arrangement of the return flow unbalance (discharge from SCW-3-4-5 and reinjection in SCW-1-2) is the only configuration tested, and that a different arrangement may have provided different results due to the position and orientation of the SCWs to the local hydraulic gradient.

As an example to illustrate the efficacy of the transfer functions illustrated in Figure 6.6, one could impose a constant ground load to each of the reinjection scenarios. If the initial ground temperature T_0 is 10 °C, and the fluid temperature must remain below 20 °C, the following heat loads could be sustained for eight hours in the various reinjection scenarios : 225 kW (full recirculation), 240 kW (inter-well reinjection), or 265 kW and 320 kW (both bleed levels, respectively).

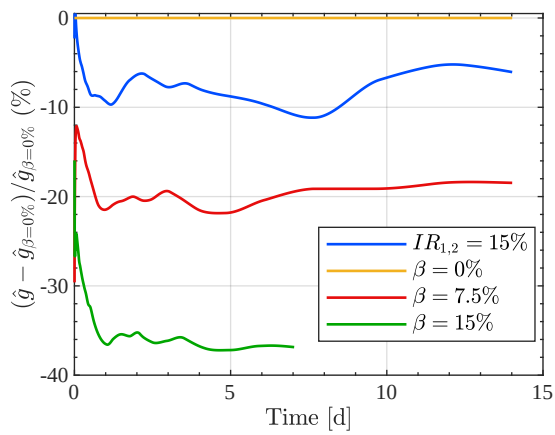

FIGURE 6.7 Relative difference between the transfer functions representing inter-well reinjection ($IR_{1,2} = 15\%$) and bleed ($\beta = 7.5\%$, $\beta = 15\%$), and the transfer function representing full recirculation ($\beta = 0$ %).

To more accurately quantify the respective efficiency gains associated with the use of inter-well reinjection and full bleed as a function of time, the relative difference between the transfer functions evaluated for these modes and the transfer function evaluated for the full recirculation mode ($\beta = 0\%$) is shown in Figure 6.7. It can be observed that approximately one day is necessary for the three relative differences to reach a plateau, indicating that after this point all the transfer functions shown in Figure 6.6 have similar slopes. From this result, it is inferred that the heat transfer rate of SCWs is significantly enhanced by inter-well reinjection and bleed during the first day of their activation, after which all efficiency gains are quite stable. Nevertheless, the relative difference between the transfer functions representing the inter-well reinjection and full recirculation modes approaches 10%, confirming that the thermal perturbation of the SCWs is significantly decreased by simply unbalancing the return flow rates. For bleed ratios of 7.5% and 15%, the relative difference is more pronounced, reaching 20% and 37% respectively. This confirms that activating the bleed in a SCW can rapidly boost its thermal efficiency, at least in permeable geological environments like the one investigated in this work. In environments where hydraulic conditions are less favorable, the observed results may differ, as the conductive heat transfer mechanism becomes the dominant process [44]. To reinforce this assertion, the proposed methodology could be replicated on a less permeable site, given that the deconvolution algorithm is model-free and not site-specific.

6.5.2 Robustness of the non-stationary deconvolution algorithm

The robustness of the non-stationary deconvolution algorithm is illustrated in Figure 6.8, which presents a comparison between the measured temperatures at the SCWs outlets during the test and the simulated temperatures obtained by feeding the experimental transfer functions and heat load function to a forward non-stationary convolution algorithm.

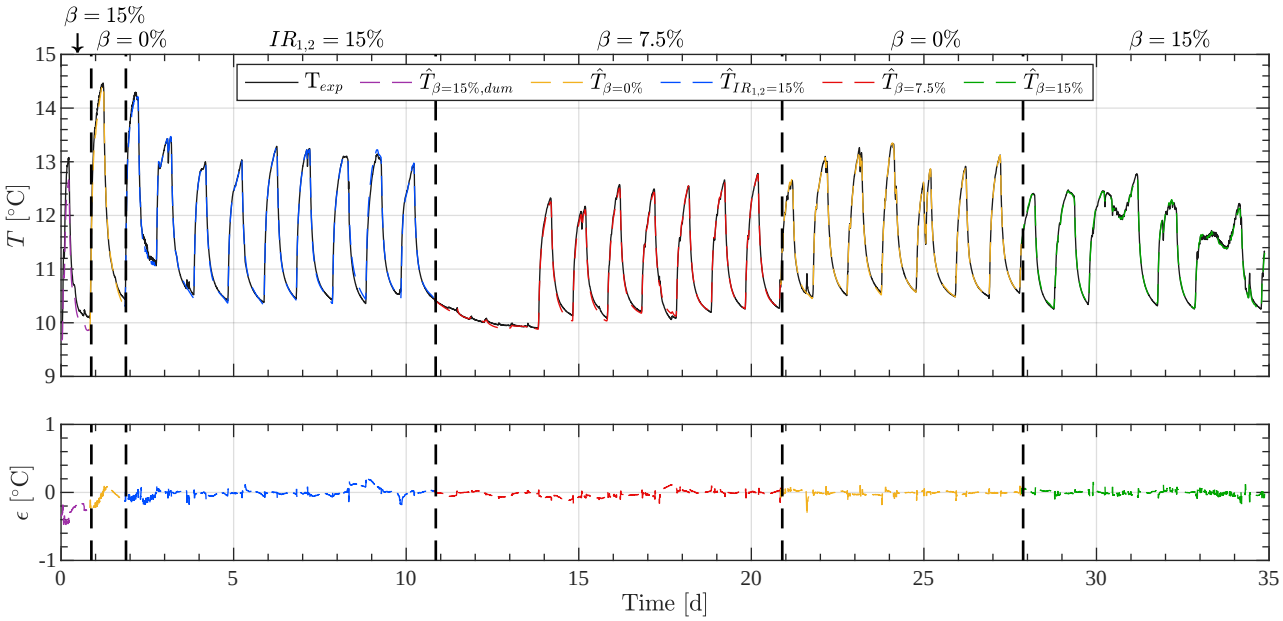

FIGURE 6.8 Simulated temperatures obtained from the experimental transfer functions compared with observed temperatures measured during the test. Top : comparison of the temperatures ; Bottom : residuals between the temperatures.

As shown in Figure 6.8, the simulated temperatures reproduce the observed temperatures very accurately, with a root mean square error (RMSE) of 0.06 °C between both data sets. The RMSE falls to 0.04 °C when the residuals of the first two days are neglected. Both these RMSEs also fall within the tolerances of the temperature sensors (± 0.2 °C).

As mentioned, the RMSE during the first two days is higher than for the rest of the test. This is explained by the fact that the system was already perturbed before the beginning of the test, as demonstrated by the higher groundwater temperature measured immediately prior to the test (10.04 °C) compared to the initial undisturbed temperature measured in 2020 by Robert et al. (2022) [27] (8.16°C). To account for this discrepancy between the initial temperatures measured at the site, a number of choices are made to facilitate the deconvolution process. Firstly, a correction is applied to the temperature at the initial time step to reproduce the lowest temperature of 9.62 °C observed prior to the test. The second is to

exclude the observations made during the first two days of the test from the objective function (Eq. 6.8). To increase the flexibility of the optimization process and to compensate for the heat perturbation prior to the initiation of the test, a dummy transfer function ($\hat{g}_{\beta=15\%,dum}$) is also estimated for the mode operated on the first day. A dummy function is defined as the creation of an additional state within the transfer function matrix $\hat{g}(t,s)$. Figure 6.9 presents a comparison of the transfer functions obtained through four supplementary deconvolutions performed with different initial solutions for the dummy function. Upon examination of the transfer functions illustrated in Figure 6.9 (a), it was determined that the initial solutions of the dummy function did not result in a significant alteration to the form of the resulting transfer functions. This finding supports the assumption that the use of a dummy function does not hinder the deconvolution algorithm's robustness.

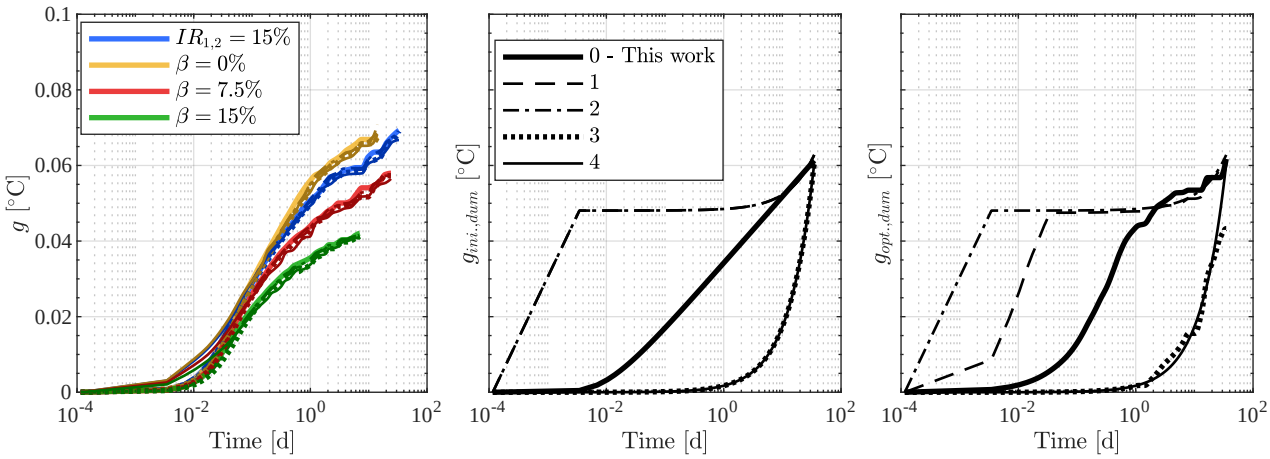

FIGURE 6.9 Impact of dummy function on reconstruction of transfer functions ; Left : Transfer functions obtained with a different initial solution for the dummy function ; Center : Initial dummy functions used for the deconvolution ; Right : dummy functions obtained through deconvolution, with transfer functions 2 and 4 imposed instead of being optimized.

Lastly, it should be noted that despite the very good accuracy of the results presented in Figure 6.8, a certain level of unsmoothness of the experimental transfer functions is observed in Figure 6.6. This is mainly explained by the architecture of the non-stationary deconvolution algorithm, which aims at reproducing the objective function of the observed temperatures. This can lead to unsmooth transfer functions if the experimental input is noisy, if operated modes are not perfectly constant and if anthropogenic perturbations happen. On a final note, it should be noted that the duration of each experimental transfer function is contingent upon the time of its activation and the remaining length of the test. To illustrate this, the transfer function associated with the mode $IR_{1,2}$ (as presented in Figure 6.4) will have the duration of 33 days because it started on day 2.

6.5.3 Numerical analysis

The numerical model is employed to generate a series of numerical transfer functions for each operating mode through a Monte Carlo experiment with 650 sets of hydraulic and thermal properties. These functions are then compared to the experimental transfer functions obtained using the non-stationary deconvolution algorithm, as shown in Figure 6.10.

For each reinjection mode, the experimental transfer functions fall within the shaded areas, which encompass all numerical transfer functions. The average RMSE between these numerical transfer functions and their experimental counterparts are 0.004 °C for the inter-well reinjection ($IR_{1,2}$), 0.003 °C for the full recirculation ($\beta = 0\%$), 0.007 °C for the first bleed level ($\beta = 7.5\%$) and 0.011 °C for the second bleed level ($\beta = 15\%$). These relatively small values of RMSE provide another verification of the robustness of the experimental transfer functions obtained by deconvolution. Note also in Figure 6.10 how the experimental functions $IR_{1,2}$ and $\beta = 0\%$ overlap well with areas of a high probability density.

The experimental transfer functions corresponding to $\beta = 7.5\%$ and $\beta = 15\%$ are located at the lower limit of the envelope that represents all numerical solutions. This indicates that the inferred distributions and assumptions used in the numerical model could be refined and that deviations occur when bleed is activated and enhances advective heat transfer. Recall that the hydraulic and thermal properties imposed in the numerical model are deduced from a TRT conducted on SCW-1 only and in full recirculation mode ($\beta = 0\%$). The procedure for this TRT has entailed the injection of heat into the aquifer, but not hydraulic stimulation. Thus, a significant finding of this study is that the use of hydraulically and thermally stimulated TRTs could contribute to a better characterization of SCWs by providing a better estimate of hydraulic properties and their effect on the heat transfer during bleed. Accordingly, calibration of the aforementioned numerical model using the experimental data would enhance the model's accuracy and facilitate further investigation in the limitations of inter-well reinjection under different operational strategies.

6.6 Conclusion

The objective of this project is to provide an experimental demonstration of inter-well reinjection performance with advanced simulation tools, including non-stationary convolution and a deconvolution algorithms. The findings are based on the results of a 35-day experimental test conducted on five standing column wells, wherein inter-well reinjection and other typical operating modes of standing column wells, namely full recirculation and bleed, were employed during the cooling operation of an actual building. Experimental transfer functions

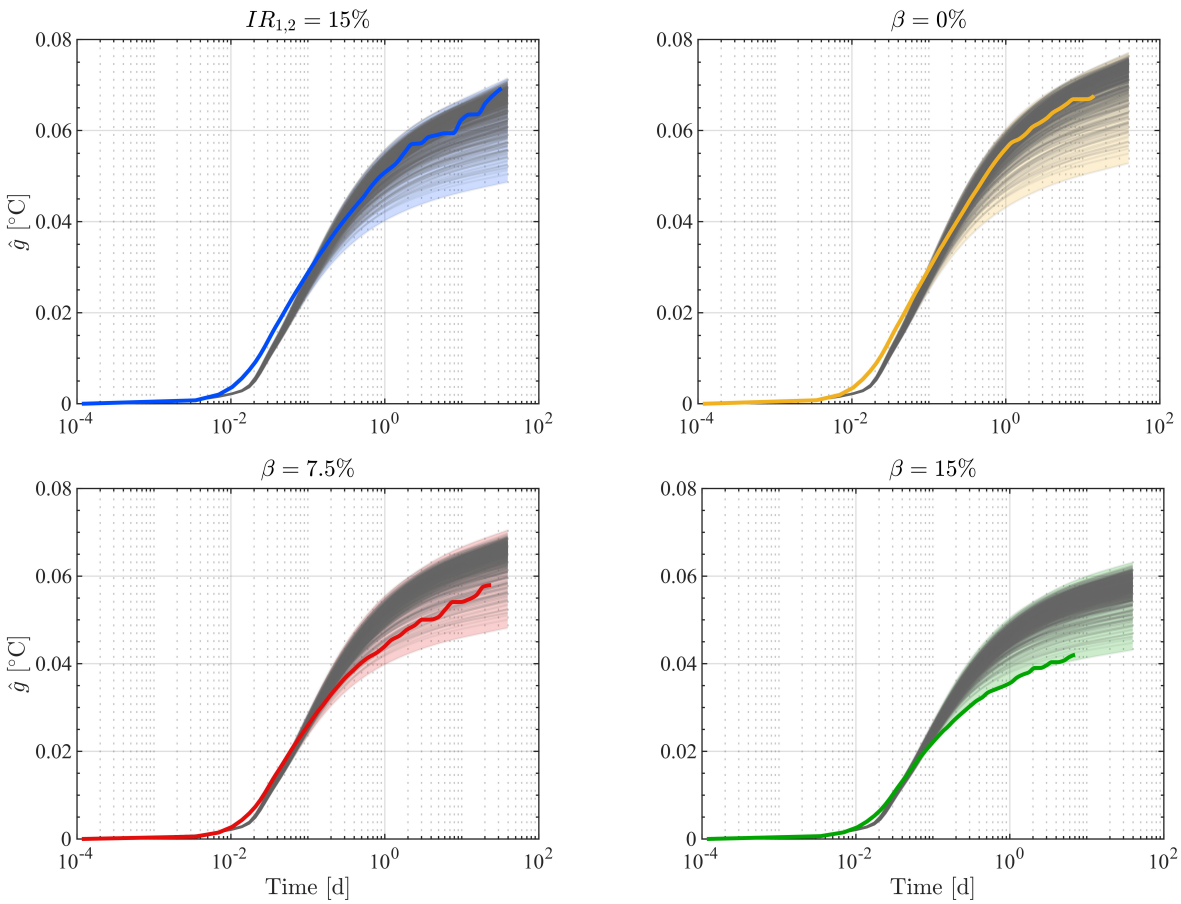

FIGURE 6.10 Numerical transfer function for each reinjection modes obtained with the numerical model through a Monte Carlo experiment. The solid colored lines are experimental transfer functions estimated with the deconvolution algorithm, while gray lines enclosed in the shaded areas are all numerical solutions.

are obtained using a recently published non-stationary deconvolution algorithm, which is applied for the first time to dynamic operating data from a full-scale multi-standing column well system. The comparison of the different experimental transfer functions indicates that underground heat transfer rates are improved by inter-well reinjection compared to full recirculation, although not as much as by bleed. Consequently, it is deduced that inter-well reinjection is a suitable and easily implemented solution that can rapidly increase the efficiency of heat transfer in SCWs while avoiding the water management issues associated with the full discharge process of bleed.

A second important finding is the demonstrated robustness of the non-stationary deconvolution algorithm for evaluating the transfer functions representing the thermal response of the SCWs to various operating flow conditions. The comparison of the simulated temperatures

obtained from the experimental transfer functions compared with observed temperatures measured during the test led to a very low RMSE of 0.04 °C.

As a final and complementary result, numerical transfer functions are calculated for each operating mode using a Monte-Carlo experiment that sampled joint distributions of the properties estimated from a thermal test conducted in the absence of hydraulic stimulation. The results show that the inadequacy of the numerical solution seems to increase proportionally with the increase of the advective component in the bleed scenarios. Thus, a final important finding is that the integration of bleed or a form of hydraulic stimulation during thermal response tests could lead to a better estimation of the hydraulic properties estimation around a SCW.

In this study, the performance of inter-well reinjection is tested on a real SCW system located in a specific permeable hydrogeological setting and using a single balancing configuration of the flow rates. To further understand the potential of this easily implemented and cost-effective reinjection mode, additional research could investigate the influence of different hydrogeological contexts, as well as various wells and flow balancing arrangements on the efficiency of underground heat transfer.

6.7 Acknowledgments

The authors acknowledge the support from partners of the Geothermal Research Chair on the Integration of SCWs in Institutional Buildings, namely Hydro-Québec, the Ministry of higher education of Québec, Mille-Îles School Service Centre, Montreal School Service Centre, Samares School Service Centre, Versaprofiles, Marmott Energies, CanmetEnergy and NSERC. Additionally, we thank the anonymous reviewers and colleagues that provided constructive comments. This work was financed by the Natural Sciences and Engineering Research Council of Canada through grant number ALLRP 544477-19.

6.8 Nomenclature

Acronyms

COP	coefficient of performance
FC	full recirculation
GHE	ground heat exchanger
GSHP	ground source heat pump
IR	inter-well reinjection

IW	injection well
GU	geological unit
HU	hydrostratigraphic unit
RM	reinjection mode
RMSE	root mean square error
SCW	standing column well
TRT	thermal response test

Greek letters

β	total discharge ratio [-]
Δ	difference [-]
ϵ	temperature residuals [°C]
λ	thermal conductivity [W/(m°C)]
ϕ	diameter [mm]
ω	weighting factor [-]

Symbols

c	constraint [-]
C	volumetric heat capacity [J/(m^3°C)]
E	objective function [-]
f	excitation function [°C]
g	transfer function for a unitary excitation [°C]
H	borehole length [m]
K	hydraulic conductivity $\log_{10}$[m/s]
n	porosity [-]
N	quantity [-]
P	proportionality factor [-]
Q	heating power [W]
r	radius [m]
s	state [-]
t	time [s]
T	observed temperature [°C]
$\hat{T}$	estimated temperature [°C]
$\overline{T}$	average temperature [°C]
v	velocity [m/s]

$\dot{V}$	flow rate [m^3/s]
W	weighting factor [-]
z	depths [m]

Subscripts

$(+)$	receiving well
$(-)$	discharging well
0	ground initial condition
exp	experimental
f	fluid
in	inlet
out	outlet
P	pumping
R	reinjection
T	total

CHAPITRE 7 DISCUSSION GÉNÉRALE

L'objectif général de ce projet de recherche, comme mentionné au chapitre 3, est d'analyser les différentes méthodes de modélisation des PCP dans des contextes expérimentaux, afin de mettre en évidence et étendre leurs capacités pour représenter les dynamiques thermiques et hydrauliques autour de ces ÉCS. Les chapitres 4, 5 et 6 ont respectivement présenté un modèle analytique d'advection et de diffusion, un modèle numérique intégrant l'hétérogénéité en couches et des modèles empiriques construits par estimation de fonctions de transfert obtenues par un algorithme de déconvolution. Bien que le résultat de chacun de ces modèles soit la variation de température du fluide à la sortie d'un PCP en réponse à un stimulus thermique, les différentes approches de modélisation ont toutes des utilités particulières et la sélection d'un modèle approprié dans un projet dépendra donc du contexte et des objectifs visés. Ainsi, le présent chapitre abordera chacun de ces modèles dans des sections distinctes, avec un bref rappel et une mise en contexte au début de chacune d'entre elles. Une discussion sur les avantages et les limites des différents modèles suivra. Plusieurs pistes d'améliorations seront ensuite présentées, puis une synthèse permettra de répondre à l'objectif général de cette thèse.

7.1 Modèle analytique intégrant l'opération de la saignée

D'abord, il est important de réitérer que le modèle analytique β-SLI [45] simule la variation de la température moyenne à la paroi du forage d'un PCP en présence d'un écoulement radial convergent induit par une opération de la saignée, et ce, dans un aquifère homogène et isotrope (voir chapitre 4 et annexe A). De plus, le modèle analytique β-SLI fournit un résultat en une fraction de seconde, soit plus de 1 000 fois plus rapidement qu'un modèle numérique axisymétrique [45], ce qui permet d'effectuer des études d'optimisation ou des analyses stochastiques dans des délais réalistes. Plus spécifiquement, la simplicité et la rapidité de calcul de ce modèle en font un candidat idéal pour les études de conception préliminaire et les analyses de sensibilité.

Le principe du modèle β-SLI est de combiner un modèle de conduction classique (SLI) à une fonction de mise à l'échelle permettant de prendre en compte l'effet de l'advection induite par l'opération de la saignée. Cette fonction de mise à l'échelle est ajustée à l'aide de poids dans une équation approximative (h_A dans l'article 4), de manière à minimiser la racine de l'erreur quadratique relative (RMSRE) entre une base de données produite avec un modèle numérique et les solutions issues du modèle β-SLI. Dans l'étude de Nguyen et al. (2025) [45], les poids

ajustés sur le modèle bidimensionnel axisymétrique ont ainsi donné un RMSRE d'une valeur de 9,8 $\times$ 10^{-3}. Pour illustrer ce résultat, on peut considérer qu'une température observée de l'ordre de 20 °C correspond à une erreur absolue d'environ 0,2 °C, soit une incertitude du même ordre que la justesse des sondes de température utilisées lors des expérimentations (±0,20 °C au chapitre 4 et ±0,25 °C au chapitre 6). Dans ce contexte, le modèle analytique β-SLI reproduit le modèle numérique bidimensionnel homogène et isotrope avec justesse.

Afin de valider expérimentalement le modèle dans un contexte *in situ*, l'article présenté au chapitre 4 propose des améliorations prenant en compte l'effet de l'hétérogénéité en couches et de l'écoulement induit par le pompage. Dans cet article, l'effet de l'hétérogénéité en couches a été validé numériquement, démontrant une valeur moyenne de RMSRE de 2,9 $\times$ 10^{-2}, soit une erreur légèrement supérieure à celle obtenue par Nguyen et al. (2025) [45] lors du développement du modèle. Expérimentalement, la combinaison des deux effets (pompage et hétérogénéité), ainsi que de la formulation permettant d'obtenir la température du fluide à la sortie du PCP, ont permis de valider la justesse du modèle analytique, avec des moyennes des erreurs absolues (MAE) variant de 0,28 à 0,37 °C. Ces faibles erreurs indiquent que le modèle analytique β-SLI, combiné aux principes présentés au chapitre 4, est juste, et ce, même dans un contexte expérimental avec une hétérogénéité en couches.

Afin d'analyser les erreurs rapportées au chapitre 4, il est important de commencer par discuter d'une hypothèse faite dans le modèle numérique axisymétrique qui a servi à optimiser les poids du modèle analytique β-SLI. Cette hypothèse concerne la conductivité hydraulique de l'eau dans la colonne du PCP (K_f), dont la valeur a été fixée à 1000 m/s. À ce sujet, mentionnons que cette hypothèse de modélisation, qui consiste à utiliser une conductivité K_f dans une physique de transport en milieu poreux, permet d'économiser un temps de calcul considérable puisque la résolution des équations de Navier-Stokes est évitée. Cette méthode de modélisation doit son origine à Deng (2004) [47] qui avait proposé que les relations de Chen et Jiao (1999) [200] soient utilisées pour calculer K_f en fonction du régime d'écoulement. Depuis, les valeurs de K_f, dans la plupart des modèles rapportés dans la littérature, s'appuient sur la proposition de Croteau (2011) [50] selon laquelle K_f doit être fonction du rabattement dans le puits. Croteau (2011) [50] souligne également l'importance de la valeur attribuée à la conductivité hydraulique des tuyaux pour simuler leur quasi-imperméabilité. En effet, une valeur trop faible peut entraîner des instabilités numériques en raison du fort contraste entre la conductivité de l'eau et celle des tuyaux dans le modèle. Il a ainsi été démontré qu'une conductivité de l'ordre de 1 $\times$ 10^{-9} permet généralement d'éviter les instabilités. Une fois les instabilités maîtrisées, la valeur de K_f est ajustée pour prendre en compte les pertes de charge dans le puits, lesquelles varient selon plusieurs facteurs, notamment la forme et la rugosité du puits, la longueur des tuyaux ou encore la présence de matières en suspension.

Ainsi, pour un même débit de circulation et des propriétés thermiques et hydrauliques identiques, la simulation de la réponse thermique de puits présentant des configurations physiques différentes peut être ajustée par la modification de la valeur de K_f.

Pour le site de Varennes (validation expérimentale au chapitre 4), il a été démontré que les propriétés thermiques et hydrauliques utilisées pour modéliser le site de Varennes conduisent à de faibles erreurs lorsque la valeur de K_f est fixée à 1000 m/s [40], soit la même valeur que celle utilisée pour la base de données servant à calculer les poids du modèle β-SLI. Mentionnons aussi que le site de Varennes est peu perméable, avec une conductivité hydraulique moyenne de 5,7 $\times$ 10^{-7} m/s, bien qu'il présente une hétérogénéité en couches à travers un réseau de fractures permettant l'utilisation de la saignée [40]. Considérant que la conductivité hydraulique du milieu homogène et isotrope a été fixée à 1 $\times$ 10^{-6} m/s dans le modèle numérique utilisé pour calibrer le modèle β-SLI, il apparaît donc que le site de Varennes possédait des caractéristiques proches de celles du modèle analytique.

Ainsi, la validation expérimentale du modèle analytique au chapitre 4 a démontré que celui-ci pouvait bien reproduire un milieu hétérogène et peu perméable. Additionnellement, une valeur de K_f de 300 m/s a été utilisée pour la validation numérique réalisée au chapitre 4 (où la conductivité de l'aquifère était de 1 $\times$ 10^{-6} m/s), ce qui a donné une valeur de RMSRE de 2,9 $\times$ 10^{-2}, indiquant que le modèle analytique conserve une justesse dans cette fourchette de la conductivité K_f. Cependant, il est possible qu'un site présentant des hypothèses très différentes conduise à des résultats moins justes, comme c'est le cas pour le site de Mirabel dont la conductivité hydraulique moyenne de l'aquifère atteignait 7,9 $\times$ 10^{-5} m/s et pour lequel une conductivité de l'eau dans la colonne du PCP d'une valeur de 10 m/s a été utilisée dans le modèle numérique (chapitre 5). Par conséquent, une validation expérimentale dans un site de forte conductivité hydraulique, tel que celui de Mirabel, serait requise pour confirmer l'exactitude du modèle β-SLI dans ce contexte. Aussi, le site de Mirabel est découpé en cinq unités hydrostratigraphiques, plutôt que trois comme dans le chapitre 4. Il serait alors également possible de valider la méthodologie de calcul des propriétés effectives pour un plus grand nombre d'unités.

Rappelons que la validation expérimentale réalisée à l'aide des essais menés à Varennes (chapitre 4) a été effectuée à l'aide des propriétés thermiques et hydrauliques du sous-sol rapportées par Beaudry et al. (2019) [40], qui ont été obtenues par l'interprétation respective d'un ERT et d'un essai de pompage. L'interprétation de l'ERT avait été réalisée avec la méthode de la pente, soit l'approximation de premier ordre de la SLI. Ainsi, il est possible qu'une interprétation de ce même ERT avec le modèle analytique β-ILS fournisse une meilleure approximation des propriétés. En effet, les propriétés pourraient être optimisées

par une méthode d'inversion, par exemple à l'aide d'algorithmes d'optimisation heuristique comme celui par échantillonnage de Thompson (TSO) [199] utilisé au chapitre 6. Dans ce contexte, les propriétés visées pourraient être de haut niveau, comme la résistance thermique ($\widetilde{R}_{f,b}$), la conductivité thermique ($\widetilde{\lambda}_s$), la diffusivité thermique ($\widetilde{\alpha}_s$) et l'amplitude de l'écoulement effectif ($\widetilde{V}_\beta$) se trouvant dans le nombre de Péclet ($\widetilde{\mathrm{Pe}}$) et le temps adimensionnel ($\widetilde{t}_a$). L'optimisation pourrait également viser des propriétés plus difficiles à obtenir en pratique, comme le rayon d'influence (r_∞) et la perte de charge due à l'aspiration (ΔH_{s^-}), ou cibler des propriétés pour des analyses spécifiques, telles que l'écoulement radial convergent induit par la recirculation dans le puits (V_{s^-}), la longueur effective liée à l'hétérogénéité ($\widetilde{L}$), ainsi que la dépressurisation de la pompe submersible ($\widetilde{L}_{s^-}$). Dans tous les cas, il serait pertinent de tester des méthodes d'inversion par optimisation dans des contextes de haute conductivité hydraulique (Mirabel) et basse conductivité hydraulique (Varennes). Cette inversion pourrait également être réalisée dans un cadre bayésien, comme présenté au chapitre 5.

L'un des avantages du modèle β-SLI est que son résultat est une fonction de transfert qui exprime la variation de température moyenne à la paroi de forage. Ainsi, il devient facile d'utiliser ce modèle dans le cadre théorique construit pour les ÉCS, c'est-à-dire les concepts de résistances thermiques et de superposition temporelle, comme présenté au chapitre 4, mais aussi le concept de superposition spatiale [201, 202]. Dans sa forme actuelle, le modèle β-SLI n'a pas été conçu pour reproduire des températures à des rayons supérieurs à celui du forage, ce qui ne garantit pas son exactitude lorsqu'il est utilisé pour une superposition spatiale. Une piste de recherche primordiale pour le dimensionnement d'un système multi-PCP consiste alors à étendre les capacités du modèle β-SLI à la simulation de la température à un rayon r quelconque du puits.

En ce qui concerne l'utilisation des résistances thermiques, un cadre théorique pour modéliser les transferts de chaleur à l'intérieur du PCP est proposé au chapitre 4, sur la base des équations développées pour des PBF de type coaxial [93, 149]. Une validation numérique de ce réseau de résistances démontre même une valeur de RMSRE de $3{,}0 \times 10^{-6}$, soit une erreur considérée comme non significative. Malgré ce résultat probant, la justesse de cette formulation est réduite si l'opération du PCP est effectuée à des débits en régime laminaire (et même légèrement en régime transitoire) dans la partie annulaire du puits. En effet, pour ces faibles débits, l'hypothèse de distribution linéaire entre la température du fluide à la sortie et à l'entrée du PCP, établie dans le chapitre 4, perd de sa validité. Pour les PBF coaxiaux, Lamarche (2023) [147] évoque une formulation pour un flux de chaleur variable le long de la paroi annulaire. Cette hypothèse pourrait constituer une solution pour augmenter la justesse à de faibles débits de circulation dans les PCP, mais aussi pour des PCP de grande profondeur pour lesquelles l'hypothèse de flux constant pourrait moins bien s'appliquer. En effet, les

équations présentées au chapitre 4 ont été testées sur un PCP de 213 m de profondeur, mais la littérature rapporte que des PCP ont été construits jusqu'à des profondeurs de 670 m.

Enfin, il convient de noter que le modèle β-SLI a été conçu en utilisant le modèle en conduction de la SLI. Afin de réduire l'incertitude du modèle β-SLI, une piste d'amélioration consisterait à réajuster les poids de l'équation approximative h_A en s'appuyant sur des modèles de conduction plus sophistiqués, comme le modèle SLF à longueur définie plutôt qu'infinie [74, 75] ou le modèle SCI qui diffuse la chaleur d'un cylindre plutôt qu'une ligne [42, 73].

En résumé, l'article du chapitre 4 a démontré que le modèle analytique reproduit avec justesse la variation de température d'un PCP opérant avec saignée, et ce, dans un contexte hydrostratigraphique d'hétérogénéité en couches possédant une faible conductivité hydraulique moyenne. La rapidité du calcul et la simplicité d'utilisation en font un modèle idéal pour des études d'optimisation ou d'analyse de sensibilité. L'interprétation d'ERT par inversion avec un algorithme d'optimisation permettrait d'obtenir des paramètres effectifs, le modèle utilisant des paramètres adimensionnels. Ainsi, il serait possible de s'affranchir des propriétés difficiles à identifier et nécessaires dans le développement au chapitre 4, mais surtout d'éviter de devoir poser une hypothèse sur la variable de conductivité hydraulique de l'eau K_f requise pour les modèles numériques. Des pistes de solutions ont été suggérées pour pallier les lacunes identifiées, à savoir la perte de justesse pour de faibles débits d'opération, le besoin d'une validation pour un milieu à haute conductivité hydraulique et l'intérêt d'étendre le modèle à des rayons plus grands que le rayon du puits.

7.2 Modèle numérique avec hétérogénéité en couches

Dans un contexte d'hétérogénéité présenté sous forme de couches horizontales, il est essentiel de prendre en compte les différentes unités hydrostratigraphiques autour d'un PCP afin de bien simuler la réponse thermique d'un PCP opérant avec la saignée [27, 40]. Ainsi, l'utilisation d'un modèle numérique d'éléments finis permet d'intégrer physiquement les différentes couches et de diviser les unités géologiques et les unités hydrostratigraphiques, comme cela a été réalisé au chapitre 5. Les modèles numériques tridimensionnels sont encore inégalés dans leur capacité à intégrer des phénomènes régionaux, comme l'écoulement de l'eau souterraine et les panaches thermiques, ainsi que les effets de la saignée pour des systèmes à plusieurs PCP [27, 53, 60]. Ces modèles sont donc utiles pour la conception détaillée d'un système et pour la recherche scientifique.

Pour représenter l'hétérogénéité en couches, Robert et al. (2022) [27] ont démontré qu'utiliser un modèle numérique tridimensionnel permet de reproduire des données expérimentales avec

justesse. En effet, les auteurs ont reproduit un ERT d'une durée de 6,5 jours avec un MAE d'une valeur de seulement 0,04 °C. Dans le chapitre 5, le même ERT a été interprété dans un cadre bayésien en considérant uniquement la phase de chauffage, qui correspond aux 3,5 premiers jours de l'essai, et en utilisant un réseau de neurones artificiel (RNA) émulant un modèle axisymétrique. Le modèle axisymétrique a été choisi pour diminuer de plus de cinq fois le temps de calcul par rapport à un modèle numérique tridimensionnel, permettant ainsi la construction d'un RNA dans un temps réaliste d'environ trois semaines. Dans le cadre de l'interprétation stochastique de cet ERT, il a été possible d'inférer des propriétés hydrauliques et thermiques avec une précision sous 18%, tout en reproduisant les températures observées avec des valeurs de MAE se situant entre 0,03 et 0,10 °C. Il est donc évident que la modélisation numérique assure une représentation juste et précise du milieu hydrostratigraphique.

D'ailleurs, les précisions de 7% à 18% rapportées au chapitre 5 pour les propriétés hydrauliques inférées sont exceptionnelles, considérant que l'interprétation a été réalisée à partir de données de températures uniquement. À cet effet, il est crucial de mentionner que le PCP étudié sur le site de Mirabel au chapitre 5 est situé dans un contexte hydrostratigraphique de haute conductivité hydraulique. En fait, Robert et al. (2022) [27] ont déterminé que l'advection contribue 265 fois plus que la conduction dans ce PCP et, également, que l'interprétation du ERT susmentionné à l'aide de l'approximation de premier ordre de la SLI a donné une conductivité thermique de 70 W/mK, soit une valeur irréaliste pour une roche. Ceci illustre donc l'importance des propriétés hydrauliques de ce site et explique en partie le niveau de précision obtenu par les résultats de l'interprétation dans un cadre bayésien présenté au chapitre 5. Dans un contexte hydrostratigraphique où la contribution de l'advection est plus faible que celle rapportée autour du PCP à Mirabel, la sensibilité du modèle aux propriétés hydrauliques pourrait être inférieure. De plus, le PCP mis à l'essai sur le site de Mirabel atteint une faible profondeur d'environ 130 m. Étant donné que les PCP tirent avantage d'être forés profondément pour augmenter la surface de contact et donc le transfert conductif, la précision des propriétés hydrauliques pourrait également diminuer pour des puits plus profonds. Il serait pertinent de vérifier l'incertitude des propriétés thermiques et hydrauliques ceinturant un PCP dans un contexte de faible conductivité hydraulique et dans pour des PCP plus profonds. Une telle étude pourrait également évaluer la précision des propriétés pour différents débits de pompage et de saignées.

Il est important de rappeler que le RNA entraîné au chapitre 5 n'est pas généralisable en dehors des conditions du site de Mirabel, c'est-à-dire aux profondeurs définies par le modèle conceptuel hydrostratigraphique, ainsi qu'aux dimensions du PCP et de son tubage. De plus, le RNA est restreint au débit de pompage constant utilisé lors de l'ERT de Robert et al. (2022) [27], ce qui ne permet pas de reproduire l'effet d'une saignée. En utilisant

une architecture à perceptron multicouche à propagation avant, il a nécessité une base de données de 29 500 simulations pour entraîner le RNA, soit plus de trois semaines de calculs sans interruption. Pour généraliser le RNA en conservant la même architecture et la même méthode d'entraînement, la base de données devrait être augmentée d'au moins un ordre de grandeur, voire davantage, en fonction de la complexité souhaitée et de la sensibilité du modèle aux nouvelles variables. En fait, Rose et al. (2025) [203] ont récemment présenté une nouvelle méthodologie permettant d'entraîner un RNA utilisant 37 propriétés d'entrée (incluant le débit de circulation, l'épaisseur des unités hydrostratigraphiques et la vitesse d'écoulement de l'eau souterraine), afin de simuler la température à la sortie d'un puits en boucle fermée. Cette méthode, qui utilise une décomposition par ondelettes, pourrait offrir une solution intéressante pour les PCP. Une autre façon de réduire le problème consiste à utiliser deux modèles distincts pour simuler la réponse à court terme et à long terme, puis à les coupler [204–206]. Par exemple, un RNA entraîné uniquement sur des données à court terme pourrait être combiné à la réponse à long terme du modèle analytique β-ILS. En effet, les résultats de la validation expérimentale du chapitre 4 ont montré que le modèle analytique avait tendance à moins bien reproduire la réponse à court terme, tandis que les modèles numériques permettent généralement de simuler aussi bien la réponse à court et à long terme [27, 40].

Pour approfondir l'analyse de la précision des modèles numériques, les fonctions de transfert simulées numériquement dans l'article du chapitre 6, à l'aide de propriétés conjointes tirées des résultats du chapitre 5, sont réutilisées dans une convolution non stationnaire afin de reproduire les températures observées lors de l'essai de réinjection entre puits. La Figure 7.1 montre les signaux de température reconstruits.

Il convient de rappeler que ces fonctions de transfert ont été réalisées à l'aide d'un modèle tridimensionnel incluant les cinq puits du système de Mirabel et simulant ainsi la dynamique thermique et hydraulique entre les différents PCP, ce qui est primordial pour le fonctionnement de la réinjection entre puits. Premièrement, l'analyse des températures simulées présentées dans la Figure 7.1, soit les signaux contenus dans l'enveloppe colorée, a permis d'estimer le MAE moyen à 0,17 °C, avec le meilleur cas affichant un MAE de 0,12 °C et le pire cas de 0,24 °C. Il est possible de constater des erreurs maximales allant jusqu'à près de 1 °C dans le pire des cas. Ces erreurs démontrent la justesse et la précision du modèle dans un contexte d'incertitudes géologiques. Rappelons que les propriétés inférées au chapitre 5 sont issues d'un essai sans opération de la saignée pour un seul PCP.

En somme, les modèles numériques restent le type de modèle le plus exact pour reproduire la réponse thermique d'un PCP et sont donc essentiels pour effectuer de la conception détaillée

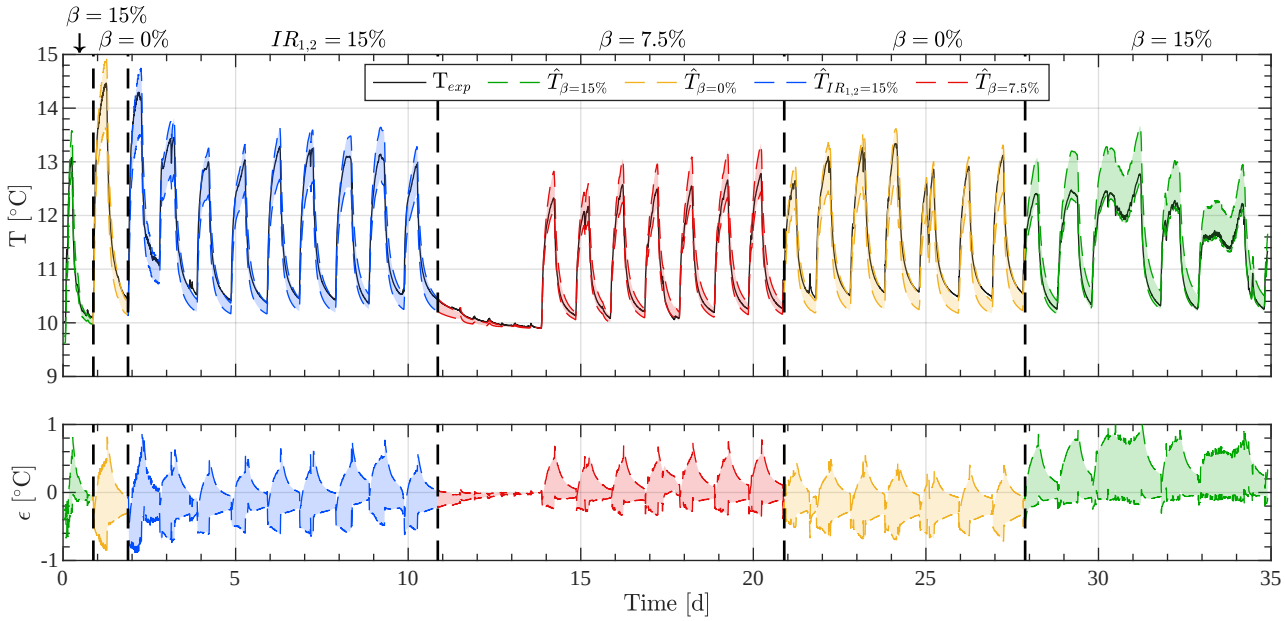

FIGURE 7.1 Comparaison des températures mesurées lors de l'essai de réinjection entre puits (ligne pleine noire) avec les températures simulées numériquement en utilisant les distributions conjointes des propriétés thermiques et hydrauliques (enveloppe colorée). Haut : comparaison des températures ; Bas : résidus entre les températures.

et faire progresser la science dans ce domaine. La méthodologie d'inférence bayésienne de propriétés a permis d'estimer avec précision des propriétés hydrauliques à partir d'un essai thermique seulement, dans un contexte où la contribution de l'advection thermique domine largement le transfert de chaleur. Toutefois, dans des contextes hydrostratigraphiques de conductivité hydraulique plus faible ou pour des puits plus profonds, le degré de précision obtenu par cette méthode ne peut être assuré et devrait donc faire l'objet d'une étude spécifique. L'utilisation des propriétés inférées au chapitre 5 pour simuler l'essai de réinjection entre puits réalisé au chapitre 6 a permis de démontrer que la modélisation numérique des PCP dans un contexte d'hétérogénéité en couches permet d'obtenir des résultats justes et précis. Parmi les travaux futurs, il faudrait développer un RNA généralisé, pour éviter les longs temps de développement et de calcul.

7.3 Modèles empiriques expérimentaux obtenus par déconvolution

Comme l'explique Dion (2023) [207], la déconvolution est un outil idéal pour estimer des fonctions de transfert, soit les modèles empiriques expérimentaux, et évaluer les performances d'un système. La comparaison des fonctions de transfert, construites pour répondre à une même fonction de perturbation unitaire et constante, permet d'accéder à des métriques temporelles,

tant en régime permanent qu'en régime transitoire. Au chapitre 6, par exemple, quatre fonctions de transfert correspondant à des stratégies d'opération des PCP distinctes (réinjection entre puits, deux paliers de saignée et circulation complète) ont été obtenues expérimentalement, et ces résultats ont permis de montrer que la réinjection entre puits constitue une stratégie efficace pour accroître l'échange thermique, tout en conservant l'eau de rejet dans le système, évitant ainsi l'utilisation du puits d'injection. Ces modèles empiriques sont donc essentiels pour l'interprétation des données *in situ*, aussi bien durant les phases de caractérisation du sous-sol que lors de la mise en service et du suivi des performances.

Le développement de ces modèles empiriques implique de mettre à l'essai chaque mode d'opération pour lequel on souhaite connaître la fonction de transfert. Par exemple, pour l'analyse présentée dans la Figure 7.2 qui comprend 17 fonctions de transfert, il faudrait expérimenter toutes les stratégies de réinjection présentées pour obtenir les modèles empiriques, ce qui nécessiterait plusieurs mois d'essais en utilisant le même protocole que celui décrit au chapitre 6. Sans cet effort, ce type de modèle n'est donc pas adapté aux études paramétriques.

Les simulations réalisées avec les fonctions de transfert obtenues par des algorithmes de déconvolution, basé sur des algorithmes d'optimisation contrainte par plusieurs critères [62, 63, 98], présentent généralement des résidus très faibles. En effet, Dion et al. (2023) [63] ont rapporté des erreurs, exprimées sous forme de racine de l'erreur quadrique (RMSE), inférieures à 0,07 °C, tandis que la valeur du RMSE rapportée au chapitre 6 était de 0,04 °C. En fait, la qualité de la fonction de transfert dépend de la stabilité des débits durant la période étudiée. Des activités anthropiques ou des effets ambiants peuvent également fausser les données et mener à des statistiques d'ajustement bien moins bonnes.

Au chapitre 6, chaque fonction de transfert déconvoluée a utilisé 30 noeuds, soit 120 noeuds à optimiser pour les quatre fonctions. Des solutions de départ ont été fournies à l'algorithme d'optimisation TSO en déplaçant aléatoirement la solution initiale issue de la première déconvolution d'un facteur de dix vers le haut ou vers le bas, tout en excluant les valeurs négatives. Dans tous les cas, l'algorithme TSO a trouvé des fonctions de transfert similaires et, surtout, convergé vers une solution. Ce dernier constat est important, puisque Dion (2023) [207] indiquait que son algorithme, couplé à l'optimisation par gradient conjugué, pouvait ne pas converger selon la définition de l'espace des variables, notamment en fonction des contraintes et des bornes choisies.

Pour interpréter les ERT, les algorithmes de déconvolution permettent non seulement de déduire plus aisément les propriétés d'un modèle souhaité [98, 207], mais aussi d'apprécier le comportement thermique du PCP en régime transitoire et permanent. Un ERT réalisé à plusieurs débits de pompage et de réinjection permet d'étudier plusieurs fonctions de transfert.

Cela permet alors de calibrer un modèle plus adéquatement, mais cela pourrait également offrir la possibilité de créer une surface de fonctions de transfert par interpolation, comme Nguyen et Pasquier (2021) [202] le proposent pour les PBF. Une surface de fonctions de transfert permet ensuite d'interpoler des fonctions pour des débits qui n'ont pas été testés. Bien entendu, la précision de cette surface varie en fonction du nombre d'états (couple de débits de pompage et réinjection) qui auront été testés durant l'ERT, et de leur exactitude.

L'utilisation de modèles empiriques expérimentaux pour des stratégies d'opération avancées des PCP, telles que la réinjection entre puits, peut contribuer au calibrage des modèles numériques, comme susmentionné. Effectivement, la comparaison présentée au chapitre 6 a montré que, plus le ratio de saignée était élevé, plus la justesse du modèle numérique était réduite par rapport aux modèles empiriques expérimentaux, les propriétés inférées étant issues d'un essai sans saignée (résultats du chapitre 5). Alors, au chapitre 6, une recommandation importante, déduite grâce à l'utilisation de modèles empiriques, est qu'un ERT sur un PCP devrait inclure des paliers de saignée, afin d'augmenter la justesse des propriétés obtenues par interprétation.

Pour mettre en valeur l'importance des modèles empiriques expérimentaux pour calibrer un modèle, une analyse comparative des différentes stratégies de réinjection entre puits est réalisée à l'aide du modèle numérique tridimensionnel présenté au chapitre 6. La calibration du modèle est alors réalisée à l'aide des propriétés thermiques et hydrauliques conjointes ayant produit la valeur de MAE la plus faible entre les fonctions de transfert expérimentales et numériques présentées au chapitre 6. Pour comparer les stratégies d'opération présentées au chapitre 6 à des stratégies alternatives, des simulations numériques sont réalisées afin de produire les fonctions de transfert présentées sur la Figure 7.2. Ces fonctions couvrent des stratégies de réinjection entre puits pour trois débits totaux de saignée distincts, y compris celui testé dans l'article du chapitre 6. Les stratégies sont décrites par l'équation $IR_i = \beta$, où les indices i désignent les PCP recevant l'eau souterraine déchargée et β le ratio du débit de pompage en rejet. Rappelons qu'à Mirabel, cinq PCP sont espacés d'environ 6 m sur une ligne quasi perpendiculaire au gradient hydraulique.

L'analyse de la Figure 7.2 montre que, pour un débit de saignée de 15%, la réinjection entre puits depuis quatre puits vers un seul récepteur ($IR_1 = 15\%$ et $IR_3 = 15\%$) permet de réduire l'interférence thermique entre les PCP plus efficacement que dans le cas testé expérimentalement ($IR_{12} = 15\%$). De plus, la position centrale du puits récepteur permet d'atteindre une efficacité de transfert thermique supérieure ($IR_3 = 15\%$) par rapport aux puits situés en bordure ($IR_1 = 15\%$). Ce phénomène peut être attribué à un transfert de chaleur advectif accru provenant du puits voisin, ce qui atténue la baisse de température.

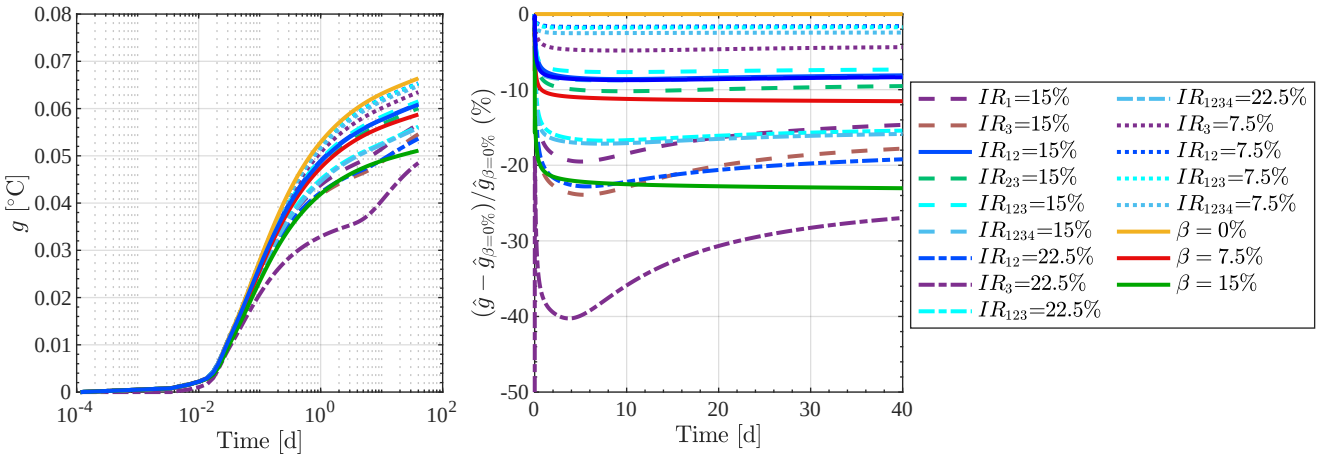

FIGURE 7.2 Comparaison des fonctions de transfert pour les quatre stratégies de réinjection présentées dans l'article (lignes pleines) et pour des stratégies additionnelles variant selon le ratio total de saignée β ainsi que le nombre et la position des PCP recevant la saignée (lignes pointillées) ; Gauche : fonctions de transfert ; Droite : différences relatives entre les stratégies de réinjection et la recirculation complète.

En fait, la stratégie la plus efficace, représentée par $IR_3 = 22{,}5\%$, consiste à effectuer une saignée à un débit plus élevé ($\beta = 22{,}5\%$, soit 112,5 L/min) dans le puits central (PCP-3). En pratique, il est néanmoins impératif de s'assurer que l'augmentation du taux de saignée n'entraîne pas un débordement dans le puits récepteur de la réinjection, et ce, en tenant compte des variations saisonnières du niveau phréatique. Toujours à partir de la Figure 7.2, une réduction du débit de purge ($\beta = 7{,}5\%$ ou 37,5 L/min) entraîne tout de même une amélioration notable de l'efficacité du transfert de chaleur par rapport à une recirculation complète.

Ainsi, le modèle numérique validé, à l'aide des modèles empiriques expérimentaux obtenus pas déconvolution, a permis d'étudier différentes stratégies de réinjection pour le système de PCP installé au site de Mirabel. Il est toutefois crucial de mentionner qu'une étude distincte et approfondie serait nécessaire pour explorer les limites globales des stratégies de réinjection entre puits, et ce afin de réaliser de nombreuses simulations supplémentaires prenant en compte un grand nombre de facteurs. Sans s'y limiter, les facteurs à prendre en compte sont le nombre et la position des PCP, la conductivité thermique et hydraulique de différent contexte hydrostratigraphique, les débits de pompage et de réinjection, les charges thermiques au sol, la vitesse de l'eau souterraine et la porosité de l'aquifère.

Pour conclure, les modèles empiriques jouent un rôle clé dans l'interprétation des données *in situ*, tant lors des phases d'investigation (ERT) que pendant la mise en service et le suivi des performances. Les modèles empiriques permettent de reproduire un état d'opéra-

tion précis, soit un débit de pompage et de réinjection constant, ce qui indique que chaque stratégie d'opération pour laquelle un modèle empirique est désiré doit être mise à l'essai. De plus, des activités anthropiques ou des effets ambiants peuvent fausser les données collectées, entraînant ainsi des biais dans l'estimation des modèles empiriques expérimentaux par déconvolution. La comparaison entre modèles empiriques et modèles physiques offre un levier important pour calibrer des modèles et affiner les pratiques, comme l'a démontré le chapitre 6 avec la recommandation d'intégrer des paliers de saignées lors des ERT sur les PCP. Enfin, pour élargir la portée des fonctions de transfert obtenues, une approche prometteuse pourrait consister à interpoler entre plusieurs fonctions.

CHAPITRE 8 CONCLUSION

La géothermie se positionne comme une solution essentielle à l'atteinte des objectifs de décarbonation au niveau pancanadien. De surcroît, les PCP constituent un type d'échangeur de chaleur souterrain permettant d'accroître l'efficacité du transfert thermique par rapport aux puits en boucle fermée actuellement préconisés dans l'industrie, ce qui permet de réduire les coûts en réduisant la longueur d'échangeur requis. Les avantages susmentionnés des PCP s'expliquent en fait grâce à la sollicitation d'un transfert de chaleur par advection, due à leur configuration ouverte au roc et à l'opération de la saignée, qui induit un écoulement radial convergent de l'eau souterraine.

Une revue de l'état de la science concernant les PCP indique que des validations expérimentales sont nécessaires pour démontrer l'exactitude des méthodes de modélisation de la dynamique thermique et hydraulique générée par ces PCP. Les modèles se présentent sous trois catégories, à savoir les modèles analytiques, numériques et empiriques. Un seul modèle analytique simule la réponse thermique d'un PCP opérant avec une saignée, et celui-ci reproduit un milieu homogène et isotrope. Les modèles numériques offrent la plus grande justesse pour simuler la réponse thermique des PCP dans un contexte hydrostratigraphique hétérogène, mais la complexité de ces modèles et les coûts de calcul élevés en limitent l'utilisation pour l'optimisation ou dans un cadre stochastique. Finalement, les modèles empiriques expérimentaux facilitent les comparaisons entre différentes stratégies d'opération des PCP, comme la réinjection entre puits, qui s'affiche comme une solution au besoin d'utiliser des puits d'injection pour gérer l'eau générée par l'opération de la saignée. L'objectif de cette thèse est donc d'améliorer l'applicabilité, la robustesse et la précision des modèles et des stratégies d'opération des PCP, afin d'en favoriser leur utilisation dans le milieu pratique.

8.1 Synthèse des travaux

La mise en commun de trois articles de revue présentés aux chapitres 4, 5 et 6, ainsi que la discussion du chapitre 7, ont permis d'atteindre l'objectif général de cette thèse. L'analyse détaillée des modèles analytiques, numériques et empiriques a mis en évidence leurs applicabilités distinctes et leurs limites respectives, tandis que les validations et démonstrations expérimentales ont permis de clarifier leurs incertitudes et d'améliorer leurs capacités. Dans l'ordre, l'objectif spécifique 1 a été accompli par la validation expérimentale du modèle analytique simulant la variation de température d'un PCP opérant avec une saignée (voir le chapitre 4 et, également, l'annexe A pour le développement du modèle). Pour accomplir

cette validation dans un contexte *in situ*, un cadre théorique a été proposé pour estimer la température du fluide à la sortie du puits à partir du résultat du modèle analytique, soit la variation de température moyenne à la paroi de forage. Parallèlement, deux approches de calcul de propriétés effectives ont été proposées pour adapter le modèle isotrope et homogène à un contexte d'hétérogénéité en couches et pour considérer l'écoulement radial convergent induit par la dépressurisation du pompage. En utilisant ces nouvelles contributions, le modèle analytique a été validé expérimentalement avec une justesse, mesurée par une moyenne des erreurs absolues, de l'ordre de 0,28 à 0,37 °C, pour trois essais distincts de six jours présentant une grande variabilité des débits de pompage et de saignée. Ces résultats démontrent de la justesse du modèle dans des conditions réalistes incluant un contexte hydrostratigraphique hétérogène.

Pour atteindre l'objectif spécifique 2, c'est-à-dire inférer les distributions conjointes des propriétés thermiques et hydrauliques des matériaux géologiques ceinturant un PCP, l'interprétation dans un cadre bayésien d'un essai de réponse thermique a été réalisé sur des données provenant du premier site de démonstration de la Chaire (voir le chapitre 5 et, en complément, l'annexe B). Pour ce faire, un réseau de neurones artificiel conçu et entraîné spécifiquement pour cette étude a émulé un modèle numérique axisymétrique considérant l'hétérogénéité en couches. En utilisant un processus stochastique robuste prenant en compte l'autocorrélation des erreurs, l'inférence des propriétés donne accès à des distributions conjointes, soit une métrique de la précision de ces dernières. Bien que les solutions obtenues ne soient pas uniques — c'est-à-dire que différentes distributions a priori en inférence bayésienne peuvent conduire à des estimations légèrement différentes —les précisions identifiées pour les différentes propriétés thermiques et hydrauliques sont toutes inférieures à 18%. Cette robustesse des résultats, obtenus uniquement à partir des données de température, montre que le modèle fournit des estimations précises malgré la non-unicité inhérente au problème. La connaissance des incertitudes liées aux propriétés géologiques est un atout significatif pour le dimensionnement d'un échangeur de chaleur souterrain.

Pour l'objectif spécifique 3, l'efficacité de la réinjection entre puits, soit une stratégie innovante d'opération d'un système de PCP permettant de conserver l'eau de saignée dans le système, a été démontrée par la comparaison de fonctions de transfert expérimentales obtenues par la déconvolution de données provenant d'un essai *in situ* de 35 jours (chapitre 6 et, en complément, annexe C). L'analyse de ces fonctions de transfert a démontré que la stratégie de réinjection testée offre une meilleure résilience face aux perturbations thermiques que la simple recirculation complète (soit un gain d'efficacité d'environ 10% dans le contexte expérimental présenté) bien qu'elle soit moins performante qu'une opération de saignée seule. Par conséquent, la réinjection entre puits s'avère être une solution efficace pour se libérer de

l'obligation d'utiliser des puits d'injection. L'utilisation des modèles empiriques expérimentaux pour simuler les températures observées a démontré une justesse élevée de 0,04 °C. De plus, une comparaison a été réalisée entre les modèles empiriques expérimentaux et les fonctions de transfert numériques générées à partir d'un modèle numérique tridimensionnel utilisant les propriétés conjointes estimées dans le cadre de l'objectif spécifique précédent. Cette comparaison a permis de tirer des conclusions importantes sur l'exactitude des distributions conjointes obtenues d'un ERT sans saignée et, aussi, de discuter des limites et avantages des modèles empiriques et numériques.

8.2 Contributions originales

La contribution principale de ce document concerne les avancements proposés pour simuler et opérer les PCP, ainsi que l'analyse et la comparaison des différents modèles disponibles pour simuler les PCP. La validation des modèles dans des contextes expérimentaux hétérogènes démontrent sans équivoque leur justesse. La présentation des avantages et des limites de chacun met en évidence leurs utilités distinctes pour concevoir, analyser et suivre le comportement hydraulique et thermique des PCP.

La validation expérimentale du modèle analytique a mené au développement d'approches novatrices pour les propriétés effectives et la dynamique à l'intérieur du puits, en développant un cadre théorique qui considère la saignée. Une méthode prenant en compte le point de balance dans un contexte hydrostratigraphique d'hétérogénéité en couches a également été proposée, ce qui était auparavant réservé aux milieux homogènes [27, 38]. Ainsi, le modèle analytique a été validé expérimentalement pour la première fois et, par sa rapidité de calcul incontestable, ce modèle a le potentiel d'accélérer le déploiement à grande échelle des PCP.

L'interprétation dans un cadre bayésien d'un essai de réponse thermique sur un PCP a permis d'extraire des propriétés hydrauliques et thermiques avec de faibles incertitudes et une justesse approchant celle du résultat d'interprétation d'un essai de pompage également réalisé sur le site. Le succès de cette méthodologie pour estimer les propriétés hydrauliques à l'aide d'un essai thermique réduit le besoin de réaliser des essais supplémentaires pour caractériser l'hétérogénéité des couches. Par ailleurs, l'obtention de l'incertitude des propriétés a le potentiel de diminuer les risques lors du dimensionnement. De plus, un premier réseau de neurones artificiel émulant un modèle numérique pour un PCP a été développé et utilisé avec succès, marquant une première étape vers la généralisation de ce type d'émulateur.

La démonstration de l'efficacité de la réinjection entre puits a révélée que cette stratégie d'opération pouvait offrir des performances accrues, même si celles-ci restent inférieures à

une saignée complète de tous les PCP. L'essai réalisé sur une période ininterrompue de 35 jours constitue un premier jeu de données comparant différentes stratégies de réinjection sur un véritable bâtiment en fonctionnement. La comparaison des solutions numériques avec les solutions expérimentales a permis de déduire qu'un ERT devrait inclure des paliers de saignée afin d'augmenter l'exactitude des propriétés thermiques et hydrauliques inférées.

8.3 Avenues de recherche

Le modèle analytique, discuté au chapitre 4, a été validé expérimentalement dans cette thèse. Les limites du modèles ont été discuté ouvertement, mettant ainsi en évidence plusieurs pistes de travaux futurs :

- Extension du modèle analytique à la simulation de rayons plus grands que celui du puits, et démonstration de son utilisation pour la superposition spatiale ;
- Ajustement de la formulation pour calculer la température du fluide à la sortie de PCP en utilisant une hypothèse de flux de chaleur variable plutôt que constant ;
- Répéter le développement du modèle β-SLI avec des modèles de conduction plus sophistiqués, tels que la SCI ou la SLF.

En fait, ces propositions mènent à soit augmenter la précision du modèle ou augmenter sa portée. Il est important de souligner que la validation expérimentale du chapitre 4 a été réalisée dans un contexte hydrostratigraphique de faible conductivité hydraulique. Malgré le succès de la validation, une validation expérimentale dans un milieu à forte conductivité hydraulique permettrait de renforcer la confiance envers le modèle. Cependant, la variable de la conductivité hydraulique de l'eau utilisée dans les modèles numériques pourrait rendre difficile cette validation. Ainsi, plutôt qu'une validation, il pourrait s'agir d'une démonstration de la puissance du modèle lorsqu'utilisé pour interpréter des données dans un cadre d'inversion des propriétés utilisant une algorithme d'optimisation heuristique.

À l'inverse, l'inférence bayésienne des propriétés présentée au chapitre 5 a été réalisée dans un contexte hydrostratigraphique avec une conductivité hydraulique d'aquifère élevé, où l'advection joue un rôle plus important que la conduction. Il serait donc intéressant de répéter l'expérience dans un contexte de basse conductivité hydraulique afin de valider la capacité de la méthode présentée à inférer des propriétés avec précision lorsque la composante advective est plus faible. Dans une perspective similaire, cette validation pourrait inclure des essais réalisés sur des PCP plus profonds, sachant que des profondeurs allant jusqu'à 670 m ont été rapportées. En revanche, le réseau neuronal spécifique au site de Mirabel ne pourrait pas être utilisé et il faudrait donc :

- Développer un réseau de neurones artificiel généralisé pour les PCP dans différents

contextes hydrostratigraphiques en considérant l'hétérogénéité, et pour plusieurs débits de pompage et de saignée ; ou
- Utiliser plutôt le modèle analytique β-SLI.

Finalement, l'efficacité de la réinjection entre puits a été démontrée au travers d'un essai de 35 jours sur un site donné, soit celui de Mirabel possédant une composante advective dominante. Pour que les meilleures pratiques de la réinjection entre puits soient déterminées, une étude plus vaste doit être réalisée. Il pourrait, par exemple, s'agir d'une étude paramétrique à l'aide d'un modèle numérique vérifiant l'efficacité de cette méthode dans divers contextes hydrostratigraphiques. Celle-ci pourrait alors étudier l'effet de différentes variables, telles que :

- le nombre de PCP et leurs espacements ;
- les débits de pompage et de réinjection ;
- la stratégie de réinjection (le nombre de puits en pompage et en réinjection et leur position) ;
- l'agencement des PCP sur le site (par exemple : sur une ligne, formant un carré, ou une forme de U) et leur position par rapport au gradient régional ; et
- l'utilisation d'un ou plusieurs puits d'injection dans certaines stratégies.

Sur cette base, l'intégration de la réinjection entre puits dans le cadre d'un contrôle efficace des PCP serait plus évidente. La gestion des débits de pompage, de saignée et de réinjection serait alors un enjeu d'optimisation pour opérer le système dans ses limites d'utilisation et minimiser les coûts d'opération.

En conclusion, l'exactitude et les limites des modèles analytiques, numériques et empiriques présentées dans cette thèses ont permises de cadrer leurs utilisations pour différentes étapes et besoins de projets. Ces nouveaux outils pourront maintenant être utilisés par les praticiens afin de simuler, caractériser, concevoir et suivre les performances des PCP, contribuant ainsi indirectement à la lutte contre les gaz à effet de serre et à la décarbonation du parc immobilier.

RÉFÉRENCES

[1] Nations Unies, “Accord de Paris,” dans *21ème Conférence des Parties*, 2015.

[2] Carbon Neutrality Coalition, “Framework for net zero climate action,” dans *UNFCCC Global Stocktake - Technical Dialogue 3 (SB 58)*, Bonn, Germany, 2023.

[3] Environment and Climate Change Canada, “Federal sustainable development strategy 2022 to 2026 : Achieving a sustainable future,” Gouvernement du Canada, 2022.

[4] S. Langlois-Bertrand et N. Mousseau, “L’état de l’énergie et des émissions de GES au Canada,” dans *Perspectives énergétiques canadiennes 3e édition.* Institut de l’énergie Trottier – Polytechnique Montréal, 2024.

[5] S. Langlois-Bertrand, N. Mousseau, K. Vaillancourt et M. Bourque, “Trajectoires pour un Canada carboneutre – Horizon 2060.” dans *Perspectives énergétiques canadiennes 3e édition.* Institut de l’énergie Trottier – Polytechnique Montréal, 2024.

[6] IEA, “Renewables 2022 - Analysis and forecast to 2027,” International Energy Agency Publications, Paris, France, Rapport technique, 2023.

[7] K. Bédard, F.-A. Comeau, J. Raymond, M. Malo et M. Nasr, “Geothermal characterization of the St. Lawrence lowlands sedimentary basin, Québec, Canada,” *Natural Resources Research*, vol. 27, n°. 4, p. 479–502, 2018.

[8] J. Majorowicz et V. Minea, “Geothermal energy potential in low enthalpy areas as a future energy resource : Identifying feasible targets, Quebec, Canada, Study case,” *Resources*, vol. 4, n°. 3, p. 524–547, 2015.

[9] D. Saner, R. Juraske, M. Kübert, P. Blum, S. Hellweg et P. Bayer, “Is it only CO2 that matters ? A life cycle perspective on shallow geothermal systems,” *Renewable and Sustainable Energy Reviews*, vol. 14, n°. 7, p. 1798–1813, 2010.

[10] D. Menegazzo, G. Lombardo, S. Bobbo, M. D. Carli et L. Fedele, “State of the art, perspective and obstacles of ground-source heat pump technology in the european building sector : A review,” *Energies*, vol. 15, n°. 7, p. 2685, 2022.

[11] P. Cui, W. Yang, W. Zhang, K. Zhu, J. D. Spitler et M. Yu, “Advances in ground heat exchangers for space heating and cooling : Review and perspectives,” *Energy and Built Environment*, vol. 5, n°. 2, p. 255–269, 2024.

[12] D. Tanguay, “État de l’industrie canadienne de la géothermie 2010 - Analyse du marché et enquête de l’industrie,” Coalition canadienne de l’énergie géothermique, Montréal, Québec, Rapport technique, 2010.

[13] I. Sarbu et C. Sebarchievici, “General review of ground-source heat pump systems for heating and cooling of buildings,” *Energy and Buildings*, vol. 70, p. 441–454, 2014.

[14] A. Nguyen, G. Beaudry et P. Pasquier, “Experimental assessment of a standing column well performance in cold climates,” *Energy and Buildings*, vol. 226, p. 110391, 2020.

[15] D. Penner, “YVR digs deep with geoexchange to help meet emission-reduction goals,” Vancouver Sun, 2019. [En ligne]. Disponible : https://vancouversun.com/news/local-news/yvr-digs-deep-with-geoexchange-to-help-meet-emission-reduction-goals

[16] S. Richter, K. Lubashevsky, J. Randow, S. Henker, J. Buchwald et A. Bucher, “Global sensitivity analysis and uncertainty quantification for design parameters of shallow geothermal systems,” *Geothermal Energy*, vol. 12, n°. 8, 2024.

[17] G. Beaudry, J. Faucher, G. Tonellato, P. Pasquier et M. Kummert, “Standing column wells in cold climates : lessons learned after one year of operating a demonstration system in Canada,” dans *Proceedings of the IGSHPA Research Track 2024*, Montréal, Québec, Canada, 2024.

[18] M. A. Bernier, “Closed-loop ground-coupled heat pump systems,” *ASHRAE Journal*, vol. 48, n°. 9, p. 12–19, 2006.

[19] D. Banks, “A review of the importance of regional groundwater advection for ground heat exchange,” *Environmental Earth Sciences*, vol. 73, p. 2555–2565, 2015.

[20] H. Javadi, S. S. M. Ajarostaghi, M. A. Rosen et M. Pourfallah, “Performance of ground heat exchangers : A comprehensive review of recent advances,” *Energy*, vol. 178, p. 207–233, 2019.

[21] C. D. Orio, A. Chiasson, C. N. Johnson, Z. Deng, S. J. Rees et J. D. Spitler, “A Survey of Standing Column Well Installations in North America,” *ASHRAE Transactions : Research*, vol. 111, n°. 2, p. 109–121, 2005.

[22] P. Pasquier, A. Nguyen, F. Eppner, D. Marcotte et P. Baudron, “10 - Standing column wells,” dans *Advances in Ground-Source Heat Pump Systems*, S. J. Rees, édit. Elsevier, 2016, p. 269–294.

[23] P.W. Grosser, “PWGC designs geothermal system for St. Patrick’s Cathedral - P.W. Grosser,” P.W. Grosser Consulting, Inc., 2017. [En ligne]. Disponible : https://pwgrosser.com/blog/geothermal-system-st-patricks-cathedral/

[24] C. A. Martin et S. P. Kavanaugh, “Ground thermal conductivity testing–controlled site analysis,” *ASHRAE Transactions : Symposia*, vol. 108, p. 945–952, 2002.

[25] G. Beaudry, P. Pasquier, D. Marcotte et A. Zarrella, “Flow rate control in standing column wells : A flexible solution for reducing the energy use and peak power demand

of the built environment," *Applied Energy*, vol. 313, p. 118774, 2022.

[26] J. D. Spitler, S. J. Rees, Z. Deng, A. Chiasson, C. D. Orio et C. Johnson, "R&D studies applied to standing column well design," *ASHRAE research project*, 2002.

[27] S. Robert, P. Pasquier et A. Nguyen, "Impact of layered heterogeneity on thermal response test interpretation performed on a standing column well operated without bleed," *Geothermics*, vol. 101, p. 102353, 2022.

[28] A. Nguyen, P. Pasquier et D. Marcotte, "Thermal resistance and capacity model for standing column wells operating under a bleed control," *Renewable Energy*, vol. 76, p. 743–756, 2015.

[29] Z. O'Neill, J. Spitler et S. Rees, "Performance analysis of standing column well ground heat exchanger systems," *ASHRAE Transactions*, vol. 112, p. 633–643, 2006.

[30] J. M. FAIA, "St. Patrick's Cathedral, New York, New York," HPB Magazine, 2019. [En ligne]. Disponible : https://www.hpbmagazine.org/st-patricks-cathedral-new-york-new-york/

[31] P.W. Grosser, "Geothermal System for St. Patrick's Cathedral - P.W. Grosser," P.W. Grosser Consulting, Inc., 2017. [En ligne]. Disponible : https://pwgrosser.com/projects/geothermal-system-st-patricks-cathedral/

[32] New York City Departement of Design and Construction, "Geothermal heat pump manuel - A design and installation guide for the New York City," New York City Departement of Design and Construction – Office of Sustainable Design, Long Island City, New York, Guide, 2013.

[33] C. D. Orio, "Geothermal heat pumps and standing column wells," *Geothermal Resources Council Transactions*, vol. 18, p. 375–379, 1994.

[34] H. J. Braud, H. Klimkowski et J. Oliver, "Earth-source heat exchanger for heat pumps," *Transactions of the American Society of Agricultural Engineers*, p. 1818–1822, 1983.

[35] C. D. Orio, C. N. Johnson et K. D. Poor, "Geothermal standing column wells : Ten years in a New England school," *ASHRAE Transactions*, vol. 112, n°. 2, p. 57–64, 2006.

[36] C. D. Orio et Z. J. Patnaude, "Eight years of operation of 615 ton geothermal nursing home in northern tier," dans *ASHRAE 2014*, vol. 120, Seatle, 2014.

[37] Chaire de recherche en géothermie, "Objectifs de la chaire," École Polytechnique de Montréal, 2025. [En ligne]. Disponible : https://www.polymtl.ca/geothermie/

[38] G. K. Yuill et V. Mikler, "Analysis of the effect of induced groundwater flow on heat transfer from a vertical open-hole concentric-tube thermal well," dans *ASHRAE transactions 1995*, Chicago, 1995, p. 173–185.

[39] J.-S. Jeon, S.-R. Lee et W.-J. Kim, “Applicability of thermal response tests in designing standing column well system : A numerical study,” *Energy*, vol. 109, p. 679–693, 2016.

[40] G. Beaudry, P. Pasquier et D. Marcotte, “The impact of rock fracturing and pump intake location on the thermal recovery of a standing column well : model development, experimental validation, and numerical analysis,” *Science and Technology for the Built Environment*, vol. 25, n°. 8, p. 1052–1068, 2019.

[41] L. Ingersoll et H. Plass, “Theory of the ground pipe heat source for the heat pump.” *Heating, Piping and Conditioning*, vol. 20, n°. 7, p. 119–122, 1948.

[42] H. S. Carslaw et J. C. Jaeger, *Conduction of heat in solids.* Oxford : Clarendon Press, 1959.

[43] K. Woods et A. Ortega, “The thermal response of an infinite line of open loop wells for ground coupled heat pump systems,” *International Journal of Heat and Mass Transfer*, vol. 54, n°. 25–26, p. 5574–5587, 2011.

[44] J. R. Kastrinos, A. Chiasson et P. Ormond, “Estimating groundwater heat exchange in a standing-column well by injection of a bromide tracer,” *Geothermics*, vol. 82, p. 121–127, 2019.

[45] A. Nguyen, L. Jacques et P. Pasquier, “An easy-to-use analytical model for standing column wells operating with bleed,” *Applied Thermal Engineering*, vol. 258, p. 124543, 2025.

[46] D. Thiéry, “Simple approximate closed-form expressions for tracer injection in aquifer with a radially converging or diverging flow field,” *Journal of Hydrology*, vol. 608, p. 127661, 2022.

[47] Z. Deng, “Modeling of standing column wells in ground source heat pump systems,” Thèse de Doctorat, Oklahoma State University, Stillwater, OK, USA, 2004.

[48] E. Abu-Nada, B. Akash, I. Al-Hinti, A. Al-Sarkhi, S. Nijmeh, A. Ibrahim et A. Shishan, “Modeling of a geothermal standing column well,” *International Journal of Energy Research*, vol. 32, n°. 4, p. 306–317, 2008.

[49] B. M. Ng, “Numerical modelling of multiple standing column wells applied to geothermal heating and cooling in UK buildings,” Thèse de doctorat, University of Northumbria, Newcastle upon Tyne, England, 2011.

[50] J. E. Croteau, “Évaluation des paramètres influençant les températures d’opération des puits à colonne permanente,” Mémoire de maîtrise ès sciences appliquées, École Polytechnique de Montréal, Montréal, QC, Canada, 2011.

[51] A. Nguyen, P. Pasquier et D. Marcotte, “Influence of groundwater flow in fractured aquifers on standing column wells performance,” *Geothermics*, vol. 58, p. 39–48, 2015.

[52] L. Champagne-Péladeau, P. Pasquier, D. Millette et J. C. Dupuis, “Delineation of the thermal plume associated with a standing column well system in a fractured aquifer using numerical modeling,” *Geothermics*, vol. 127, p. 103260, 2025.

[53] V. Laroche, P. Pasquier et B. Courcelles, “Integration of standing column wells in urban context : A numerical investigation-case in the City of Montreal,” *Sustainable Cities and Society*, vol. 78, p. 103513, 2022.

[54] F. Eppner, P. Pasquier et P. Baudron, “A coupled thermo-hydro-geochemical model for standing column well subject to CO2 degassing and installed in fractured calcareous aquifers,” *Geomechanics for Energy and the Environment*, vol. 11, p. 14–27, 2017.

[55] L. Cerclet, B. Courcelles et P. Pasquier, “Reactive transport model predicting calcite precipitation : Case of a dynamically operated standing column well,” *Geothermics*, vol. 115, p. 102828, 2023.

[56] C. Yavuzturk et J. D. Spitler, “A short time step response factor model for vertical ground loop heat exchangers,” *ASHRAE Transactions*, vol. 105, n°. 2, p. 475–485, 1999.

[57] M. A. Bernier, “Ground-coupled heat pump system simulation,” *ASHRAE Transactions*, vol. 107, n°. 1, p. 605–616, 2001.

[58] L. Lamarche, “A fast algorithm for the hourly simulations of ground-source heat pumps using arbitrary response factors,” *Renewable Energy*, vol. 34, n°. 10, p. 2252–2258, 2009.

[59] D. Marcotte et P. Pasquier, “Fast fluid and ground temperature computation for geothermal ground-loop heat exchanger systems,” *Geothermics*, vol. 37, n°. 6, p. 651–665, 2008.

[60] G. Beaudry, P. Pasquier et D. Marcotte, “A fast convolution-based method to simulate time-varying flow rates in closed-loop and standing column well ground heat exchangers,” *Renewable Energy*, vol. 174, p. 55–72, 2021.

[61] G. Beaudry, P. Pasquier et A. Nguyen, “New formulations and experimental validation of non-stationary convolutions for the fast simulation of time-variant flowrates in ground heat exchangers,” *Science and Technology for the Built Environment*, vol. 30, n°. 3, p. 208—-219, 2023.

[62] G. Dion, P. Pasquier et D. Marcotte, “Deconvolution of experimental thermal response test data to recover short-term g-function,” *Geothermics*, vol. 100, p. 102302, 2022.

[63] G. Dion, P. Pasquier, D. Marcotte et G. Beaudry, “Multi-deconvolution in non-stationary conditions applied to experimental thermal response test analysis to obtain

short-term transfer functions," *Science and Technology for the Built Environment*, vol. 30, n°. 3, p. 220–233, 2023.

[64] G. Dion, P. Pasquier et D. Marcotte, "Application of deconvolution to interpretation of distributed thermal response test (DTRT) and to determination of thermal conductivity profiles," *Applied Thermal Engineering*, vol. 236, p. 121680, 2024.

[65] R. B. Roka, A. J. P. d. Figueiredo, A. M. C. P. Vieira et J. C. d. P. Cardoso, "A systematic review on shallow geothermal energy system : a light into six major barriers," *Soils and Rocks*, vol. 46, n°. 1, p. e2023007622, 2022.

[66] ANSI/CSA/IGSHPA, "C448 series-16 : Design and installation of ground source heat pump systems for commercial and residential buildings (r2021)," CSA, Norme SKU : 2423716, 2016.

[67] Z. Deng, S. J. Rees et J. D. Spitler, "A model for annual simulation of standing column well ground heat exchangers," *HVAC&R Research*, vol. 11, n°. 4, p. 637–655, 2005.

[68] B. M. Ng, C. P. Underwood et S. L. Walker, "Standing column wells—Modeling the potential for applications in geothermal heating and cooling," *HVAC&R Research*, vol. 17, n°. 6, p. 1089–1100, 2011.

[69] C. V. Theis, "The relation between the lowering of the Piezometric surface and the rate and duration of discharge of a well using ground-water storage," *Eos, Transactions American Geophysical Union*, vol. 16, n°. 2, p. 519–524, 1935.

[70] J. D. Spitler et S. E. Gehlin, "Thermal response testing for ground source heat pump systems—An historical review," *Renewable and Sustainable Energy Reviews*, vol. 50, p. 1125–1137, 2015.

[71] X. Zhang, Z. Han, Q. Ji, H. Zhang et X. Li, "Thermal response tests for the identification of soil thermal parameters : A review," *Renewable Energy*, vol. 173, p. 1123–1135, 2021.

[72] P. Mogensen, "Fluid to duct wall heat transfer in duct system heat storages," dans *Proceedings of the International Conference on Subsurface Heat Storage in Theory and Practice*. Stockholm, Sweden : Swedish Council for Building Research, 1983, p. 652–657.

[73] L. Ingersoll, O. Zobel et A. Ingersoll, *Heat Conduction with Engineering, Geological and Other Applications*. New York : McGraw-Hill, 1954.

[74] P. Eskilson, *Thermal analysis of heat extraction boreholes*. Lund : Grahns Boktryckeri AB, 1987.

[75] J. Claesson et S. Javed, “An analytical method to calculate borehole fluid temperatures for time-scales from minutes to decades,” *ASHRAE Transactions*, vol. 117, p. 279–288, 2011.

[76] P. Pasquier et D. Marcotte, “Short-term simulation of ground heat exchanger with an improved TRCM,” *Renewable Energy*, vol. 46, p. 92–99, 2012.

[77] J. Raymond, R. Therrien, L. Gosselin et R. Lefebvre, “Numerical analysis of thermal response tests with a groundwater flow and heat transfer model,” *Renewable Energy*, vol. 36, n°. 1, p. 315–324, 2011.

[78] V. Wagner, P. Bayer, M. Kübert et P. Blum, “Numerical sensitivity study of thermal response tests,” *Renewable Energy*, vol. 41, p. 245–253, 2012.

[79] J. Raymond et L. Lamarche, “Simulation of thermal response tests in a layered subsurface,” *Applied Energy*, vol. 109, p. 293–301, 2013.

[80] K. Zhou, J. Mao, Y. Li, H. Zhang et C. Li, “A numerical investigation to analyze the effect of changing ambient conditions on accurate and stable identification of thermal conductivity of ground source heat pump system using thermal response test,” *Sustainable Energy Technologies and Assessments*, vol. 46, p. 101275, 2021.

[81] H. Esen, M. Inalli, A. Sengur et M. Esen, “Performance prediction of a ground-coupled heat pump system using artificial neural networks,” *Expert Systems with Applications*, vol. 35, n°. 4, p. 1940–1948, 2008.

[82] M. K. Mudunuru, S. Karra, D. R. Harp, G. D. Guthrie et H. S. Viswanathan, “Regression-based reduced-order models to predict transient thermal output for enhanced geothermal systems,” *Geothermics*, vol. 70, p. 192–205, 2017.

[83] T. Li, Y. Gao, D. Han, F. Yang et B. Yu, “A novel POD reduced-order model based on EDFM for steady-state and transient heat transfer in fractured geothermal reservoir,” *International Journal of Heat and Mass Transfer*, vol. 146, p. 118783, 2020.

[84] P. Pasquier, A. Zarrella et R. Labib, “Application of artificial neural networks to near-instant construction of short-term g-functions,” *Applied Thermal Engineering*, vol. 143, p. 910–921, 2018.

[85] B. Dusseault et P. Pasquier, “Efficient g-function approximation with artificial neural networks for a varying number of boreholes on a regular or irregular layout,” *Science and Technology for the Built Environment*, vol. 25, n°. 8, p. 1023–1035, 2019.

[86] P. Pasquier et D. Marcotte, “Robust identification of volumetric heat capacity and analysis of thermal response tests by Bayesian inference with correlated residuals,” *Applied Energy*, vol. 261, p. 114394, 2020.

[87] B. Dusseault et P. Pasquier, “Usage of the net present value-at-risk to design ground-coupled heat pump systems under uncertain scenarios,” *Renewable Energy*, vol. 173, p. 953–971, 2021.

[88] S. Gehlin, “Thermal response test : in situ measurements of thermal properties in hard rock,” Licentiate thesis, Luleå University of Technology, Luleå, Sweden, 1998.

[89] W. A. Austin III, “Development of an in situ system for measuring ground thermal properties,” Mémoire de maîtrise ès sciences appliquées, Oklahoma State University, Stillwater, OK, USA, 1998.

[90] D. Marcotte et P. Pasquier, “On the estimation of thermal resistance in borehole thermal conductivity test,” *Renewable Energy*, vol. 33, n°. 11, p. 2407–2415, 2008.

[91] P. Pasquier, “Stochastic interpretation of thermal response test with TRT-SInterp,” *Computers & Geosciences*, vol. 75, p. 73–87, 2015.

[92] J. D. Spitler et M. Bernier, “2 - Vertical borehole ground heat exchanger design methods,” dans *Advances in Ground-Source Heat Pump Systems*, S. J. Rees, édit. Woodhead Publishing, 2016, p. 29–61.

[93] L. Lamarche, “Analytic models and effective resistances for coaxial ground heat exchangers,” *Geothermics*, vol. 97, p. 102224, 2021.

[94] V. Wagner, P. Bayer, G. Bisch, M. Kübert et P. Blum, “Hydraulic characterization of aquifers by thermal response testing : Validation by large-scale tank and field experiments,” *Water Resources Research*, vol. 50, n°. 1, p. 71–85, 2014.

[95] A. Liuzzo Scorpo, B. Nordell et S. Gehlin, “A method to estimate the hydraulic conductivity of the ground by TRT analysis,” *Groundwater*, vol. 55, n°. 1, p. 110–118, 2017.

[96] M. Antelmi, L. Alberti, A. Angelotti, S. Curnis, A. Zille et L. Colombo, “Thermal and hydrogeological aquifers characterization by coupling depth-resolved thermal response test with moving line source analysis,” *Energy Conversion and Management*, vol. 225, p. 113400, 2020.

[97] B. Zhang, K. Gu, P. Bayer, H. Qi, B. Shi, B. Wang, Y. Jiang et Q. Zhou, “Estimation of groundwater flow rate by an actively heated fiber optics based thermal response test in a grouted borehole,” *Water Resources Research*, vol. 59, n°. 1, 2023.

[98] R. A. Beier, “Deconvolution and convolution methods for thermal response tests on borehole heat exchangers,” *Geothermics*, vol. 86, p. 101786, 2020.

[99] L. Jacques, “Influence des erreurs de modèle et de mesure sur les résultats d’interprétation d’un essai de réponse thermique,” Mémoire de maîtrise ès sciences appliquées, École Polytechnique de Montréal, Montréal, QC, Canada, 2015.

[100] W. Choi, H. Kikumoto, R. Choudhary et R. Ooka, “Bayesian inference for thermal response test parameter estimation and uncertainty assessment,” *Applied Energy*, vol. 209, p. 306–321, 2018.

[101] W. Choi, K. Menberg, H. Kikumoto, Y. Heo, R. Choudhary et R. Ooka, “Bayesian inference of structural error in inverse models of thermal response tests,” *Applied Energy*, vol. 228, p. 1473–1485, 2018.

[102] H. Choi, G. Yoo, K. Lim, S. Lee et C. Lee, “Characteristic analysis of bleeding effect on standing column well (SCW) type geothermal heat exchanger,” *Journal of Central South University*, vol. 19, p. 3202–3207, 2012.

[103] G. Beaudry, P. Pasquier et D. Marcotte, “Hydrogeothermal characterization and modelling of a standing column well experimental installation,” dans *Proceedings of the IGSHPA Research Track 2018*, Stockholm, Sweden, 2018.

[104] C. Lee, “Thermal performance of a standing column well geothermal heat exchanger system using re-injection of bleeding water,” *Geothermics*, vol. 82, p. 73–80, 2019.

[105] H. J. Witte, “Error analysis of thermal response tests,” *Applied Energy*, vol. 109, p. 302–311, 2013.

[106] F. Heße, A. Comunian et S. Attinger, “What we talk about when we talk about uncertainty. Toward a unified, data-driven framework for uncertainty characterization in hydrogeology,” *Frontiers in Earth Science*, vol. 7, p. 118, 2019.

[107] W. Choi, R. Choudhary et R. Ooka, “Development of chiller-attached apparatus for accurate initial ground temperature measurement : Insights from global sensitivity analysis of thermal response tests,” *Energy and Buildings*, vol. 238, p. 110841, 2021.

[108] T. Bayes, “LII. An essay towards solving a problem in the doctrine of chances. By the late Rev. Mr. Bayes, F. R. S. communicated by Mr. Price, in a letter to John Canton, A. M. F. R. S,” *Philosophical Transactions of the Royal Society of London*, vol. 53, p. 370–418, 1763.

[109] P. C. Leube, Geiges, A. et Nowak, W., “Bayesian assessment of the expected data impact on prediction confidence in optimal sampling design,” *Water Resources Research*, vol. 48, n°. 2, 2012.

[110] S. P. Neuman, L. Xue, M. Ye et D. Lu, “Bayesian analysis of data-worth considering model and parameter uncertainties,” *Advances in Water Resources*, vol. 36, p. 75–85, 2012.

[111] L. Xue, D. Zhang, A. Guadagnini et S. P. Neuman, “Multimodel Bayesian analysis of groundwater data worth,” *Water Resources Research*, vol. 50, n°. 11, p. 8481–8496, 2014.

[112] W. Nowak et A. Guthke, “Entropy-based experimental design for optimal model discrimination in the geosciences,” *Entropy*, vol. 18, n°. 11, p. 409, 2016.

[113] J. Allgeier, A. González-Nicolás, D. Erdal, W. Nowak et O. A. Cirpka, “A stochastic framework to optimize monitoring strategies for delineating groundwater divides,” *Frontiers in Earth Science*, vol. 8, p. 509 ;1–22, 2020.

[114] T. Hermans, F. Nguyen et J. Caers, “Uncertainty in training image-based inversion of hydraulic head data constrained to ERT data : Workflow and case study,” *Water Resources Research*, vol. 51, n°. 7, p. 5332–5352, 2015.

[115] T. Hermans, F. Nguyen, M. Klepikova, A. Dassargues et J. Caers, “Uncertainty quantification of medium-term heat storage from short-term geophysical experiments using bayesian evidential learning,” *Water Resources Research*, vol. 54, n°. 4, p. 2931–2948, 2018.

[116] S. Huang, W. Zuo et M. D. Sohn, “A Bayesian Network model for predicting cooling load of commercial buildings,” *Building Simulation*, vol. 11, n°. 1, p. 87–101, 2018.

[117] W. Tian, Y. Heo, P. d. Wilde, Z. Li, D. Yan, C. S. Park, X. Feng et G. Augenbroe, “A review of uncertainty analysis in building energy assessment,” *Renewable and Sustainable Energy Reviews*, vol. 93, p. 285–301, 2018.

[118] K. Menberg, A. Bidarmaghz, A. Gregory, R. Choudhary et M. Girolami, “Multi-fidelity approach to Bayesian parameter estimation in subsurface heat and fluid transport models,” *Science of The Total Environment*, vol. 745, p. 140 846 ; 2–13, 2020.

[119] H. Soltan Mohammadi, L. M. Ringel, C. Bott, S. Erol et P. Bayer, “Bayesian uncertainty quantification in temperature simulation of borehole heat exchanger fields for geothermal energy supply,” *Applied Thermal Engineering*, vol. 265, p. 125210, 2024.

[120] F. Pianosi, K. Beven, J. Freer, J. W. Hall, J. Rougier, D. B. Stephenson et T. Wagener, “Sensitivity analysis of environmental models : A systematic review with practical workflow,” *Environmental Modelling & Software*, vol. 79, p. 214–232, 2016.

[121] M.-J. Shin, J. H. A. Guillaume, B. F. W. Croke et A. J. Jakeman, “Addressing ten questions about conceptual rainfall–runoff models with global sensitivity analyses in R,” *Journal of Hydrology*, vol. 503, p. 135–152, 2013.

[122] W. Choi, H. Kikumoto et R. Ooka, “Probabilistic uncertainty quantification of borehole thermal resistance in real-world scenarios,” *Energy*, vol. 254, n°. Part C, p. 124400, 2022.

[123] S. J. Rees, J. D. Spitler, Z. Deng, C. D. Orio et C. N. Johnson, “A study of geothermal heat pump and standing column well performance,” *ASHRAE Transactions : Research*,

vol. 110, n°. 1, p. 3–13, 2004.

[124] C. Beurcq, “Control strategies for standing column wells in a cold climate,” Mémoire de maîtrise ès sciences appliquées, École Polytechnique de Montréal, Montréal, QC, Canada, 2019.

[125] L. Burté, C. Cotiche Baranger, L. Aquilina, T. Le Borgne, N. Frechin et M.-F. Gérard, “Clogging of shallow geothermal doublets : Hydrologic, geochemical and microbiological observations in a pilot site,” dans *Proceedings of the Conference : European Geothermal Congress 2016*, Strasbourg, France, 2016.

[126] H. Kim, J.-K. Mok, Y. Park, D. Kaown et K.-K. Lee, “Composition of groundwater bacterial communities before and after air surging in a groundwater heat pump system according to a pyrosequencing assay,” *Water*, vol. 9, n°. 11, p. 891, 2017.

[127] L. Cerclet, B. Courcelles et P. Pasquier, “Impact of standing column well operation on carbonate scaling,” *Water*, vol. 12, n°. 8, p. 2222, 2020.

[128] D. Banks, *An introduction to thermogeology : ground source heating and cooling*, 2e éd. Hoboken, NJ : John Wiley & Sons, Ltd, 2012.

[129] L. Ni, R. Wang, X. Sun, Y. Yao et D. Qv, “Water exchange of a standing column well with aquifer : A numerical study,” *Thermal Science*, vol. 22, p. 481 – 490, 2018.

[130] M. A. Ben Aoun, P. Pasquier et A. Nguyen, “On the use of an underground storage tank for disposing bleed water in standing column well systems,” *Geothermics*, vol. 119, p. 102969, 2024.

[131] D. Kim, M. Lim, B. Yu et C. Lee, “Smart heating and cooling heat pump system by standing column well and cross-mixing balancing well heat exchangers,” *Applied Sciences*, vol. 10, n°. 21, p. 7643, 2020.

[132] K. Lim et C. Lee, “Coefficient of performance and heating and cooling thermal performance characteristics using a standing column well and cross-mixing balancing well heat exchanger methods,” *Energy Reports*, vol. 7, p. 1444–1459, 2021.

[133] J.-H. Cho, Y. Nam et H.-C. Kim, “Performance and feasibility study of a Standing Column Well (SCW) system using a deep geothermal well,” *Energies*, vol. 9, n°. 2, p. 108, 2016.

[134] W. Song, L. Ni et Y. Yao, “Experimental research on bleeding performance of single well ground-water heat pump,” *Procedia Engineering*, vol. 205, p. 3162–3169, 2017.

[135] V. Mikler, “A theoretical and experimental study of the" energy well" performance,” Thèse de doctorat, Pennsylvania State University, College Township, PA, USA, 1993.

[136] M. Lim et C. Lee, “Thermal performance comparison of standing column well and cross-mixing balancing well heat exchangers,” *Geothermics*, vol. 91, p. 102037, 2021.

[137] J. You et C. Lee, “Comparative analysis of geothermal energy in Korea based on closed borehole and single-and two-well standing column well geothermal heat exchange systems,” *Applied Sciences*, vol. 10, n°. 7, p. 2467, 2020.

[138] L. Jacques et P. Pasquier, “Obtaining the hydraulic and thermal properties of the main hydrostratigraphic units surrounding a standing column well using a thermal response test,” *Journal of Hydrology*, vol. 623, p. 129823, 2023.

[139] L. Jacques, P. Pasquier, G. Dion et G. Beaudry, “Experimental assessment of inter-well reinjection in standing column wells by analysis of transfer functions obtained from non-stationary deconvolution,” *Geothermics*, vol. 125, p. 103184, 2025.

[140] N. Molina-Giraldo, P. Blum, K. Zhu, P. Bayer et Z. Fang, “A moving finite line source model to simulate borehole heat exchangers with groundwater advection,” *International Journal of Thermal Sciences*, vol. 50, n°. 12, p. 2506–2513, 2011.

[141] Y. Guo, J. Zhao et W. V. Liu, “Effects of varying heat transfer rates for borehole heat exchangers in layered subsurface with groundwater flow,” *Applied Thermal Engineering*, vol. 247, p. 123007, 2024.

[142] S. Erol et B. François, “Multilayer analytical model for vertical ground heat exchanger with groundwater flow,” *Geothermics*, vol. 71, p. 294–305, 2018.

[143] P. Pasquier et L. Lamarche, “Analytic expressions for the moving infinite line source model,” *Geothermics*, vol. 103, p. 102413, 2022.

[144] P. Pasquier et D. Marcotte, “Efficient computation of heat flux signals to ensure the reproduction of prescribed temperatures at several interacting heat sources,” *Applied Thermal Engineering*, vol. 59, n°. 1–2, p. 515–526, 2013.

[145] A. Nguyen, P. Pasquier et D. Marcotte, “Borehole thermal energy storage systems under the influence of groundwater flow and time-varying surface temperature,” *Geothermics*, vol. 66, p. 110–118, 2017.

[146] S. Morchio, P. Pasquier, M. Fossa et R. A. Beier, “A spectral method aimed at explaining the role of the heat transfer rate when the Infinite Line Source model is applied to Thermal Response Test analyses,” *Geothermics*, vol. 111, p. 102722, 2023.

[147] L. Lamarche, *Fundamentals of Geothermal Heat Pump Systems : Design and Application.* Cham : Springer Nature Switzerland, 2023.

[148] G. Hellström, *Ground heat storage : Thermal analyses of duct storage systems*, ser. Department of Mathematical Physics. University of Lund, Sweden, 1991.

[149] D. Bauer, W. Heidemann, H. Müller-Steinhagen et H.-J. G. Diersch, “Thermal resistance and capacity models for borehole heat exchangers,” *International Journal of Energy Research*, vol. 35, n°. 4, p. 312–320, 2011.

[150] J. Claesson et S. Javed, “Explicit multipole formulas and thermal network models for calculating thermal resistances of double U-pipe borehole heat exchangers,” *Science and Technology for the Built Environment*, vol. 25, n°. 8, p. 980–992, 2019.

[151] M. P. Anderson, W. W. Woessner et R. J. Hunt, *Applied groundwater modeling : simulation of flow and advective transport*, 2e éd. Elsevier, Academic Press, 2015.

[152] G. Thiem, *Hydrologische Methoden*. J. M. Gebhardt’s Verlag, 1906.

[153] E. Bresciani, R. N. Shandilya, P. K. Kang et S. Lee, “Well radius of influence and radius of investigation : What exactly are they and how to estimate them ?” *Journal of Hydrology*, vol. 583, p. 124646, 2020.

[154] H. Seol, S. Jeong, C. Cho et K. You, “Shear load transfer for rock-socketed drilled shafts based on borehole roughness and geological strength index (GSI),” *International Journal of Rock Mechanics and Mining Sciences*, vol. 45, n°. 6, p. 848–861, 2008.

[155] F. Dittus et L. Boelter, “Heat transfer in automobile radiators of the tubular type,” dans *Publications in Engineering*, University of California, Berkeley, 1930, p. 443.

[156] O. Todorov, K. Alanne, M. Virtanen et R. Kosonen, “Different approaches for evaluation and modeling of the effective thermal resistance of groundwater-filled boreholes,” *Energies*, vol. 14, n°. 21, p. 6908, 2021.

[157] D. K. Todd et L. W. Mays, *Groundwater Hydrology*, 3e éd. Hoboken, NJ : John Wiley & Sons, 2005.

[158] M. M. Mansour, A. G. Hughes, A. E. F. Spink et J. Riches, “Pumping test analysis using a layered cylindrical grid numerical model in a complex, heterogeneous chalk aquifer,” *Journal of Hydrology*, vol. 401, n°. 1, p. 14–21, 2011.

[159] S.-Y. Hamm, M. Kim, J.-Y. Cheong, J.-Y. Kim, M. Son et T.-W. Kim, “Relationship between hydraulic conductivity and fracture properties estimated from packer tests and borehole data in a fractured granite,” *Engineering Geology*, vol. 92, n°. 1, p. 73–87, 2007.

[160] H.-C. Kao, P.-Y. Chou, N.-C. Wu, C.-T. Wang et N.-S. Hsu, “A new wireline 2-in-1 inflatable-packer system for aquifer characterization,” *Measurement*, vol. 173, p. 108751, 2021.

[161] M. Cardiff, T. Bakhos, P. K. Kitanidis et W. Barrash, “Aquifer heterogeneity characterization with oscillatory pumping : Sensitivity analysis and imaging potential,” *Water Resources Research*, vol. 49, n°. 9, p. 5395–5410, 2013.

[162] D. Marco, A. Zanini et C. Fausto, “Oscillatory pumping test to estimate aquifer hydraulic parameters in a Bayesian geostatistical framework,” *Mathematical Geosciences*, vol. 50, n°. 6, p. 169—-186, 2018.

[163] F. J. Molz, R. H. Morin, A. E. Hess, J. G. Melville et O. Güven, “The Impeller Meter for measuring aquifer permeability variations : Evaluation and comparison with other tests,” *Water Resources Research*, vol. 25, n°. 7, p. 1677–1683, 1989.

[164] J. F. Devlin, *Groundwater velocity.* Guelph, Ontario, Canada : The Groundwater Project, 2020.

[165] C. Keller, “A new rapid method for measuring the vertical head profile,” *Groundwater*, vol. 55, n°. 2, p. 244–254, 2017.

[166] Z. Jiang, S. Zhang, C. Turnadge et T. Xu, “Combining autoencoder neural network and Bayesian inversion to estimate heterogeneous permeability distributions in enhanced geothermal reservoir : Model development and verification,” *Geothermics*, vol. 97, p. 102262, 2021.

[167] H. J. L. Witte, “4 - In situ estimation of ground thermal properties,” dans *Advances in Ground-Source Heat Pump Systems*, S. J. Rees, édit. Woodhead Publishing, 2016, p. 97–116.

[168] J. W. Lund et A. N. Toth, “Direct utilization of geothermal energy 2020 worldwide review,” *Geothermics*, vol. 90, p. 101915, 2021.

[169] M. Mahmoud, M. Ramadan, S. Naher, K. Pullen et A.-G. Olabi, “Advances in grout materials in borehole heat exchangers,” dans *Encyclopedia of Smart Materials*, A.-G. Olabi, édit. Oxford : Elsevier, 2022, p. 334–342.

[170] S. Emad Dehkordi, R. A. Schincariol et B. Olofsson, “Impact of groundwater flow and energy load on multiple borehole heat exchangers,” *Ground Water*, vol. 53, n°. 4, 2014.

[171] R. A. Beier, “Use of temperature derivative to analyze thermal response tests on borehole heat exchangers,” *Applied Thermal Engineering*, vol. 134, p. 298–309, 2018.

[172] P. Pasquier, A. Zarrella et D. Marcotte, “A multi-objective optimization strategy to reduce correlation and uncertainty for thermal response test analysis,” *Geothermics*, vol. 79, p. 176–187, 2019.

[173] M. I. Vélez Márquez, J. Raymond, D. Blessent, M. Philippe, N. Simon, O. Bour et L. Lamarche, “Distributed thermal response tests using a heating cable and fiber optic temperature sensing,” *Energies*, vol. 11, n°. 11, 2018.

[174] Y. Nian, X. Wang, Z. Deng et W. Cheng, “Estimation method for layered ground thermal conductivity using genetic algorithm based on a 2-D heat transfer model,” *Energy and Buildings*, vol. 258, p. 111841, 2022.

[175] R. A. Beier, S. Morchio et M. Fossa, “Thermal response tests on deep boreholes through multiple ground layers,” *Geothermics*, vol. 101, p. 102371, 2022.

[176] G. Dalla Santa, P. Pasquier, L. Schenato et A. Galgaro, “Repeated ETRTs in a complex stratified geological setting : high-resolution thermal conductivity identification by multiple linear regression,” *Journal of Geotechnical and Geoenvironmental Engineering*, vol. 148, n°. 4, p. 04022007, 2022.

[177] N. Simon, O. Bour, N. Lavenant, G. Porel, B. Nauleau, B. Pouladi, L. Longuevergne et A. Crave, “Numerical and experimental validation of the applicability of active-dts experiments to estimate thermal conductivity and groundwater flux in porous media,” *Water Resources Research*, vol. 57, n°. 1, 2021.

[178] M. V. Klepikova, T. L. Borgne, O. Bour et P. Davy, “A methodology for using borehole temperature-depth profiles under ambient, single and cross-borehole pumping conditions to estimate fracture hydraulic properties,” *Journal of Hydrology*, vol. 407, n°. 1, p. 145–152, 2011.

[179] M. V. Klepikova, T. L. Borgne, O. Bour, K. Gallagher, R. Hochreutener et N. Lavenant, “Passive temperature tomography experiments to characterize transmissivity and connectivity of preferential flow paths in fractured media,” *Journal of Hydrology*, vol. 512, p. 549–562, 2014.

[180] N. Linde, D. Ginsbourger, J. Irving, F. Nobile et A. Doucet, “On uncertainty quantification in hydrogeology and hydrogeophysics,” *Advances in Water Resources*, vol. 110, p. 166–181, 2017.

[181] S. K. Hansen, J. He et V. V. Vesselinov, “Characterizing the impact of model error in hydrologic time series recovery inverse problems,” *Advances in Water Resources*, vol. 111, p. 372–380, 2018.

[182] N. D. Ward et C. Fox, “Identification of aquifer parameters from pumping test data with regard for uncertainty,” *Journal of Hydrologic Engineering*, vol. 17, n°. 7, p. 769–781, 2012.

[183] M. T. Demir, N. K. Copty, P. Trinchero et X. Sanchez-Vila, “Bayesian estimation of the transmissivity spatial structure from pumping test data,” *Advances in Water Resources*, vol. 104, p. 174–182, 2017.

[184] R. G. Agarwal, “A new method to account for producing time effects when drawdown type curves are used to analyze pressure buildup and other test data,” dans *Proceedings of the SPE Annual Technical Conference and Exhibition 1980*, Dallas, Texas, 1980.

[185] M. Karamanis et F. Beutler, “Ensemble slice sampling : Parallel, black-box and gradient-free inference for correlated & multimodal distributions,” *Statistics and Computing*, vol. 31, n°. 5, p. 61, 2021.

[186] R. M. Neal, “Slice sampling,” *The Annals of Statistics*, vol. 31, n°. 3, p. 705 – 767, 2003.

[187] A. Gelman, J. B. Carlin, H. S. Stern, D. B. Dunson, A. Vehtari et D. B. Rubin, *Bayesian Data Analysis*, 3e éd., ser. Texts in Statistical Science. Chapman and Hall/CRC, 2014.

[188] A. Nguyen, P. Pasquier et D. Marcotte, “Development of an ode model featuring a three level bleed control and an off-loading sequence for standing column wells,” dans *13th Conference of International Building Performance Simulation Association*, Chambéry, France, 2013, p. 9.

[189] L. Kocis et W. J. Whiten, “Computational investigations of low-discrepancy sequences,” *ACM Trans. Math. Softw.*, vol. 23, n°. 2, p. 266–294, 1997.

[190] Comsol Multiphysics®, “COMSOL Multiphysics Reference Manual,” 2021. [En ligne]. Disponible : www.comsol.com

[191] A. Puy et A. Saltelli, “4 – mind the hubris : Complexity can misfire,” dans *The politics of modelling : Numbers between science and policy*, A. Saltelli et M. Di Fiore, édit. Oxford University Press, 2023.

[192] J.-P. Chiles et P. Delfiner, *Geostatistics : modeling spatial uncertainty*, 2e éd., ser. Wiley series in probability and statistics. Hoboken, N.J : Wiley, 2012.

[193] United Nations Environment Programme, “2022 Global status report for buildings and construction : Towards a zero-emission, efficient and resilient buildings and construction sector,” Penrose CDB, Nairobi, Rapport technique DTI/2482/PA, 2022.

[194] D. Tirelli et D. Besana, “Moving toward net zero carbon buildings to face global warming : A narrative review,” *Buildings*, vol. 13, n°. 3, p. 684, 2023.

[195] G. Dion, P. Pasquier, G. Beaudry et D. Marcotte, “Stationary and non-stationary deconvolution to recover long-term transfer functions,” dans *Proceedings of the IGSHPA Research Track 2022*, Las Vegas, Nevada, USA, 2022.

[196] J. Raymond, F.-A. Comeau, K. Bédard, R. Lefebvre, R. Therrien et M. Malo, “Assessing the geothermal potential of the St. Lawrence Lowlands sedimentary basin in Quebec, Canada,” dans *International Association of Hydrogeologists 2012 Congress*, Niagara Falls, Canada, 2012, p. 8.

[197] J. Claesson et A. Dunand, *Heat extraction from the ground by horizontal pipes : a mathematical analysis*. Stockholm : Swedish Council for Building Research, 1983.

[198] E. Heim, P. Pasquier, G. Dion, P. Stoffel et N. Klitzsch, “Reconstruction of experimental thermal response functions from monitoring data of a borehole heat exchanger field,” dans *Proceedings of the IGSHPA Research Track 2024*, Montréal, Québec, Canada, 2024.

[199] A. Nguyen, “Dynamic metaheuristic selection via Thompson Sampling for online optimization,” *Applied Soft Computing*, vol. 158, p. 111566, 2024.

[200] C. Chen et J. J. Jiao, “Numerical simulation of pumping tests in multilayer wells with non-darcian flow in the wellbore,” *Groundwater*, vol. 37, n°. 3, p. 465–474, 1999.

[201] B. Dusseault, P. Pasquier et D. Marcotte, “A block matrix formulation for efficient g-function construction,” *Renewable Energy*, vol. 121, p. 249–260, 2018.

[202] A. Nguyen et P. Pasquier, “A successive flux estimation method for rapid g-function construction of small to large-scale ground heat exchanger,” *Renewable Energy*, vol. 165, p. 359–368, 2021.

[203] C. Rose, P. Pasquier, A. Nguyen et R. Labib, “Efficient construction of short-term transfer functions for closed-loop boreholes in stratified aquifers under groundwater flow using neural networks and wavelet decomposition,” *Science and Technology for the Built Environment*, 2025, in press.

[204] C. Yavuzturk, A. Chiasson et J. Nydahl, “Simulation model for ground loop heat exchangers.” *Ashrae Transactions*, vol. 115, n°. 2, 2009.

[205] S. Javed et J. Claesson, “New analytical and numerical solutions for the short-term analysis of vertical ground heat exchangers,” *ASHRAE Transactions*, vol. 117, p. 3–12, 2011.

[206] Y. Brussieux, et M. Bernier, “Universal short time g*-functions : generation and application,” *Science and Technology for the Built Environment*, vol. 25, n°. 8, p. 993–1006, 2019.

[207] G. Dion, “Identification robuste de fonctions de transfert par déconvolution pour l’interprétation d’essais de réponse thermique,” Thèse de doctorat, Polytechnique Montréal, Montréal, QC, Canada, 2023.

[208] G. Florides et S. Kalogirou, “Ground heat exchangers—A review of systems, models and applications,” *Renewable Energy*, vol. 32, n°. 15, p. 2461–2478, 2007.

[209] T. G. Choe et I. J. Ko, “Method of simulation and estimation of SCW system considering hydrogeological conditions of aquifer,” *Energy and Buildings*, vol. 163, p. 140–148, 2018.

[210] A. Nguyen et P. Pasquier, “An adaptive segmentation Haar wavelet method for solving thermal resistance and capacity models of ground heat exchangers,” *Applied Thermal Engineering*, vol. 89, p. 70–79, 2015.

[211] D. Marcotte et P. Pasquier, “The effect of borehole inclination on fluid and ground temperature for GLHE systems,” *Geothermics*, vol. 38, n°. 4, p. 392–398, 2009.

[212] A. F. Moench, “Convergent radial dispersion : A Laplace transform solution for aquifer tracer testing,” *Water Resources Research*, vol. 25, n°. 3, p. 439–447, 1989.

[213] ——, “Flow to a well in a water-table aquifer : An improved Laplace transform solution,” *Groundwater*, vol. 34, n°. 4, p. 593–596, 1996.

[214] K.-H. Lai, C.-W. Liu, C.-P. Liang, J.-S. Chen et B.-R. Sie, “A novel method for analytically solving a radial advection-dispersion equation,” *Journal of Hydrology*, vol. 542, p. 532–540, 2016.

[215] I. J. D. Craig, A. M. Thompson et W. J. Thompson, “Practical numerical algorithms why Laplace transforms are difficult to invert numerically,” *Computer in Physics*, vol. 8, n°. 6, p. 648–653, 1994.

[216] C. L. Epstein et J. Schotland, “The bad truth about Laplace’s transform,” *SIAM Review*, vol. 50, n°. 3, p. 504–520, 2008.

[217] K. L. Kuhlman, “Review of inverse Laplace transform algorithms for Laplace-space numerical approaches,” *Numerical Algorithms*, vol. 63, n°. 2, p. 339–355, 2013.

[218] J. Bear, *Dynamics of fluids in porous media.* Courier Corporation, 1972.

[219] L. Zhang, G. Huang, Q. Zhang et J. Wang, “An hourly simulation method for the energy performance of an office building served by a ground-coupled heat pump system,” *Renewable Energy*, vol. 126, p. 495–508, 2018.

[220] A. Nguyen, “Determination of the ground source heat pump system capacity that ensures the longevity of a specified ground heat exchanger field,” *Renewable Energy*, vol. 169, p. 799–808, 2021.

[221] A. L. Snijders et B. C. Drijver, “9 - Open-loop heat pump and thermal energy storage systems,” dans *Advances in Ground-Source Heat Pump Systems*, S. J. Rees, édit. Woodhead Publishing, 2016, p. 247–268.

[222] C. Lehr et I. Sass, “Thermo-optical parameter acquisition and characterization of geologic properties : A 400-m deep BHE in a karstic alpine marble aquifer,” *Environ Earth Sci*, vol. 82, p. 1403–1419, 2014.

[223] J. Rouleau, L. Gosselin et J. Raymond, “New concept of combined hydro-thermal response tests (H/TRTS) for ground heat exchangers,” *Geothermics*, vol. 62, p. 103–114, 2016.

[224] W. M. Pallard et A. Lazzarotto, “Thermal response tests : A biased parameter estimation procedure ?” *Geothermics*, vol. 97, p. 102221, 2021.

[225] Comsol Multiphysics®, “COMSOL Multiphysics Reference Manual,” 2022. [En ligne]. Disponible : www.comsol.com

[226] J. W. Lund, G. W. Huttrer et A. N. Toth, “Characteristics and trends in geothermal development and use, 1995 to 2020,” *Geothermics*, vol. 105, p. 102522, 2022.

[227] C. Beurcq, M. Kummert et P. Pasquier, “Optimized control for standing column wells in cold climate,” dans *10th International Conference on System Simulation in Buildings*, Liège, Belgium, 2018, p. 2.

[228] J. Sang, X. Liu, C. Liang, G. Feng, Z. Li, X. Wu et M. Song, “Differences between design expectations and actual operation of ground source heat pumps for green buildings in the cold region of northern China,” *Energy*, vol. 252, p. 124077, 2022.

[229] L. Cerclet, B. Courcelles et P. Pasquier, “Column experiments to anticipate clogging of standing column wells,” dans *Proceedings of the IGSHPA Research Track 2022*, Las Vegas, Nevada, USA, 2022.

ANNEXE A ARTICLE – AN EASY-TO-USE ANALYTICAL MODEL FOR STANDING COLUMN WELLS OPERATING WITH BLEED

Alain Nguyen[a], Louis Jacques[a,b,*], Philippe Pasquier[b]
Applied Thermal Engineering, Volume 258 (A), October 9, 2024, Pages 124543-124551
[a] CanmetENERGY, Naturel Resources Canada, 1615 Lionel-Boulet, P.O. Box 4800, Varennes, J3X 1S6, QC, Canada
[b] Department of Civil, Geological and Mining Engineering, Polytechnique Montréal, P.O. Box 6079 Station Centre-Ville, Montreal H3C 3A7, QC, Canada.
* Corresponding author : louis.jacques@polymtl.ca
Keywords : Standing column well, Advection–diffusion, Radial flow field, Analytical model, Finite element model

Abstract

Accurate assessment of subsurface heat transport is vital for the design of standing column well systems. When bleed is utilized, the mathematical problem is governed by coupled heat transfer and groundwater flow within a radially convergent flow field, making the development of models challenging. While numerical models exist to simulate these transient processes, the absence of simple and accessible analytical solutions limits their broader application. This study addresses this gap by developing a novel easy-to-use analytical model to accurately represent the heat advection–diffusion problem in standing column wells operating with bleed. The proposed model combines the well-known infinite line source model with an innovative scaling function, inspired from the field of solute transport, through a simple convolution product. Notably, the developed model depends on only three dimensionless parameters : dimensionless advection time, Péclet number, and bleed ratio. Rigorous validation against two distinct sets of reference numerical solutions demonstrated the model's efficiency, accuracy, and reliability across a broad spectrum of nine physical parameters. Key results include relative root mean square errors on the order of 10^{-3} across 200 reference solutions, confirming the model's robustness. These findings highlight the model's potential to significantly advance both research and practical applications in the design and optimization of standing column wells.

Introduction

Ground source heat pump (GSHP) systems have gained worldwide recognition for providing the thermal needs of residential, commercial, and industrial buildings [13] owing to their high energy efficiency, reduced greenhouse gas emissions, and potential for significant cost savings over their operational lifespan. GSHPs offer stable operating temperatures by harnessing thermal energy stored in the subsurface through an underground infrastructure known as a ground heat exchanger (GHE) [208]. In short, GHEs play a crucial role by facilitating the efficient transfer of thermal energy between the ground, serving as a heat source or sink, and the working fluid circulating within the GSHP system.

Among the various GHE configurations, standing column well (SCW) systems have emerged as a promising cost-effective alternative to conventional closed loop systems, leading to improved system efficiency and performance in areas with favorable hydrogeological conditions [22]. SCWs enact superior heat exchange rates by recirculating groundwater in a single uncased vertical borehole and have the ability to provide additional operational flexibility with the "bleed" operation. By diverting a portion of the circulating fluid, bleed creates a converging radial flow field around the SCW that generates advective transport and thereby greatly enhances heat transfer in the aquifer. While SCW systems offer unique advantages associated with the direct use of groundwater in comparison to their closed loop counterpart, their complex nature necessitate a more comprehensive understanding of their behavior to effectively predict their performance. To date, the literature remains scarce in terms of research focusing on SCW systems, despite their proven efficiency in the north-eastern part of the United States [21] and Canada [14].

For gaining insights into the fundamental thermohydraulic processes that occurs in the aquifer and the complexity involved in SCW systems, advanced numerical methods (i.e. finite differences, finite elements, and finite volumes) are generally used for solving the advection–diffusion equation. While limited in number, there exist published works focusing on the numerical investigation and analysis of SCWs with different degrees of complexity, from simple one-dimensional [67], to more complex transient coupled three-dimensional models. Rees et al. (2004) [123] developed a 2D finite volume numerical model of coupled groundwater flow and heat transfer in SCWs and revealed that bleed was the most important parameter. Abu-Nada et al. (2008) [48] developed a 2D-axial finite volume numerical model of SCWs to study the optimal bleed ratio. Woods and Orteha (2011) [43] proposed a symmetrical 2D numerical model to study a line of evenly spaced wells, operating concurrently. Eppner et al. (2007) [54] developed a 2D-axial coupled thermo-hydro-geochemical finite element numerical model that allows for predicting reaction rate of calcite. Beaudry et al. (2018) [103] develo-

ped a 2D-axial finite element numerical SCW model to study the location of the submersible pump and validated it using experimental data. They further developed their model in [40] to study the effect of fractures. Choe and Ko (2018) [209] proposed a decoupled model for SCWs, where the borehole is modeled in 1D discrete elements, and the aquifer is modeled in 2D-axial. Robert et al. (2022) [27] developed a multi-layer 3D finite element SCW model to study the effect of heterogeneity.

Naturally, the integration of groundwater flow, heat transfer, and other intricate processes like bleed in numerical models are computationally demanding, hindering their routine use for simulation and design purposes. Prior research have suggested employing thermal resistance and capacity models [28, 51] and Haar wavelets [210] to effectively reduce the governing equations to a system of ordinary differential equations, thus reducing the computational burden without significant accuracy losses. Yet, these solutions still suffer from numerical complexity that makes them inadequate for practitioners.

On the other hand, analytical models have the ability to provide simplified and computationally efficient solutions, allowing for faster analysis, parameter sensitivity studies, and improved understanding of the underlying physical phenomena. Traditionally, analytical models have considered GHEs as line or cylinder [42,73] sources of heat, assuming uniform radial diffusion along their lengths. Over the past decades, a wide range of features, such as axial effects [75], inclination [211], and regional groundwater flow [143], have been incorporated into these models, thereby enhancing their ability to simulate increasingly complex systems.

Despite existing research, there is a clear gap in solutions, as none of the available analytical models address the unique characteristics of SCWs. This is because SCW systems operating with bleed necessitate the consideration of heat advection–diffusion in a radially convergent flow field. Indeed, mathematical problems that involve both radial advection and diffusion, such as in SCWs, typically require Laplace inversions [212–214] for obtaining exact solutions, which are quite difficult to compute and cannot be used easily by practitioners due to the numerical back-transformation of the solutions in the Laplace domain to the time domain [215–217].

To circumvent this difficulty, one can resort to approximate solutions instead of exact ones, balancing between computational efficiency and sufficient accuracy. One notable work in the field of solute transport in groundwater is the recent work of Thiéry (2022) [46] which proposed easy-to-use approximate expressions describing the mass advection–diffusion phenomena within a radially converging flow field for tracer tests. Given the inherent similarities between mass and heat transport processes, this important contribution provides valuable insights and methodologies that can be adapted to derive simple expressions for SCWs.

The work presented hereinafter is inspired of the previous work of Thiéry (2022) [46] and aims to address the aforementioned gap of knowledge (no available analytical models for SCWs) by presenting a comprehensive easy-to-use approximate expression for SCW operating with bleed. The proposed analytical expression incorporates key parameters such as thermal properties of the subsurface and groundwater flow characteristics to accurately predict the normalized thermal response of a SCW under a constant heat load and bleed rate.

The novelty of this work is threefold : (1) To the best of the authors' knowledge, this is the first study to propose an easy-to-use analytical model for SCWs operating with bleed ; (2) since this proposed model is very efficient to compute, it allows fast simulations and parametric analysis at the design stage and for the efficient incorporation of cost–benefit and marginal economic considerations at a later stage ; and (3) it paves the way for developing new analytical models for other systems that involve multi-physics such as advection–diffusion.

Theoretical background

Consider a homogeneous and isotropic aquifer, of infinite horizontal extent and constant thickness (L). Then, Fig. A.1 exhibits a schematic diagram illustrating the two operating modes of a SCW system, given a borehole radius (r_b), heat injection/extraction rate (Q), pumping flow rate (V) and bleed flow rate (B). In subfigure a), the system recirculates the entire groundwater flow, and heat transport in the aquifer occurs by radial diffusion only. In subfigure b), the system bleeds a portion of the groundwater flow, thereby generating a radially convergent flow field around the SCW. In this case, heat transport in the aquifer occurs by radial diffusion and advection. Recall that many analytical models are readily available in the literature to predict the temperature response resulting from operation of a GHE in radial diffusion only. For this work, the classic model of the infinite line source (ILS) [42, 73] is chosen to evaluate the unitary transfer function of a SCW operating without bleed, which is given by :

$$g_0(t) = \frac{Q}{4\pi k L} \int_u^\infty \frac{e^{-x}}{x}\, dx \tag{A.1}$$

$$u = \frac{r^2}{4\alpha t} \tag{A.2}$$

where r is the distance from the line source, t is the time, k is the ground thermal conductivity and α is the ground thermal diffusivity. To represent the normalized thermal response, the terms Q and L can simply be replaced with 1. From this point, it should be noted that Equation A.1 will serve as the foundational basis for the subsequent stages of the methodology

for modeling SCWs operating with bleed.

Mathematical formulation for SCWs operating with bleed

Rather than analytically deriving a mathematical expression directly from the governing equations involved in SCWs operating with bleed, one could combine two simpler analytical expressions and replicate the equivalent phenomena. The main idea of the proposed analytical model revolves around employing a convolution product between two functions : 1) a base function (f) representing the increment of the transfer function given in Eq. A.1 and 2) a scaling function (h), such that :

$$g(t) = (f * h)(t) \tag{A.3}$$

$$f(t_i) = g_0(t_i) - g_0(t_{i-1}) \quad \forall i, 1 \leq i \leq n \tag{A.4}$$

where g is the resulting transfer function, i is the vector index, n is the vector length, $g_0(t_0) = 0$ and $t_0 = 0$. The convolution product is a powerful mathematical operation that integrates the individual functions over their respective domains, considering the entire range of interactions between them. Hence, performing the convolution of functions f and h, one can combine their characteristics and account for the cumulative influence of advection and diffusion across different locations and times, allowing a more accurate and realistic representation of the overall heat transport in g.

Since h aims at accounting for the sole contribution of heat advection due to bleed, it should be monotonically decreasing. The proposed formulation for h exploits inherent similarities between mass and heat transport in porous media and is adapted from the expression proposed by Thiéry (2022) [46] for modeling advective solute transport, which originated from Bear (1972) [218] :

$$h(t) = \epsilon_1(1 - \epsilon_2\beta)\left(1 + \mathrm{erf}\left(\frac{\sqrt{\mathrm{Pe}}}{\epsilon_3}\left(\frac{1 - t_a^{\epsilon_4}}{t_a^{\epsilon_4}}\right)\right)\right) \tag{A.5}$$

$$\mathrm{Pe} = \frac{B/(2\pi L)}{\alpha} \tag{A.6}$$

$$t_a = \frac{Bt}{\pi L r^2} \tag{A.7}$$

(a)

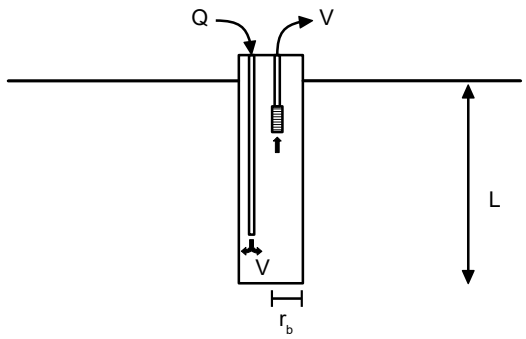

(b)

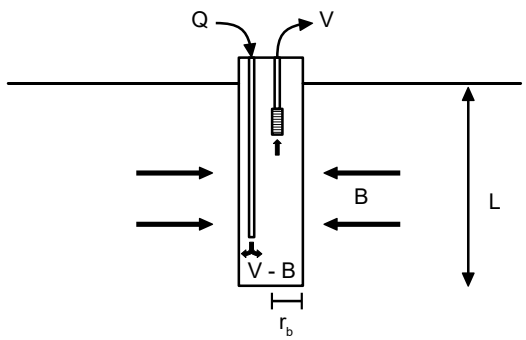

FIGURE A.1 Illustration of a) the SCW operation without bleed, and b) the operation with bleed.

$$B = V\beta \tag{A.8}$$

where β is the bleed ratio, Pe is the Péclet number and t_a is the dimensionless advection time, while ϵ_1,ϵ_2, ϵ_3 and ϵ_4 are correction coefficients. Here, the Péclet number is defined as the ratio of heat advection to heat diffusion. As in Thiéry (2022) [46], it was observed that these correction coefficients depend only of Pe, and followed the form of power functions :

$$\epsilon_i = a_i \mathrm{Pe}^{b_i} + c_i \tag{A.9}$$

which leads to a total of 12 coefficients. Here, the reader should also observe that, ultimately, Eq. A.5 depends solely on three dimensionless parameters : β, Pe and t_a.

Note that Eq. A.3 is computationally efficient and straightforward to evaluate, utilizing only two special functions (i.e. the exponential integral and the error function) and a convolution product. The convolution product in Eq. A.3 is widely recognized as a straightforward operation that is relatively easy to compute due to its inherent mathematical properties and efficient algorithms. For example, it can be expressed in the discrete-time domain as a simple non-recurrent summation :

$$g(t) = (f * h)(t) = \sum_{j=1}^{i} f(t_j) \cdot h(t_i - t_{j-1}) \quad \forall i, 1 \leq i \leq n \tag{A.10}$$

For more efficient computation, g can also be rapidly computed in the spectral domain using the well-known FFT method [59, 144, 219, 220]. Finally, because $g(t)$ also assumes the role of a transfer function, it can be utilized to calculate the temperatures of a stationary operation that is subjected to heat perturbations at varying rates of Q/L. This is achieved by further convolving $g(t)$ with another impulse function.

Determination of model coefficients

The 12 coefficients of Eq. A.9, which play a crucial role in the proposed model, can be effectively determined through an iterative optimization process. This involves fine-tuning the values of these coefficients to minimize the discrepancy between the model predictions based on Eq. A.3 and a large set of reference solutions, thereby ensuring an optimal fit and reliable results.

Two sets of reference solutions were generated to carry out the optimization process. The first set, based on a simple 1D-axial model of SCW, was used to verify the presented me-

thodology in a more straightforward scenario and, ultimately, to confirm the capability of the scaling factor h to account for advection affects. The second set, derived from a more complex 2D-axial model, was employed to assess the model's accuracy in a more detailed and realistic geometrical and physical context. By comparing the optimized values of the coefficients derived from both sets, a comprehensive understanding of the system's behavior can be obtained, accounting for both simplified and more realistic modeling approaches.

A total of 200 reference solutions were generated, with 100 solutions carefully allocated to each of the two distinct sets. These reference solutions were meticulously chosen to ensure an extensive and well-balanced representation of the domain of reference, enhancing the accuracy and reliability of the analysis.

All reference solutions correspond to the temperature evolution at the borehole wall (i.e. $r = r_b$) for various combinations of parameters, within the range specified in Table A.1. Notably, this range of parameters is broad enough to encompass most configurations in practical applications [22]. The parameters in Table A.1 are related via the dimensionless parameters Pe and β by means of Eq. A.6 and Eq. A.8, respectively. Accordingly, the reference domain, delineated by Pe and β and concisely illustrated in Fig. A.2, ensures a comprehensive coverage of realistic operational scenarios.

The objective function is defined as the relative root mean square error (RRMSE) between the reference solutions and the solutions obtained from the proposed model. Using the RRMSE as the objective function is essential for optimizing the model's performance across different scales, ensuring a thorough evaluation of thermal responses in a range of model complexities. Hence, the proposed model is designed as "one fit-for-all" solutions, provided the parameters remain within the specified range in Table A.1 and Fig. A.2. Finally, the optimization was carried out using a dynamic metaheuristic selection algorithm proposed by Nguyen (2024) [199].

Reference numerical solutions : 1D-axial

Firstly, a one-dimensional model is developed with the intention of emulating a simple case of heat advection–diffusion within a steady-state radially convergent flow field. Similarly to the ILS model described in Eq. A.1, the 1D model follows an axisymmetric geometry and uses homogeneous and isotropic properties [67]. This simple model uses finite elements to solve the heat transfer equation described by :

$$C\frac{\partial T}{\partial t} + Cv \cdot \nabla T = \nabla \cdot (k \nabla T) \tag{A.11}$$

Tableau A.1 Parameters range used for the construction of the database

Parameter	Units	Lower bound	Upper bound
t	yr	0	50
r_b	m	0.076	0.102
L	m	100	500
k	W/(m °C)	1.0	5.0
C	MJ/(m^3 °C)	2.1	2.6
V	L/min	54	600
B	L/min	0.72	449
β	-	0.01	1
Pe	-	0.05	1

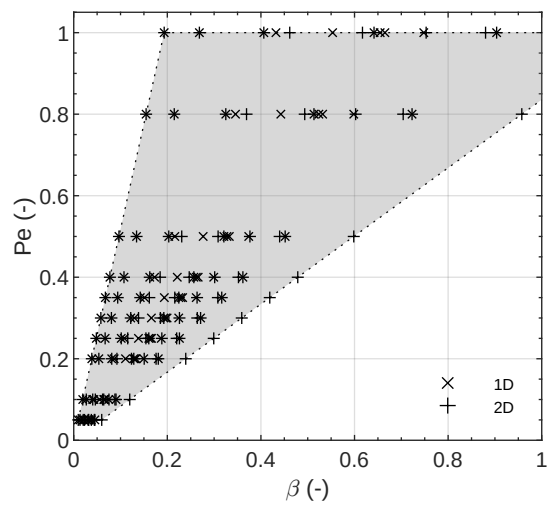

Figure A.2 The reference domain constrained by the bleed ratio (β) and Péclet number (Pe), inside the gray area, and all the parameter combinations used to generate the reference solutions for the distinct 1D and 2D databases, respectively shown with "x" and "+" markers. Note that a "$*$" appears when the "x" and "+" overlaps.

where C is the volumetric heat capacity and v is the radial velocity. The boundary conditions are defined in Figure A.3.

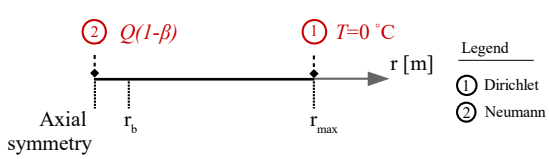

Figure A.3 Schematic representation of the 1D-axial finite element model and its boundary conditions.

An adapted heat flux, considering the fraction bled out of the system β, is applied along

the central axis. Also, a constant nil temperature is applied at the far-field radius r_{max} of 1000 m, an extent sufficient to guarantee compliance with the assumptions of the ILS model. Between r_{max} and r_b, the radial velocity v varies according to the bleed flow as described by

$$v = \frac{B}{2\pi r L} \tag{A.12}$$

Reference numerical solutions : 2D-axial

Thereafter, the aim of the 2D model is to validate the accuracy of the analytical model, more specifically that of the scaling function h, under more realistic assumptions. While sharing the axisymmetry of the 1D model, the 2D model explicitly represents the SCW by integrating additional geometrical and physical details (i.e. water columns and pipe), mimicking the upstream and downstream flow inside the SCW, to more fully consider the groundwater residence time and incorporate the transient behavior of groundwater flow in the aquifer [28, 40].

More importantly, the physics of this model couples groundwater flow to heat transfer. Hence, the velocity field in Eq. A.11 is computed using Darcy's law (Eq. A.13) :

$$v = \frac{-K}{\rho g}\nabla P \quad \text{and} \quad \rho S_s \frac{\partial P}{\partial t} = -\nabla \cdot (\rho v) \tag{A.13}$$

where S_s is the specific storage of the aquifer, ρ is the density, P is the hydraulic pressure and K is the hydraulic conductivity of the ground. Here, S_s and K were fixed at values of 5×10^{-5} (1/m) and 1×10^{-6} (m/s), respectively. This strategy was chosen based on consistent findings from numerous studies, including this one, indicating that both S_s and K have minimal influence on the model's thermal response for homogeneous aquifers.

To simulate groundwater acting as the heat carrier fluid, a unitary heat flux Q is added at a rate of ΔT, evaluated according to Eq. A.14. This allows the model to consider the flow (V) and the volumetric heat capacity of the fluid (C_f), and thereby the thermal inertia of the SCW. Overall, this model better aligns with the functioning of the SCW compared to the line source assumption of the 1D model.

$$\Delta T = \frac{Q}{V C_f} \tag{A.14}$$

To reproduce the operation of a SCW under bleed operation, only the fraction of groundwater that is not bled out is returned in the concentric area around the pumping pipe while the full flow is extracted at the center. This strategy ensures an accurate response of the aquifer

under bleed conditions.

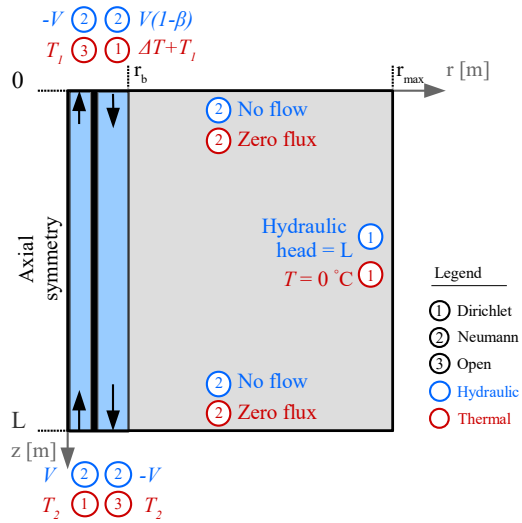

FIGURE A.4 Schematic representation of the 2D-axial coupled finite element model and its boundary conditions, where the blue areas are groundwater, the black separation is a pipe and the gray area is the ground.

In summary, the geometry and boundary conditions are presented in Figure A.4. This model simulate operation where groundwater is pumped from the bottom and reinjected at the top [103]. Note that a thorough examination of mesh independence was conducted for the range of parameters studied in this work. To speed up computation, all simulations were completed in a geometric progression and then interpolated [59], following the modified Akima cubic interpolation method.

Results and discussion

For the first set of reference solutions (i.e. 1D-axial), a RRMSE of 8.2×10^{-4} was obtained after optimization of the 12 constants (Table A.2). It is worth noting that the RRMSE achieved in this case is small, signifying a high level of accuracy between the modeled and reference

TABLEAU A.2 Coefficients a_i, b_i and c_i used in Eq. A.9 to evaluate ϵ_i for the 1D-axial model.

i	a_i	b_i	c_i
1	-0.2262	0.6390	0.9920
2	0.4955	-0.0001	0.5046
3	0.4950	0.7417	0.3947
4	0.1284	0.5631	-0.0009

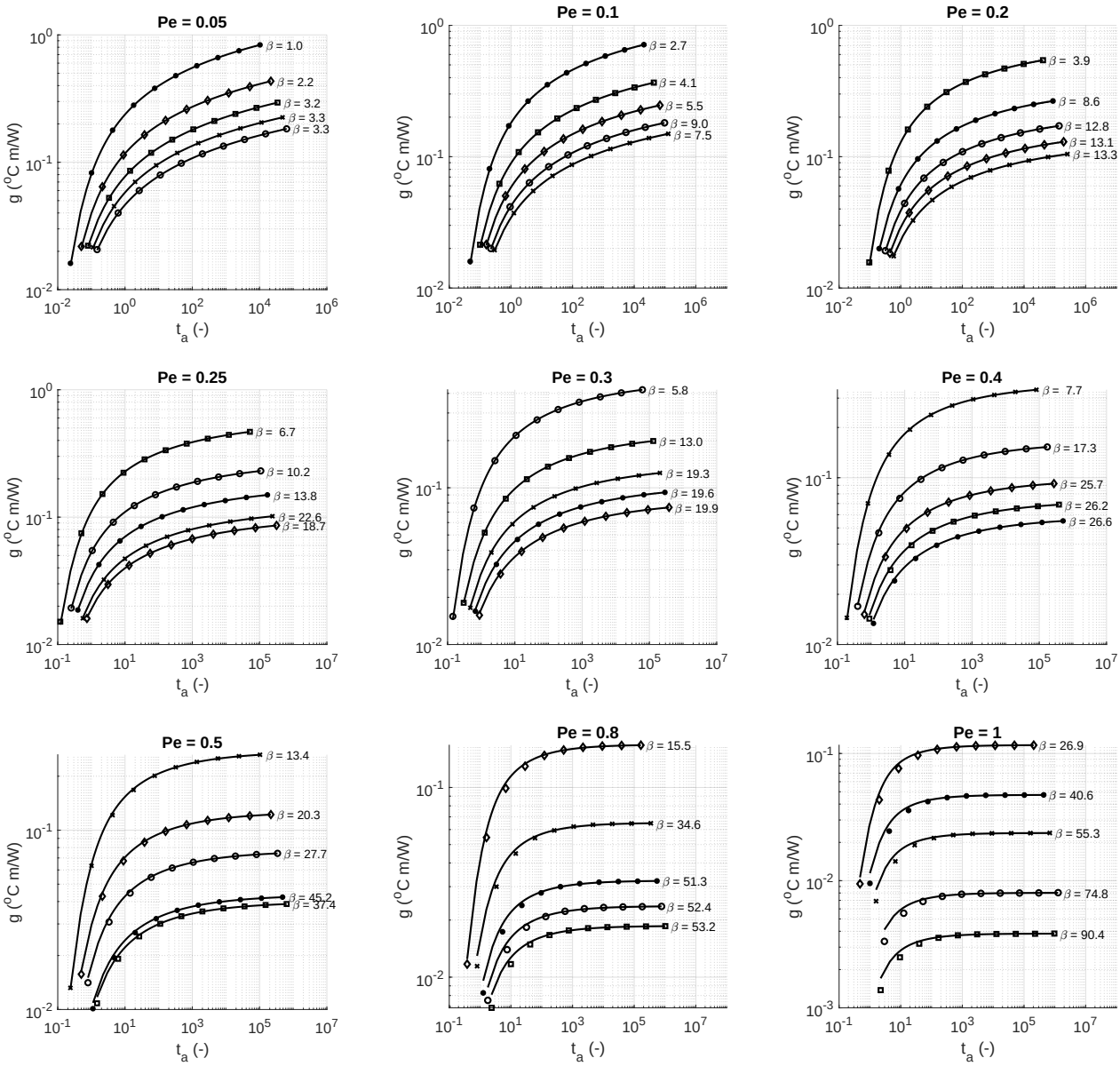

FIGURE A.5 Comparison between the solutions obtained from proposed analytical model (dotted) and the reference 1D-axial model (solid) for various Pe number. For readability, β is multiplied by a factor of 100.

solutions. This accuracy holds true for a wide range of parameters, further highlighting the model's robustness and reliability.

To illustrate this, Fig. A.5 presents a sample comparison between solutions obtained from the proposed analytical model (dotted) and the reference 1D-axial model (solid) for various Pe number and β. Please note that the specific pumping rate is not explicitly illustrated and varies across the functions. As observed, both β and Pe exert a significant influence on g,

underscoring the pivotal role of advection in heat transfer mechanism. A trained eye might notice that the error tends to slightly increase with higher Pe number and higher β ratio. This reveals that large variations in advection parameters can lead to significant thermal breakthrough effects, resulting in rapid and substantial temperature changes. In other words, more advection usually leads to functions with sharp gradients that rapidly transition to steady states. However, bear in mind that this discrepancy is naturally exaggerated when displaying in log scales.

Upon examining the optimized constants a_i, b_i and c_i (Table A.2), three observations can be made on the values of ϵ_i given by Eq. A.9 :

1. ϵ_1 starts at quasi-one and decreases non linearly with Pe ;
2. ϵ_2 is quasi-constant and close to one ; and
3. ϵ_4 starts at quasi-zero and increases linearly with Pe.

Surely, these quasi-whole numbers confirms that the relationship between the ILS model and 1D-axial model is relatively straightforward and direct. Thus, it is not so surprising that the proposed model can accurately reproduce this set of reference solutions as the main distinction between the 1D-axial model and the ILS model lies in the presence of advection through a steady-state radially convergent flow field.

For the second set of reference solutions (i.e. 2D-axial), a RRMSE of 9.8×10^{-3} was obtained after optimization of the 12 constants (Table A.3). Despite the RRMSE being one order higher than that of the 1D-axial model, the fit remains strong, as shown in Fig. A.6, indicating a high level of accuracy in modeling the intricate physical and geometrical features of SCWs.

In most cases, the predominant errors are concentrated in the short term of the functions. These errors are attributed to several factors : the recirculation of groundwater inside the SCW that acts as a heat carrier fluid, the residence time of the groundwater in the SCW, the large thermal inertial in the SCW itself and the transient behavior of the groundwater flow in the aquifer. Other sources of error arise from the vertical variations of Darcy velocity in cases where the specific pumping rate is high (i.e. V/L). Also, when β is high (i.e. > 0.7), the proposed model shows a more pronounced relative error ; however the absolute error remains

Tableau A.3 Coefficients a_i, b_i and c_i used in Eq. A.9 to evaluate ϵ_i for the 2D-axial model.

i	a_i	b_i	c_i
1	-0.4478	0.7110	1.0011
2	0.1288	-0.7595	0.7339
3	0.6458	0.7838	0.2383
4	0.1483	0.5114	-0.0100

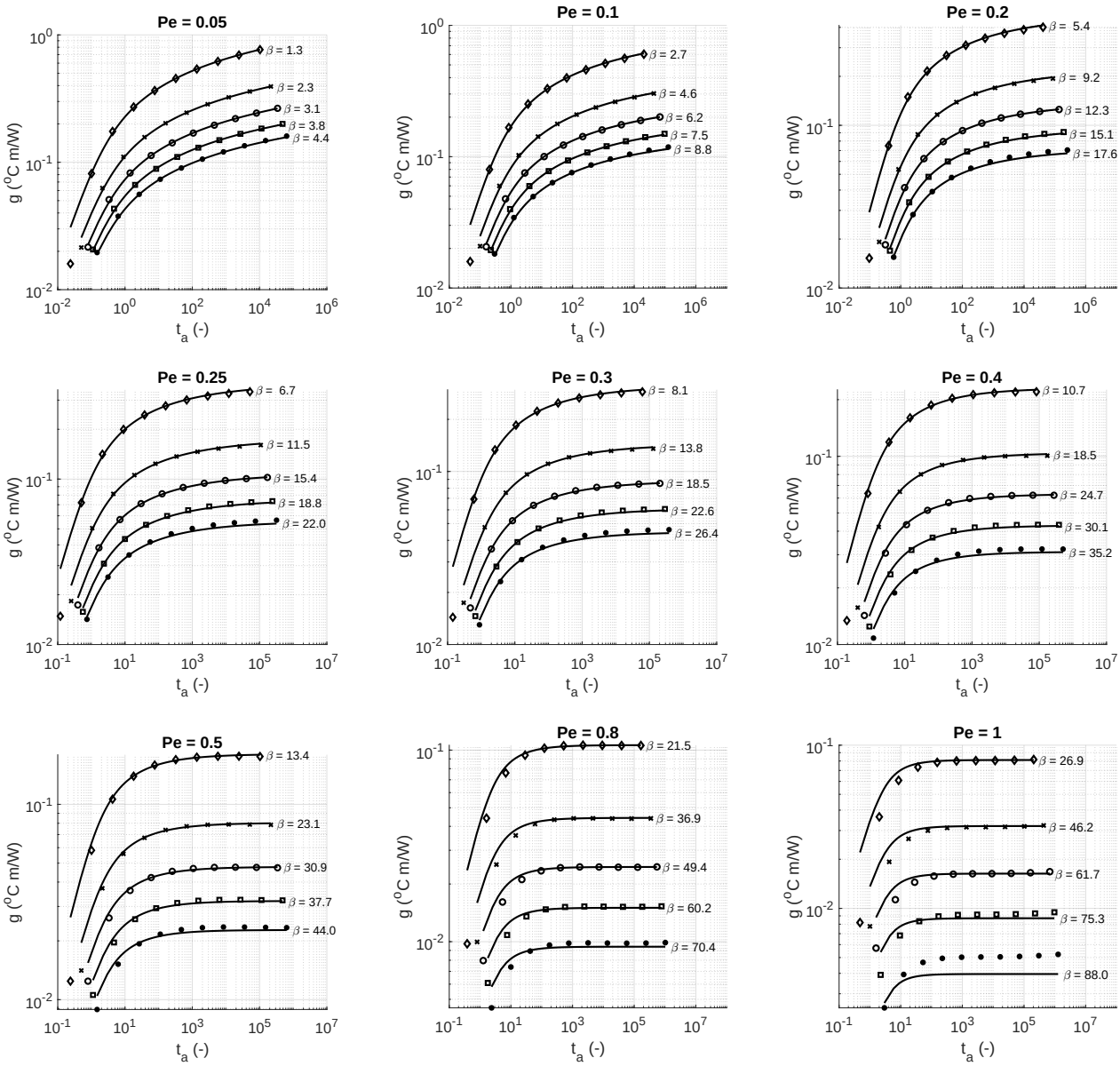

FIGURE A.6 Comparison between the solutions obtained from proposed analytical model (dotted) and the reference 2D-axial model (solid) for various Pe number. For readability, β is multiplied by a factor of 100.

fairly small. It is worth reminding that this discrepancy is naturally amplified in log scales.

The optimized constants for the 2D-axial model differ slightly from the ones for the 1D-axial model. The key distinction lies in the non-linear behavior of ϵ_1, which plays a critical role in incorporating the essential adjustments required to faithfully replicate the intricate characteristics of the 2D-axial model. The fact that ϵ_1 alone can accomplish this is quite interesting as the 2D-axial model is much more complex than its 1D counter part, both in

term of physics and geometry.

In sum, these results provide clear evidence of the proposed model's ability to incorporate the spatial and temporal variations of both advection and diffusion in SCWs operating with bleed. This is in part due to the convolution product's inherent capability to account for the entire range of interactions between Eq. A.4 and A.5, ensuring that their combined influence is appropriately accounted for across the entire domain of interest. In other words, the convolution product naturally handles scenarios where the spatial and temporal scales of advection and diffusion processes differ significantly (i.e. for different Pe numbers). In fact, the concept of combining two simpler functions through the convolution product extends beyond the realm of advection–diffusion problems and may find applicability in diverse fields, opening new avenues for enhanced modeling and analysis across various domains.

Finally, it is worth mentioning that the proposed analytical model incurs minimal computational cost. Actually, generating the set of 200 functions required less than 1 second of computation time on a standard Windows 10 workstation (Intel Xeon, 3.7 GHz, 32 Go of RAM). To put this in perspective, it required a total of 20 minutes for generating the set of solutions using the 1D-axial model and 18 hours for the set using the 2D-axial model.

With the proposed model demonstrating notable accuracy and speed, it offers a promising avenue for efficient analysis SCW systems. For instance, the model shows potential for integration with advanced techniques such as non-stationary convolution [25,60,61], enabling the simulation of systems operating with time-varying heat load inputs and dynamic bleed flow controls. It can also be used for uncertainty quantification through stochastic analysis [138]. Ultimately, such a tool would allow practitioners to efficiently incorporate cost–benefit and marginal economic considerations, thereby reducing project risk while ensuring a thorough, automated, search of potential design solutions.

Proposed model limitations

While the proposed model demonstrates high accuracy and applicability, it is important to acknowledge certain limitations and uncertainties. The generalizability of the model's prediction is limited to the conditions specified in this study, and caution should be exercised when applying the results to different contexts. Assumptions, such as the homogeneity and isotropy of the aquifer, may impact the accuracy, especially in scenarios where these conditions do not apply (e.g., in the presence of large fractures). Additionally, the range of parameter values considered in this study was based on conditions and configurations typically observed in practical applications, and accuracy may vary with parameters outside this range. These

limitations should be taken into account when applying the model to different contexts.

Conclusion

Currently, no analytical models are available to address the heat advection–diffusion phenomena in converging radial flow fields, a unique characteristics of SCWs operating with bleed. Hence, obtaining easy-to-use mathematical expressions for SCW systems is highly beneficial as they provide equations that allow for efficient and direct calculations, enhancing the speed, simplicity, and interpretability of the model. In this work, an analytical approach based on the well-known infinite line source model was developed to approximate the thermal response of a SCW operating with bleed. The proposed analytical model is fast, easy to implement and takes the form of a simple convolution product. Indeed, it is over a thousand times faster than the equivalent numerical model.

The developed model accurately reproduces SCW reference numerical solutions across a wide range of practical configurations, with relative root mean square errors around 10^{-3} based on 200 reference solutions. This confirms the model's precision and highlights its potential for rapid simulations and parametric analysis. For instance, the proposed model will allow researchers and practitioners to quickly evaluate the impact of design factors such as well depth, flow rate, bleed conditions, and subsurface characteristics on SCW system efficiency, offering insights into optimizing performance and advancing SCW GSHP technology.

To conclude, it is worth stressing that the approach used in this work is not limited to SCWs and could probably lead to new analytical models for systems that involve multiphysics such as advection–diffusion. Future work in this field could potentially yield novel approaches beneficial for designing increasingly complex ground heat exchangers.

Acknowledgments

The authors wish to thank the anonymous referees who reviewed this work and provided helpful and constructive comments and suggestions. The authors would like to acknowledge the funding received by the Office of Energy Research and Development (OERD) of Canada through the Energy Innovation Program (EIP) to undertake this research.

Nomenclature

Acronyms

GHE	Ground heat exchanger
SCW	Standing column well
GSHP	Ground source heat pump
ILS	Infinite line source
RRMSE	Relative root mean square error

Greek Letters

α	Thermal diffusivity [m^2/s]
β	Bleed ratio [-]
ϵ	Correction coefficient [-]
ρ	Density [kg/m^3]

Greek Letters

b	Borehole
f	Fluid

Greek Letters

Q	Heat flux [W]
k	Thermal conductivity [W/(m°C)]
C	Volumetric heat capacity [J/(m^3°C)]
T	Temperature [°C]
P	Pressure [kPa]
S_s	Specific storage [-]
t	Time [s]
t_a	Dimensionless advection time [-]
r	Radius [m]
v	Radial velocity [m/s]
L	Aquifer thickness [m]
V	Pumping flow [m^3/s]
B	Bleed flow [m^3/s]
Pe	Péclet number [-]
g	Unitary transfer function [(°Cm)/W]
f	Incremental transfer function [(°Cm)/W]
h	Scaling function [-]

ANNEXE B ARTICLE – UNCERTAINTY ASSESSMENT OF THE HYDRAULICS PROPERTIES SURROUNDING A STANDING COLUMN WELL WITH A THERMAL RESPONSE TEST

Louis Jacques*, Philippe Pasquier
Proceedings of the IGSHPA Research Conference, Las Vegas, December 6-8, 2022
Department of Civil, Geological and Mining Engineering, Polytechnique Montréal, P.O. Box 6079 Station Centre-Ville, Montreal H3C 3A7, QC, Canada.
* Corresponding author : louis.jacques@polymtl.ca

Asbtract

The standing column well (SCW) is known for being a highly efficient ground heat exchanger as it relies on both conduction and advection heat transfer processes. Therefore, the interpretation of a thermal response test (TRT) is strongly influenced both by the hydraulic and thermal properties surrounding the SCW. In this study, it is shown that a TRT can allow identifying the thermal and hydraulic properties around a SCW. The analysis is conducted in a Bayesian framework allowing an accurate and robust identification of the hydraulic properties and their uncertainties. A closed-form expression of the likelihood is used to consider the autocorrelation of the residuals between observed and simulated temperatures. A coupled numerical model is used to generate a training database for an artificial neural network. Then, the latter serves as an emulator of the SCW's short-term g-function given various input parameters. A case study is presented based on a 100-hour TRT performed on a SCW built at a demonstration site located in the city of Mirabel, Canada. For the specific site studied, hydraulic properties were identified with an uncertainty of less than 30 % at a two-sigma level. Such important results lead to more appropriate and efficient design of SCWs.

Introduction

A ground source heat pump system using SCWs can provide significant energy savings and low peak power usage for buildings [25]. Such ground heat exchangers are also particularly suitable for dense urban areas [22, 53]. In a SCW, advective and conductive heat transfer processes are active within the borehole and the geological material surrounding it. Therefore, the design of SCWs requires identifying both thermal and hydraulic properties [22]. To identify hydraulic conductivities, common practice includes hydrogeological investigations,

drilling of a test well and pumping tests [103, 221]. For the estimation of thermal properties, a TRT can be conducted. For SCWs, estimating the thermal properties with purely conductive models can lead to unrealistic values when hydraulic conductivity is high [27, 39]. However, the interpretation of such a TRT can be done with coupled hydraulic and thermal numerical models [27, 103]. Indeed, Robert et al. (2022) [27] recently interpreted a TRT in the presence of high hydraulic conductivity ($>5 \times 10^{-5}$ m/s) and obtained a mean absolute error of 0.04 ºC between the modelled and measured temperatures. To construct their numerical model, the values of the layered hydraulic conductivity were chosen based on the groundwater cumulative flow observed during drilling and matched with the mean hydraulic conductivity estimated with a pumping test. In this model, the hydrostratigraphic properties are essential to accurately reproduce the measured temperatures [40]. For closed-loop ground-heat exchangers, the identification of hydraulic flux with a thermal response test has been demonstrated in presence of advection. Indeed, interpretation methods have proposed to use the Peclet number to deduce groundwater velocities [222, 223] and average hydraulic conductivity [94]. Moreover, Lehr & Sass (2014) [222] made use of the groundwater cumulative flow observed during drilling to correlate Peclet number to the thermal conductivity along the profile. Altogether, no TRT interpretation method has yet offered a robust identification of the hydraulic properties around SCWs. Robustness implies that the methodology employed leads to accurate results, while also dealing with any error it faces. For TRT, errors come from three sources according to Witte (2013) [105]. These are measurement errors (instrument precision and resolution), parameter errors (fixed parameters such as borehole length or radius) and model errors (accuracy of the conceptual model itself). For a simple analytical model, an analytical expression of the uncertainty can be used to describe the confidence interval of the variables [105]. For more complex mathematical models, Pallard & Lazzarotto (2021) [224] developed a methodology in a stochastic framework taking into account the measurement error and allowing for bias estimation. With a similar goal in mind, Choi et al. (2018a) [100] used Bayesian inference to obtain the statistical distributions of unknown thermal properties. Yet, their approach neglected the temporal correlation of the residuals, which is present in temporal series. To solve this problem and accelerate inference, Pasquier & Marcotte (2020) [86] proposed a closed-form equation for the likelihood and an artificial neural network for direct simulations. In a similar way, this article proposes to use Bayesian inference to assess both the hydraulic and thermal properties surrounding a SCW with TRT data. The methodology used provides the marginal and joint distributions of the properties and, thus, an uncertainty quantification. Since the approach requires millions of simulations, an efficient direct model in the form of a neural network is trained to reproduce the temperatures measured at an experimental SCW. The following sections describe the

methodology, an overview of the experimental setup and the main results obtained.

Methodology

Bayesian inference

The Bayesian inference framework leads to the marginal and joint distributions of variables θ by drawing from the posterior distribution $P(\theta|\mathbf{x})$ given observations $\mathbf{x}$. In the case of a TRT, these observations are the residuals between the simulated and observed temperatures. The posterior is sampled using a Markov Chain Monte Carlo (MCMC) algorithm which makes use of the simplified Bayes Theorem (Equation B.1).

$$P(\theta|\mathrm{x}) \propto P(\theta) \cdot P(\mathrm{x}|\theta) \tag{B.1}$$

Prior distributions $P(\theta)$. Firstly, the prior is defined before observations are available. Indeed, a prior reflects an expert judgment of a random variable behaviour. Previously, both Choi et al. (2018a) [100] and Pasquier & Marcotte (2020) [86] opted for non-informative uniform priors for all variables. The inference results for these studies showed Gaussian marginal distributions for the thermal properties. Considering these past results, Choi et al. (2018b) [101] used triangular prior for the effective thermal conductivity. Again, they obtained marginal distributions following a Gaussian model. On this basis, the present study is using Gaussian distribution as prior, but large standard deviations (σ) are used for each variable. A similar approach was used for hydraulic conductivity as this assumption allows the mean hydraulic conductivity to stay closer to the one deduced from the pumping test.

Likelihood function $P(\mathbf{x}|\theta)$. The second step is to evaluate the likelihood function which expresses the probability of making observations conditional to some input properties. The likelihood of the residuals is described by a zero-mean multi-Gaussian distribution which considers temporal correlation, as expressed by Equation B.2.

$$P(\mathrm{x}|\theta) = (2\pi)^{(-n/2)} \mid \Sigma \mid^{-1/2} e^{-1/2\mathrm{x}'\Sigma^{-1}\mathrm{x}} \tag{B.2}$$

For large covariance matrix (Σ), evaluation of Equation 2 is costly and this work used the exact closed-form solution proposed by Pasquier & Marcotte (2020) [86] to ease its evaluation. The solution requires modeling the variogram of the residuals and estimation of the variance and correlation range.

Posterior sampling $P(\theta|\mathbf{x})$. To sample the posterior distribution an ensemble slice sampler based on the work of Karamanis & Beutler (2021) [185] and allowing for a parallel and efficient

inference was used. The sampler was employed with 50 parallel chains and 100 000 samples per chain. Since the acceptance rate was around 15%, the direct model was called more than 33 million times. A fast and efficient direct model is therefore required to complete the inference in a realistic time frame.

Direct model and training database

A coupled numerical model was constructed within the Comsol Multiphysics environment (Comsol, 2022) [225] to simulate groundwater flow and heat transfer. This model was used to assemble a training database that was used later to train an artificial neural network (ANN) designed to construct the short-term g-function of the SCW. The numerical modelling strategy is the same as the one described by Beaudry et al. (2019) [40]. An axisymmetric model is used to represent the SCW with the center of the well located on the symmetry axis. Table B.1 presents the main components of the numerical model as reported by Robert et al. (2022) [27] for the study site. The thermal conductivities of the subsurface materials ($k_{s,i}$) and the hydraulic conductivities of the hydrostratigraphic layers ($K_{h,j}$) are variable in the inference. The thermal boundary conditions are composed of a null heat flux at the bottom of the model and a constant temperature at the surface and at the far field. These boundary conditions are based on the quasi-constant temperature observed in the wells during three different thermal profile logging. Regarding the hydraulic boundary conditions, flow was restricted at the bottom and top of the model and a constant hydraulic head was applied at the far-field limit to represent the fact that groundwater was 2.5 m deep. Finally, the groundwater flow was simulated under a steady state since a long continuous circulation phase is conducted in the TRT before heat injection.

Artificial neural network and simulation approach

The numerical model exploits an optimized mesh and efficient solver. However, computation of the g-functions is still long for the current purpose of this study. Indeed, every call of the numerical model requires more than a minute and the inference process would converge after multiple years of computation. To accelerate the inference, an ANN inspired from Pasquier et al. (2018) [84] and Pasquier & Marcotte (2020) [86] was used as a surrogate model. The ANN architecture includes 10 hidden layers with 50 neurons each and an output layer of 95 neurons. The input layer is composed of seven parameters (θ) and nine enriched parameters (ψ), chosen to accelerate network training. Here, these parameters are the thermal diffusivity ($\omega = k/C$), hydraulic transmissivity ($K \cdot b$) and the weighted average of k and K ($\bar{k}$ and $\bar{K}$). Table B.2 summarizes these parameters. Before training the ANN, a transformation is applied

Tableau B.1 Numerical model main components for the SCW and subsurface materials

Parameter	Units	Water/ Well	HDPE	Till	Sandy dolomite	Quartz arenite
Thickness (b)	m	133.20	0.00549	10.05	89.01	34.14
Diameter (ϕ)	m	0.152	0.0493/ 0.0603	150*	150*	150*
Porosity	%	–	0.001	20	2.2	5.9
Volumetric heat capacity (C)	MJ/(m^3 K)	4.18	2.28	2.30	2.31	2.18
Thermal conductivity (k)	W/(m K)	0.56	0.42	θ	θ	θ

*This diameter represents the extension of the axisymmetric numerical model.

to the short-term g-function as it also helps the training process. Moreover, a normalization between -1 and +1 is applied to all input and output.

The ANN directly provides the g-function corresponding to the entering water temperature (EWT) at the TRT unit (Figure B.1 a)). Then, the leaving water temperature (LWT) signal is obtained efficiently using fast Fourier transforms (see Marcotte & Pasquier, 2008 [59]; Pasquier et al. 2018 [84]) through :

$$LWT(t) = T_{i=0} + (f * g)(t) + \Delta T(t) \tag{B.3}$$

where g is the short-term g-function and f is the excitation function specified by Equation B.4.

$$f(t) = \Delta T(t_i) - \Delta T(t_{i-1}) = \frac{\dot{Q}(t_i) - \dot{Q}(t_{i-1})}{\dot{V}C} \tag{B.4}$$

Tableau B.2 Training parameters (θ) and enriched parameters (ψ)

Parameter	Till	Sandy dolomite	Quartz arenite	Hydrostratigraphic layers			
θ	$k_{s,1}$	$k_{s,2}$	$k_{s,3}$	$K_{h,2}$	$K_{h,3}$	$K_{h,4}$	$K_{h,5}$
ψ	$\alpha_{s,1}$	$\alpha_{s,2}$	$\alpha_{s,3}$	$K_{h,2} \cdot b_{h,2}$	$K_{h,3} \cdot b_{h,3}$	$K_{h,4} \cdot b_{h,4}$	$K_{h,5} \cdot b_{h,5}$
	$\bar{k}$(weighted average)			$\bar{K}$(weighted average)			

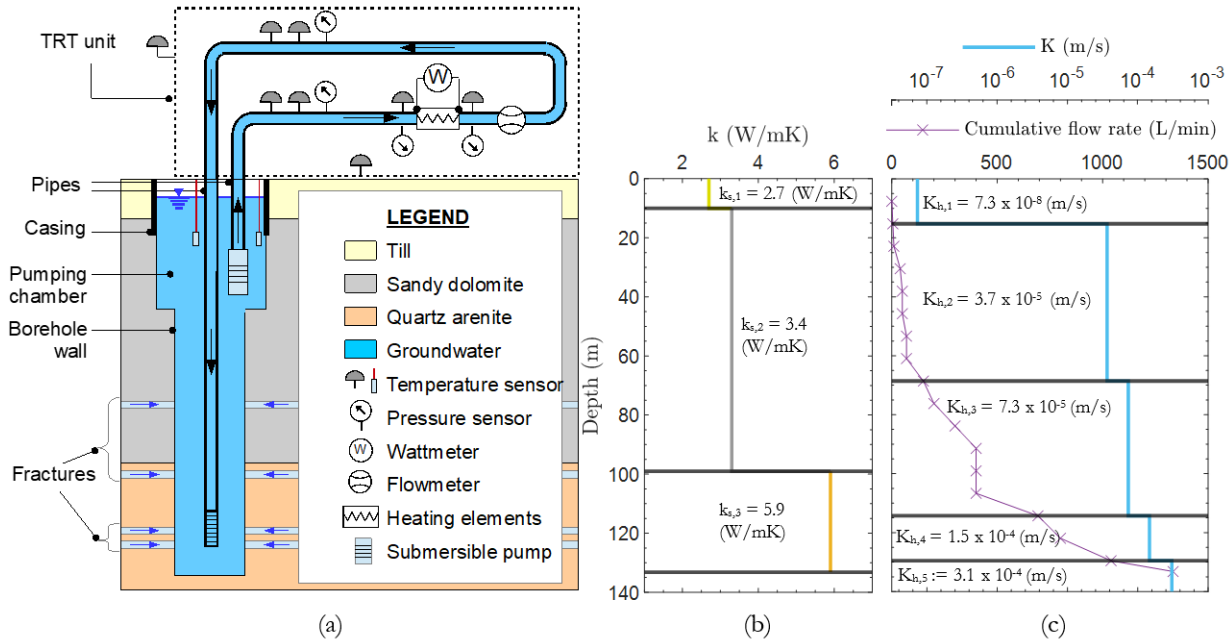

FIGURE B.1 a) Stratigraphy, experimental SWC and TRT unit. b). Stratigraphy and base case values of thermal conductivity (k_s,i for i=1, 2 and 3) for each subsurface materials. c) Hydrostratigraphy, groundwater flow rates observed during drilling and base case values of hydraulic conductivity ($K_{h,j}$ for j=1,2,3,4 and 5) for each hydrostratigraphic layers is shown in pale blue.

Experimental case study

A TRT was conducted at an experimental site located in the city of Mirabel, Québec. The study site is described in detail by Robert et al. (2022) [27]. Figure B.1a) presents the TRT unit connected to the SCW. The TRT unit includes monitoring of the entering and leaving water temperature (EWT and LWT). For their base case, Robert et al. (2022) [27] demonstrated an optimal fit of temperatures with specific values of thermal and hydraulic conductivities. Figure B.1b) shows these base case values for the thermal conductivity varying according to the three subsurface materials. Figure B.1c) shows the hydraulic conductivity following the five different hydrostratigraphic units (light blue). These hydrostratigraphic units are based on the variation of groundwater flow regime in the materials and their delimitation is independent of the nature of these materials. This hydraulic conductivity profile matches the groundwater cumulative flow observed while drilling and the mean value of 6.5×10^{-5} m/s obtained by the pumping test [27]. Also, Figure B.1c) illustrates groundwater cumulative flow rates observed while drilling.

Figure B.2 (upper left) presents the observed LWT during the TRT and the simulated tem-

peratures. The temperature variation ΔT is used to evaluate the excitation function $f(t)$ shown on the right axis. This TRT is separated in two phases. The first one is a continuous circulation phase that lasted for approximately 18 hours. Afterwards, the heating phase was started and lasted 83 hours. During this phase, the heating elements were powered at around 21 kW. Figure B.2 (lower left) presents the residuals between simulated and observed temperatures during the heating phase. Note that the first 4.67 hours were discarded. Indeed, the circulation pump was interrupted for 103 minutes prior to the heating phase and fitting the model to the data was more difficult at the onset of the TRT. Finally, Figure B.2 (right) shows the variogram corresponding to the optimal residuals as obtained by a single multidimensional optimization. The variogram has a variance of $\sigma^2 = 1.2 \times 10^{-3}$ °C^2 and a correlation range of $a = 12$ h.

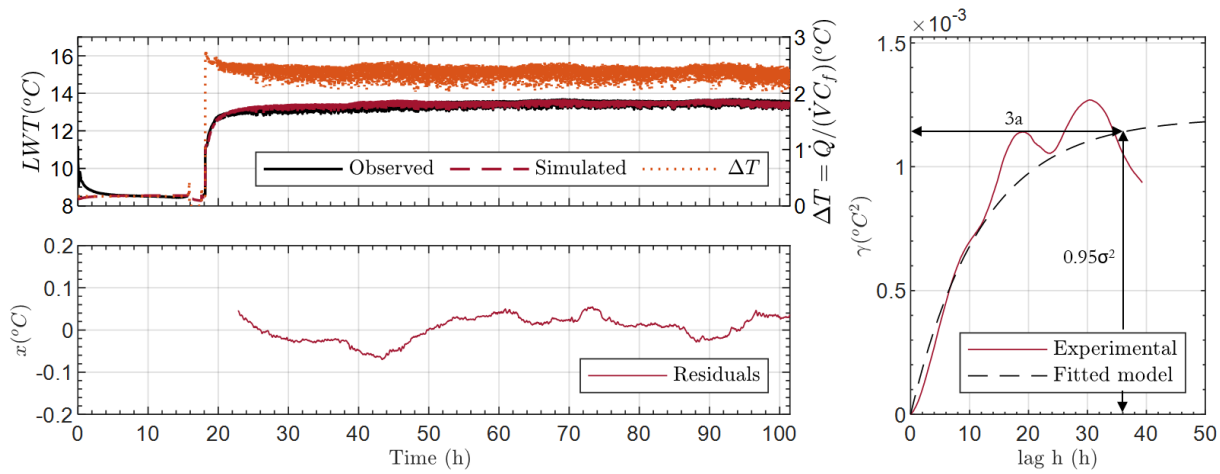

FIGURE B.2 Upper left : Observed and optimal simulated leaving water temperatures used to compute residuals x and temperature variation ΔT used to compute excitation function f. Bottom left : temperature residuals used to compute experimental variogram. Right : experimental variogram (γ) and fitted covariance model.

Results and discussion

A Bayesian inference was conducted using the parameters of the experimental variogram to evaluate the likelihood. Gaussian priors were set for the three subsurface thermal conductivities ($k_{s,i}$ for i=1, 2 and 3) and for the four deepest hydraulic conductivities ($K_{h,j}$ for j=2 to 5). Indeed, the first hydrostratigraphic layer is not inferred as this layer is sealed with a casing for most of its depth. Hence, we observed that this layer's hydraulic conductivity has no significant influence on the evolution of EWT.

The Bayesian inference is completed with a posterior distribution of 100 000 samples for each of the 50 chains, for a total of 5 million samples. The acceptance rate reached 14.4%, resulting in a total of 34.7 million simulations and a computation time of approximately 116 hours. A burn-in period of 50 000 samples per chain was used to analyze the marginal and joint distributions. Accordingly, Figure B.3 presents these distributions, along with a scatter plot showing the correlation between each pair of variables. On the diagonal, the marginal samples are plotted in orange, while the green line corresponds to the prior distributions. As an indication of the success of the inference, the mean absolute error of the corresponding residuals stands between 0.02 °C and 0.04 °C (at a two-sigma level). These results correspond to the mean absolute error (MAE) of 0.04 °C obtained by Robert et al. (2022) [27] for their base case and which correspond to the vertical black lines in Figure B.3.

Marginal (diagonal) and joint (lower triangle) distributions of the hydraulic conductivity of the four deepest hydrostratigraphic layers (Kh,i for j=2, 3, 4 and 5) and thermal conductivity of the different subsurface materials (ks,i for i=1, 2 and 3). Scatter plots and correlation (upper triangle). On the diagonal, the Gaussian prior are drawn in green and the dashed black lines represents the base case values from Robert et al. (2022) [27].

The most striking result is the fact that inferred distributions are all well defined Gaussian-like distributions and all significantly differ from their priors. Even more interesting is the fact that the mean hydraulic conductivity obtained in this work is almost the same as the one obtained by a pumping test. Indeed, Figure B.4 a) presents the weighted average for all samples of K using the unit's thickness b as weight. The mean value inferred is 7.5×10^{-5} m/s while a value of 6.5×10^{-5} m/s was obtained with a pumping test, leading to a difference of +1.5% of their logarithmic value. Therefore, inferring hydraulic properties with a TRT is feasible and can be done with great accuracy.

Figure B.4b) presents a comparison with the reference case from Robert et al. (2022) [27] for the inferred hydraulic conductivities. The mean values of the marginal distributions for the three deepest units are all inferior (orange dashed line) to the reference case, while the value of the second layer is higher. Thus, the inferred mean values observed on Figure B.4b) contradict the pattern of the reference case that was based on the cumulative groundwater flow observed during drilling (see Figure 1). In fact, these drilling observations are prone to increasing error as the cumulative flow rise. This is somehow illustrated by the fact that confidence interval for the hydraulic conductivities increases with depth with values of 6%, 18%, 19% and 22%. Even so, all hydraulic conductivities from the reference case are within the uncertainty of the inferred hydraulic conductivities.

For the thermal conductivities, Figure B.4c) indicates that the values of the first and last

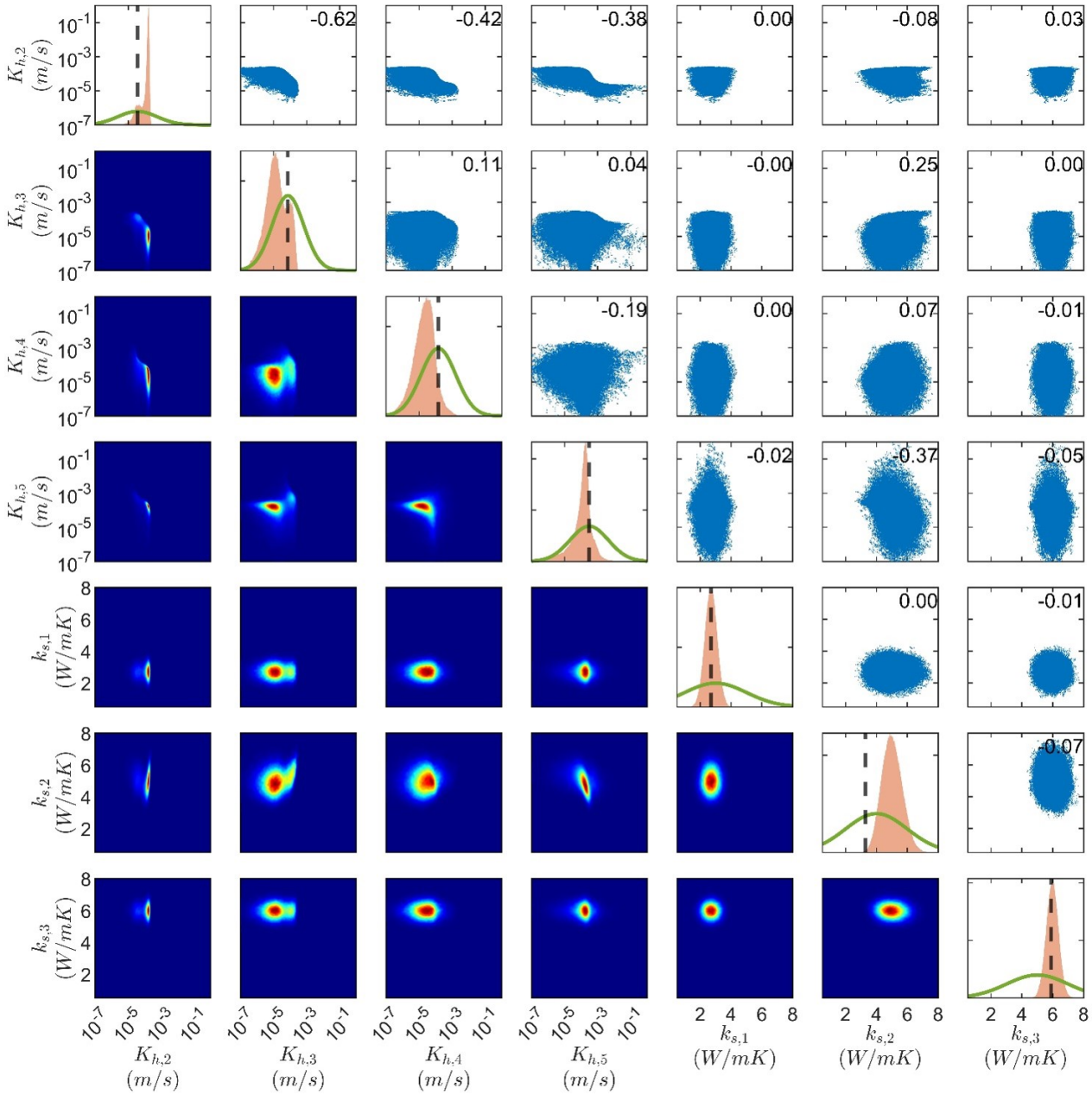

FIGURE B.3 Marginal (diagonal) and joint (lower triangle) distributions of the hydraulic conductivity of the four deepest hydrostratigraphic layers ($K_{h,i}$ for j=2, 3, 4 and 5) and thermal conductivity of the different subsurface materials (k_s,i for i=1, 2 and 3). Scatter plots and correlation (upper triangle). On the diagonal, the Gaussian prior are drawn in green and the dashed black lines represents the base case values from Robert et al. (2022) [27].

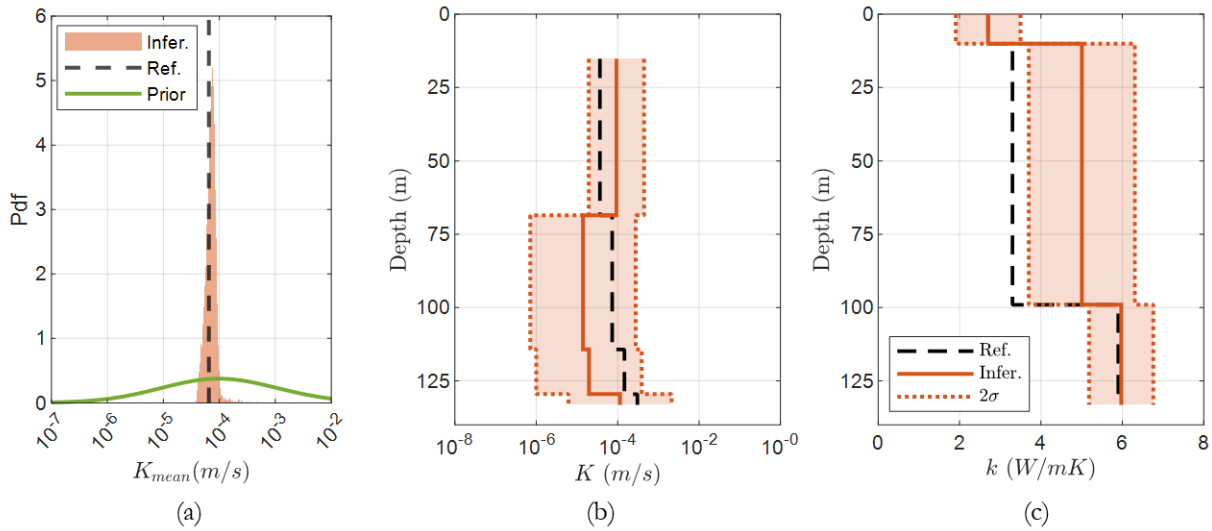

FIGURE B.4 a) Weighted average of the hydraulic conductivities. Values obtained by inference (orange), by a pumping test (black) or given by the prior (green). b) Mean hydraulic conductivties for each hydrostratigraphic unit and c) and thermal conductivity of subsurface materials and their uncertainties at a two-sigma level.

subsurface materials are unchanged in comparison with the reference case. However, the value inferred for the sandy dolomite ($k_{s,2}$) reached 5.0 W/(mK) in contrast with expected value of 3.4 W/(mK), leading to a difference of 47%. It should be noted, however, that the value of 3.4 W/(mK) comes from a laboratory test performed on a rock sample gathered a few kilometers from the study site. To finish, we mention that as reported by Jeon et al. (2016) [39], it is difficult to obtain accurate thermal conductivity in a context of high hydraulic conductivity ($>5 \times 10^{-5}$ m/s).

Conclusion

In this paper, a methodology is proposed to infer hydraulic conductivities and their uncertainties with a thermal response test (TRT) conducted on a standing column well (SCW). In a Bayesian framework, the computation of likelihood is completed considering residuals between measured and simulated temperatures. To ease the evaluation of the likelihood, an exact closed-form solution of the likelihood is employed. The temperature is simulated with an artificial neural network mimicking a numerical model that couples heat transfer and groundwater flow. A case study presents a TRT conducted on a SCW. High cumulative groundwater flows were observed during drilling. Thus, advective heat transfer plays an important role for this case study. Using Bayesian inference, it was shown that identification

of hydraulic properties is possible with a thermal test. The average hydraulic conductivity inferred has a diffrence of 1.5% in comparison with the results of a pumping test conducted on the same SCW. Moreover, the highest confidence interval reached 22% for the hydraulic properties.

Acknowledgments

The authors acknowledge the support from partners of the Geothermal Research Chair on the Integration of SCWs in Institutional Buildings, namely Hydro-Québec, the Ministry of higher education of Québec, Mille-Îles School Service Centre, Montreal School Service Centre, Samares School Service Centre, Versaprofiles, Marmott Energy, CanmetEnergy and NSERC. Additionally, we thank the anonymous reviewers and colleagues (A. Courchesne and M. Arbi Ben Aoun) that provided constructive comments. This work was financed by the Natural Sciences and Engineering Research Council of Canada through grant number ALLRP 544477-19.

Nomenclature

Symbols

α	thermal diffusivity (m^2/s)
b	thickness (m)
C	volumetric heat capacity ($J/(m^3K)$)
f	excitation function (°C)
g	short term g-function (-)
γ	variogram function ($units^2$)
ϕ	diameter (m)
k	thermal conductivity (W/(mK))
K	hydraulic conductivity (m/s)
n	number of residuals (-)
P	probability
$\dot{Q}$	heating power (W)
σ	standard deviation
T	temperature (°C)
θ	parameters
ψ	enriched parameters
x	temperature residuals (°C)

$\dot{V}$	circulation flow rate (m^3/s)

Subscripts

h	hydrostratigraphic layer
s	subsurface layer

ANNEXE C ARTICLE – INVESTIGATION OF EFFECTIVE BLEED STRATEGIES FOR STANDING COLUMN WELLS USING EXPERIMENTAL TRANSFER FUNCTIONS

Louis Jacques*, Philippe Pasquier
Proceedings of the IGSHPA Research Conference, Montréal, May 28-30, 2024
Department of Civil, Geological and Mining Engineering, Polytechnique Montréal, P.O. Box 6079 Station Centre-Ville, Montreal H3C 3A7, QC, Canada.
* Corresponding author : louis.jacques@polymtl.ca

Abstract

Standing column wells are an efficient type of ground heat exchanger that continuously recirculates groundwater in an uncased borehole. To increase heat exchange during peak load periods, a process called "bleed" is used. This process creates groundwater discharges that must be managed in accordance with local regulations and may incur additional costs, for example, if directed to injection wells. Alternatively, inter-well reinjection can be used to reroute the discharged water to other standing column wells. This study presents experimental results of a standing column well system operated during 35 days under four different reinjection modes. A full recirculation mode, basic mode, is compared to two levels of bleed and to the proposed inter-well reinjection mode. The experimental data were used with a robust deconvolution algorithm to extract a transfer function for each mode. These functions represent the thermal response of the system to a unit excitation, allowing for comparison of reinjection modes under the same heat load. Analysis of these transfer functions showed that, at the specific experimental site studied, the inter-well reinjection can be as efficient as a bleed operation. Thus, inter-well reinjection can successfully extend system use during peak load periods, while decreasing groundwater discharge to injection wells.

Introduction

In the building sector, energy demand continues to grow and record carbon emissions are being reported [193]. This is driving the need for more sustainable solutions for heating and cooling buildings. Ground source heat pumps (GSHP) are a promising solution with rapid growth potential [226]. An efficient type of ground heat exchanger is the standing column well (SCW), an open-loop system that recirculates groundwater in a unique uncased well.

The recirculation favours both direct conduction with the rock surface as well as advection through fractures and rock porosity [27]. Advective heat transfer can be enhanced by the use of bleed, which diverts a fraction of the pump flow outside the SCW [51]. The result is a radially convergent flow of groundwater toward the SCW, which increases the thermal output of the SCW and extends heat pump operation during periods of peak load [25, 227]. However, water discharges are generated by the bleed operation. Where permitted by law, discharged water can be disposed of in local sewers, or infiltrated into above-ground infiltration installations [22]. Otherwise, dedicated injection wells (IW) are built, elevating project costs and potentially impacting system efficiency if thermal interference between the IW and SCWs develops [53].

An alternative discharge strategy is to divert the bleed flow rate from one or several SCWs into the remaining SCWs [131]. In a series of thermal response tests, Kim et al. (2020) [131] used inter-well reinjection between a pair of 300-meter-deep SCWs. In this study, it was shown that inter-well reinjection outperformed full recirculation. Indeed, reinjection increased the coefficients of performance (COP) by 23 % in cooling mode and 12 % in heating mode. Although a direct comparison with bleed operations was not undertaken, analyzes suggest that inter-well reinjection is similarly efficient [136]. Consequently, it can provide a solution for reducing the amount of water discharged to injection wells, in jurisdictions that do not allow surface discharge.

Until now, inter-well reinjection has only been experienced through thermal response tests and has not yet been used under realistic building operating conditions. In thermal response tests, heating power and flow rates are meticulously controlled and are chosen to be as constant as possible [167]. Nevertheless, the data obtained from these tests may be subject to a high degree of variation due to interruptions or fluctuations in the power supply, for example [98]. For buildings, predicting the heat loads of a GSHP system is complex and prone to several external factors [228]. To test the performance of inter-well reinjection under realistic building operating conditions, a method of analysis under variable thermal loads is required.

To overcome the limitations of analyzing signals subjected to variable excitation, recent advances in the application of deconvolution algorithms are applied to thermal response tests [62, 98] and on long-term GHE simulations for synthetic data [195]. Developed deconvolution algorithms allow extracting a transfer function from a system subjected to a time-varying thermal signal. The transfer function then represents the response of a ground heat exchanger to a unit and constant thermal excitation for a given operation mode. If transfer functions are obtained for different operating modes, such as varying the circulating and bleed flow rates

[25, 63], the thermal response of these modes can then be compared. Thus, a deconvolution algorithm is a promising tool for analyzing performance of ground heat exchangers operated under different modes [198]. The deconvolution algorithm can fill gaps in the validation of the performance of inter-well reinjection in operational buildings, which has never been done. Previous studies [131, 136] have only used inter-well reinjection with thermal response tests to compare it with full reinjection, but not with bleed operation. Through deconvolution, transfer functions can be extracted to experimentally assess the effectiveness of different modes of reinjection. The transfer functions of inter-well reinjection can be compared to other reinjection modes, such as with or without bleed, to gain insights into the heat exchange process.

This study presents the results of a 35-day experimental test on five standing column wells used to provide cooling energy to an elementary school. The experiment is designed to validate the efficiency of inter-well reinjection under realistic operating conditions. Four modes of operation are tested : inter-well reinjection, full recirculation and two bleed levels. A robust deconvolution algorithm is used to retrieve the experimental transfer functions corresponding to the four modes of operation. Based on the experimental transfer functions, the different operating modes of SCWs are compared and conclusions are drawn about the efficiency of inter-well reinjection for the specific experimental site studied.

Methodology of the experimental study

Experimental setup, strategy and data acquisition

The experimental site is located in Mirabel, Canada [17, 27] and the GHE, composed of five SCWs, is illustrated in Figure C.1. Connected to an institutional building, the SCWs and an IW were constructed to depths of about 135 m. For each SCWs, a steel casing enclosed the 10 m thick overburden. Then, drilling operations revealed sub-horizontal sedimentary rocks. During drilling, cumulative flow rates of up to 1325 L/min were observed and interpreted to be from a productive fractured aquifer located mainly at the base of the boreholes [27]. Based on field observations, it is assumed that the main fractures are sub-horizontal. This results in a horizontal regional gradient, which is nearly perpendicular to the line formed by the SCWs. Cerclet et al. (2022) [229] have demonstrated that there are no significant risks of clogging at this site. Thermal profiles yielded an undisturbed temperature of 8.16 °C. Interpretation of a thermal response test and pumping tests improved understanding of the site while a Bayesian inference indicated a mean hydraulic conductivity of 8.2×10^{-5} m/s, a mean thermal conductivity of 3.95 W/(m K) and mean volumetric heat capacity of

2.41 MJ/(m^{3}K) [138]. In addition, a detailed model analysis indicated that advective heat transfer is active even under a full recirculation of the SCW, that is a SCW operated without bleed [27]. As the site presents good thermal and hydraulic conditions for the operation of SCWs, it was decided to compare various operation modes experimentally.

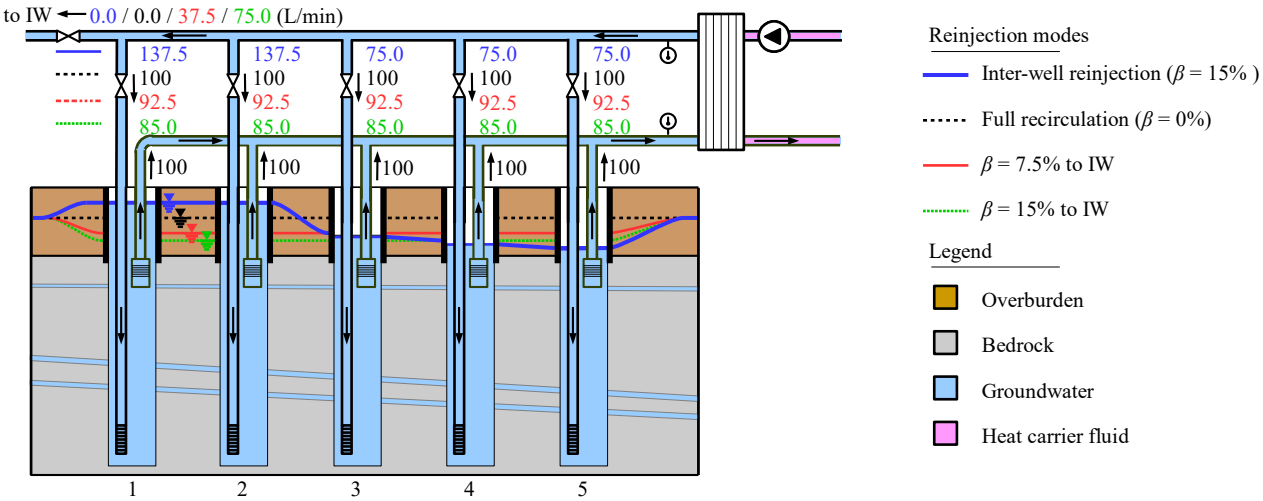

FIGURE C.1 Experimental site featuring five SCWs and four operating modes that vary reinjection flow rates (values reported along the return pipes), bleed ratios relative to total flow rates (β) and simplified water table levels (corresponding colored lines in the overburden area) ; Note that the injection well (IW) is not shown.

The goal of the experimental test is to gain insight into the efficiency of inter-well reinjection between SCWs. The methodology consisted to operate the SCWs under four reinjection modes. A constant overall flow rate of approximately 500 L/min (100 L/min per SCW) is maintained throughout all operation modes. The reinjection flow rates are shown in Figure C.1 over each well along with simplified groundwater levels in matching colors. Inter-well reinjection unbalances the water levels in the SCWs. Indeed, 15 % of the total flow rate is bled from SCW-3, SCW-4 and SCW-5 and reinjected into SCW-1 and SCW-2. In other words, 25 % of the individual pumping flow rate (100 L/min) is bled from these three wells. The reinjection was performed in SCW-1 and SCW-2 due to their position at an outer bound, which reduces thermal interference with the other SCWs. The baseline reinjection mode is the full recirculation mode and corresponds to a case where no bleed is activated (Figure C.1). In this mode, the pump flow rate is equal to the reinjection flow rate. Therefore, no significant changes in water levels are experienced. The last two modes represent bleed activation at ratios (β) of 7.5 % and 15 % of the total pumping flow rate. They result in a general lowering of the water table. In these two modes, the groundwater is discharged into the injection well located 22 m downstream of the SCWs.

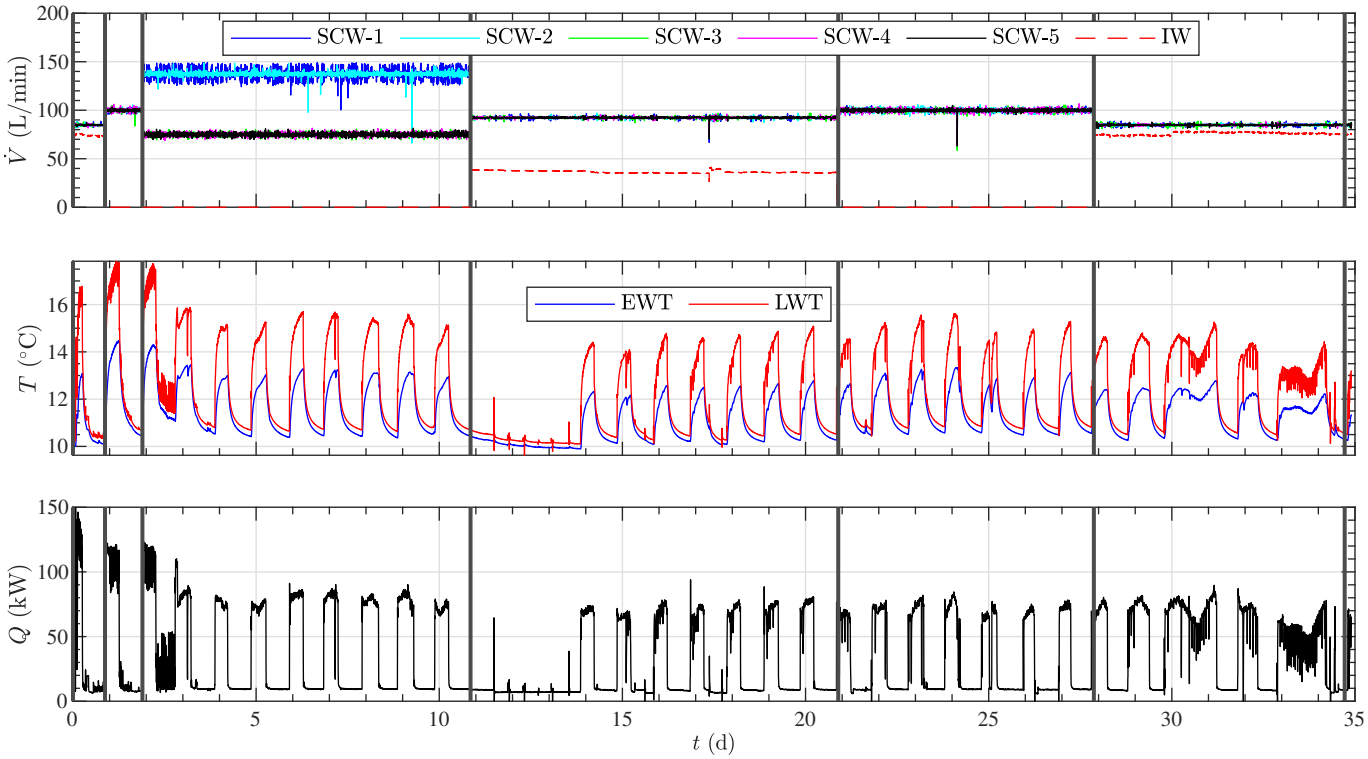

FIGURE C.2 Experimental data collected over a 35-day period. Top : flow rates at the SCWs and injection well (IW) ; Middle : entering (EWT) and leaving (LWT) water temperatures ; Bottom : ground loads based on total flow rates and temperature variations.

As depicted by the flow changes (vertical lines) at the top of Figure C.2, the operating modes changed six times over the course of the 35-day experimental test. The first two changes lasted one day and are not used in this study. Each mode change was designed to occur at the end of a recovery period during which heat is not actively transferred to the ground (bottom of Figure C.2). This choice was made to return the fluid temperature near the initial ground temperature. The first mode studied was inter-well reinjection and lasted from day 2 to day 11. The second mode ($\beta = 7.5$ %) started with three days of recovery and lasted 7 days. Finally, the third (full recirculation, $\beta = 0$ %) and fourth ($\beta = 15$ %) modes each lasted 7 days. It should be noted that the ground heat loads originate from the real cooling operation of the studied building. Therefore, the extent of the thermal restitution periods is limited by the heat demand of the building and a complete temperature recovery is not always met, as seen at day 13 in Figure C.2.

The middle and bottom of the Figure C.2 present the recorded temperatures and ground loads. When the building was occupied, cooling was activated for periods of approximately 8 to 10 hours each day, apart from 35 hours on day 30 and 32 hours on day 33. On day 1,

the ground loads rose to a maximum of 156 kW, and averaged 125 kW during the 3-hour peak. Over the entire test period, these loads averaged 71 kW. In each cycle, ground loads were followed by a period of recovery. In the latter, heat gains were observed between the entering (EWT) and the leaving water temperatures (LWT), for an average of 9 kW. Given these significant load variations, a deconvolution algorithm was chosen to analyze the data and extract transfer functions.

Deconvolution algorithm

The deconvolution algorithm used to identify the experimental transfer functions g is described in Dion et al. (2022a) [62] and summarized here. The algorithm iterates directly on the transfer function, so that it satisfies the objective functions and the deconvolution constraints. The transfer function is the system's response to a uniform and constant perturbation for constant operating conditions. This problem is expressed by :

$$T_{exp}(t) = (f * g)(t) + T_0 \tag{C.1}$$

In the previous equation, $T_{exp}(t)$ represents the observed temperatures, T_0 is the initial ground temperature, and f is the incremental load function. Specifically, $T_{exp}(t)$ corresponds to the entering water temperature at the heat pump (**EWT**) and f is given by Equation C.2.

$$f(t) = Q(t_i) - Q(t_{i-1}) \quad \text{with} \quad Q(t) = \dot{V}(t)C_f(LWT(t) - EWT(t)) \tag{C.2}$$

where Q is the heat loads (W), $\dot{V}$ is the total flow rate (m^3/s), C_f is the volumetric heat capacity of the fluid ($J/(m^3\ °C)$) and **LWT** is the leaving water temperature (°C). Note that f and g are vectors. As described by Dion et al. (2022a) [62] and shown in Equation C.3, the deconvolution algorithm optimizes the transfer function through a minimization problem under a set of constraints. The problem is as follows :

$$\hat{g} = argmin_g E(t_1, ..., t_m)|\mathrm{C}_1, \mathrm{C}_2 \tag{C.3}$$

where $\hat{g}$ is the deconvolved transfer function, E is the multi-objective function defined by Equation C.4 and C_1 and C_2 are linear inequality constraints that enforces the transfer function to have a certain form, as defined in Dion et al. (2023) [63]. The objective function

is as follows :

$$E(t_1, ..., t_m) = \underbrace{\left[\sum_{i=1}^{m} W(t_i) \cdot \left(\hat{T}(t_i) - T_{exp}(t_i)\right)^2\right]^{1/2}}_{E_{\hat{T}}} + \underbrace{P_{\hat{g}'} \cdot \left[\sum_{i=1}^{m} (\hat{g}')^2\right]^{1/2}}_{E_{\hat{g}'}} + \underbrace{P_{\hat{g}''} \cdot \left[\sum_{i=1}^{m} (\hat{g}'')^2\right]^{1/2}}_{E_{\hat{g}''}} \tag{C.4}$$

where $E_{\hat{T}}$ is the root mean square errors (RMSE) of the difference between the calculated ($\hat{T}$) and the observed T_{exp} (EWT), $E_{\hat{g}'}$ and $E_{\hat{g}''}$ are the RMSEs of the transfer function's first and second derivatives. The weighting factor $W(t_i)$ assigns a higher value to the first 5 % of the temperature fit values to ensure good early time reconstruction of the transfer function. In this case, the first 5 % of the signal is given a value of three and the rest is given a value of one. $P_{\hat{g}'}$ and $P_{\hat{g}''}$ are proportionality factors that regulate the effect of additional constraints and are set to 10 and 100, respectively, in this study. Minimizing this objective function with a constrained nonlinear solver yields the transfer function of the GHE under constant operating conditions.

Results and discussion

Computed temperatures from the deconvolutions

The deconvolution algorithm was used to analyze each mode of operation. Figure C.3 shows the computed temperatures from the deconvolutions, superimposed to the selected periods. About five days of data is included in each deconvolution. The residuals between the experimental and temperature signals obtained by deconvolution are shown at the bottom of Figure C.3. Also printed over the residuals are the RMSE associated with each computed segment.

The deconvolution algorithm has proven its effectiveness in tests conducted under constant operation and undisturbed initial conditions [62]. It has also been successfully applied to long-term GHE simulations for synthetic data [195]. This particular experiment involves variable operating conditions, i.e., reinjection flow rates. Therefore, after careful examination of the signal, it was chosen to discard at least one cooling cycle per operating mode. This was to allow proper heat dissipation from the previous mode. For the inter-well reinjection mode, four cycles were excluded, as it was preceded by two days of heat perturbation with different operating conditions.

Due to the short recovery times, initiating the deconvolution algorithm with a period as close to the undisturbed ground temperature as possible proved to be a challenge. As a

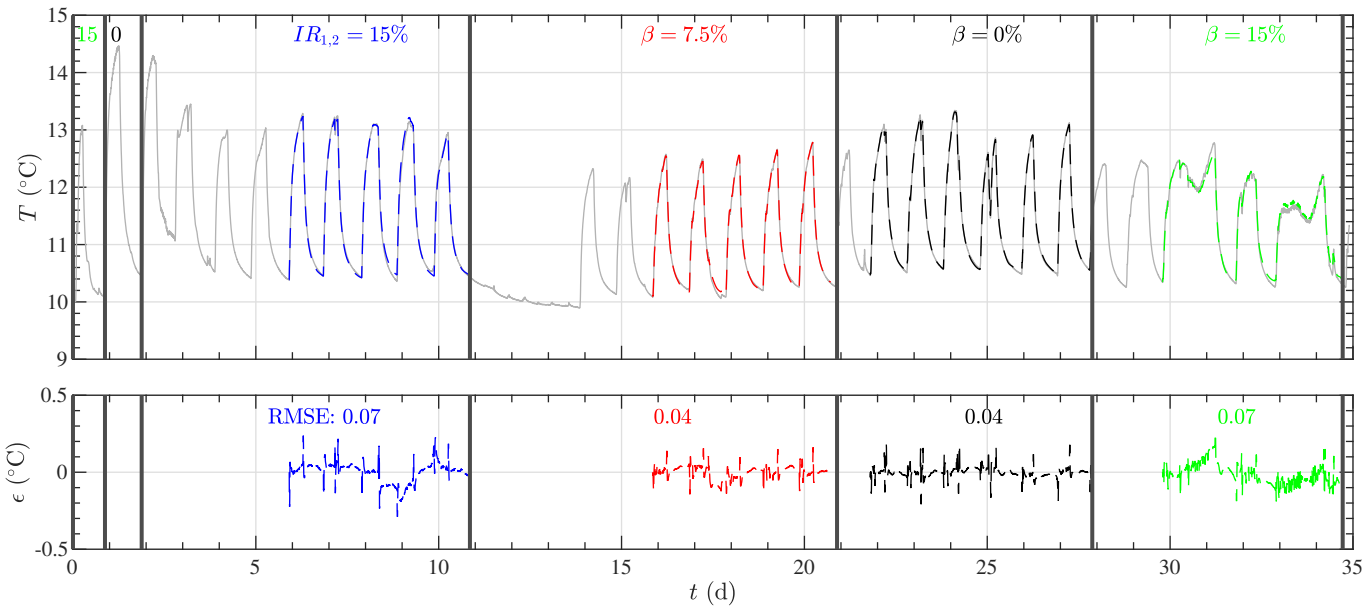

FIGURE C.3 Representation of the data selected for each deconvolution ; Top : experimental temperatures compared to computed temperatures using the estimated $\hat{g}$; Bottom : residuals between the experimental and computed temperatures, along with their root mean square errors (RMSE).

result, the most appropriate candidate for the deconvolution was the cycle starting with the lowest temperature. For meaningful comparisons, maintaining consistent settings for each mode was found to be important.

Estimated transfer functions

The resulting transfer functions for the four different modes of operation are shown on the left side of Figure C.4. The right side shows the relative difference between the baseline transfer function ($\hat{g}_{\beta=0\%}$) and the other functions ($\hat{g}_i$). As shown in the right panel of Figure C.4, the transfer function of the inter-well reinjection reached a maximum relative difference of 10 %, compared to the baseline ($\beta = 0$ %). This result indicates that the use of inter-well reinjection helps to limit ground temperature variations compared to the baseline operation. For this cooling-only study, this translates into lower ground temperatures. Consequently, inter-well reinjection has similar benefits to bleed operation on peak load periods with the added advantage of avoiding water discharge outside the system.

The deconvolution algorithm successfully yields four smooth transfer functions with periods of about 5 days (left of Figure C.4). In accordance with the literature, the transfer functions for t=5 days are lower with bleed activation than with a full recirculation [25, 63, 195]. As

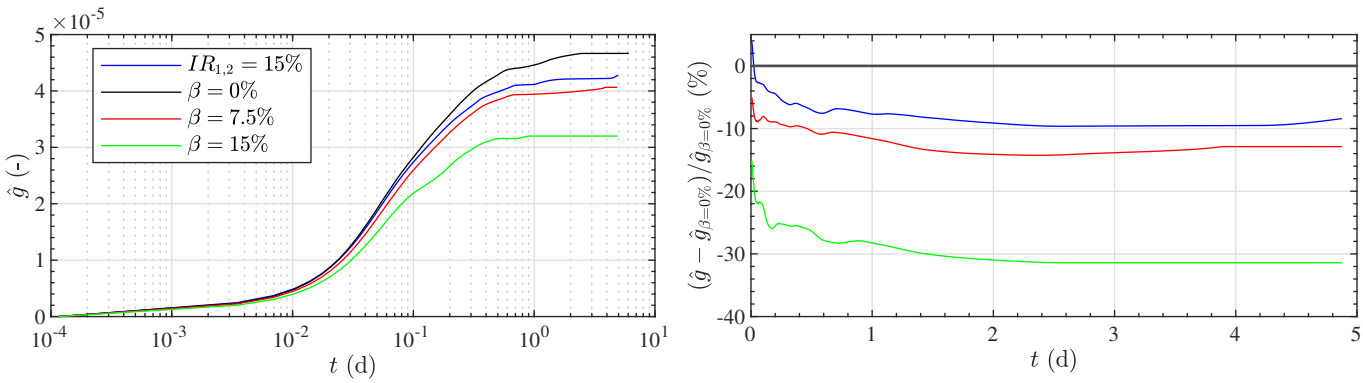

FIGURE C.4 Result of the deconvolution algorithm for the four modes of operation ; Left : experimental transfer functions $\hat{g}_i$; Right : relative difference between the baseline $\hat{g}_{\beta=0\%}$ and the other experimental $\hat{g}_i$.

bleed ratios increase from 7.5 % and 15 %, one can also see in Figure C.4 how the transfer functions decrease. All functions show a change in trend after about 1.5×10^{-2} days (22 minutes). This is equivalent to the theoretical residence time of the fluid in the SCW that includes 2 minutes for the downward path and 20 minutes for the upward path. All four functions reach steady state in about a day, with short-term behavior being similar for all operating modes. This underscores the exceptional performance of the SCWs at this site, also reported by Robert et al. (2022) [27]. On the other hand, the results obtained by the deconvolution algorithm are less smooth after one day.

Inter-well reinjection performed better than the full recirculation (right side of Figure C.4). After two days, the transfer function is about 10 % lower than the full recirculation mode (β=0 %). Although not as efficient as a 15 % bleed ratio, inter-well reinjection is almost as efficient as the operation mode with a 7.5 % bleed ratio. At the site studied, full recirculation is already very efficient, with advection reportedly contributing about 265 times more to the thermal response than conduction [27]. However, in geologic settings where groundwater flow rates are not high (less than 1×10^{-6} m/s), Kastrinos et al. (2019) [44] reported conduction as the dominant heat transfer process. At a site with less favorable hydraulic properties, the relative difference between full recirculation and inter-well reinjection should then be greater.

Conducted with a GSHP system in operation, this simple experiment demonstrates that inter-well reinjection is a viable candidate to replace bleed. In fact, the presented inter-well reinjection method discharged only 15 % of the total flow rate, resulting in a performance similar to the one obtained with bleed ratio of 7.5 %. One could imagine that increasing the discharged flow rate could result in a performance equivalent to a bleed ratio of 15 %.

Conclusion

This article investigates the efficiency of standing column wells (SCW) operated with inter-well reinjection. To accomplish this, an experimental test is performed in which a building is cooled by five standing column wells. During this 35-days experiment, the SCWs are operated with four reinjection modes, namely the inter-well reinjection, full recirculation and two bleed levels of 7.5 % and 15 %. The inter-well reinjection mode bled 15 % of the total flow in three SCWs and reinjected in the other two. A robust deconvolution algorithm is used to obtain transfer functions for the four reinjection modes. Using the transfer functions, it is shown that inter-well reinjection maintains the advantages of the bleed, while not requiring a costly injection well. Indeed, the transfer function from the inter-well reinjection is almost as high as the one with a bleed ratio of 7.5 %. For simplicity, it is thus worthwhile to integrate inter-well reinjection strategies when designing the GHE field.

Since inter-well reinjection has the same impact as bleed, no additional steps are required to design a SCW system that incorporates this reinjection mode. State-of-the-art SCW design requires careful development of a site-specific conceptual model of the hydrostratigraphic context through, at a minimum, an exploratory well, a thermal response test, and pumping tests. Data from these tests are then used to calibrate a numerical model that simulates both hydraulic and thermal processes. To date, no research study has verified model calibration for inter-well reinjection simulations. Once this gap is filled, site-specific models can be used to improve the efficiency of standing column well systems with inter-well reinjection strategies. In the meantime, site operators could repeat this paper methodology to estimate the thermal responses of different reinjection modes at their site.

Acknowledgments

The authors acknowledge the support from partners of the Geothermal Research Chair on the Integration of SCWs in Institutional Buildings, namely Hydro-Québec, the Ministry of Higher Education of Québec, Mille-Îles School Service Centre, Montreal School Service Centre, Samares School Service Centre, Versaprofiles, Marmott Energy, CanmetEnergy and NSERC. Additionally, we thank the anonymous reviewers and colleagues that provided constructive comments. This work was financed by the Natural Sciences and Engineering Research Council of Canada through grant number ALLRP 544477-19.

Nomenclature

Symbols

β	Discharge ratio (%)
C	Volumetric heat capacity (J/(m^3 °C))
ϵ	Residuals (°C)
E	Objective function value (−)
f	Incremental heat load function (W)
μ	Average (−)
$g, \hat{g}$	Transfer function and its estimation (−)
P	Objective function terms' proportion (−)
Q	Heating power (W)
σ	Standard deviation (−)
t	Time array (s)
$T, \hat{T}$	Temperature and its estimation (°C)
$\dot{V}$	Flow rate (m^3/s)
W	Weights in the objective function (−)

Subscripts

0	initial
exp	experimental
f	fluid